Artificial Intelligence-Enabled Big Sensing Data Security for Wireless Sensor Networks

Lead Guest Editor: Xin Liu
Guest Editors: Hongjian Sun and Qingquan Sun

Artificial Intelligence-Enabled Big Sensing Data Security for Wireless Sensor Networks

Artificial Intelligence-Enabled Big Sensing Data Security for Wireless Sensor Networks

Lead Guest Editor: Xin Liu
Guest Editors: Hongjian Sun and Qingquan Sun

De Rosal Ignatius Moses Setiadi ⓘ,
Indonesia
Wenbo Shi, China
Ghanshyam Singh ⓘ, South Africa
Vasco Soares, Portugal
Salvatore Sorce ⓘ, Italy
Abdulhamit Subasi, Saudi Arabia
Zhiyuan Tan ⓘ, United Kingdom
Keke Tang ⓘ, China
Je Sen Teh ⓘ, Australia
Bohui Wang, China
Guojun Wang, China
Jinwei Wang ⓘ, China
Qichun Wang ⓘ, China
Hu Xiong ⓘ, China
Chang Xu ⓘ, China
Xuehu Yan ⓘ, China
Anjia Yang ⓘ, China
Jiachen Yang ⓘ, China
Yu Yao ⓘ, China
Yinghui Ye, China
Kuo-Hui Yeh ⓘ, Taiwan
Yong Yu ⓘ, China
Xiaohui Yuan ⓘ, USA
Sherali Zeadally, USA
Leo Y. Zhang, Australia
Tao Zhang, China
Youwen Zhu ⓘ, China
Zhengyu Zhu ⓘ, China

Contents

WILEY | Hindawi

Corrigendum

Corrigendum to "Randomization-Based Dynamic Programming Offloading Algorithm for Mobile Fog Computing"

Wenle Bai ,[1] Zhongjun Yang ,[2] and Jianhong Zhang [3]

[1]*Information Science and Technology, North China University of Technology, Shijingshan District, Beijing 100043, China*
[2]*School of Information Science and Technology, North China University of Technology, Shijingshan District, Beijing 100043, China*
[3]*North China University of Technology, Beijjing, China*

Correspondence should be addressed to Zhongjun Yang; 1076943446@qq.com

In the article titled "Randomization-Based Dynamic Programming Offloading Algorithm for Mobile Fog Computing" [1], one of the coauthors Rajiv Kumar has no contribution and was added incorrectly. The correct author list is shown above.

References

[1] W. Bai, Z. Yang, J. Zhang, and R. Kumar, "Randomization-Based Dynamic Programming Offloading Algorithm for Mobile Fog Computing," *Security and Communication Networks*, vol. 2021, Article ID 4348511, 9 pages, 2021.

WILEY | Hindawi

Research Article

ACPEC: A Resource Management Scheme Based on Ant Colony Algorithm for Power Edge Computing

Zhu Liu [ID],[1,2] **Xuesong Qiu** [ID],[1] **and Nan Zhang**[2]

[1]*State Key Laboratory of Networking and Switching Technology, Beijing University of Posts and Telecommunications, Beijing 100876, China*
[2]*State Grid Information & Telecommunication Group Co., Ltd, Beijing 102211, China*

Correspondence should be addressed to Zhu Liu; 13811068052@139.com

With the development of power IoTs (Internet of Things) technology, more and more intelligent devices access the network. Cloud computing is used to provide the resource storage and task computing services for power network. However, there are many problems with traditional cloud computing such as the long-time delay and resource bottleneck. Therefore, in this paper, a two-level resource management scheme is put forward based on the idea of edge computing. Furthermore, a new task scheduling algorithm is presented based on the ant colony algorithm, which realized the resource sharing and dynamic scheduling. The data of simulation show that this algorithm has a good effect on the performance of task execution time, power consumption, and so on.

1. Background

With the rapid development of smart grid, plenty of power equipment accesses into the Internet. The demand for power services shows exponential growth trend. For cloud computing technology, it not only can provide computing service but also has many advantages such as scalability, flexibility, and security [1].

Cloud computing can provide technical support and theoretical support for power design, data storage, disaster recovery, intelligent power consumption, and power grid simulation analysis system. Furthermore, cloud data center can integrate and manage the data and resources coming from different business systems in power grid uniformly, and these data and resources are the basic of resource sharing for smart grid. However, the total cost of a cloud will increase when the scale decreases, as shown in a survey of Microsoft [2]. Though the computational resource in the edge node is generally limited and the resource in the remote cloud is abundant [3], the resource features between edge cloud and the remote are different.

Edge computing can reduce the distance between user demand and computing servers [4, 5]. With edge computing, not only the computation latency of these tasks can be shortened but also the requirements of users on computation capability and power supply can be reduced [6]. Therefore, the computation tasks especially the latency-sensitive ones can be uploaded to edge nodes. The computation task can be received and executed locally, and the computation result can be sent to the users directly [7].

Heterogeneous cloud is suggested to better serve users with different Quality of Service (QoS) requirements [8]. Furthermore, to some computation-intensive tasks, tasks need to be divided into some subtasks and be executed by resource cooperation. In this paper, a new two-level resource management scheme is proposed based on edge computing. For the new resource management scheme, the computing tasks can be executed in local nodes, and the time delay can be decreased compared with cloud computing. Furthermore, according to the characteristic of edge computing, we present a task allocation algorithm based on the ant colony algorithm in this paper. The resources of the local edge nodes

can be used for providing computation-intensive tasks by resource sharing and cooperation.

2. Related Work

A rational resource management and task assignment scheme is very important to ensure the efficiency and stability of the power cloud computing system. There are many researchers who studied the resource management of cloud computing [9, 10]. For the resource management schemes on saving energy consumption, the authors in [11] proposed a new method to reduce the power consumption by decreasing the processor speed. The balance of load is considered in [12] and realized by effective virtual machine migration strategy; Furthermore, the authors proposed a new scheme for intelligent load migration and resource allocation by machine learning. For the resource management schemes of increasing resource utilization, the authors in [13] designed a two-level resource scheduling scheme and realized a new resource allocation algorithm by the heuristic algorithm. Furthermore, the authors in [14] proposed a new resource scheduling procedure which can realize a real-time vehicle cloud service. The authors in [15] proposed a QoS-based mobile cloud resource scheduling algorithm, which can minimize the communication and computing consumption. In addition, the genetic algorithm has also been used for saving energy consumption resource scheduling in [16, 17]. Furthermore, based on NOMA technology, the authors in [18, 19] introduced the resource allocation methods for cluster-based cognitive industrial and multi-beam satellite industrial.

For edge computing, one main service requirement is to have a low service delay, which would be the output of its request, i.e., the time it takes for the user to receive its results [20]. The authors of [21] proposed that the problem of time delay can be addressed by executing task applications on resource providers external to the edge device. In addition, to control the data transmission of computation tasks effectively according to the channel information, a delay-optimal problem is studied through adopting a Markov decision process approach [22]. The authors in [23] proposed an effective computation offloading strategy and investigated a green edge computing system with rechargeable devices. Furthermore, the authors in [24, 25] considered the balance between the cost of the system and the mean offloading delay, which studied the workload sharing between the edge and the remote cloud. For communication elements, one existing technique called access point scheduling is considered, in [26, 27], which can associate the user and the closest cloudlet in order to minimize transmission distance and improve signal quality and propagation time. In addition, in [28, 29], transmission power control is proposed where the transmission power of the cloudlets is carefully set with the final goal of lowering the latency. The authors in [30, 31] considered to provide fair services by allocating the available resources, such as channel bandwidth.

For the optimization of the QoS in the edge computing system, there are many research studies. The authors in [32]

considered the joint optimization of radio and computational resources to minimize the overall energy consumption of mobile users in edge computing. To minimize the total energy consumption of users, the authors proposed an algorithm for uplink and downlink beamforming and computational resource allocation [33]. In [34], the authors derived the optimal radio and computational resource allocation policy considering the scenario of TDMA networks. The authors in [35] designed a task offloading algorithm to study the energy-delay tradeoff in edge computing.

Such computing paradigm, called edge computing, has drawn extensive attention from both academy and industry [36, 37]. With the help of edge computing, application tasks running on the devices can be offloaded to the edge servers in edge computing to get better service. Generally speaking, the computing resources at the edge computing system are still limited compared with remote cloud data centers. Therefore, an edge computing is customarily backed by a remote back-end cloud via the Internet [38].

To a certain extent, above research studies solve some resource management problems. However, for the problem of the resource management power information system, there is not much research in the existing literature. Therefore, in this paper, a power resource management scheme based on edge computing is studied.

3. The Power Resource Management Scheme Based on Edge Computing

With the rapid development of cloud computing, more and more intelligent terminals access into the network. For traditional cloud computing, computing resource and storage resource are in the cloud data center and all tasks will be transferred to the cloud. For the power network, the power equipment includes a large amount of data information. Therefore, in power network, resource bottleneck of traditional cloud computing cannot be avoided, and the real-time performance cannot be ensured.

In the edge of power network, there are a lot of devices which include considerable resources. If the resources of these devices can be used for providing computing services, the computing energy of data center can be effectively supplemented [39]. In this paper, a new power cloud resource management scheme based on edge computing is proposed. In this scheme, some computing tasks in cloud servers will be sank to the edge devices, and the local computing tasks will also be performed in local edge devices.

In the new resource management scheme, as shown in Figure 1, there are two-level computing nodes: the first level includes the analysis control nodes which are in the cloud servers and the second level includes computing nodes which are in the edge devices. The first-level nodes are used to perform computation-intensive tasks and manage the second-level nodes, and the second-level nodes are used to perform local computational tasks. The resources in second-level nodes should be subjected to the scheduling of the first-level nodes. The application scenarios of this new resource management scheme can be the power supply service command system and big data platform, the hot spot
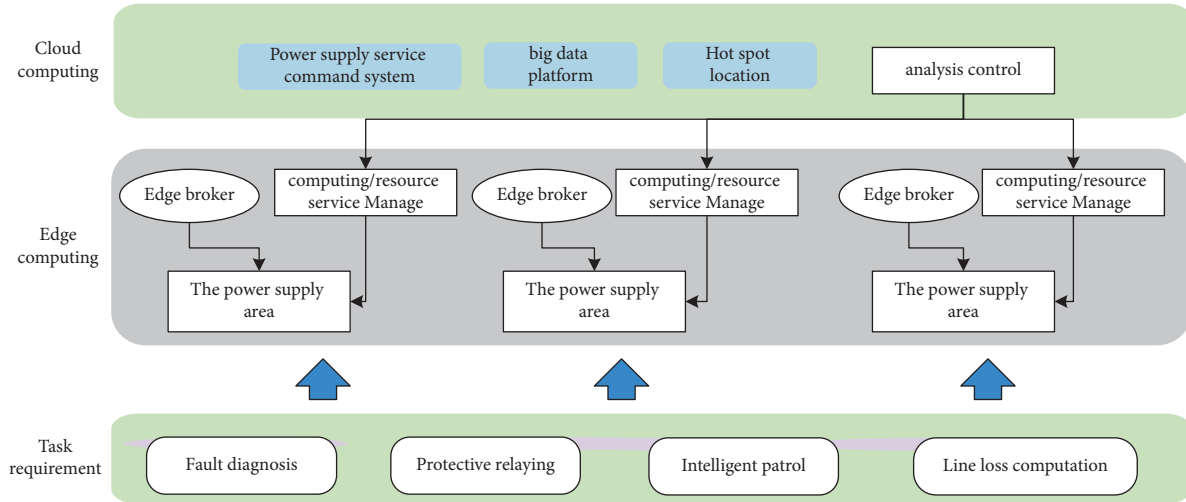
Figure 1: The resource management scheme based on edge computing for smart grid.

location, and so on. And the task requirement of this new resource management scheme can be fault diagnosis, protective relaying, intelligent patrol, line loss computation, and so on.

In this resource management scheme, the resource in the second-level nodes is limited and some tasks will be divided into many subtasks and be assigned to different edge nodes. The tasks will be executed by resources sharing and node cooperation.

In this paper, we consider an actual application scenario. As shown in Figure 2, this area represents a distribution power supply area, which includes many transformers, some intelligent terminals, and some users. In this situation, the intelligent terminals are set as the edge nodes to provide task computing services.

4. The Task Scheduling Method Based on Ant Colony Algorithm

The ant colony algorithm is an intelligent optimization algorithm, which is an optimization process for solving complex problems. The ant colony algorithm can be used for resolving resource allocation problem. In the paper, the edge nodes are always resource-limited to execute a computation-intensive task alone. Therefore, the computation-intensive tasks will be divided into many subtasks and be allocated on many different edge nodes. In this paper, we presented a new tasks allocation algorithm based on the ant colony algorithm to allocate appropriate resources for subtasks.

4.1. Introduction of Ant Colony Algorithm. The ant colony algorithm is a novel simulated evolvement algorithm solving complicated combinatorial optimization problem, and its typical feature is swarm intelligence. For the ant colony algorithm, a colony consisting of many ants is considered to perform a highly complex task that an ant alone cannot accomplish. The ant regulates their behavior through collaboration and information exchange. For the ant colony algorithm, pheromones play a very important role, which

can help ants judge the next direction of transfer by sensing the presence and concentration of pheromones.

The ant colony algorithm is a random search algorithm evolved from the behavior of ants foraging. In the process of simulating ant foraging, positive feedback and distributed cooperation are mainly used to find the optimal path. There are some characteristics in the behaviors of ant foraging shown as follows: firstly, the pheromone concentration along the path will change over time and the ant will choose the path according to the pheromone concentration of different paths. Secondly, to avoid the process of path choosing getting trapped in local optimality, the paths that have already been chosen before will not be allowed to be selected again. Thirdly, the pheromone of paths will decrease over time, and the length of the path will affect pheromone concentration.

4.2. The Detailed Design of Task Scheduling Algorithm. Recently, the task scale in power network increases rapidly, so the issue of task resource scheduling is increasingly complex. However, the rational scheduling among resources and tasks is very important for increasing the resource utilization and task completion rate.

For the resource management scheme proposed in this paper, the resources in the edge nodes are limited to complete some computation-intensive tasks along. The computation-intensive tasks will be often divided into some subtasks and be assigned to different edge nodes. Therefore, it is a very key issue that how to assign the tasks among the different edge nodes, which will be solved in this section.

The ant colony algorithm is an intelligent optimization algorithm, which is used to solve complicated combinatorial optimization problem. For the ant colony algorithm, distributed computing is relatively easy to implement and it is easy to merge with other algorithms to become a new algorithm. Because of these advantages, the ant colony algorithm will usually be applied to resolve resource-task scheduling and optimization problem.
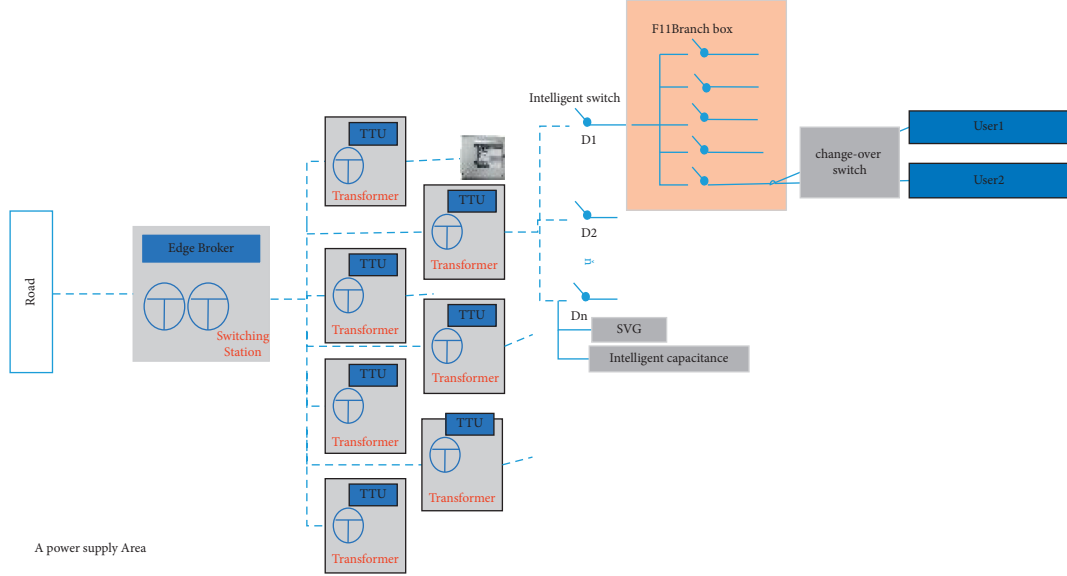
FIGURE 2: Edge computing application of the power supply area.

For example, in [40], a task scheduling algorithm is proposed, named "DSFACO," which is assigned to decrease the execution time for several tasks on the same scheduling queue. This algorithm improves the running efficiency of virtual machine resources.

In the second-level nodes, the computation-intensive tasks will be usually divided into many subtasks and the edge nodes will complete the tasks by cooperation with each other. Therefore, in this paper, the ant colony algorithm is considered to realize the resource sharing among the edge nodes.

4.2.1. Mathematical Model. For the ant colony algorithm, some parameters are introduced in Table 1. Furthermore, in this section, we introduced the computational model for pheromones, the update model for pheromones, and the state transition probability model of nodes.

(1) Computational Model for Pheromones. In this model, the pheromone of resource node can be calculated by its attribute values. Some attributes are considered: CPU utilization, power consumption, memory utilization, external storage utilization, and node security. In this paper, the pheromone of a resource node can be calculated as follows:

$$Ph_i(t) = \partial_1 * Ph_i^{cu}(t) + \partial_2 * Ph_i^{pc}(t) + \partial_3 * Ph_i^{mu}(t) + \partial_4 * Ph_i^{su}(t) + \partial_5 * Ph_i^{ns}(t), \tag{1}$$

where $\partial_1, \partial_2, \partial_3, \partial_4$, and ∂_5 represent the important degree of resource attributes on node pheromones. In addition, $Ph_i^{cu}(t)$, $Ph_i^{pc}(t)$, $Ph_i^{mu}(t)$, $Ph_i^{su}(t)$, and $Ph_i^{ns}(t)$ represent the CPU utilization, power consumption, memory utilization, external storage utilization, and node security grade of node i after normalization. At the beginning, $\tau_i(0) = C$. Furthermore, the power consumption of edge node i can be expressed as follows:

$$Ph_i^{pc}(t) = PC_{no}(i) + \left(\frac{\sum_{j=1}^n f_{i,j}}{f_i^{max}}\right)^2 (PC_{max}(i) - PC_{no}(i)), \tag{2}$$

where $PC_{no}(i)$ is the power consumption when there is no task assigned on this edge node. $PC_{max}(i)$ is the power consumption when this edge node is full load. $f_{i,j}$ is the processing speed of task i on edge node j. f_i^{max} is the max value of processing speed.

To resign a unified computing method of node pheromone, the values of attribute are normalized before being integrated. Therefore, the SAW (simple additive weighting) technology is used in this paper [41]. The attributes are divided into two categories: the first kind of attribute values is positively correlated with node pheromones, which means that the value of node pheromones will increase with the value of attribute, such as node security grade; the second kind of attribute values is negatively correlated with node pheromones, which means that the value of node pheromones will decrease with the value of attribute, such as CPU utilization, power consumption, memory utilization, and external storage utilization. The normalization process of the first kind of attribute can be expressed as formula (2), and the normalization process of the second kind of attribute can be expressed as formula (3). Furthermore, $l_x^+(Ph_i^x)$ and $l_x^-(Ph_i^x)$ represent the normalized value of x-th attribute. On the contrary, $p_x(Ph_i^x)$ represents the initial value before

TABLE 1: Parameters.

Name	Introduction
n	Number of computing nodes
m	Number of task
n	Number of resource nodes
Tabu_k	Tabu table of ant k
ΔPh_i	Pheromone increment in node i
ΔPh_i^k	Pheromone increment when ant k assigns task to node i
$P_{ij}^k(t)$	Transfer probability when ant k transfers from node i to node j at time t
d_{ij}	Distance between node i and node j
θ_{ij}	Heuristic factor, the inspired degree from i to j
δ	Pheromone persistence (the residual coefficient), $0 < \rho < 1$
τ_i	Pheromones in node i

normalization. In addition, max p_x and min p_x represent the maximum value and the minimum value of x-th attribute.

$$l_x^+(\text{Ph}_i^x) = \begin{cases} \dfrac{p_x(\text{Ph}_i^x) - \min p_x}{\max p_x - \min p_x}, & \max p_x - \min p_x \neq 0, \\ \\ 1, & \max p_x - \min p_x = 0, \end{cases} \tag{3}$$

$$l_x^-(\text{Ph}_i^x) = \begin{cases} \dfrac{\max p_x - p_x(\text{Ph}_i^x)}{\max p_x - \min p_x}, & \max p_x - \min p_x \neq 0, \\ \\ 1, & \max p_x - \min p_x = 0. \end{cases} \tag{4}$$

(2) Update Model for Pheromones. In the ant colony algorithm, effective nodes are those useful nodes searched by the ant, and the effective nodes are used to perform computational tasks. In this paper, the effective node is defined as a node whose pheromone is not less than a certain threshold after being assigned tasks. When a node is assigned tasks, its CPU utilization, memory utilization, and external storage utilization will increase. Therefore, to ensure the load balance of each resource node, the node pheromone should be decreased whose resource utilizations are relatively high. In that case, the nodes whose resource utilizations are high will have lower probability to be assigned tasks. Therefore, the pheromone update model can be expressed as follows:

$$\text{Ph}_i(t + n) = (1 - \delta)\text{Ph}_i(t) - \Delta\text{Ph}_i, \tag{5}$$

where δ is the pheromone persistence coefficient, that is, the affect degree of existing pheromone to pheromone update process. In addition, when node i is assigned task, the probability it will be assigned tasks next time can be changed, so ΔPh_i^k is the pheromone variation to node i when it is assigned tasks by ant k, and $\Delta\text{Ph}_i = \sum_{k=1}^{m} \Delta\text{Ph}_i^k$ is the sum of pheromone affect. The pheromone incremental effect of task i when it is assigned task k can be expressed as follows:

$$\Delta\text{Ph}_i^k = \Delta\text{Ph}_i^{k,\text{cu}}(t) + \Delta\text{Ph}_i^{k,\text{pc}}(t) + \Delta\text{Ph}_i^{k,\text{mu}}(t) + \Delta\text{Ph}_i^{k,\text{su}}(t) + \Delta\text{Ph}_i^{k,\text{ns}}(t). \tag{6}$$

(3) Probability Model for State Transition. When selecting the next transition node, ants always tend to choose the neighbor node with the highest transfer probability. The transfer probability calculation formula can be expressed by

$$p_{ij}^k(t) = \begin{cases} \dfrac{[\text{Ph}_{ij}(t)]^\lambda [\theta_{ij}(t)]^\chi}{\sum_{S \in jk(i)} [\text{Ph}_{ij}(t)]^\lambda [\theta_{ij}(t)]^\chi}, & \text{if } j \in j_k(i), \\ \\ 0, & \text{else,} \end{cases} \tag{7}$$

wherer λ is the importance degree of pheromones and χ is the importance degree of heuristic factor. In addition, $j_k(i)$ is the node set which can be selected in next step for ant k. Heuristic factor θ_{ij} can be calculated as follows:

$$\theta_{ij}(t) = \frac{1}{d_{ij}}, \tag{8}$$

where d_{ij} means the distance of node i and node j. When ant k selects the next transfer node, the smaller d_{ij} is, the less the communication cost between node i and node j is, and the bigger probability that node j is selected as the next transfer node. In addition, $\theta_{ij}(t)$ is expectation level of ant k moving from node i to node j.

4.2.2. Algorithm Flow. In this section, we will introduce the specific flow of the proposed resource management algorithm. The specific flow is shown in Figure 3.

(1) The node pheromone is initialized.

(2) The ants are placed, and the timer is started.

(3) The ant will select the next transfer node according to the state transition probability and determine whether that node is a valid node. If the selected node is a valid node, the node information will be recorded and returned; if the selected node is not the valid
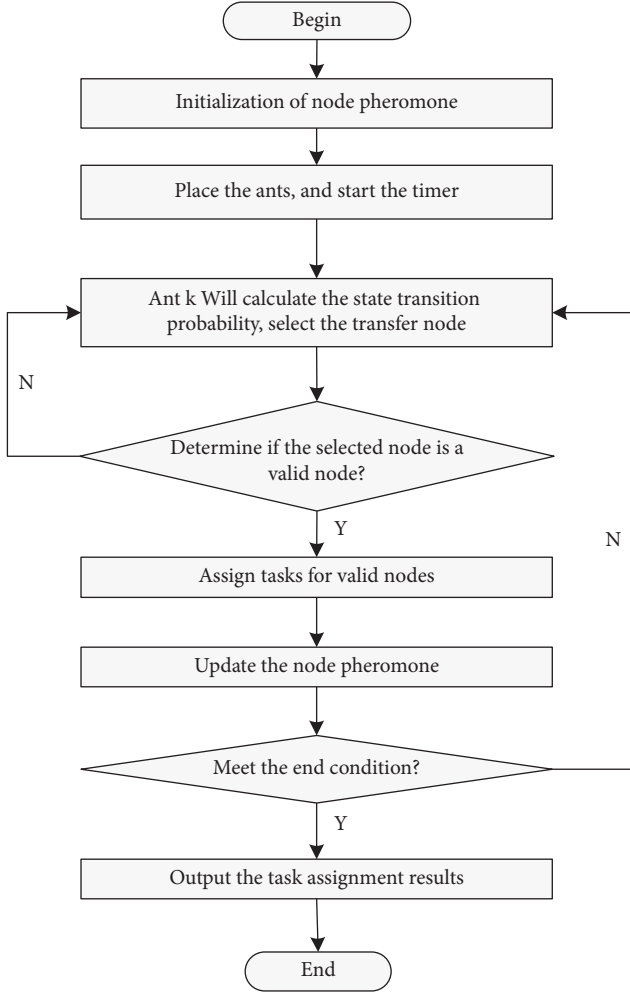
FIGURE 3: The task scheduling algorithm based on the ant colony algorithm.

node, the ant will continue to choose the next transfer node and determine if it is a valid node.

(4) The tasks are assigned for the valid nodes, and the node pheromone is updated.

(5) The timer ends.

5. Simulations

In the new resource management scheme based on the idea of edge computing, we propose a task scheduling algorithm based on the ant colony algorithm. In this section, we will simulate the performance of the new algorithm. Without loss of generality, all the data are the average values of ten experiments. In the experiments, $\partial_1, \partial_2, \partial_3, \partial_4$, and ∂_5 are set as 0.25. The simulation parameters are expressed in Table 2, and we set some contrast algorithms to verify the effectiveness of the new algorithm. In this section, two comparing algorithms are set. One is the modified round robin algorithm, and the other is the generalized priority algorithm.

(i) *Modified Round Robin Algorithm (RRA, for Short).* This algorithm is proposed in [42], which can randomly assign free resources for task execution

TABLE 2: Parameters introduction.

Parameters	Values
Number of edge nodes	[20, 500]
Node security grade of node	[0.5–1)
Number of tasks	30–350
Processing speed	100–1000 MIPS
Length of the task	1000–10000 MI
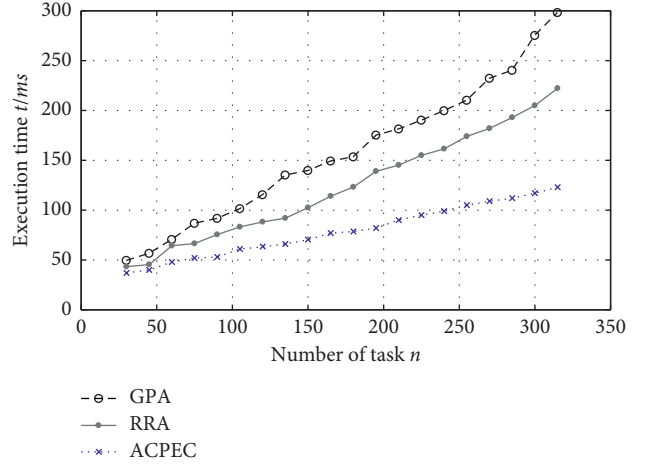
FIGURE 4: The comparison of task completion time.

(ii) *Generalized Priority Algorithm (GPA, for Short).* This algorithm is proposed in [43], which is an efficient optimal algorithm of task scheduling in cloud computing environment

(iii) *Ant Colony Algorithm in Power Edge Computing (ACPEC, for Short).* This algorithm is the resource scheduling algorithm proposed in this paper

In this section, we simulate the performance of RRA, GPA, and ACPEC on the task execution time with different number of tasks. As shown in Figure 4, we can find that the task execution times of ACPEC are always shorter than those of GPA and RRA. With the increase in task scale, the advantages become more and more obvious. When the number of task reaches 320, the advantage of ACPEC is very obvious, as shown in Figure 4.

The task wait delay is a key factor affecting the real-time response of the system. As shown in Figure 5, the task waiting time always increases with the increase in task scale. Compared with GPA and RRA, the ACPEC algorithm is more complex, so the required time for task assigning is always longer slightly. However, compared with the total amount of time for task execution, a small increase in task wait time is acceptable for users.

The performances on power consumption cost are shown in Figure 6. For the ACPEC algorithm, the tasks can be assigned to different resource nodes according to the purpose of reducing power consumption. Therefore, when the task scale is the same, the power consumption with ACPEC is always less than the power consumption with FSFC and RRA. And as the task scale increases, the advantage tends to be obvious.
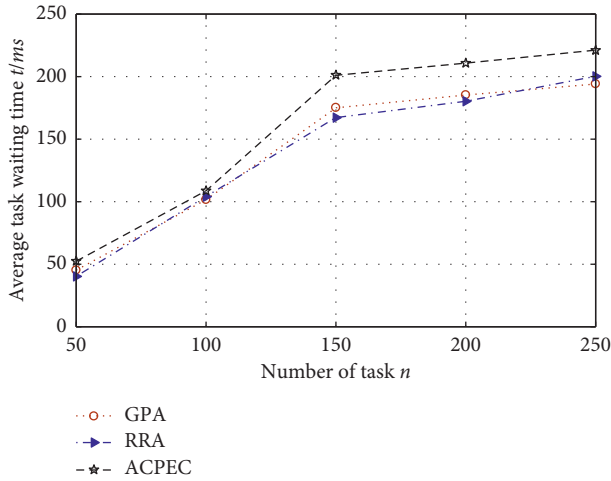
Figure 5: The comparison of average waiting delays.
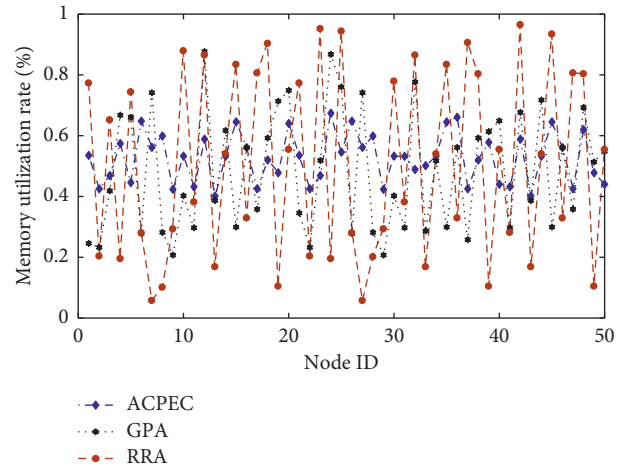
Figure 8: The comparison of memory utilization.
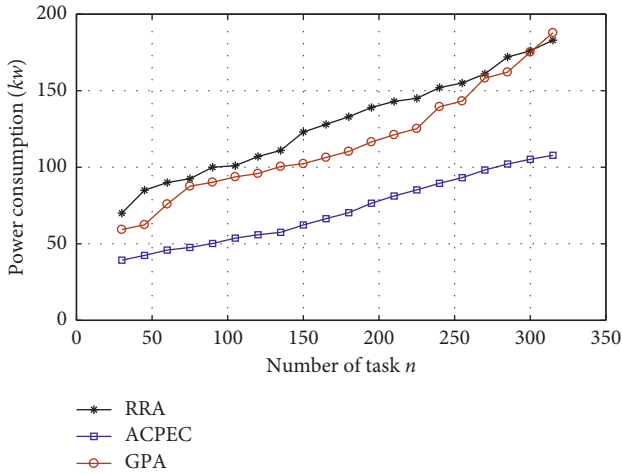
Figure 6: The comparison of power cost.
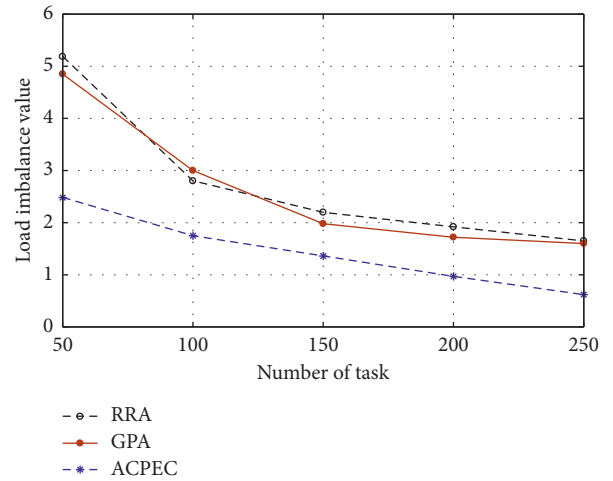
Figure 9: The comparison of unbalanced load value.
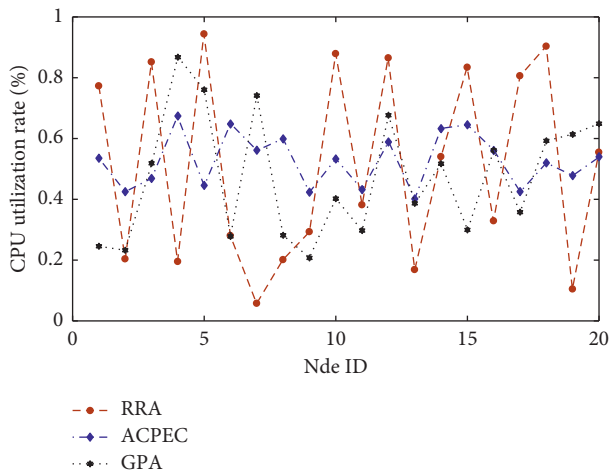
Figure 7: The comparison of CPU utilization.

When the number of tasks is 100, the CPU utilization with 20 edge nodes and the memory utilization with 50 nodes are simulated as shown in Figures 7 and 8. We can find that the CPU utilization and memory utilization of some nodes fluctuate greatly when using GPA and RRA. Furthermore, some nodes are under low load state when using GPA and RRA. When using the ACPEC algorithm, the CPU utilization and memory utilization among different nodes have become average. Compared with RRA, the average CPU utilization increased from 38.8% to 69.9%, and the average memory utilization increased from 38% to 68%.

In this section, we will evaluate the performance of these task scheduling algorithms on load imbalance. In this section, M_{DI} (degree of imbalance) represents the level of load imbalance, which can be calculated as follows:

$$M_{DI} = \frac{M_{max} - M_{min}}{M_{avg}}, \tag{9}$$

where $M_{\max}$, $M_{\min}$, and M_{avg} represent the longest time, the shortest time, and the average time for task performing. The load imbalance levels of different algorithms are shown in Figure 9. We can find that the load imbalance levels decrease gradually with the increase in task scale. This is because the assigning of tasks is gradually balanced with the increase in task scale. Compared with GPA and RRA, the values of M_{DI} with ACPEC are lower. The performance of ACPEC on load balance is better than that of GPA and RRA as shown in Figure 9.

6. Conclusion

To ensure the efficient and stable operation of the power cloud computing system and make full use of the advantages of edge nodes, in this paper, we propose a new resource management scheme based on edge computing. In this scheme, the computing tasks can be executed in local edge nodes instead of uploading to the cloud. In this new scheme, although the resources of single edge node are limited, the resource among edge nodes can cooperate with each other to complete the computation-intensive task. To realize the optimal allocation between edge nodes and tasks, in this paper, a task allocation algorithm based on the ant colony algorithm is proposed. This algorithm has good performance in task execution time, waiting delay, CPU utilization, memory utilization, and load balancing. The communication overhead is greatly affected by network environment; therefore, the communication overhead of data transmission and the difference of system power consumption should be considered in resource management issue, which may become our future work.

Data Availability

The simulation data used to support the findings of this study are included within the supplementary information file.

Conflicts of Interest

The authors declare that they have no conflicts of interest.

Acknowledgments

References

[1] A. Fox, R. Griffith, A. Joseph, and Armando, "Above the clouds: a berkeley view of cloud computing," *Dept. Electrical Eng. and Comput. Sciences, University of California, Berkeley, Rep. UCB/EECS*, vol. 28, no. 13, pp. 3–5, 2009.

[2] R. Harms and M. Yamartino, *The Economics of the Cloud*, Microsoft whitepaper, Microsoft Corporation, Redmond, Washington, 2010.

[3] T. Zhao, S. Zhou, X. Guo, Y. Zhao, and Z. Niu, "A cooperative scheduling scheme of local cloud and internet cloud for delay-aware mobile cloud computing," in *Proceedings of the 2015 IEEE Globecom Workshops (GC Wkshps)*, pp. 1–6, San Diego, CA, USA, December 2015.

[4] C. Wang, F. R. Yu, C. Liang, Q. Chen, and L. Tang, "Joint computation offloading and interference management in wireless cellular networks with mobile edge computing," *IEEE Transactions on Vehicular Technology*, vol. 66, no. 8, pp. 7432–7445, 2017.

[5] X. Chen, L. Jiao, W. Li, and X. Fu, "Efficient multi-user computation offloading for mobile-edge cloud computing," *IEEE/ACM Transactions on Networking*, vol. 24, no. 5, pp. 2795–2808, 2016.

[6] Y. Mao, C. You, J. Zhang, K. Huang, and K. B. Letaief, "A survey on mobile edge computing: the communication perspective," *IEEE Communications Surveys & Tutorials*, vol. 19, no. 4, pp. 2322–2358, 2017.

[7] S. E. Mahmoodi, R. N. Uma, and K. P. Subbalakshmi, "Optimal joint scheduling and cloud offloading for mobile applications," *IEEE Transactions on Cloud Computing*, vol. 7, no. 2, pp. 301–313, 2019, to be published.

[8] Z. Sanaei, S. Abolfazli, A. Gani, and R. Buyya, "Heterogeneity in mobile cloud computing: taxonomy and open challenges," *IEEE Communications Surveys & Tutorials*, vol. 16, no. 1, pp. 369–392, 2014.

[9] N. Zhang, X. Yang, M. Zhang, and Y Sun, "Crowd-Funding: a new resource cooperation mode for mobile cloud computing," *PloS One*, vol. 11, no. 12, pp. e0167657–989, 2016.

[10] Y. Sun and N. Zhang, "A resource-sharing model based on a repeated game in fog computing," *Saudi Journal of Biological Sciences*, vol. 24, no. 3, pp. 687–694, 2017.

[11] G. Von Laszewski, L. Wang, A. J. Younge, and X. He, "Power-aware scheduling of virtual machines in dvfs-enabled clusters," in *Proceedings of the IEEE International Conference on Cluster Computing 2009*, pp. 1–10, New Orleans, LA, USA, September 2009.

[12] J. L. Berral, I. Goiri, R. Nou, and F. Julià, "Towards energy-aware scheduling in data centers using machine learning," in *Proceedings of the 1st International Conference on Energy-Efficient Computing and Networking*, pp. 215–224, ACM, New York, NY, USA, April 2010.

[13] R. Jayarani, S. Sadhasivam, and N. Nagaveni, "Design and implementation of an efficient two-level scheduler for cloud computing environment," in *Proceedings of the 2009 International Conference on Advances in Recent Technologies in Communication and Computing*, pp. 884–886, IEEE, NW Washington, DC, October 2009.

[14] M. Shojafar, N. Cordeschi, and E. Baccarelli, "Energy-efficient adaptive resource management for real-time vehicular cloud services," *IEEE Transactions on Cloud computing*, vol. 7, no. 1, pp. 196–209, 2016.

[15] M. Shojafar, N. Cordeschi, J. H. Abawajy, and E. Baccarelli, "Adaptive energy-efficient Qos-aware scheduling algorithm for TCP/IP mobile cloud," in *Proceedings of the 2015 IEEE Globecom Workshops (GC Wkshps)*, pp. 1–6, IEEE, San Diego, CA, USA, December 2015.

[16] G. Portaluri, S. Giordano, D. Kliazovich, and B. Dorronsoro, "A power efficient genetic algorithm for resource allocation in cloud computing data centers," in *Proceedings of the 2014 IEEE 3rd International Conference on Cloud Networking (CloudNet)*, pp. 58–63, IEEE, Luxembourg, October 2014.

[17] N. Zhang, X. Yang, M. Zhang, Y. Sun, and K. Long, "A genetic algorithm-based task scheduling for cloud resource crowd-funding model," *International Journal of Communication Systems*, vol. 31, no. 1, Article ID e3394, 2018.

[18] X. Liu, X. B. Zhai, W. Lu, and C. Wu, "QoS-guarantee resource allocation for multibeam satellite industrial internet of things with NOMA," *IEEE Transactions on Industrial Informatics*, vol. 17, no. 3, pp. 2052–2061, 2021.

[19] X. Liu and X. Zhang, "NOMA-based resource allocation for cluster-based cognitive industrial internet of things," *IEEE Transactions on Industrial Informatics*, vol. 16, no. 8, pp. 5379–5388, 2020.

[20] L. Gkatzikis and I. Koutsopoulos, "Migrate or not? Exploiting dynamic task migration in mobile cloud computing systems," *IEEE Wireless Communications*, vol. 20, no. 3, pp. 24–32, 2013.

[21] N. Fernando, S. W. Loke, and W. Rahayu, "Mobile cloud computing: a survey," *Future Generation Computer Systems*, vol. 29, no. 1, pp. 84–106, 2013.

[22] J. Liu, Y. Mao, J. Zhang, and K. B. Letaief, "Delay-optimal computation task scheduling for mobile-edge computing systems," in *Proceedings of the IEEE ISIT*, pp. 1451–1455, Barcelona, Spain, July 2016.

[23] Y. Mao, J. Zhang, and K. B. Letaief, "Dynamic computation offloading for mobile-edge computing with energy harvesting devices," *IEEE Journal on Selected Areas in Communications*, vol. 34, no. 12, pp. 3590–3605, 2016.

[24] R. Deng, R. Lu, C. Lai, and T. H. Luan, "Towards power consumptiondelay tradeoff by workload allocation in cloud-fog computing," in *Proceedings of the 2015 IEEE International Conference on Communications (ICC)*, pp. 3909–3914, London, UK, June 2015.

[25] E. Gelenbe, R. Lent, and M. Douratsos, "Choosing a local or remote cloud," in *Proceedings of the Network Cloud Computing and Applications (NCCA), 2012 Second Symposium on*, pp. 25–30, IEEE, London, UK, December 2012.

[26] Y. Li and W. Wang, "The unheralded power of cloudlet computing in the vicinity of mobile devices," in *Proceedings of the IEEE Global Commun. Conf.*, pp. 4994–4999, London, UK, December 2013.

[27] K. Suto, K. Miyanabe, H. Nishiyama, N. Kato, H. Ujikawa, and K.-I. Suzuki, "QoE-Guaranteed and power-efficient network operation for cloud radio access network with power over fiber," *IEEE Transactions on Computational Social Systems*, vol. 2, no. 4, pp. 127–136, 2015.

[28] G. von Zengen, F. Bsching, W. B. Pttner, and L. Wolf, "Transmission power control for interference minimization in WSNs," in *Proceedings of the Int. Wireless Commun. Mobile Comput. Conf.*, pp. 74–79, New York, NY, USA, August 2014.

[29] T. Aota and K. Higuchi, "A simple downlink transmission power control method for worst user throughput maximization in heterogeneous networks," in *Proceedings of the 7th Int. Conf. Signal Process. Commun. Syst.*, pp. 1–6, China, December 2013.

[30] M. Peng, K. Zhang, J. Jiang, J. Wang, and W. Wang, "Energy-efficient resource assignment and power allocation in heterogeneous cloud radio access networks," *IEEE Transactions on Vehicular Technology*, vol. 64, no. 11, pp. 5275–5287, 2015.

[31] J. Armstrong, "OFDM for optical communications," *Journal of Lightwave Technology*, vol. 27, no. 3, pp. 189–204, 2009.

[32] S. Sardellitti, G. Scutari, and S. Barbarossa, "Joint optimization of radio and computational resources for multicell mobile-edge computing," *IEEE Transactions on Signal and Information Processing over Networks*, vol. 1, no. 2, pp. 89–103, 2015.

[33] J. Cheng, Y. Shi, B. Bai, and W. Chen, "Computation offloading in cloud-ran based mobile cloud computing system," in *Proceedings of the 2016 IEEE International Conference on Communications (ICC)*, pp. 1–6, Kuala Lumpur, Malaysia, May 2016.

[34] C. You, K. Huang, H. Chae, and B. H. Kim, "Energy-efficient resource allocation for mobile-edge computation offloading," *IEEE Transactions on Wireless Communications*, vol. 99, p. 1, 2016.

[35] Y. Mao, J. Zhang, S. H. Song, and K. B. Letaief, "Power-delay tradeoff in multi-user mobile-edge computing systems," in *Proceedings of the 2016 IEEE Global Communications Conference (GLOBECOM)*, pp. 1–6, Abu Dhabi, UAE, December 2016.

[36] W. Shi, J. Cao, Q. Zhang, Y. Li, and L. Xu, "Edge computing: vision and challenges," *IEEE Internet of Things Journal*, vol. 3, no. 5, pp. 637–646, 2016.

[37] J. Ren, H. Guo, C. Xu, and Y. Zhang, "Serving at the edge: a scalable IoT architecture based on transparent computing," *IEEE Network*, vol. 31, no. 5, pp. 96–105, 2017.

[38] H. Tan, Z. Han, X.-Y. Li, and F. C. M. Lau, "Online job dispatching and scheduling in edge-clouds," in *Proceedings of the IEEE INFOCOM IEEE Conf. Comput. Commun.*, pp. 1–9, Toronto, ON, Canada, May 2017.

[39] H. Li, G. Shou, Y. Hu, and Z. Guo, "Mobile edge computing: progress and challenges," in *Proceedings of the 2016 4th IEEE international conference on mobile cloud computing, services, and engineering (MobileCloud)*, pp. 83-84, IEEE, Oxford, UK, April 2016.

[40] Q. Y. Guo and F. D. Zhu, "Cloud computing resource scheduling algorithm based on ant colony algorithm and leap frog algorithm," *Bulletin of Science and Technology*, vol. 33, no. 5, pp. 167–170, 2017.

[41] C. Wang and Z. Li, "Parametric analysis for adaptive computation offloading," *ACM SIGPLAN Notices*, vol. 39, no. 6, pp. 119–130, 2004.

[42] P. Pradhan, P. K. Behera, and B. N. B. Ray, "Modified round robin algorithm for resource allocation in cloud computing," *Procedia Computer Science*, vol. 85, pp. 878–890, 2016.

[43] A. Agarwal and S. Jain, "Efficient optimal algorithm of task scheduling in cloud computing environment," *International Journal of Computer Trends and Technology*, vol. 9, no. 7, 2014.

WILEY | Hindawi

Research Article
Deepfake Detection Method Based on Cross-Domain Fusion

Fang Sun [ID],[1] **Niuniu Zhang** [ID],[1] **Pan Xu,**[1] **and Zengren Song**[2]

[1]*School of Computer and Information Technology, LiaoNing Normal University, Dalian 116023, China*
[2]*National Computer Network Emergency Response Technical Team, Coordination Center of China, China*

Correspondence should be addressed to Fang Sun; sunfang@lnnu.edu.cn

In recent years, despite its wide use in various fields, deepfake has been abused to generate hazardous contents such as fake movies, rumors, and fake news by manipulating or replacing facial information of the original sources and, thus, exerts huge security threats to the society. Facing the continuous evolution of deepfake, research on active detection and prevention technology becomes particularly important. In this paper, we propose a new deepfake detection method based on cross-domain fusion, which, on the basis of traditional spatial domain features, realizes the fusion of cross-domain image features by introducing edge geometric features of the frequency domain and, therefore, achieves considerable improvements on classification accuracy. Further evaluations of this method have been performed on publicly deepfake datasets, and the results show that our method is effective particularly on the Meso-4 DeepFake Database.

1. Introduction

With the rapid development of the Internet of Things (IoT), society has entered a new era [1]. The IoT has many distinct advantages, such as security, real time, automation, embeddedness, interoperability, and interconnection. In the context of the Internet of Things and 5G, the speed of the network is constantly improving, which not only brings convenience to people, but also facilitates information fraud [2, 3]. At the same time, deep learning is booming as a new technology. The widespread application of deep learning technology has not only brought unprecedented innovation in various fields, but also created convenient criminal conditions for offenders. For example, the deepfake technique, which has caused bad influence to the society recently, can not only generate realistic fake images, videos, and audio contents, but also forge evidence for electronic crime. The abuse of this technique has seriously threatened the network information and data security of both individuals and the society. Therefore, the research of deepfake detection technology is of great significance to ensure the authenticity of video, image, and audio transmitted in the network.

In the process of generating fake face image, to ensure fidelity, fuzzy functions are usually used.

To process the face region to match the background region, however, such operations lead to edge differences between the face and background regions in the forged image, resulting in inconsistent resolution on both sides of the boundary. This paper introduces a new method of deepfake detection based on cross-domain fusion. Our method uses a network to gain the image's spatial domain feature vectors and extracts the edge geometric features in frequency domain, in order to obtain a vector set containing both high-level semantic features and low-level edge features of the image.

The main contributions of this paper are as follows:

(1) We propose a new deepfake detection approach to improve the detection accuracy, which fuses spatial domain features extracted from the image and features extracted from the frequency domain to capture more detailed forgery trails and get more comprehensive face features.

(2) We further propose a better fusion strategy. On the one hand, the spatial domain features of the full connection layer in the meso-net network are extracted to ensure the high-level semantic features of the image; on the other hand, frequency domain features of the face

image are extracted to ensure the low-level texture features. Thus, we obtain cross-domain features through the fusion of two feature vectors, which includes not only frequency features of the edge geometric features, but also spatial features of the face image. Finally, we test this feature set with a classifier.

(3) In order to analyze the effectiveness of the detection method, we evaluate the performance of the model on the deepfake datasets and compare it with other deepfake detection methods. At the same time, we also evaluate the performance of the algorithm on the cross-datasets. Our detection model shows effectiveness and superiority in these experiments.

The structure of the paper is as follows. In Section 1, we briefly overview the development status of deepfake and the contributions of our work; Section 2 describes related works. In Section 3, we introduce the architecture, innovation, and advantages of our deepfake detection method in detail; in Section 4, we present our experimental setup and report our detection performance results; Section 5 gives a summary and introduces future work.

2. Related Work

2.1. Deepfake. The word "deepfake" is the combination of "deep learning" and "fake." It is mainly the product of neural network in machine learning and particularly refers to the forgery of image, video, and audio generated by Generative Adversarial Network (GAN). Deepfakes can promote the development of entertainment, cultural exchange, and education industry, which can improve not only the teaching level in the field of education, but also the quality of life. However most of the time, deepfake is used to generate fake news and forge electronic evidence, which misleads the public and disturbs social order. This technology has become the most advanced means of network attack. Deepfake can produce fake images/videos that are difficult to distinguish with human eyes and results in social chaos. For example, Trump's forged video, together with the release of former President Barack Obama's fake speech video, has caused public panic about deepfake [4].

The creation of deepfakes mainly falls into the following categories, i.e., face synthesis, facial reenactment, face replacement, and face editing (such as hair color and skin color). According to the different focus of forgery technology, four types of forged images are employed as shown in Figure 1. Figure 1 (a) shows a computer-generated face synthesis, Figure 1 (b) is generated by editing the real face image attributes with a beauty camera, Figure 1 (c) is from Celeb-DF dataset, and Figure 1(d) is from the FaceForensics++ dataset [5]. Obviously, human eyes can hardly distinguish between the real and fake images. If this technology is abused to spread false information to the society, the public may be misled, and the related consequences might be unknown.

2.2. Deepfake Detection Technology. According to the human five senses, deepfake can be divided into visual detection technology and auditory detection technology. Visual

detection includes image detection and video detection. Image detection is based on either traditional digital image forensics technology, convolution neural network model, or authenticity difference of generation principle. Video detection, however, is more complex. One type of detection is based on (a) temporal characteristics of cross video frame group, (b) visual artifacts within video frame, or (c) emerging technologies such as block chain. Another type of video detection is to extract each frame from the video and convert it into a static image and, therefore, convert dynamic deepfake video detection to static deepfake image detection. Auditory detection mainly detects the difference between the real and fake biological signals such as speech speed, voiceprint, and spectrum distribution in audio [6].

To deal with the potential threat of deepfake, researchers are exploring the classification method of real and fake images. As deepfake method is a special branch of traditional image tampering, early detection methods learn from the traditional forensics methods. Recently, people began to study the generation process of deepfake and reverse the use of deep neural network to detect forged images.

According to the principle of traditional detection methods, Zhou et al. [7] proposed a two-stream CNN network for face forgery detection. Tan et al. [8] proposed a feature set to capture the statistical information of color images and then identify forged images. Cozzolino et al. [9] extracted the camera fingerprint of the deep forgery image for the detection task and proposed a camera model fingerprint method called "noise print." Hu Yongjian proposed a network using image segmentation to detect deep false face video [10].

McCloskey et al. [11] show that GAN has obvious differences in color and saturation with the actual camera in color processing to distinguish real and fake images. Nataraj et al. [12] proposed a method using cooccurrence matrix and deep learning to detect forged images generated by GAN. Zhang et al. [13] proposed a GAN simulator, AutoGAN, which can simulate artifacts generated by a common channel shared by multiple GAN models. According to Mohammed Akram Younnus, if a blur function is added in the generation process of deep forgery video to reach the level of real video, the detection technology should be able to distinguish the authenticity by detecting the blur degree between the face and background boundary [14].

Christian Szegedy et al. [15] extended the network by using proper convolution kernel and regularization and proposed the InceptionV3 network. Darius Afchar et al. proposed two networks. One of them is Meso-4, which is composed of a series of continuous convolution and pooling layers. At the same time, in order to improve the generalization ability of the model, the convolution layer uses ReLu excitation function to normalize the input to avoid gradient disappearance. The other network is MesoInception4 network, which replaces the first two layers of Meso-4 network by introducing a series of induction modules in [16]. It uses 3 * 3 dilated convolutions [17] rather than 5 * 5 convolutions of the original module to avoid high semantics. Moreover, multiple convolution layers with different core sizes are stacked to increase the function space of the optimization model and realize parallel detection [18].

Fake

Real

(a)   (b)   (c)   (d)

FIGURE 1: Deepfakes classification. (a) Face synthesis. (b) Face editing. (c) Face replacement. (d) Facial reenactment.

Run Wang et al. [19] proposed using MNC average neurons to monitor the behavior of neurons in each layer and extract the low-level features of each layer to make the detection more accurate. Nguyen et al. [20] proposed an architecture based on capsule network to detect deep forgery images. Ekraam Sabir et al. [21] designed a best strategy for combining variations in some networks along with domain specific face preprocessing techniques for forgery video detection. Mattern et al. [22] used the missing facial texture features and facial markers in eyes and teeth to generate feature vectors to judge the authenticity of the image. Li and Lyu only generate limited resolution images based on deepfake algorithm, and the fake image needs to be further deformed to match the real face.

In the real video, this deformation leaves a unique artifact in the forged video. Therefore, they propose to detect the unique artifact in the forged video to judge the authenticity of the video [23].

Stehouwer et al. [24] proposed using attention mechanism to process and improve the feature map of classification task instead of multitask learning method of detecting deep fake image and predicting forgery region at the same time. Sohail Ahmed Khan et al. [25] proposed a fusion network, using VGG16, InceptionV3, and XceptionNet parallel tests and average prediction results to obtain the final prediction result.

3. Method

In this paper, we propose a deepfake detection method based on cross-domain fusion, which utilizes frequency domain features to extract edge geometric features of the image (blue box in Figure 2); at the same time, spatial domain features of the image are integrated to extract the high-level features of the image under neural network (green box in Figure 2). To get more comprehensive facial features, low-level features

and high-level features are fused to form feature vectors of the image (red box in Figure 2). The detailed model structure is illustrated in Figure 2.

3.1. Cross-Domain Features Extraction. Through the analysis of the image in frequency domain, we can see that the edge of the face is fuzzy, and the background is clear in the transformed forged face image. It clearly shows that the geometric features of the face edge in frequency domain provide a significant contribution to deepfake detection (Figure 4). The bottom network layer of neural network extracts low-level features (edge features, geometric features), the middle network layer extracts middle-level features (texture features), and the top network layer extracts high-level features of the image, the essence of which is the recombination of middle-level features, which can highly summarize the image attributes. It can be seen that, with the increase of neural network layers, low-level features gradually disappear, and their proportion in the final feature set is extremely low. On the other hand, neural network with less layers produces incomplete generalization of image attributes. In this paper, Haar transform is used to extract low-level features of face image such as edge features to ensure the contribution of low-level features. At the same time, a four-layer neural network is used to extract high-level features of image to ensure the influence strength of high-level features. The fusion of the two can achieve a comprehensive face image feature set with both low-level frequency domain features and high-level spatial domain features.

A sized $m \times n$ image I is resized to $r \times c$ size. To ensure generalization of the detection model, according to the convex optimization theory and data probability distribution theory, we know that the data centralization conforms to data distribution law and is easier in obtaining the generalization effect after training. In this paper, we define the image standardization operation, so that data can be
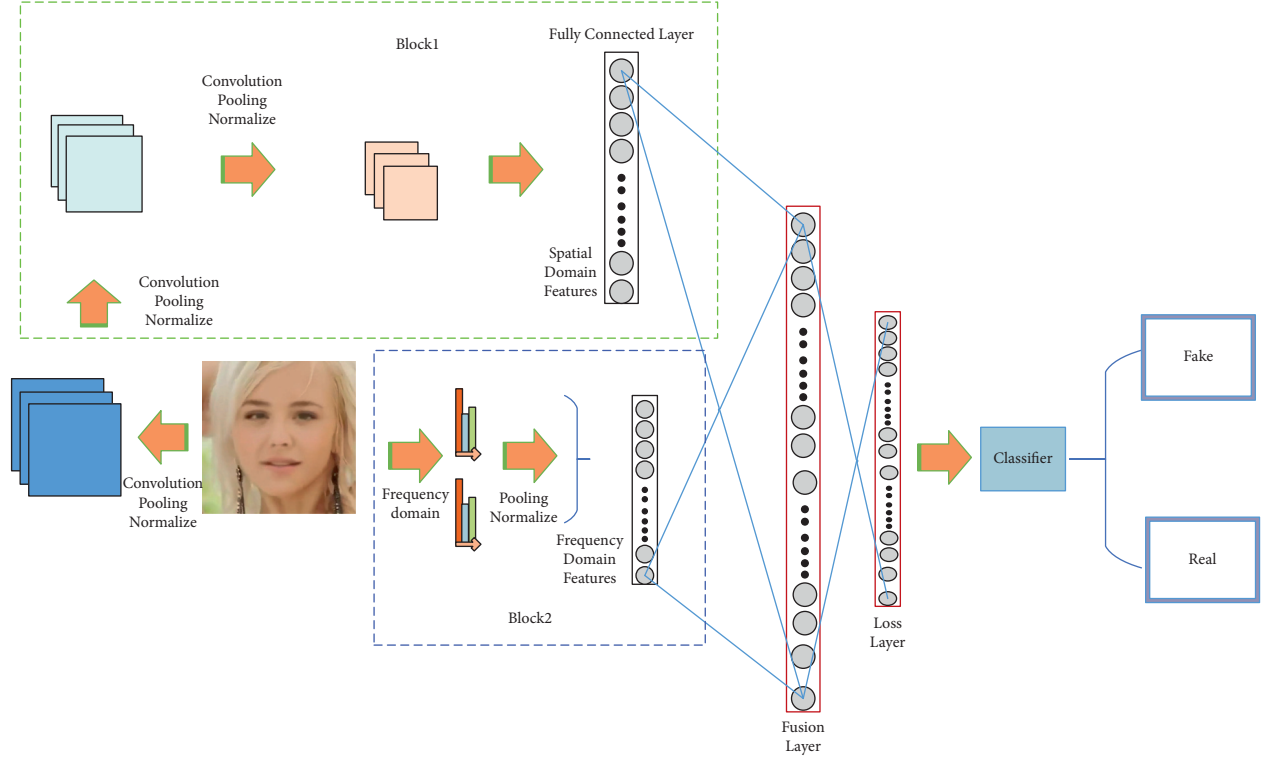
FIGURE 2: Cross-domain detection model. The model consists of three parts: extracting spatial domain features (Block1), extracting frequency domain features (Block2), and fusion layer. The detailed diagram of cross-domain network structure is illustrated in Figure 3.

centralized by means of deaveraging. X_{rc} is defined as the image matrix, and the image I data standardization formula is as follows:

$$X_{rc}^{\wedge} = \frac{X_{rc} - \text{mean}(I_{rc})}{\text{std}[I_{rc}]},$$

$$\text{std}[I_{rc}] = \max\left(\sigma, \frac{1.0}{\sqrt{N}}\right), \tag{1}$$

where $\text{mean}(I_{rc})$ is the mean value of the image, $X_{rc}^{\wedge}$ is the normalized image matrix, σ is the standard deviation, and N is the number of pixels of the image I_{rc}.

As the closer the distribution of data learned from the model and that of the training data are, the narrower the gap between the prediction label and the actual label would be, this paper uses cross entropy loss function to adjust the model parameters and, at the same time, avoids overfitting of the model and effectively improves the training efficiency. The loss function is defined as follows:

$$L = -\left[y \cdot \log(y^{\wedge}) + (1 - y) \cdot \log(1 - y^{\wedge})\right], \tag{2}$$

where y refers to the real label and $y^{\wedge}$ means the model prediction label.

In this paper, Adam optimization algorithm based on adaptive moment estimation [26] is used to adjust the learning rate of each epoch of the model due to its nature of lower memory requirement and higher computational efficiency. Meanwhile, the algorithm is able to adaptively adjust learning rate parameters according to training situation and, therefore, is more efficient than the traditional random gradient descent algorithm.

We define X_{CA}, X_{CH}, X_{CV}, and X_{CD} as the approximation of the original image, the edge texture information along horizontal direction, the edge texture information along vertical direction, and the edge texture information along diagonal direction, respectively. $X_{\alpha \in \{CA,CH,CV,CD\}}(i, j)$ is the pixel value of i row and j column in each direction.

The definition is as follows:

$$X_{CA}(i, j) = X_{rc}(2i - 1, 2j - 1) + X_{rc}(2i - 1, 2j) + X_{rc}(2i, 2j - 1) + X_{rc}(2i, 2j),$$
$$X_{CH}(i, j) = -X_{rc}(2i - 1, 2j - 1) + X_{rc}(2i - 1, 2j) + X_{rc}(2i, 2j - 1) + X_{rc}(2i, 2j),$$
$$X_{CV}(i, j) = -X_{rc}(2i - 1, 2j - 1) - X_{rc}(2i - 1, 2j) + X_{rc}(2i, 2j - 1) + X_{rc}(2i, 2j), \tag{3}$$
$$X_{CD}(i, j) = X_{rc}(2i - 1, 2j - 1) - X_{rc}(2i - 1, 2j) - X_{rc}(2i, 2j - 1) + X_{rc}(2i, 2j).$$

In order to ensure that the extracted edge texture information vectors in frequency domain can be fused with the traditional spatial features, we map the three edge texture information vectors of image into a feature matrix by two norms. The mapping function is defined as follows:

$$X_{rc}^{\wedge} = \|X_{CH} + X_{CV} + X_{CD}\|_2 = \sqrt{X_{CH}^2 + X_{CV}^2 + X_{CD}^2}. \tag{4}$$

At the same time, $X_{rc}^{\wedge}$ is normalized [27] and pooled, and the range of matrix pixel value is limited within a fixed range to guarantee the correct fusion with spatial characteristics for subsequent network processing. We define f as the pixel value of $X_{rc}^{\wedge}$, and $f_{O \in \{R,G,B\}}(X_{rci \times j}^{\wedge})$ as the pixel value of column j in row i of the matrix, and the normalization formula for $X_{rc}^{\wedge}$ is as follows:

$$f_{O \in \{R,G,B\}}^{\wedge}(XX_{rci \times j}^{\wedge}) = \frac{f_{O \in \{R,G,B\}}^{\wedge}(X_{rci \times j}^{\wedge}) - \min\left(f_{O \in \{R,G,B\}}^{\wedge}(XX_{rci \times j}^{\wedge})\right)}{\max\left(f_{O \in \{R,G,B\}}^{\wedge}(XX_{rci \times j}^{\wedge})\right) - \min\left(f_{O \in \{R,G,B\}}^{\wedge}(XX_{rci \times j}^{\wedge})\right)}, \tag{5}$$

where $f^{\wedge}$ is to standardize the image of each channel, $\text{mean}(f_{O \in \{R,G,B\}}^{\wedge}(X_{rci \times j}^{\wedge}))$ is the mean value of image I_{rc} in each channel, and $\text{std}(f_{O \in \{R,G,B\}}^{\wedge}(X_{rci \times j}^{\wedge}))$ is the standard deviation of image I in each channel.

3.2. Features Fusion. In order to obtain more comprehensive facial features, we retain the high-level spatial domain features of neural network to capture more small traces of forgery. $f_s^{\wedge}(I_{rc})$ is defined as the output of the last layer of convolution neural network, and the spatial domain feature extraction results are normalized by formula (5).

In this paper, we design the edge feature vector in the frequency domain and the advanced feature vector in the spatial domain to be merged into an image feature set in a splicing mode. Define $X_{rc}^{(1)}$ to mean the frequency domain edge feature matrix that has undergone tiling vectors, and $X_{rc}^{(2)}$ to mean the finally extracted spatial domain high-level feature matrix, define the ϕ function as matrix splicing, and then define the following fusion formula:

$$\varphi = \phi\left(\left[X_{rc}^{(1)}, X_{rc}^{(2)}\right]\right) = \left\{ \begin{array}{c} x_1 \\ x_2 \\ . \\ . \\ . \\ x_{n-1} \\ x_n \end{array} \right\}, \tag{6}$$

where ϕ is the final image feature vector. Then, ϕ participates in the classification through formula (7) to obtain a predicted value, which is defined as follows:

$$y^{\wedge} = \text{soft} \max(Z) = \text{soft} \max(W \cdot \varphi + b) = \frac{e_k^z}{\sum_{k=1}^{K} e_k^z}, \tag{7}$$

where W means the neuron weight, b is the bias term, k refers to the classification value, and K is defined as the number of classification categories, and finally, it obtains a prediction result $y^{\wedge}$.

We extract features in the spatial domain based on Meso-4 network and retain the first four layers of neural networks. The first layer uses a $3 * 3$ convolution kernel, and the second, third, and fourth layers use a $5 * 5$ convolution kernel, while ensuring that the first two layers have 8 channels and the last two layers have 16 channels. Excitation function, normalization, and pooling operations are added to each layer to prevent overfitting of the network (great performance on the training set and unable to generalize well to the verification set and test set). The pooling core ensures that the first three layers have $2 * 2$ parameters, and the last layer has $4 * 4$ parameters. Finally, $16 * 8 * 8$ features are obtained for tiling operations, so that the three-dimensional features become $1024 * 1$ vector and are ready for fusion with frequency domain features. As deepfake usually blurs the fake image in the last step of production to achieve a realistic result, the blur extent at the edge of the face and the background are different. Therefore, extraction of edge frequency domain features contributes more to the detection.

We choose the Haar transform, which is sensitive in the horizontal, vertical, and diagonal directions, to extract edge features in the three directions. The features in the three directions are mapped to the same image through formula (4) to obtain a boundary map, and this feature is also stimulated, normalized, and pooled, so it can be connected and matched with spatial domain features. A $2 * 2$ pooling kernel is used in the process, and finally a $3 * 32 * 32$ frequency domain feature is obtained, also presented as a $3072 * 1$ vector feature. Next, we fuse spatial domain and frequency domain features to obtain more comprehensive facial features to improve detection accuracy. The key algorithm of Cross-domain model is described in Algorithm 1. Through vector splicing, a high-level feature vector of 4096 ($64 * 8 * 8$) is obtained and sent to the fully connected layer for classification. We use a $64 * 1$ feature vector for final classification to ensure the comprehensiveness of features. In the fully connected layer, the Dropout [28] specification is used to improve the robustness of the model, to prevent the occurrence of model over fitting, and to stop the training process in time to achieve better results. The specific parameter details are illustrated in Figure 3.
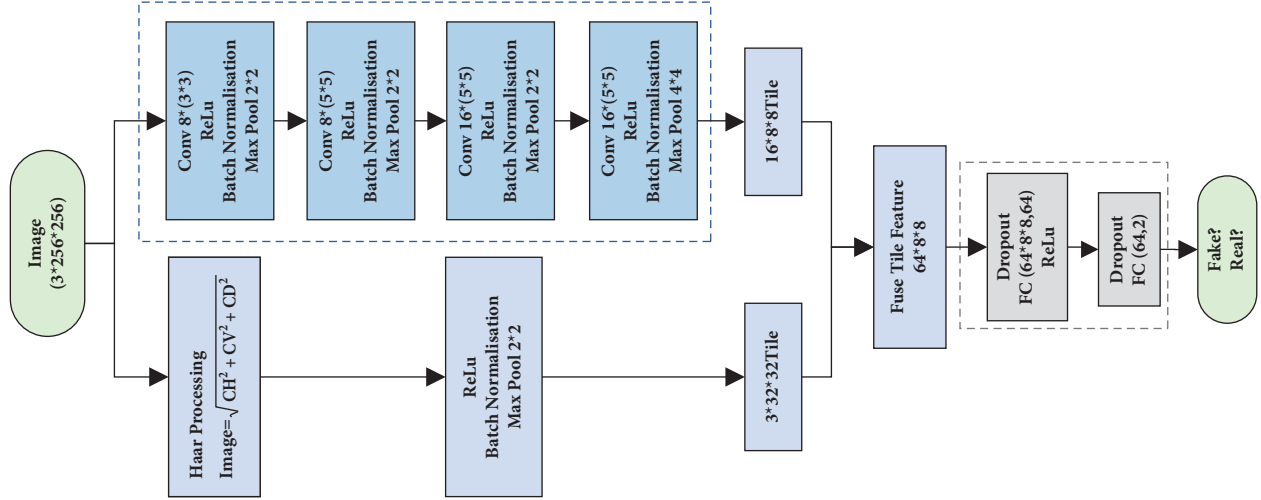
FIGURE 3: Detailed configuration of cross-domain network structure.

/* Frequency domain feature extraction process */
Input: preprocessed image X_{rc}.
Output: frequency domain feature $X_{rc}^{(1)}$.
 (1) Use formula (3) to calculate X_{CH}, X_{CV}, X_{CD}.
 (2) X_{CH}, X_{CV}, X_{CD} is mapped into an edge matrix $X_{rc}^{\wedge}$ by formula (4).
 (3) Q = operate $X_{rc}^{\wedge}$ on ReLu layer, batch normalization layer, and maximum pooling layer.
 (4) $X_{rc}^{(1)}$ = the tile of Q.
/*Obtain high-level semantic spatial domain feature*/
Input: preprocessed image X_{rc}.
Output: high-level semantic spatial domain feature $X_{rc}^{(2)}$.
 (5) For $i \leq 4$ do
 (6) P = operate $X_{rc}^{\wedge}$ on convolution layer, ReLu layer, batch normalization layer, and maximum pooling layer.
 (7) End for
 (8) $X_{rc}^{(2)}$ = the tile of P.
/*Fuse features */
Input: frequency domain feature $X_{rc}^{(1)}$ and spatial domain feature $X_{rc}^{(1)}$.
Output: the image facial feature vector ϕ.
 (9) Obtain image feature vector by formula (6).
(13) Return

ALGORITHM 1: The key algorithm of Cross-domain model.

4. Results and Discussion

In this section, we introduce the setup of the experiment, show the processing of the datasets, and discuss the experimental results on the commonly used datasets. In addition, we also compare our method with the two networks proposed by Darius Afchar et al. and with the traditional InceptionV3 network, as well as the FAW method of Li et al.

4.1. Dataset. We use two public datasets to evaluate our method. We optimize our model on the training set and the validation set and obtain the detected AUC value on the test set.

4.1.1. Deepfake Database. The Deepfake Database dataset is proposed by Afchar et al. [18], including training set and

validation set. All face images in this dataset are collected from a wide range of Internet sources, including videos that are manually processed to eliminate misalignment and false face detection. In this database, the training set has a total of 12355 images, and the verification set has 7106 images, which always contain 7950 deep forged face images and 11511 real face images. The specific details are illustrated in Table 1. During the experiment, we extracted a part of data from the training set at a ratio of 5 : 1 as the experimental verification set, and the remaining part of training set was used as the experimental training set. The verification set of the original database was used as the experimental test set to ensure the extensiveness of experimental data.

4.1.2. FaceForensics++. The FaceForensics++ dataset was proposed by A. Ro¨ssler and others at the ICCV conference

(a)

(b)
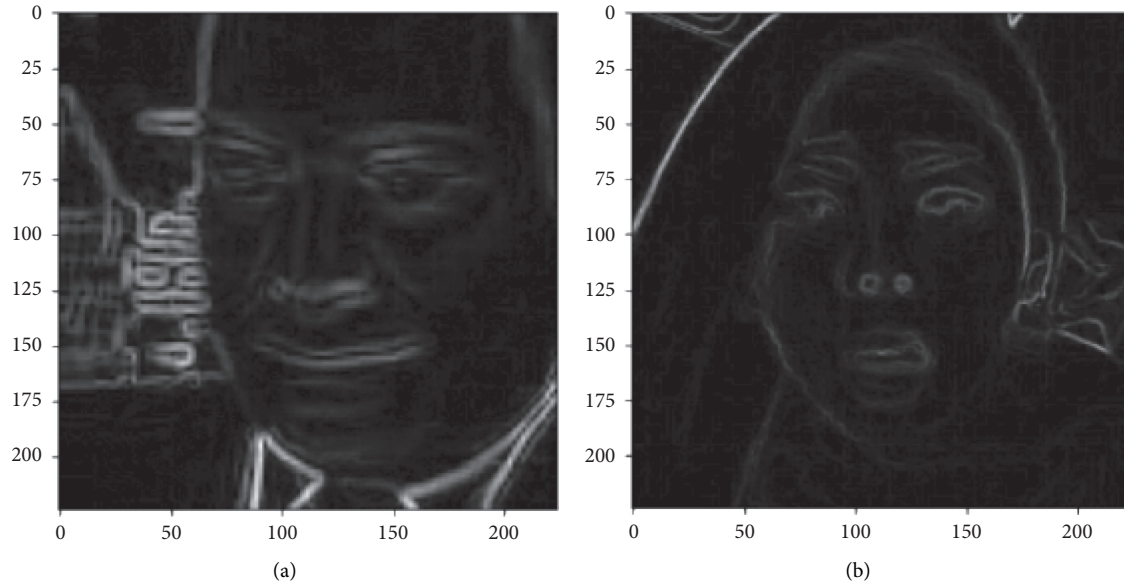
Figure 4: Face image in frequency domain. (a) Real image and (b) fake image (the edge of the face is fuzzy, and the background is clear).

Table 1: Deepfake Database dataset details.

Deepfake database	Train	Val
df	5104	2846
real	7251	4260
total	12355	7106

in 2019 [5]. The dataset contains four different types of forged datasets (high and low resolution). FF++ consists of 1000 original video sequences. The four automatic face fraud methods used are DeepFake, FaceSwap, Face2Face, and Neural Textures. The data comes from 977 YouTube videos, all of which contain a trackable frontal face, enabling automatic tampering methods to generate realistic fake faces. All videos have three resolutions, namely, uncompressed original quality, high-quality using 23 quantized light compression, and low-quality using 40 quantized heavy compression. We conduct experiments on two resolution datasets separately. During the experiment, the ratio of training set and test set is 7 : 3. We use the training set in the dataset for model training and test the model on the validation set in the dataset.

4.2. Experiment Environment. We used the above public datasets for experiments and implemented the tests on a PC with Intel(R) Core(TM) i5-7500 CPU @ 3.40 GHz 3.41 GHz and 4Gram.

On the Deepfake Database dataset, we resize the image to $256 * 256 * 3$. The initial learning rate of 0.1 is divided by 10 every 1000 iterations down to $10-6$. We set the weight attenuation to 0.1, the epoch to 20, and the batch size to 64. Finally, the detection result is optimal when the learning rate is 0.001, and the weight attenuation is 0.1.

On the FF++ Database dataset, the initial experimental setup is the same as the Deepfake Database dataset, and the

best effect is achieved through fine tuning. The parameters of fine tuning for different datasets are as follows:

(1) For the DeepFake 40 dataset experiment, we set the parameter of weight attenuation 0.1 and set the base learning rate as 0.001 divided by 70 every 5 epochs

(2) For the DeepFake 23 dataset experiment, we set the parameter of weight attenuation 0.3 and set the base learning rate as 0.001 divided by 50 every 5 epochs

(3) For the Face2Face 40 dataset experiment, we set the parameter of weight attenuation 0.03 and set the base learning rate as 0.001 divided by 30 every 5 epochs

(4) For the Face2Face 23 dataset experiment, we set the parameter of weight attenuation 0.1 and set the base learning rate as 0.001 divided by 10 every 5 epochs

(5) For the FaceSwap 40 dataset experiment, we set the parameter of weight attenuation 0.05 and set the base learning rate as 0.001 divided by 50 every 5 epochs

(6) For the FaceSwap 23 dataset experiment, we set the parameter of weight attenuation 0.05 and set the base learning rate as 0.001 divided by 60 every 5 epochs

In order to prove the advantages of the deepfake detection model in this paper, we analyze the detection AUC value of our method on different datasets and show the ROC curve graph. Moreover, we compare and analyze it with other deepfake detection methods.

4.3. Comparison Method. In order to prove the effectiveness of the model in this paper, we implemented a number of comparative experiments on the Deepfake Database dataset, and the experimental results are illustrated in Figure 5(a).

(a)

(b)
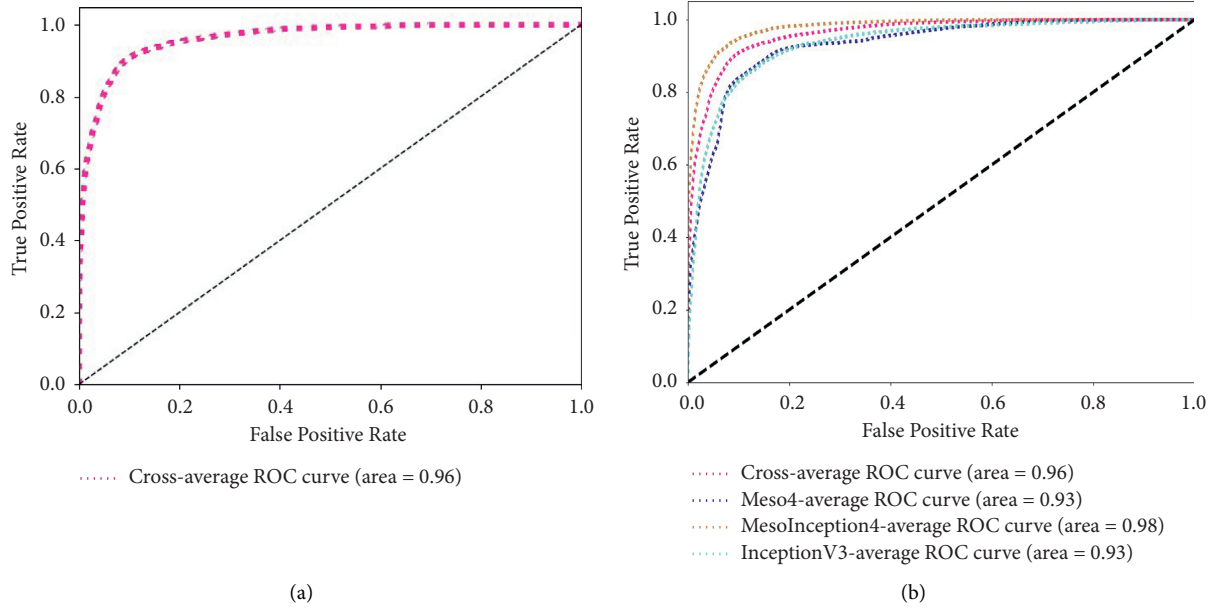
FIGURE 5: Experiment result of detection on the Deepfake Database dataset. (a) Cross-domain model performance and (b) ROC curves of Meso4, MesoInception4, InceptionV3, and Cross-domain model.

TABLE 2: The accuracy on the testing set on Deepfake Database dataset.

Method	Deepfake database (%)
Meso4 [15]	87.05
MesoInception4 [15]	92.50
InceptionV3 [12]	88.05
FAW [20]	64.30
Our method	**90.50**

(a)

(b)
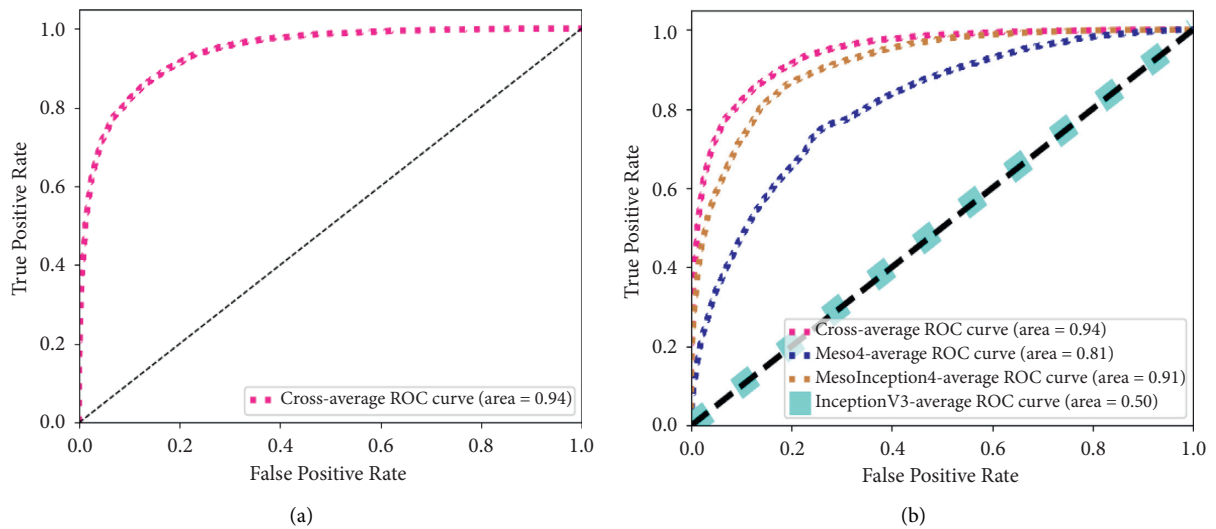
FIGURE 6: Continued.
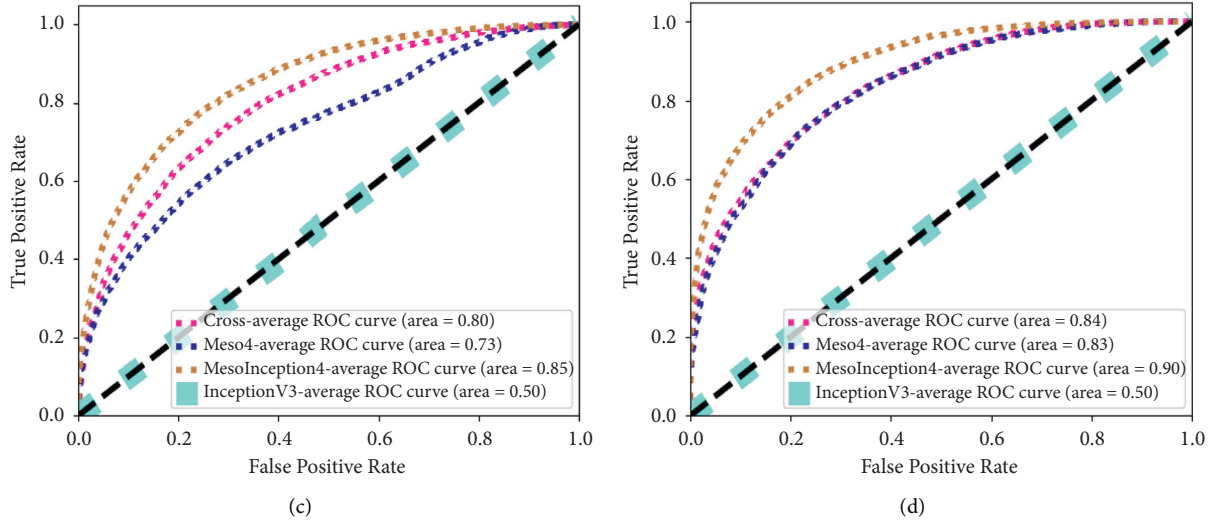
Figure 6: Experiment result of detection on the FF++ low-quality dataset. (a) Cross-domain model performance on the DP40 dataset, (b) ROC curves of comparison methods on the DP40, (c) ROC curves of comparison methods on the FS40, and (d) ROC curves of comparison methods on the F2F40.
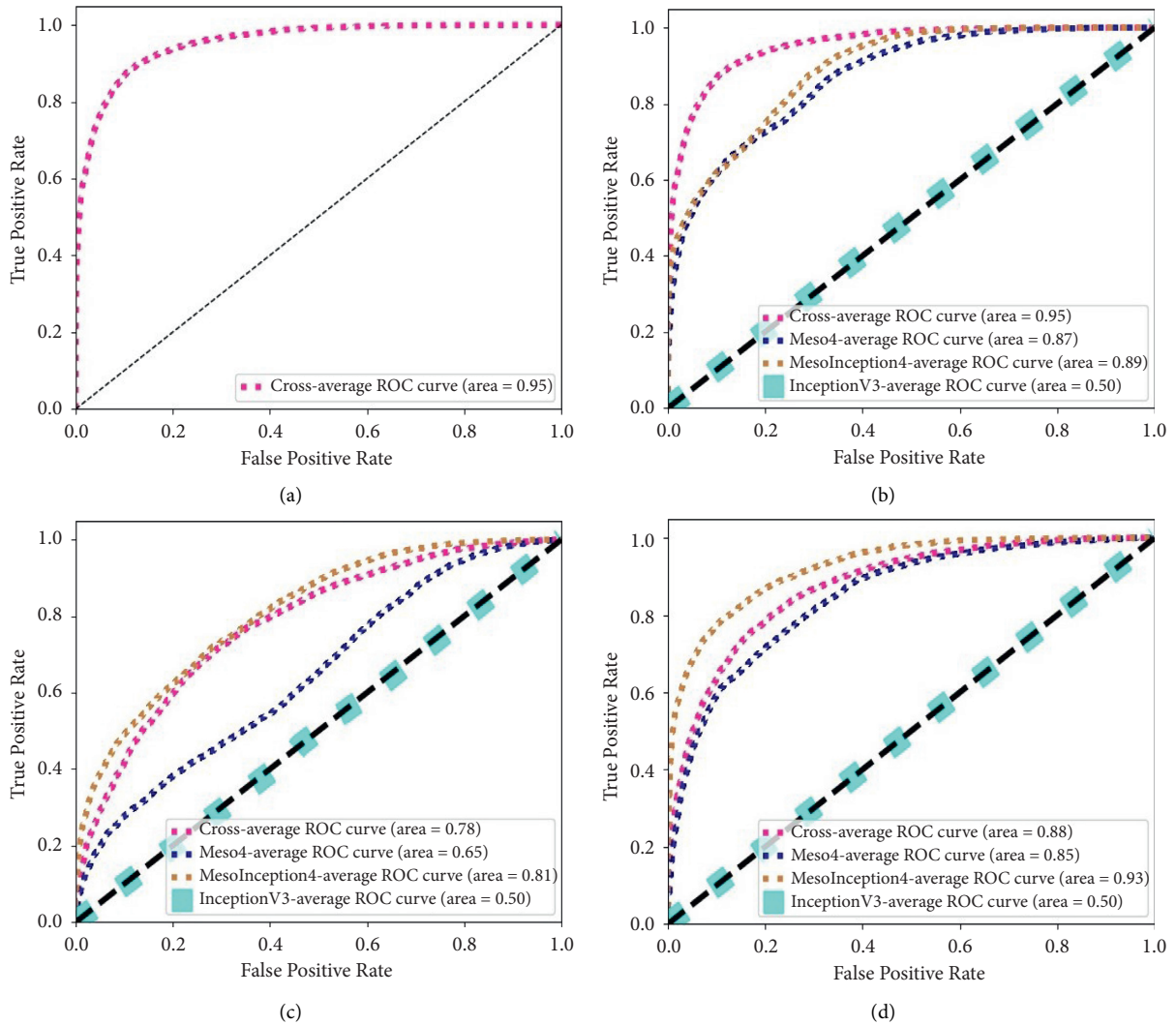
Figure 7: Experiment result of detection on the FF++ high-quality dataset. (a) Cross-domain model performance on the DP23 dataset, (b) ROC curves of comparison methods on the DP23, (c) ROC curves of comparison methods on the FS23, and (d) ROC curves of comparison methods on the F2F23.

TABLE 3: The AUC value of testing on FF++ high-quality dataset with training model on FF++ low-quality dataset.

Method	DP40-model test DP23	F2F40-model test F2F23	FS40-model test FS23
Meso4 [15]	0.87	0.75	0.75
MesoInception4 [15]	0.94	0.90	0.89
InceptionV3 [12]	0.50	0.50	0.50
Our method	**0.97**	**0.84**	**0.83**

The bold is the detection result of our method.

The results indicated that the AUC value of our detection method reached 0.96. At the same time, we also compare our approach with the InceptionV3 network in [15]and the Meso4 and MesoInception4 networks in [18], and the results are illustrated in Figure 5(b). Figure 5(b) signifies that the Meso4 network and the traditional InceptionV3 network achieve an AUC value of 0.93, while the MesoInception4 network achieves an AUC value of 0.98. Our cross-detection model achieves an AUC value of 0.96, right after Meso-Inception4 network. Meanwhile, we use the method presented in [23] to perform the test, and the accuracy results are illustrated in Table 2.

In order to better demonstrate the effectiveness of our method, we test the model in different databases. Detailed parameter settings are introduced in section 4.2. We firstly selected low-quality and high-quality images in FF++ for training and testing. The DP40 data showed that our model reached an AUC value of 0.94, which is relatively a good result as shown in Figure 6(a). Comparison results with other methods are illustrated in Figure 6(b). The experimental results for the FS40 and F2F40 datasets are illustrated in Figures 6(c) and 6(d). Our model reached an AUC value of 0.80 on the FS40 dataset and had an AUC value of 0.84 on the F2F40 dataset. It can be seen from the AUC value in the figures that the detection method in this paper has a better performance. Figure 7(a) indicates that our model has reached an AUC of 0.95 in the DP23 dataset, which is an increase of 0.01 better than the result in the DP40 dataset. Also compared with the results of the other three detection methods, our result is the best, illustrated in Figure 7(b). Our method reached an AUC value of 0.78 on the FS23 dataset, and 0.88 on the F2F23 dataset, illustrated in Figures 7(c) and 7(d). For all of the above, it is shown that our method has better performance no matter in high quality or low quality. Our method has the best on deepfake dataset, and second on other datasets. This is because our method on DeepFake dataset has fully taken face edge features into account, and the forgery traces of this dataset are clearly exposed on the edge features. However, on other forgery methods datasets, it has less consideration on subtle features such as lips, eye, and nose. This is the direction to be diligent in the future.

In addition, we use models trained on low-quality datasets to test high-quality datasets in order to verify the cross-database performance. Experimental results are illustrated in Table 3. The performance of our method will not degrade with the change of datasets. On the contrary, our method achieved an AUC of 0.97 on DP23 dataset and had an AUC value of 0.84 and 0.83 on F2F23 dataset and FS23 dataset, respectively.

5. Conclusion

In this paper, we propose a new deepfake detection method based on cross-domain fusion, where edge geometric features in frequency domain are introduced to image feature set and fused with high-level semantic features in spatial domain for better detection accuracy. Experimental analysis shows that our detection method is effective and has better cross-database performance when the target datasets are forged using deepfake technology. This is due to the fact that our method has fully taken face edge features into account. However, our method is less effective on Neural Textures dataset as it has less consideration on subtle features such as lips, eye, and nose. In the future, we will further investigate the extraction of subtle facial features and continue to enhance detection robustness and cross-dataset performance.

Data Availability

The data used to support the findings of this study are included within the article.

Conflicts of Interest

The authors declare that they have no conflicts of interest.

Acknowledgments

References

[1] X. Liu, X. Zhai, W. Lu, and C. Wu, "QoS-guarantee resource allocation for multibeam satellite industrial Internet of Things with NOMA," *IEEE Transactions on Industrial Informatics*, no. 99, p. 1, 2019.

[2] X. Liu and X. Zhang, "Rate and energy efficiency improvements for 5G-based IoT with simultaneous transfer," *IEEE Internet of Things Journal*, vol. 6, no. 99, p. 1, 2018.

[3] X. Liu, X. Zhang, W. Lu, and M. Xiaong, "Energy efficiency maximization for green cognitive internet of things with energy harvesting," *Machine Learning and Intelligent Communications*, Springer, New York, Ny, USA, 2019.

[4] Y. Mirsky and W. Lee, "The creation and detection of deepfakes: a survey," 2020, https://arxiv.org/abs/2004.11138.

[5] A. Ro¨ssler, D. Cozzolino, L. Verdoliva, C. Riess, and J. Thies, "M. Nie?ner, Faceforensics++: learning to detect manipulated facial images," in *Proceedings of the 2019 IEEE/CVF International Conference on Computer Vision (ICCV)*, pp. 1–11, Seoul, Korea, November 2019.

[6] R. Tolosana, R. Vera-Rodriguez, J. Fierrez, A. Morales, and J. Ortega-Garcia, "Deepfakes and beyond: a survey of face manipulation and fake detection," *Information Fusion*, vol. 64, pp. 131–148, 2020.

[7] P. Zhou, X. Han, V. I. Morariu, and L. S. Davis, "Two-stream neural networks for tampered face detection," in *Proceedings of the 2017 IEEE Conference on Computer Vision and Pattern Recognition Workshops (CVPRW)*, pp. 1831–1839, IEEE, Honolulu, HI, USA, July 2017.

[8] H. Li, B. Li, S. Tan, and J. Huang, "Detection of deep network generated images using disparities in color components," 2018, https://arxiv.org/abs/1808.07276.

[9] D. Cozzolino and L. Verdoliva, "Noiseprint: a CNN-based camera model fingerprint," *IEEE Transactions on Information Forensics and Security*, vol. 15, pp. 144–159, 2019.

[10] Y. Hu, Y. Gao, B. Liu, and G. Liao, "Deepfake videos detection based on image segmentation with deep neural networks," *Journal of Electronics and Information Technology*, vol. 43, no. 1, pp. 162–170, 2021.

[11] S. McCloskey and M. Albright, "Detecting GAN-generated imagery using color cues," 2018, https://arxiv.org/abs/1812.08247.

[12] L. Nataraj, T. Mohammed, S. Chandrasekaran, A. Flenner, J. H. Bappy, and B. S. Anjunath, "Detecting GAN generated fake images using co-occurrence matrices," 2019, https://arxiv.org/abs/1903.06836.

[13] X. Zhang, S. Karaman, and S.-F. Chang, "Detecting and simulating artifacts in gan fake images," 2019, https://arxiv.org/pdf/1907.06515.

[14] M. A. Younus and T. M. Hasan, "Effective and fast DeepFake detection method based on haar wavelet transform," in *Proceedings of the 2020 International Conference on Computer Science and Software Engineering (CSASE)*, Jeju, Korea, December 2020.

[15] C. Szegedy, V. Vincent, S. Ioffe, J. Shlens, and Z. Wojna, "Rethinking the inception architecture for computer vision," in *Proceedings of the IEEE Conference on Computer Vision and Pattern Recognition (CVPR)*, IEEE, Las Vegas, NV, USA, July 2016.

[16] C. Szegedy, W. Liu, Y. Jia et al., "Going deeper with convolutions," in *Proceedings of the 2015 IEEE conference on computer vision and pattern recognition (CVPR)*, pp. 1–9, Boston, MA, USA, July 2015.

[17] F. Yu and V. Koltun, "Multi-scale context aggregation by dilated convolutions," 2016, https://arxiv.org/abs/1511.07122.

[18] D. Afchar, V. Nozick, J. Yamagishi, and I. Echizen, "MesoNet: a compact facial video forgery detection network," 2018, https://arxiv.org/abs/1809.00888.

[19] R. Wang, F. Juefei-Xu, L. Ma et al., "Fakespotter: a simple yet robust baseline for spotting AI-synthesized fake faces," 2019, https://arxiv.org/abs/1909.06122.

[20] H. H. Nguyen, J. Yamagishi, and I. Echizen, "Capsule-forensics: using capsule networks to detect forged images and videos," in *Proceedings of the IEEE International Conference on Acoustics, Speech and Signal Processing (ICASSP)*, IEEE, Brighton, United Kingdom, May 2019.

[21] S. Ekraam, J. Cheng, A. Jaiswal, W. AbdAlmageed, I. Masi, and P. Natarajan, "Recurrent convolutional strategies for face manipulation detection in videos," in *Proceedings of the IEEE/CVF Conference on Computer Vision and Pattern Recognition (CVPR) Workshops*, pp. 80–87, IEEE, Long Beach, CA, USA, June 2019.

[22] F. Matern, C. Riess, and M. Stamminger, "Exploiting visual artifacts to expose deepfakes and face manipulations," in *Proceedings of the 2019 IEEE Winter Applications of Computer Vision Workshops (WACVW)*, pp. 83–92, IEEE, Waikoloa Village, HI, USA, January, 2019.

[23] Y. Li and S. Lyu, "Exposing deepfake videos by detecting face warping artifacts," 2019, https://arxiv.org/abs/1811.00656.

[24] J. Stehouwer, H. Dang, F. Liu, X. Liu, and A. Jain, "On the detection of digital face manipulation," 2020, https://arxiv.org/abs/1910.01717.

[25] S. A. Khan, A. Artusi, and H. Dai, "Adversarially robust deepfake media detection using fused convolutional neural network predictions," 2021, https://arxiv.org/abs/2102.05950.

[26] D. P. Kingma and J. Ba, "Adam: a method for stochastic optimization," 2015, https://arxiv.org/abs/1412.6980.

[27] S. Ioffe and C. Szegedy, "Batch normalization: accelerating deep network training by reducing internal covariate shift," 2015, https://arxiv.org/abs/1502.03167.

[28] N. Srivastava, G. E. Hinton, A. Krizhevsky, I. Sutskever, and R. Salakhutdinov, "Dropout: a simple way to prevent neural networks from overfifitting," *Journal of Machine Learning Research*, vol. 15, pp. 1929–1958, 2014.

WILEY | Hindawi

Research Article

Intelligent Tea-Picking System Based on Active Computer Vision and Internet of Things

Jing Zhang [ID][1] **and Zhaochun Li** [ID][2]

[1]*Engineering Training Center, Nanjing Forestry University, Nanjing 210037, China*
[2]*College of Mechanical and Electronic Engineering, Nanjing Forestry University, Nanjing 210037, China*

Correspondence should be addressed to Jing Zhang; zj2016_nl@njfu.edu.cn

Intelligent farming machines are becoming a new trend in modern agriculture. The intelligence and automation allow planting to become data-driven, leading to more timely and cost-effective production and management of farms and improving the quality and output of farm products. This paper presents a proposal for developing a type of intelligent tea picking machine based on active computer vision and Internet of Things (IoT) techniques. The intelligent tea picking machine possesses an active vision system for new tip positioning and can automatically implement tea picking operation in the natural environment. The active vision system provided with a cross-light path of projection and camera is designed according to the actual characteristics of picking surface, where new tips can be recognized by referring to the color factor and their height information is easily acquired by fringe projection profilometry. Furthermore, the machine attaches wireless communication equipment to transmit the real-time status of the tea picking process to an intermediary platform and eventually to the Internet for extensive data analysis. The data such as color factor and quantity of new tips collected through IoT can be used for different quality and production evaluations. The focus of this paper can promote the automation and intelligence of tea pickers and agricultural machinery.

1. Introduction

Tea is an aromatic material for the beverage that originated in China at the earliest [1]. Its history spreads across multiple cultures over thousands of years. So far, tea is the most widely consumed beverage in the world [2]. Every year, a large amount of readymade tea comes from several main producing areas to fit the global demand. However, picking tea is an arduous job because of the long working time and high-labor intensity during the harvest period. In China, the harvest of high-quality tips is commonly completed by hand. The traditional agricultural economy is facing the pressure of a shortage of labor resources and increased manufacturing costs. Even some tea manufacturers have to give up harvesting under challenging times. To enhance the tea quality and balance the industry economically, it is necessary to promote extensive use of tea picking machines.

Actually, during the past years, the emergence of various agricultural machinery has largely replaced manual planting and harvesting, alleviating the challenges posed by a labor shortage and rising production costs for agricultural sustainability. More intelligent agricultural equipment is expected to play an essential role in improving farming activities. The latest trend is to enable these farming machines to operate over the Internet [3, 4]. The basis of this new approach is a complete set of IoT servers and wireless sensors. Agricultural producers can realize the interoperability of various production links by building regional Internet of Things (IoT) and wireless sensor networks (WSNs) [5]. In this framework, agricultural machinery, sensors for crop environmental factors, conveying equipment, farmers' mobile terminals, and databases from higher-level agricultural departments are connected as a whole [6, 7]. By monitoring the planting of crops on the farm and uploading it to the server through the analysis of big data by higher-level departments and then accurately regulating

planting, fertilization, irrigation, and picking, it can allocate land more scientifically and plant crops more reasonably, and ultimately achieve a large increase in production and significant improvement in quality [8]. In addition, IoT technology uses low-latency networks to drive farm machinery work. It liberates farmers and dramatically reduces production costs [9].

Currently, the available tea harvesting machines are mostly used for cutting operations over a large area. Their high efficiency helps manufacture a huge quantity of low-grade goods. However, their harvesting style without any selection may result in the tea product composition of many stalks and old leaves, while only the new tips and one leaf below new tips are supposed to be high-grade tea. Hence, it is necessary to redesign the picking style and develop such an intelligent tea picking system that can automatically locate new tips and realize a kind of data-driven harvesting.

The main contribution of this paper can be highlighted as follows:

(i) A new intelligent machine for high-grade tea picking has to be developed, which involves two critical designs: the construction of an active vision system for new tip positioning and the other application of IoT for collecting various harvest information.

(ii) The active vision system is designed as the fundamental unit for artificial intelligence like eyes for humans. The visual system is constructed with a cross-light path of projection and camera according to the actual characteristics of the picking surface. It can implement the recognition of new tips by referring to the color factor and applying the fringe projection profilometry to acquire the height information of the tips.

(iii) IoT is applied to collect real-time status about the tea picking process to the server, and extensive data analysis is used to assess the quality and yield of tea to improve integrated farm management.

The remainder of this paper is organized as follows: Section 2 gives the details of the system materials and methods, including the design of regional IoT and three-dimensional positioning systems. Section 3 presents the experiments to demonstrate the effectiveness of the new design. Finally in Section 4, concluding remarks are given.

2. Materials and Methods

2.1. Data Collection Based on IoT. IoT ensures data flow between sensors and other devices, making it possible to obtain data by automatic processing, analysis, and access, leading to more timely and cost-effective high-grade tea production and management effort on farms [10, 11]. Simultaneously, IoT eases the supervision of different activities as well as the traceability of products and control in farms by the appropriate authorities.

The wireless communication module is applied to collect harvest information such as the color and height of new tips, picking time, and environmental conditions. The data such as color factor and humidity can be used to illustrate the tea quality. The quantity of new tips is taken into account in the overall data to evaluate production before frying. Figure 1 presents that, with IoT, some necessary information about the tea production process, such as tea making, packaging, and transportation, are transmitted to the Internet for data analysis and product control. Even various operating parameters of the running machines can also be uploaded and displayed to the operator in real-time.

2.2. Three-Dimensional Positioning System. Fringe projection profilometry is one of the most widely used techniques of three-dimensional (3D) optical measurement, because of its qualities of noncontact, low-cost, and high-resolution [12]. Based on the classical principle of triangulation optics, fringe patterns that consist of a sinusoidal distribution of gray scale patterns are projected onto the object, and the distorted patterns are then captured by the imaging system. Further processing by phase unwrapping, exact 3D information can be obtained [13].

Unlike other measurement methods of structured light, fringe patterns project a spatial field distributed by period. The parameter being measured is encoded in the form of a two-dimensional (2D) distorted fringe, from which the phase map retrieved can describe the whole and continuous plane. Therefore, the profilometry can perform the measurement of the planar objects in the field of imaging by one projection.

In this work, an intelligent tea-positioning system is designed based on the profilometry fringe projection. As shown in Figure 2, the system consists of a DLP projector, a digital camera with resolution 1028×964, a computer, and a reference plane. It is noted that, in the optical system, the line joining the optical center of the camera and the projective center should be parallel to the reference plane, the projective axis should be set perpendicular to the reference plane, and the projective axis and the optical axis of the camera should either intersect the reference plane. The distance l_0 between the center of the camera and the projector is set as 45 cm, and the distance between the optical center of the camera and the reference plane is defined as 110 cm. Two steps should be performed for tea-positioning: identifying and ascertaining the new tips growing above the tea canopy and providing their horizontal coordinates; applying fringe projection profilometry to extract their actual height information relative to the reference plane.

2.3. Tips Identification under Natural Conditions. Identifying the tea tips from the natural background is the first step towards the intelligent tea picking machine. In the early spring, the color differences are distinct between the fresh tips and the background consisting of soil, old leaves, and the debris of plants. These differences make it possible for the image segmentation of distinguishing new tips from the gray background.
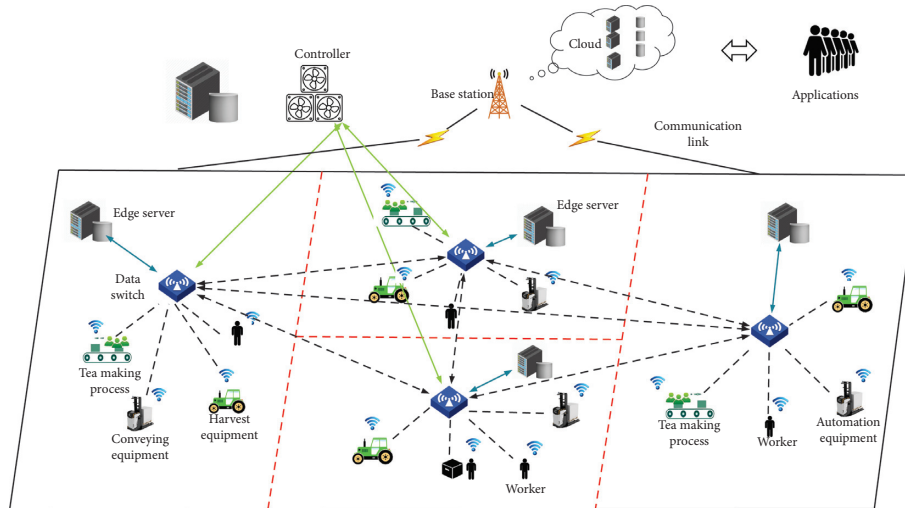
FIGURE 1: Agricultural Internet of Things.
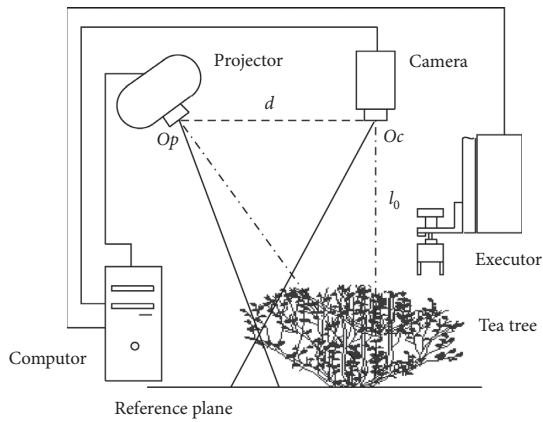
FIGURE 2: Tea tips positioning system.

FIGURE 3: Tea in early spring.

The color analysis on the new tips and the image segmentation from their background had been discussed in Reference [14], and a tip identification method is developed as preliminary guidance for the positioning system. Several color indices, including the difference between cyan and magenta color in CMY color space, channels B, Q, $i3$, and Yb in LAB, YIQ, i1i2i3, and RGB color spaces [15], are studied and tested. In order to ensure a desirable result of image segmentation, the gray level image is transformed into a binary image by the Otsu method [16], and an area filter is used to sweep away the randomly spotted noise. Finally, a centroidal method is applied to identify the center pixels of the tips, and then their horizontal coordinates are obtained.

Figure 3 depicts the famous Longjing tea pictured by CCD in early spring in a tea farm located in Jintan, Jiangsu province of China. The figure can be processed by the aforementioned procedures to identify the new tips, whose results are shown in Figure 4. By comparing Figure 3 with Figure 4, we can see that most new tips are identified accurately and match the centroidal pixels well, where the centroidal pixels are marked by the green dots. The results
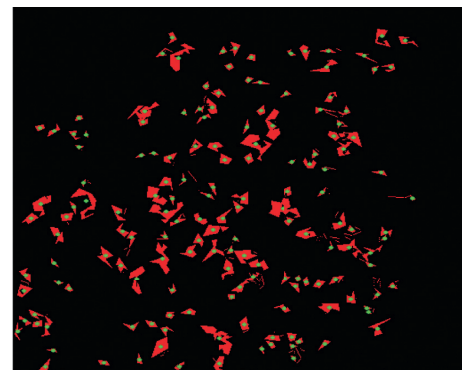
FIGURE 4: The central points of tea tips.

illustrate that the automated identification of new tips is performed successfully.

2.4. Height Measurement by Fringe Projection Profilometry.
In the past three years, we have carried out many experiments on several prevalent technologies to measure the depth distribution of objects. Finally, the fringe projection

profilometry is adopted as a reliable solution. As introduced above, the fringe projection profilometry is implemented by projecting a set of sinusoidal fringes to the measured object, grabbing the modulated fringe images by the measured object, and processing these images for the unwrapped phase and height information [17]. It is easy to implement with simple hardware and more applicable to the object lying over a plane.

Let us focus on the cultivation pattern of the tea trees. In most farms, the tea trees are planted line by line with a path between the rectangular raised-fields. During each raised field, these trees are planted side by side. When the trees are mature, their branches and leaves will extend together as a shrub. Generally, the crown of the shrub will be pruned into a flat or arc plateau. So it is convenient to the large-scale plucking by machines. If the picking surface is considered as an object, the profilometry is exactly a rational solution to acquire the height information of each pixel.

2.4.1. Obtaining the Phase Value.

A typical fringe projection profilometry usually yields four phase-shifted images for the extraction of the phase information. The phase retrieval can be completed by two steps: wrapped phase retrieval and phase unwrapping [18]. First, the sinusoidal fringe patterns which have $\pi/2$ phase shifts relatively are projected onto the object as shown in Figure 2, and the distorted pattern captured by the CCD camera can be used to calculate the wrapped phase by Equation (1). Second, the obtained wrapped phase can be demodulated into an absolute phase map by the phase-unwrapping algorithm [13]:

$$\phi^w(x, y) = \arctan\frac{I_3 - I_1}{I_0 - I_2}, \tag{1}$$

where (x, y) is the image coordinates, $\phi^w(x, y)$ is the wrapping phase, I_i is the gray intensity distribution of the fringe image, and i means the ith phase-shifting fringe image $(i = 0, 1, 2, 3)$.

According to the above inverse tangent function, the modulated phase is limited in the range of $[-\pi, \pi]$, which leads to the periodical distribution of the phase map. Phase unwrapping is carried out to restore the unknown multiple of 2π for each pixel [12]. But since noise, fringe under-sampling, and shadow problems exist in the acquired phase map, if the phase-unwrapping path traverses these regions, 2π-phase errors will occur. Unwrapping errors can easily be accumulated and propagated along the unwrapping path. Thus, many methods based on reliability ordering have been presented in this field aiming to alleviate the error propagation, such as water flood algorithms and modulation-based algorithms. However, error accumulation and propagation are still an obstacle, if only passing through invalid areas with global discontinuities is needed [13].

In order to avoid stubborn error propagation, a more complex method of the temporal phase-unwrapping algorithm is implemented in this system. There are four kinds of fringes with different wavelengths designed and projected to the object by turns. The wavelength numbers of fringes are 1, 4, 16, and 64, respectively. Each ϕ_k^w corresponding to a

different kind of fringe can be disposed by Equation (1), but the unwrapping phase is given by the following equation:

$$\phi_k^u = \begin{cases} \phi_k^w, & k = 1, \\ \\ \phi_k^w + 2\pi \cdot \text{Round}\left(\dfrac{\phi_{k-1}^u \cdot m_k/m_{k-1} - \phi_k^w}{2\pi}\right) & k > 1, \end{cases} \tag{2}$$

where a sequence of incremental phase maps can be assembled and integrated into the final phase-difference map. The basic meaning of the temporal is that the phase at each pixel can be calculated as a function of time. Unwrapping is carried out along the time axis for each pixel independently from the others, which is so-called path-independent. In this 3-D phase distribution, the local discontinuities keep unchanged along the time axis, provided that these discontinuities do not change with time, and therefore can be avoided completely during the process of unwrapping along the path parallel to the time axis [19]. Therefore, temporal phase unwrapping performs better in alleviating phase ambiguity and error in contrast to other implemented approaches [18].

An example of the unwrapping phase process is shown in Figure 5. Figures 5(a)–5(d) present the wrapped phases of each wavelength fringe, which can be demodulated by Equation (2) to the absolute phase maps. There are many abnormal peaks and abrupt points in these figures, and these points are all low-reliability pixels and should not be utilized. However, these bad points do not propagate and contaminate the rest of the unwrapping results and also testify the robust ability of the unwrapping phase algorithm.

When the fringes are projected on the reference plane, the absolute phase of reference ϕ^r is available and the difference between the reference plane and the objects at the pixel (x, y) can be written as

$$\Delta\varphi(x, y) = \phi^u(x, y) - \phi^r(x, y). \tag{3}$$

in which the full height information is preserved.

2.4.2. Phase-Height Mapping.

In order to obtain the height information conveniently and accurately, establishing appropriate height mapping with the unwrapped phase is necessary. Traditional calibration technique based on ray tracing derives the following phase-height formula with the aid of the similarity of space triangles referring to the triangulation profilometry [20].

$$h(x, y) = \frac{l_0 \Delta\varphi(x, y)}{\Delta\varphi(x, y) + 2\pi d/\lambda_0}, \tag{4}$$

where λ_0 denotes the equivalent wavelength of the 64 fringes ($\lambda_0 = 8.3$ mm). However, in practice, the higher the measured object, the more severely defocused the camera lens will be. Even worse, both the optical projection system and the image formation parts can inevitably introduce optical aberrations. Due to these problems, the theoretical equation as Equation (4) cannot deduce the accurate height value.
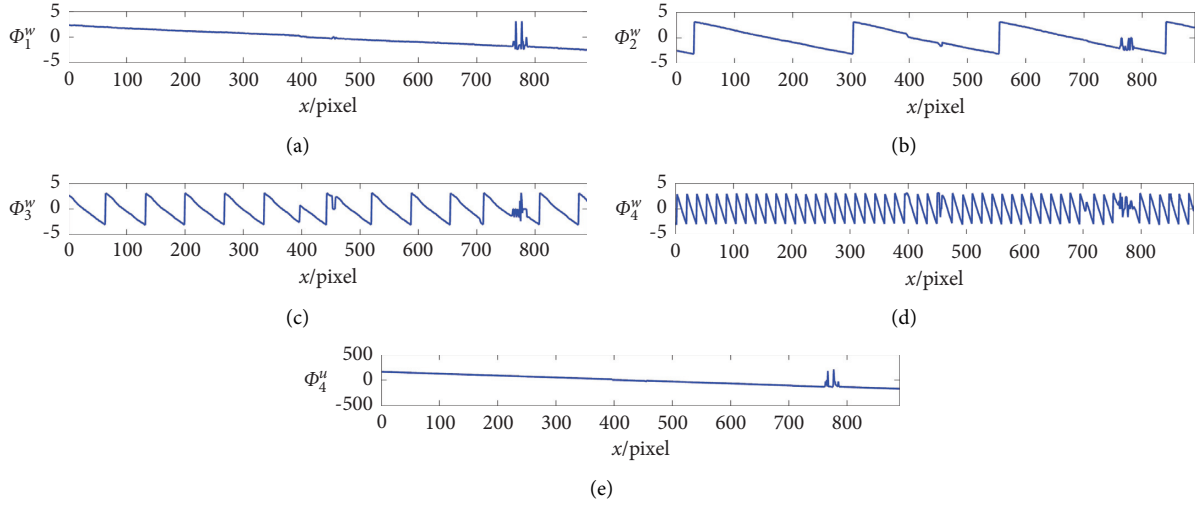
FIGURE 5: Temporal phase unwrapping.

Therefore, how to improve the accuracy of height calculation is another thinking point. Fortunately, a triple-parabolic fitting described in Equation (5) is proposed to rebuild the phase-height mapping, and then their nonlinear relationship is corrected completely.

$$\frac{1}{h(x, y)} = a + b\frac{1}{\Delta\varphi(x, y)} + c\left[\frac{1}{\Delta\varphi(x, y)}\right]^3, \quad (5)$$

where a, b, and c are the system adjustment parameters obtained by a series of calibrations. It should be noted that the real value of a set of parameters for one point is actually different from the other, but a, b, and c can be calculated, respectively, by the approximation of average.

3. Results and Discussion

For the visual positioning system, it is necessary to testify its functionality and reliability before application. Hence, some experiments listed below are performed.

First of all, an artificial model of landscape grass is placed as the measured object, whose leaves are independent because of obvious height differences, but overlapped or covered by each other. The model is used to simulate the natural tea plant in a farm provided with the typically discontinuous and complex crown surface. Figure 6 shows that the grating stripe is projected on the surface of the grass model. Grabbing the image by CCD, and calculating the height using Equation (5), a three-dimensional topography for the grass model is obtained eventually as shown in Figure 7. In this figure, we can see the presence of a large amount of irregular noise especially near the object edges, which has even completely concealed their real shapes and failed the measurement.

That result in itself is no surprise since the temporal phase unwrapping can reduce the propagation of the phase errors caused by any noise, shadow, or other reasons, but it cannot avoid the single error points and the discrete noise in view. Hence, a lot of large noises and serious phase errors
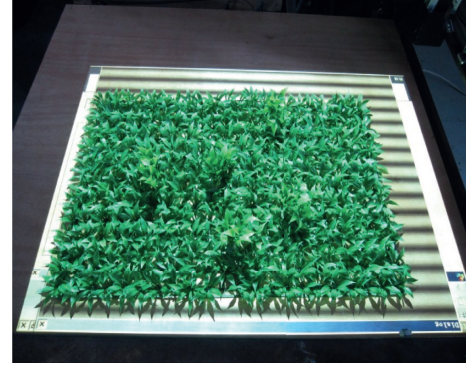
FIGURE 6: The artificial grass and the fringe pattern.
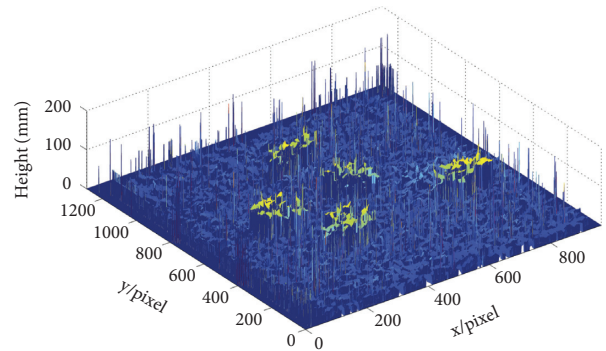
FIGURE 7: The three-dimensional contour of the artificial grass before filtering and processing.

emerge near the amplitude-variation boundary when an inconsistent surface is involved.

In order to enhance the accuracy of the measurement, the necessary filtered methods are applied or proposed to restrain the discrete noise. In this system, besides some traditional noise elimination methods such as the phase relationship verdict between neighboring pixels and area

filtering, some other effective methods are also introduced to ensure the better phase unwrapping result, which is listed below.

(a) The modulation M is defined as a reliability map. A threshold is set and the pixels with M higher than the threshold will be considered as the valid points. On the contrary, those pixels whose modulation is lower than the threshold can be deemed as invalid points and be reset directly to zero. The modulation M can be computed by the following equation:

$$M = \frac{1}{2} \sqrt{\left(\sum_{i=0}^{3} I_i \sin \frac{2\pi i}{4} \right)^2 + \left(\sum_{i=0}^{3} I_i \cos \frac{2\pi i}{4} \right)^2}, \quad (6)$$

where I_i is the ith phase-shifted fringe pattern whose wavelength should be the highest one in the four fringe patterns. The higher the frequency of the fringe, the more serious is the noise disturbance. Our experiments indicate that when M is chosen high enough, the noise can be reduced effectively. However, high M may erode the contour of the surface, especially the edge around the object. After many tests, the threshold to identify the valid point is set as 2.

(b) Morphological filter is introduced to process the absolute phase map and to remove the stains. For the map that has been disposed by the modulation method described above, an open operation consisting of erosion operation in advance and swell operation afterwards presents enough superiority. The erosion operation can delete the islets and summits less than the structural element. The selection of erosion structural elements is a crucial step. The excessive little structural element has no obvious effect on the filtered result, but the sufficiently big one may damage the integrity of the object. By comparison, an element "Disk" whose radius is 3 is picked up finally.

Figure 8 depicts the final effect after the processing by these filtering methods related by (a) and (b). It can be seen that the noisy map becomes neat and all boundaries of the inside leaves are preserved well. The topographical map is exquisite and detailed enough to reflect the real shape of the artificial object. This satisfactory result verifies the functioning of the methods (a) and (b) against the stubbornly large noise.

Aimed to verify the precision of height measurement, some columns with known height values are implanted as fixed points, as shown in Figure 9. Figure 10 presents their three-dimensional topography after projection and processing. If we fit the point data at the top of each column with a plane and calculate the average value on the top, we can obtain the measurement heights of these columns. The actual height of the objects, the measurement results, and the height errors are also listed in Table 1, which reveals that the maximum error is less than 2 mm for all points. It is an adaptable accuracy, referred to the tolerance of 3 mm for the
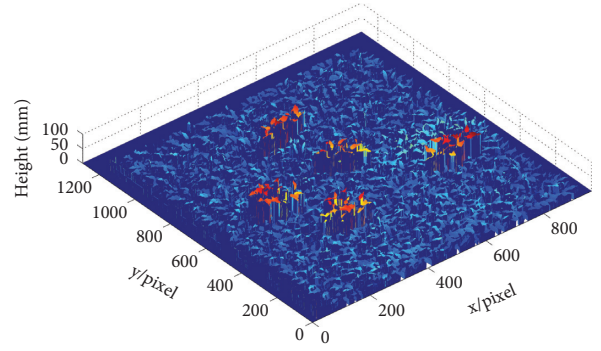
FIGURE 8: The three-dimensional contour of the artificial grass.
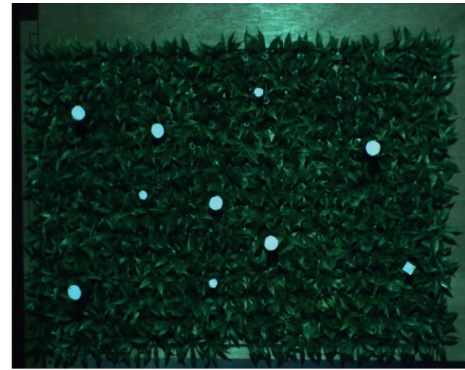
FIGURE 9: The altitude target.
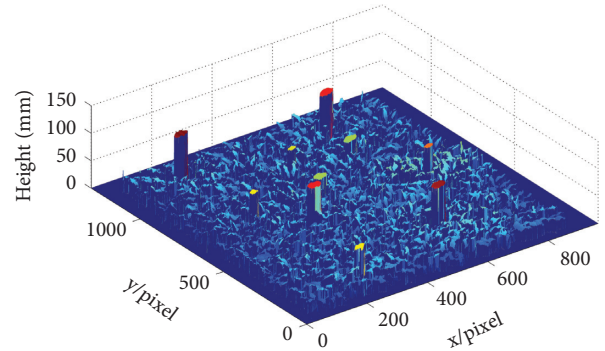
FIGURE 10: The three-dimensional contour of the altitude target.

TABLE 1: The target height measurement (mm).

Objects	Actual height	Measurement result	Height error
1	89.0	90.9	1.9
2	56.5	55.4	−1.1
3	57.0	56.1	−0.9
4	79.0	80.2	1.2
5	47.0	45.4	−1.6
6	53.0	52.1	−0.9
7	88.0	89.4	1.4
8	47.0	45.1	−1.9
9	78.0	78.5	0.5
10	69.0	69.1	0.1

FIGURE 11: Harvesting experiments in farms.

tea picking machine executor. The results indicate that the new visual positioning system meets the practical requirement completely.

At present, the vision system and IoT techniques have been applied in a project of "Tea Garden Robot," and the picking experiments in tea farms were carried out, as shown in Figure 11. The experimental results are satisfactory and the target of automatic picking-task for tea robot is achieved. Of course, the tea picking machine still has some deficiencies, such as low efficiency and repeated picking action in vain. The problem of low efficiency should be resolved by reforming hardware to promote the execution speed of the grating projection and manipulator. Repeated picking action is mainly caused by the multiple-recognition problem which creates some false points for an actual bud. Hence, further studies on the identification algorithm ought to be propelled in the future. But we are certain that the applications of active visual technology and IoT in tea picking equipment are successful and their prospective application in the agricultural field is expected.

4. Conclusions

Intelligence and automation are promoting more efficient and economical agricultural production. In order to assist the modern and precision tea planting, a type of intelligent tea picking equipment for high-grade tea production is developed. The machine is equipped with two critical techniques, new tip positioning, and an IoT system.

For new tip positioning, a solution scheme based on active vision is proposed. In this scheme, an entire vision framework provided with a cross-light path of projection and camera is designed. Tip identification based on the color factor method is carried out to determine the horizontal position of tips. Especially, the application of fringe projection profilometry for the acquisition of height information is discussed in detail. During the process of height measurement, a cubic polynomial approximation approach is applied to correct the nonlinear error which is attributed to the principle model of fringe projection profilometry. A morphological filter is designed to reduce noise pollution in maps and to enhance the precision of phase unwrapping. Eventually, systematic error is controlled less than 2 mm in the entire measured region, which is acceptable

measurement accuracy. Experimental results also reveal that this tip positioning system based on the fringe projection profilometry is stable and performs accurately.

The machine provided with wireless communication equipment to transmit the real-time status of the tea picking process to an intermediary platform, and eventually to the Internet for big data analysis. The data such as color factor and quantity of new tips collected through IoT can be used for further quality and production evaluation. The development of the intelligent picking machine can further facilitate the tea planting and promote tea production.

Data Availability

The image data used to support the findings of this study are currently under embargo while the research findings are commercialized. Requests for data, 12 months after publication of this article, will be considered by the corresponding author.

Conflicts of Interest

The authors declare that they have no conflicts of interest.

References

[1] M. L. Heiss and R. J. Heiss, *The story of tea: A Cultural History and Drinking Guide*, Random House, New York, NY, USA, 2011.

[2] A. Macfarlane and I. Macfarlane, *The empire of tea*, The Overlook Press, New York, NY, USA, 2009.

[3] A. Villa-Henriksen, G. T. C. Edwards, L. A. Pesonen, O. Green, and C. A. GrønSørensen, "Internet of Things in arable farming: implementation, applications, challenges and potential," *Biosystems Engineering*, vol. 191, pp. 60–84, 2020.

[4] F. Li, K. Y. Lam, Z. Sheng, X. Zhang, K. Zhao, and L. Wang, "Q-learning-based dynamic spectrum access in cognitive industrial Internet of Thing," *Mobile Networks and Applications*, vol. 23, pp. 1636–1644, 2018.

[5] A. Nurzaman, D. Debashis, and H. M. Iftekhar, "Internet of Things (IoT) for smart precision agriculture and farming in rural areas," *IEEE Internet of Things Journal*, vol. 5, pp. 4890–4899, 2018.

[6] A. Kaloxylos, A. Groumas, V. Sarris et al., "A cloud-based farm management system: architecture and implementation," *Computers and Electronics in Agriculture*, vol. 100, pp. 168–179, 2014.

[7] S. Khanal, J. Fulton, and S. Shearer, "An overview of current and potential applications of thermal remote sensing in precision agriculture," *Computers and Electronics in Agriculture*, vol. 139, pp. 22–32, 2017.

[8] P. Jain, S. Sanat, P. Bhatt, and S. Pappula, "Development of an energy-efficient adaptive IoT gateway model for precision agriculture," in *Proceedings of the Global Internet of Things Summit (GIoTS)*, Bilbao, Spain, June 2018.

[9] D. D. Bochtis, C. G. C. Sørensen, and P. Busato, "Advances in agricultural machinery management: a review," *Biosystems Engineering*, vol. 126, pp. 69–81, 2014.

[10] X. Liu, X. B. Zhai, W. Lu, and C. Wu, "QoS-guarantee resource allocation for multibeam satellite industrial Internet of Things with NOMA," *IEEE Transactions on Industrial Informatics*, vol. 17, pp. 2052–2061, 2021.

[11] X. Liu and X. Zhang, "NOMA-based resource allocation for cluster-based cognitive industrial Internet of Things," *IEEE Transactions on Industrial Informatics*, vol. 16, pp. 5379–5388, 2020.

[12] D. Zheng and F. Da, "Self-correction phase unwrapping method based on Gray-code light," *Optics and Lasers in Engineering*, vol. 50, no. 8, pp. 1130–1139, 2012.

[13] L. Song and H. Yue, "Phase unwrapping method based on reliability and digital point array," *Optical Engineering*, vol. 50, no. 4, Article ID 043605, 2011.

[14] X. Jin, Y. Chen, and H. Zhang, "High-quality tea tips detection under natural conditions using computer vision," *Journal of Digital Content Technology and Its Applications*, vol. 6, no. 18, pp. 600–606, 2012.

[15] I. Philipp and T. Rath, "Improving plant discrimination in image processing by use of different color space transformations," *Computers and Electronics in Agriculture*, vol. 35, no. 1, pp. 1–15, 2002.

[16] X. P. Burgos-Artizzu, A. Ribeiro, M. Guijarro, and G. Pajares, "Real-time image processing for crop/weed discrimination in maize fields," *Computers and Electronics in Agriculture*, vol. 75, no. 2, pp. 337–346, 201.

[17] S. Gai and F. Da, "A novel phase-shifting method based on strip marker," *Optics and Lasers in Engineering*, vol. 48, no. 2, pp. 205–211, 2010.

[18] L. Huang and A. K. Asundi, "Phase invalidity identification framework with the temporal phase unwrapping method," *Measurement Science and Technology*, vol. 22, no. 3, pp. 1–5, 2011.

[19] J. M. Huntley and H. Saldner, "Temporal phase-unwrapping algorithm for automated interferogram analysis," *Applied Optics*, vol. 32, no. 17, pp. 3047–3052, 1993.

[20] X. Su, W. Song, and Y. Cao, "Phase-height mapping and coordinate calibration simultaneously in phase-measuring profilometry," *Optical Engineering*, vol. 43, no. 3, pp. 708–712, 2004.

WILEY | Hindawi

Research Article

Technoeconomic Assessment Based on Active Context-Knowledge Orchestration for Power Internet of Things

Yuanshuo Zheng [ID],[1] **Shujuan Sun,**[1] **Chenyang Li,**[1] **Jingtang Luo** [ID],[2] **Jiuling Dong,**[1] **Yudong Wang,**[3] **and Xiaolong Yang** [ID][1]

[1]*School of Computer and Communication Engineering, University of Science and Technology Beijing, Haidian District, Beijing 100083, China*
[2]*State Grid Sichuan Economic Research Institute, Wuhou District, Chengdu 610041, China*
[3]*State Grid Economic and Technological Research Institute Co., Ltd, Changping District, Beijing 102209, China*

Correspondence should be addressed to Jingtang Luo; 406996203@qq.com

Power Internet of Things (abbreviated as PIoT) is the information infrastructure to provide ubiquitous perception ability for smart grid (abbreviated as SG). To better deploy and utilize PIoT, its perception ability must be comprehensively assessed in terms of technical performance and economic benefits. However, at present, there is no assessment framework for PIoT due to the high diversity and heterogeneousness of SG scenarios. Additionally, there is information overlap between metrics in the assessment framework. The assessment model which could remove redundant information between metrics and simplify the assessment framework is an urgent demand to improve the effectiveness and timeliness of assessment. Consequently, first, aiming at the power system requirements of complex and diverse, a general assessment framework is put forward to assess the ability of PIoT in terms of technology and economy. Next, the requirement characteristics of power distribution scenario (abbreviated as PDS) are precisely analyzed with active context-knowledge orchestration technology. The general assessment framework is instantiated to build an instantiation assessment scheme in PDS. Moreover, an assessment model is established based on the instantiation assessment scheme to assess the efficiency of PIoT in Beijing. Finally, the assessment model is further refined with the machine learning technology to improve the efficiency of assessment. This refinement model achieves the extraction of 4-dimensional metrics from 23-dimensional metrics for assessment and finally improves assessment efficiency by 82.6%.

1. Introduction

As being a hub of the energy system, smart grid (abbreviated as SG) has the important mission that it not only unblocks the energy industry chain but also promotes the achievement of carbon peaks and carbon neutrality goals [1]. Consequently, it is necessary to continuously strengthen the integration of power grid (abbreviated as PG), information network, and energy network to form a new energy ecosystem with SG as the main body [2, 3]. Meanwhile, with the continuous upgrading and transformation of the power system, the Internet of Things (abbreviated as IoT) plays an increasingly important role in it [4]. The IoT is a network

form that uses information sensing equipment to connect objects and the Internet to communicate in accordance with an agreed protocol to achieve intelligent tracking and management of objects. As a research hotspot in academia and industry, it has attracted widespread attention. For instance, Xin and Zhang studied the resource allocation of the Cognitive Industrial Internet of Things (abbreviated as CIIoT) and proposed a cluster-based CIIoT to improve sensing and transmission performance of the CIIoT [5]. Additionally, in order to improve the transmission performance, Liu et al. also proposed a multibeam satellite Industrial Internet of Things (abbreviated as IIoT) with nonorthogonal multiple access (abbreviated as NOMA),

while guaranteeing the QoS for the satellite IIoT, including the required transmission rate and transmission delay [6]. The IoT combines communications, information, sensing, automation, and other technologies. It widely deploys various intelligent sensing devices with certain perception, computing power, and execution capabilities in all aspects of power production, transportation, consumption, and management. Importing IoT technology to power system can effectively integrate the communication infrastructure resources and power system infrastructure resources, which can improve the information level of power system and the utilization efficiency of the existing infrastructure and provide important technical support for power generation, transmission, transformation, and distribution [7]. The Power Internet of Things (abbreviated as PIoT) is a network system formed by connecting all objects related to power [8]. It is the specific manifestation of the IoT in the power industry as well as the infrastructure for SG to achieve information interaction [9]. In power systems, communication between a large number of devices required the need for greater capacity, greater connectivity, and higher data rates which can be achieved by merging 5G with IoT. This is because the 5G cellular network has promising features to provide much lower latency, increased integration within the mobile network, and longer range [10]. The PIoT uses widely deployed terminal to collect massive data, which can provide data support for the organic fusion of PG, information network, and energy network [11, 12]. PIoT is made up of various IoT sensors, smart terminals, cloud platforms, and other devices with collecting massive data connected through various communication networks [13]. Analyzing and processing of collected data, the overall operation law of the SG can be discovered with the data relationship, which can improve the visibility of the SG [14]. Accordingly, the visibility and controllability of the PIoT will affect the operation security of SG.

The efficiency assessment for PIoT is a significant way to measure the development of PIoT. However, there is a lack of relevant work about the efficiency assessment of PIoT. The study in related fields can provide research ideas, such as the SG assessment and the Energy Internet assessment [15–19].

In the field of SG assessment, Li designed an evaluation model integrating TOPSIS and grey management analysis method, which is successfully applied to evaluating the development of economic benefit in five service areas of power supply in Zhejiang province [20]. Hall and Foxon applied the cost-benefit method to quantitatively analyze the economic benefits of the SG in a certain area of the United Kingdom [21]. However, the above research studies only analyzed the economic benefit of the SG, neglected the multiattribute problem of the SG from the technical, environmental, and other aspects, and failed to build a multilevel evaluation model to comprehensively evaluate the SG. Unlike them, Zeng et al. built a modified comprehensive evaluation index system of demand response benefit covering economy and environment to provide effective guidance for scientific investment decision-making of the intelligent distribution network [22]. Li and Chen designed

an indicator system to evaluate the potential for regional electric energy substitution in China from the aspects of socioeconomic level, energy consumption structure, and environmental protection constraints [23]. Next, the TOPSIS method with improved connection degree was used to comprehensively evaluate the regional power substitution potential.

SG is the core of the Energy Internet, which is the grid with distributed, open and shared based on renewable energy. In the area of Energy Internet efficiency evaluation, Fang et al. presented an evaluation index system containing intermittent energy indicators based on the analysis of influential factors of operation and economic efficiency of the power system [24]. Nevertheless, this study only evaluated the PG from two aspects of operating efficiency and investment benefits, which made the research perspective slightly single. Lu et al. constructed a novel evaluation criteria system from the economic aspect, environmental aspect, technical aspect, energy aspect, and service aspect [25]. This system can make assessment comprehensive and objective for energy management system of regional integrated. However, literature [24] and literature [25] did not consider the demand differences of research subjects in different power system scenario (abbreviated as PSS) when evaluating research subjects. Liu et al. proposed a unified evaluation model to assess the adjustable capability of distributed energy systems under typical scenarios at a single moment, and the impact of economic constraints on the adjustable capability was also extensively analyzed [26].

The abovementioned works generally assess the object of study from economic and technical, which can provide a useful reference for the subsequent assessment of PIoT. Nevertheless, existing research studies on PIoT are rare, and there are still some problems which are needed to be solved. The main problems are listed as follows:

(1) There lacks a general assessment framework for PIoT. PIoT is the basis for SG to collect data. Analyzing massive data, the operation rules and potential risks of the SG can be found, which can achieve stable operation and optimal allocation of resources for the power system. Accordingly, we need to assess whether the efficiency of PIoT meets the requirement for SG development.

(2) There lacks an instantiation assessment scheme for PIoT in typical scenario. The types of PIoT nodes in different PSS are different, and the perception requirements are complex and diverse. Consequently, the requirement abilities of PIoT differ in different PSS. Hence, the assessment framework should be specific to certain scenarios.

(3) There lacks a dimensionality reduction model for instantiation assessment scheme. The phenomenon of information intersection will inevitably occur among the indexes of the instantiation assessment scheme. Accordingly, the main features of the instantiation assessment scheme are extracted by using the dimensionality reduction model, which can

reduce the dimensionality of the instantiation assessment scheme. It weakens the complexity of the assessment model and improves timeliness of the assessment.

To fill these gaps mentioned above, this paper closely integrates the current internal environmental factors such as the requirement and the development direction of the PG and external environmental factors such as technological development and national policies, which were faced by the current development of PIoT. Additionally, the technical route is adopted in this paper: first, building a general assessment framework; next, reshaping the instantiation assessment scheme in certain scenarios; then, establishing an assessment model; finally, achieving the comprehensive assessment and refinement analysis of PIoT.

The main contributions of this study are as follows:

(1) To comprehensively assess the efficiency of PIoT in terms of ubiquitous perception, security protection, etc., the general assessment framework of PIoT is built

(2) The core requirements of the power distribution scenario (abbreviated as PDS) are explored by using Active Context-Knowledge Orchestration Technology (abbreviated as ACKOT), and an instantiation assessment scheme with the requirement characteristics of the PDS is built

(3) The assessment model based on PCA and AHP is designed to assess the efficiency of PIoT

(4) A refinement model based on machine learning technology (abbreviated as MLT) is proposed to reduce redundant information between metrics to achieve dimensionality reduction of the instantiation assessment scheme

2. Building an Assessment Framework

With the in-depth development of SG, the number of functional subjects and data scale of SG are increasing rapidly. As the basis and link, PIoT will play a more prominent role in the aspects of ubiquitous perception, efficient processing of information, convenient and flexible application, and so on. Consequently, this paper refers to some standards such as the GB/T36468-2018 system evaluation index system of Internet of Things and GB/T37025-2018 information security technology-security technical requirements of data transmission for Internet of Things to build an assessment framework of PIoT [27–29].

2.1. Technical Index. Since there are many types of terminals in the links of transmission, transformation, and distribution and so on, such as data transfer unit, laser ranging sensor, and smart meter, the operation and maintenance efficiency of the equipment are reduced. It is particularly important to implement scientific maintenance management of the terminal. Moreover, the collection and analysis of the massive data are realized through widely distributed terminals, which can provide early warning of hidden dangers to avoid failure of PG equipment. In the meantime, different power services and power scenarios have diversified requirements for the QoS of PIoT, and some important control services have strict requirements for QoS, such as relay protection and dispatching control. Thus, we need to measure the ability of PIoT's QoS to meet application requirements. Additionally, since the data collected by the terminal contains user privacy and corporate information, and its forms are complex and diverse, the security protection of the data should be taken seriously. Consequently, the ability of PIoT is assessed to meet the requirements of the power system from ubiquitous perception, applications' QoS guarantee, security protection, and maintenance management.

The maintenance management ability is used to assess the stable operation level of the terminal. It can provide prerequisites for achieving the ubiquitous perception of PIoT. Additionally, the applications' QoS guarantee obtains massive data through the ubiquitous perception ability to meet the diverse needs of the power system. Meanwhile, security protection ability is used to assess the data security during transmission and sharing, which can provide a basic guarantee for data security.

2.1.1. Ubiquitous Perception Ability. The ability of a ubiquitous perception is using widely deployed sensing devices to obtain massive data. Hence, we intend to comprehensively assess the ubiquitous perception ability from terminal deployment coverage, rate of successful data collection, variety of terminal perception frequency, accuracy of data collection, and diversity of sensing data.

By analyzing and processing of the data, the visibility of the device status and management status in the SG can be improved. Collecting data relies on terminal equipment. Here, the terminal deployment coverage is used to measure the coverage fraction of terminal in PIoT. Meanwhile, aiming at the diversity and heterogeneity of perception data, diversity of sensing data is used to measure the diversity of massive data. Additionally, the variety of terminal perception frequency is used to measure the degree of intelligence of the terminal setting perception frequency according to the location, time, and situation. For the collection of massive data, the rate of successful data collection is used to measure the ability of PIoT successfully collecting perceptual data. Meanwhile, accuracy of data collection is used to measure the closeness between the collected data information and the real data information.

2.1.2. Applications' QoS Guarantee. PIoT is the basic information infrastructure of SG to meet the application requirement of every link from power generation to distribution. Thus, we intend to consider the applications' QoS guarantee of PIoT from the ability of data sharing, reliability for meeting application requirements, communication quality of service, and quality of data processing. It can respond to the diverse needs in the power system of massive data transmission, Internet of Everything, flexible response, and extensive perception.

Among them, the ability of data sharing can be used to assess the ability of PIoT to meet the requirements of massive data transmission in the power system. Reliability for meeting application requirements is used to measure the ability of terminal in PIoT to always meet the application requirements in SG. The flexible compatibility of PIoT is the basis for realizing Internet of Everything in the power system. Communication quality of service is used to measure the communication effect of PIoT. For example, there are many scenarios of cooperative control in the power system. In these scenarios, power travels at the speed of light, and the end-to-end delay is less than 10 ms which can provide support for the power system to respond flexibly to various changes. Quality of data processing is used to measure the degree which data processing technology meets application requirement. For example, in recent years, the Edge TPU chip developed by Google has the capability of massive data processing and edge computing, which will improve the extensive perception ability of the terminal.

2.1.3. Security Protection Ability.

For SG, its core is the application of massive data in power system. Hence, the security and privacy of data are particularly important. However, at present, the data interaction methods and sharing behaviors between the entities of the PG lack security guarantee, which weaken the ability of data security sharing and circulation in the entire PG. There are some security risks faced by PIoT, specifically the environmental security of data, security protection of data, and preventing the terminal from extreme disasters.

Firstly, the environmental security protection of data includes user environmental security protection and transmission environmental security protection. On the one hand, user electricity consumption data are related to user privacy. Thus, we need to ensure the privacy security of different participants when we share the data. Based on this situation, we use security and robustness to assess the security performance of the user environment. On the other hand, the extensive perception also brings challenges to communication security. Ensuring the integrity and confidentiality of data during transmission is a core issue. Accordingly, the ability of anti-interference for communication network is used to measure the security of the data transmission environment. Secondly, in view of the security protection of the data, we intend to use the ability of preventing data leakage to assess the performances for anti-attack and antitheft of the data. Finally, we also need to focus on the issue of how PIoT can effectively defend against extreme disasters. Since data collection relies on various terminals, it is essential to ensure the normal operation of device in extreme disaster situation. Consequently, the ability of resisting natural is used to measure the defense ability of PIoT in response to extreme disasters.

2.1.4. Maintenance Management Ability.

The maintenance management is manifested in the inspection, maintenance, and upgrade of equipment during the operation of the power system. It is the main link to ensure the safe and stable operation of the SG. Consequently, the assessment for management ability of operation and maintenance include the degree of equipment maintenance automation, the ability of precise equipment management, and the flexibility of equipment delivery and configuration.

The degree of equipment maintenance automation is used to measure the automation degree of equipment maintenance in the power system. Relying on the construction of PIoT, the equipment maintenance in the power system is more automated. For example, we use 5G technology to integrate real time and offline information on grid feeders and users to realize the monitoring, protection, and control of the equipment in power system. The ability of precise equipment management is used to measure the ability of PIoT manage equipment. The flexibility of equipment delivery and configuration can measure the ability of PIoT to provide different service functions according to application scenarios.

2.2. Economic Index.

If promoting the construction of PIoT cannot create considerable economic benefits, the technical breakthrough will be meaningless. This paper assesses the economic benefits for the PIoT in integration with other economic indexes such as cost and direct benefits.

All in all, the multidimensional assessment framework of PIoT is shown in Table 1.

3. Designing Assessment Scheme and Case Study

3.1. Using ACKOT to Design PIoT Assessment Scheme under PDS

3.1.1. ACKOT and Application.

The assessment framework for PIoT in Section 1 is a universal assessment template. This template can meet the requirement for the ability assessment of PIoT in power generation, transformation, transmission, and distribution. However, the core abilities of PIoT have different focuses in different PSS. Since different PSS have requirements of common and difference for the core abilities of PIoT, the assessment framework should be personalized according to specific scenarios. Hence, we use ACKOT to reshape the assessment framework under different PSS. The ACKOT aims to dig deeper into the requirement characteristics of different PSS. The general assessment template can be instantiated according to the requirements of PSS. In this way, the index that can measure ability of PIoT to meet the requirements of different PSS can be found.

Assessment template containing commonality and individuality are built for different PSS. Next, the assessment template is applied to the diversified PSS, and an assessment scheme is designed that is compatible with PIoT abilities—PSS requirements. The scheme design process is shown in Figure 1.

Compared with other PSS, the distribution network is closely related to every user and device in every household. Additionally, in the SG, the interdependence between the distribution network and the communication network

TABLE 1: The multi-dimensional assessment framework of PIoT.

First-level index	Second-level index	Third-level index
Technical	Ubiquitous perception ability	Terminal deployment coverage
		Rate of successful data collection
		Accuracy of data collection
		Variety of terminal perception frequency
		Diversity of sensing data
	Applications' QoS guarantee	Ability of data sharing
		Reliability for meeting application requirements
		Communication quality of service
		Quality of data processing
	Security protection ability	Security and robustness
		Ability of preventing data leakage
		Ability of anti-interference for communication network
		Ability of resisting natural disasters
	Maintenance management ability	Degree of equipment maintenance automation
		Degree of precise equipment management
		Flexibility of equipment delivery and configuration
Economic	Cost	Cost of construction
		Cost of maintenance
	Direct benefits	Saved investment of PG construction
		Decreased cost of human resource
		Saved cost of equipment operation
	Indirect benefits	User satisfaction
		Improved quality of power supply
		The level of line loss management in the same period
	Comprehensive index	Payback period
		Net present value
		Annual cost

makes them inseparable. The distribution network provides energy source for the communication network, and the communication network provides information support for the distribution network, which means they are mutualistic symbiosis. Consequently, the SG in the 5G era will coruscate more vitality and better promote the interconnection of distribution network and communication network. Thereafter, the construction of a new type of power system is accompanied by the access of a large number of new energy sources with distributed and fragmented, which will pose a greater challenge to the distribution network. Hence, we need to build an assessment scheme of PIoT in the PDS to provide a solid guarantee foundation for the reasonable planning of the distribution network. ACKOT is used to reshape the assessment framework of PIoT in PDS.

3.1.2. Designing the Assessment Scheme of PIoT under the PDS. The starting point of the distribution network is connected to transmission lines, and the end point is connected to various power consumers. Hence, if the security and robustness of PIoT in the distribution network is not improved, it will affect the power demand of end users. For example, because of the malfunctions of the aggregation node and the distribution box, the power supply ability of the PG is affected, which will not be able to meet the power demand of the end users. The power consumption information of users is related to the power purchase privacy of end users, and the accuracy of power consumption information also affects the power dispatching planning of

distribution network. Thus, the ability of preventing data leakage is used to measure the system's ability to protect the confidentiality and integrity of data information. Moreover, extreme disasters will damage the terminal, which will affect the data collection abilities of the PIoT, and make the PIoT unable to meet the data requirements of the distribution network. Hence, it is necessary to assess the ability of resisting natural disasters of the terminal and strengthen the deployment of disaster prevention facilities in the distribution network.

In the above analysis, first, ACKOT is used to explore the characteristics of the requirement for security protection ability of PIoT in PDS. Next, indexes such as security and robustness, ability of preventing data leakage, and ability of resisting natural disasters are found in the assessment framework. The following will continue to use this technology to explore the remaining requirement characteristics of PIoT and reshape the assessment framework in PDS.

Smart meters are the most typical sensors in power distribution systems. It can collect the user's power consumption data in real time to meet the basic needs of PG companies for power dispatch. The higher the accuracy of collection data, the higher the reference value for PG. Here, we use the accuracy of data collection to measure the similarity between collection data and real data. To prevent accidents, the distribution station must monitor the operation of various equipment as well as collecting user electricity consumption data. Thus, a huge amount of data needs to be collected. The collection of massive data relies on the extensive deployment of terminals. The terminal
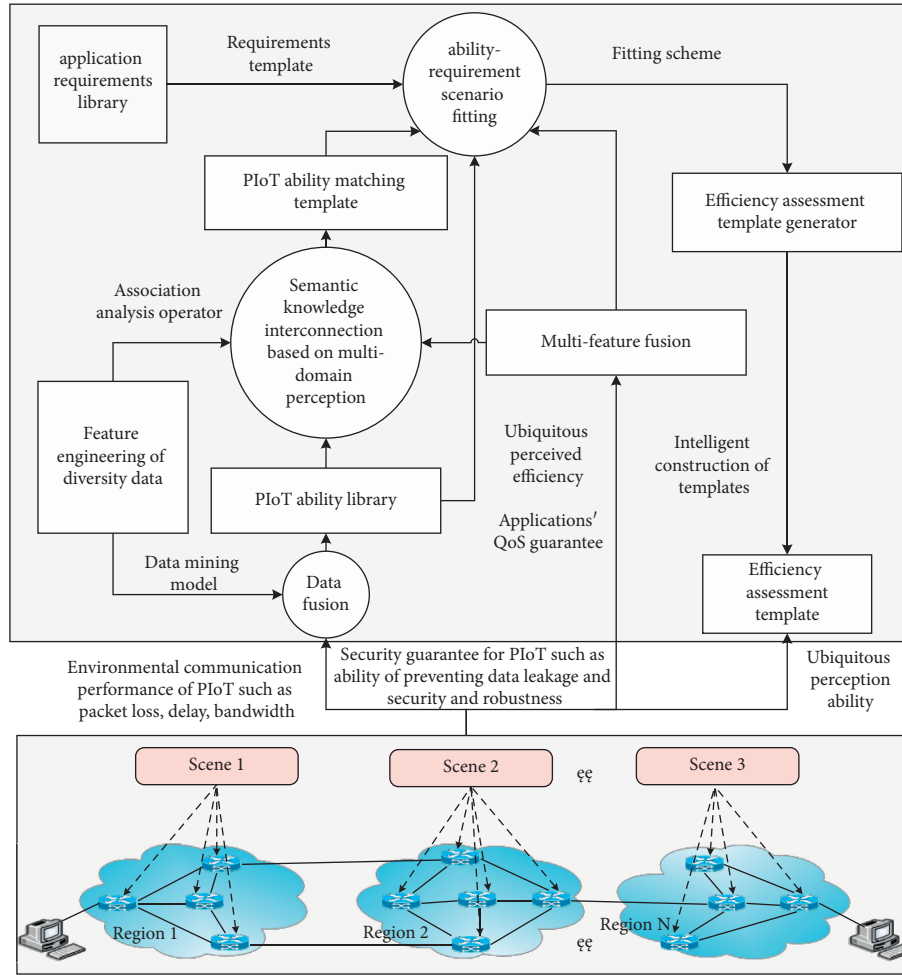
Figure 1: The instantiate generation scheme of the assessment framework by using ACKOT. The general assessment framework is instantiated by using this generation scheme according to the requirement of different PDS.

deployment coverage is used to measure the coverage level of the terminal. Different types of data are collected by the terminal. For this reason, the diversity of sensing data and the variety of terminal perception frequency are indispensable indexes to measure the ubiquitous perception ability of the distribution network.

To facilitate data sharing between users and the PG, the distribution network should establish a data sharing mechanism. Consequently, the ability of data sharing can be used to assess the performance of the data sharing mechanism in the distribution network. Reliability for meeting application requirements is used to measure the ability of the terminal to always meet the application requirements of the distribution network, for example, whether the signal and power of the wireless terminal can meet the requirement for the collection and transmission of electricity information. The deep coupling between the distribution network and the communication network makes the communication system of the PIoT very flexible in the PDS. Here, the communication quality of service is used to measure the communication ability of the terminal. Meanwhile, using smart chips will improve the terminal's ability to process massive data. Quality of data

processing is used to measure the ability of terminal processing data.

The amount of data in the system needs to be transmitted, stored, and processed rapidly if the number of perceived terminals and users of the distribution network increases in varying degrees. Consequently, the PIoT should have a certain functional extensibility. Based on this, we should improve the flexibility of equipment delivery and configuration to cope with possible changes in work volume in the future. Relying on the construction of PIoT, the management of the distribution station is refined, which can improve the ability of precise equipment management. Furthermore, we can improve the automation level of distribution terminal with improving the degree of equipment maintenance automation. The work efficiency of power distribution equipment will increase with the enhancement of the automation level of distribution terminal.

The improvement of the work efficiency of power distribution equipment can reduce the cost of construction and labor input, which decreased the cost of human resource. The function of the distribution station is to supply power to users within the radiation range and share data with users. Users can interact with the power distribution system in real time through smart terminals in the station area. Thus, users can

obtain more comprehensive data information according to their own needs to improve user satisfaction. Furthermore, with the rapid development of power industry and energy industry, distributed power supply has become an indispensable and useful supplement to the power supply of PG. The addition of distributed power sources to the distribution network will greatly increase the complexity and uncertainty of the investment in the construction of the distribution system. Thus, reasonable capital planning and allocation is very necessary. The payback period, annual costs, and net present value can be used to assess the scientific planning and precise investment of the distribution network.

In summary, the assessment scheme of PIoT in the PDS is designed, as shown in Figure 2.

3.2. Comprehensive Assessment Model for PIoT Based on the Collaboration of PCA and AHP.

The assessment scheme built in Section 2.1 has many dimensions. Hence, firstly, we need to simplify the dimension of index before assessing the efficiency of PIoT. Principal component analysis (PCA), as a method to simplify data sets, is often used to reduce the dimension of datasets [30]. Secondly, we need to assign index weights according to the importance of each index. Analytic hierarchy process (AHP) is to compare the importance of indexes in pairs, which is more helpful to the reasonable distribution of index weights [31].

In summary, an assessment model of PIoT based on the collaboration of PCA and AHP is designed. The specific process of the assessment model design is shown in Figure 3. The assessment process of PIoT is summarized as follows:

Step 1: referring to national standards, the PIoT assessment framework is designed according to the principles of index system construction

Step 2: we need to determine the normalization standard and normalize the original measured value

Step 3: using PCA to compute the secondary index value

① Normalizing the three-level index.
② Computing the eigenvalues and eigenvectors of the index covariance matrix.
③ Constructing the assessment function: we determine the number of the principal component by setting the variance contribution rate threshold and sorting the cumulative contribution rate or eigenvalues of the principal component. The expression of the comprehensive assessment function is formulated as follows:

$$f = \alpha_1 F_1 + \alpha_2 F_2 + \alpha_3 F_3 + \cdots + \alpha_m F_m. \quad (1)$$

Here, $F_1, F_2, \ldots, F_m$ are the new principal component, and $\alpha_1, \alpha_2, \ldots, \alpha_m$ are the weight of the new principal component.
④ We can obtain the value of the second-level index if the normalized value of each third-level index is brought into the assessment function obtained in Step 3, that is, $f_1, f_2, \ldots, f_k$.

Step 4: Computing the assessment value of the PIoT.

The mathematical expression of the assessment model of the PIoT is given as follows:

$$\begin{cases} V_1 = \sum_{n=1}^{4} W_{1n} V_{1n}, \\ V_2 = \sum_{m=1}^{4} W_{2m} V_{2m}, \end{cases} \quad (2)$$

$$C = W_1 V_1 + W_2 V_2. \quad (3)$$

Here, V_1 and V_2 represent the value of technical index and economic index, respectively, $W_{11}, W_{12}, \ldots, W_{1n}$ and $W_{21}, W_{22}, \ldots, W_{2m}$ represent the weight of each secondary index which belongs to the technical index and economic index, respectively, $V_{11}, V_{12}, \ldots, V_{1n}$ and $V_{21}, V_{22}, \ldots, V_{2m}$ represent the value of each secondary index which belongs to the technical index and economic index respectively, C represents the assessment value of PIoT, W_1 and W_2 represent the index weight of technical and economic, respectively.

Step 5: Determine the efficiency level of the PIoT.

When computing the assessment value of the PIoT, the range of assessment value and weight is [0-1]. We can determine the efficiency level of the PIoT by Table 2 after computing the assessment value.

3.3. Case Study.

Beijing being one of the major cities to promote electric vehicles (EVs), the impact of massive EV access to the distribution network cannot be ignored. To implement the national policy on the development of EV, the Special Plan for Beijing Electric Vehicle Charging Infrastructure (2016–2020) has been put forward in Beijing. According to the plan, about six hundred thousand EVs will be needed in the city by 2021, and about four hundred and thirty-five thousand EV charging piles will be built. The popularization of EV will bring unprecedented impact and challenges to the distribution network. Thus, the assessment of PIoT under the PDS in Beijing is particularly important.

Step 1. Computing the normalized value of the third-level index.

We use charging piles to collect the original values of the three-level index and convert them to [0-1]. The normalized value of the index is shown in Table 3.

Step 2. Using PCA to compute the secondary index value.

First, we seek the opinions of many experts in the electric power and communication fields anonymously. Next, the expert opinions are counted, processed, analyzed, and summarized. Finally, conduct multiple rounds of consultation, feedback, and adjustment of expert opinions. The scoring results of the experts on the three-level index are shown in Table 4.

The PIoT assessment scheme in PDS is composed of 23 three-level indexes. Firstly, we treat these 23 indexes as 23 random variables, denoted as $x_1, x_2, \ldots, x_{23}$. Secondly, we
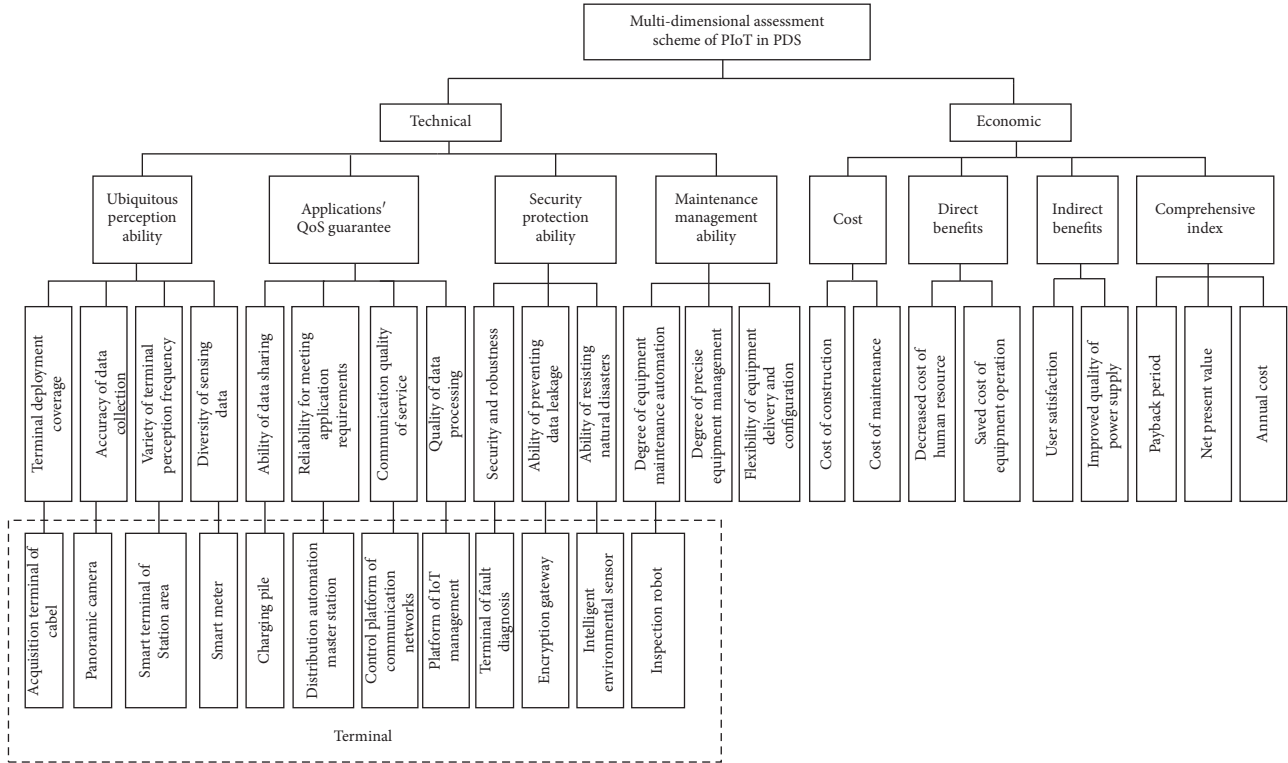
FIGURE 2: The assessment scheme of PIoT in PDS. This assessment scheme can be used as a template for assessing PIoT requirement ability in PDS.
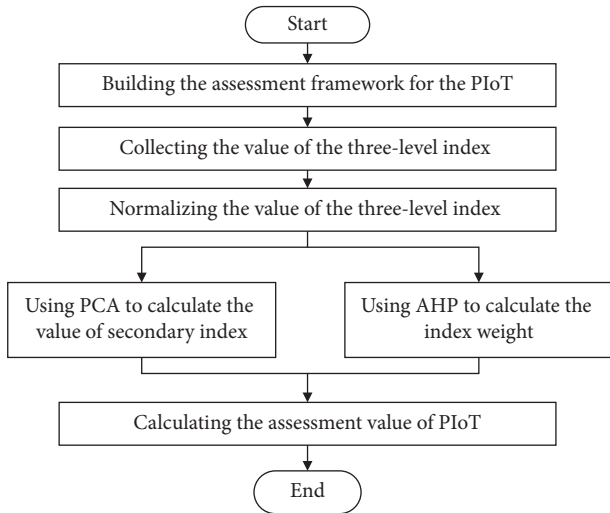
FIGURE 3: The design process of the assessment model based on the collaboration of PCA and AHP. This assessment model is used to assess the efficiency of PIoT.

TABLE 2: The judgment level for the efficiency of PIoT.

Efficiency level	Danger	Poor	Medium	Good	Excellent
Assessment value	0-0.2	0.2-0.4	0.4-0.6	0.6-0.8	0.8-1

use PCA to transform these 23-dimensional indexes into linear combinations grouped by the secondary index. Thirdly, computing the eigenvalues and eigenvectors of the

corresponding index covariance matrix according to the secondary index grouping, which can obtain the new principal component and its weight. The new principal component and its weight are shown in Table 5. Finally, we get the value of the three-level index to compute the value of the second-level index by formula (1). The value of the secondary index is shown in Table 6.

Step 3. Computing the index weight based on AHP.

Using AHP to assign weight to index. The weight distribution results are shown in Table 7.

Step 4. Computing the assessment value of the PIoT.

First, combining the value and the weight of the secondary index in Tables 6 and 7, respectively, the value of the technical index and economic index are calculated by using formula (2). Next, combining the weight and the value of the technical index and economic index, the assessment value of the PIoT is calculated by using formula (3).

Step 5. Determining the efficiency level of the PIoT.

According to the computation in Step 4, the assessment value of PIoT is 0.8687, which belongs to (0.8, 1). The assessment level of the PIoT is excellent with reference to Table 2, which further verifies the feasibility and effectiveness of the assessment model.

Step 6. Analyzing the results of PIoT efficiency assessment.

Analyzing the assessment value of PIoT, we found that the values of indirect benefits and comprehensive index are

Table 3: The normalizing value of the three-level index.

Secondary index	Three-level index	The value of three-level index
	Terminal deployment coverage	0.89
	Accuracy of data collection	0.86
Ubiquitous perception ability	Variety of terminal perception frequency	0.91
	Diversity of sensing data	0.92
	Ability of data sharing	0.87
	Reliability for meeting application requirements	0.88
Applications' QoS guarantee	Communication quality of service	0.94
	Quality of data processing	0.90
	Security and robustness	0.90
Security protection ability	Ability of preventing data leakage	0.92
	Ability of resisting natural disasters	0.96
	Degree of equipment maintenance automation	0.91
Maintenance management ability	Degree of precise equipment management	0.86
	Flexibility of equipment delivery and configuration	0.85
Cost	Cost of construction	0.84
	Cost of maintenance	0.83
Direct benefits	Decreased cost of human resource	0.82
	Saved cost of equipment operation	0.88
Indirect benefits	User satisfaction	0.85
	Improved quality of power supply	0.86
	Payback period	0.85
Comprehensive index	Net present value	0.87
	Annual cost	0.91

Table 4: The scoring results of the experts on the three-level index.

Three-level index	Score 1	Score 2	Score 3	Score 4	Score 5	Score 6	Score 7	Score 8	Score 9	Score 10
Terminal deployment coverage, X_1	8.8	9.0	8.6	9.1	8.7	8.8	8.6	8.7	8.9	9.0
Accuracy of data collection, X_2	9.0	8.7	8.7	8.6	8.5	9.1	8.6	8.7	8.2	8.4
Variety of terminal perception frequency, X_3	8.7	8.9	9.0	8.7	8.7	8.7	8.9	9.1	8.6	8.8
Diversity of sensing data, X_4	8.9	8.7	8.9	8.3	8.5	9.0	8.4	8.5	9.1	8.7
Ability of data sharing, X_5	8.4	8.6	8.7	8.5	9.0	8.7	8.6	8.8	8.5	9.0
Reliability for meeting application requirements, X_6	8.6	9.0	8.8	8.7	9.1	8.7	8.9	8.6	9.1	8.9
Communication quality of service, X_7	9.1	9.3	8.7	8.9	7.7	8.7	8.4	8.6	9.0	8.5
Quality of data processing, X_8	8.9	8.8	9.0	8.6	8.4	8.7	8.6	8.4	9.1	8.9
Security and robustness, X_9	9.2	8.9	8.7	9.0	8.8	8.8	9.2	8.9	9.0	8.7
Ability of preventing data leakage, X_{10}	8.9	8.7	9.1	8.6	8.7	9.0	8.7	8.8	8.6	8.4
Ability of resisting natural disasters, X_{11}	9.0	8.8	8.7	8.9	9.2	9.1	8.8	9.0	9.2	8.7
Degree of equipment maintenance automation, X_{12}	8.4	9.0	8.6	8.4	8.3	8.3	8.4	8.7	8.4	8.4
Degree of precise equipment management, X_{13}	8.7	8.6	8.3	8.9	8.9	8.7	8.6	8.4	8.5	8.7
Flexibility of equipment delivery and configuration, X_{14}	8.5	8.7	8.4	8.6	8.5	8.32	8.7	8.4	8.5	8.7
Cost of construction, X_{15}	8.8	9.3	8.9	8.6	9.0	8.7	9.0	8.5	8.3	9.0
Cost of maintenance, X_{16}	9.0	9.5	9.0	8.9	8.8	8.9	8.6	8.8	8.6	8.8
Decreased cost of human resource, X_{17}	9.2	9.3	8.9	9.1	9.2	8.9	9.0	8.7	8.9	9.0
Saved cost of equipment operation, X_{18}	8.8	8.8	9.0	9.1	9.0	8.6	8.8	9.0	8.7	8.6
User satisfaction, X_{19}	9.1	9.1	9.0	9.0	8.7	8.8	8.9	8.7	9.2	9.0
Improved quality of power supply, X_{20}	9.0	9.2	9.2	9.4	8.8	9.0	8.8	9.1	9.0	9.3
Payback period, X_{21}	9.2	9.0	8.8	9.1	9.1	8.9	8.9	8.7	8.9	9.0
Net present value, X_{22}	8.6	8.4	8.3	8.4	8.5	8.1	8.3	8.2	8.3	8.5
Annual cost, X_{23}	8.5	8.6	8.4	8.5	8.7	8.2	8.4	8.4	8.5	8.6

low as seen in Table 6. Due to the generalization of the secondary index, it is impossible to give specific reference suggestions for the improvement and optimization of the PIoT. Consequently, we refine the result analysis to the third-level index, such as user satisfaction and payback period.

As one of the major cities that vigorously promote EV, the penetration rate of EV is increasing year by year in an

TABLE 5: The weight of new principal components.

Secondary index	New principal components	Weight
Ubiquitous perception ability	F_1	0.80683
Applications' QoS guarantee	F_2	0.60520
	F_3	0.32156
Security protection ability	F_4	0.84632
Maintenance management ability	F_5	0.572306
	F_6	0.30843
Cost	F_7	0.79049
Direct benefits	F_8	0.81023
Indirect benefits	F_9	0.82495
Comprehensive index	F_{10}	0.80791

TABLE 6: The value of secondary index by using PCA.

Secondary index	Value
Ubiquitous perception ability	0.9154
Applications' QoS guarantee	0.9512
Security protection ability	0.9397
Maintenance management ability	0.8991
Cost	0.8508
Direct benefits	0.7816
Indirect benefits	0.7007
Comprehensive index	0.6402

TABLE 7: The distribution result of index weight.

First-level index	First-level index weight	Secondary index	Secondary index weight
Technical	0.67	Ubiquitous perception ability	0.27
		Applications' QoS guarantee	0.28
		Security protection ability	0.19
		Maintenance management ability	0.26
		Cost	0.25
Economic	0.33	Direct benefits	0.3
		Indirect benefits	0.29
		Comprehensive index	0.16

exponential manner. The access of large-scale EV has brought profound changes to the scale and structure of the distribution network. Among them, the problem of a sharp increase in power load is more prominent. The insufficiency of power supply during the peak load period will force users to change their inherent power consumption habits, which greatly affects user satisfaction. Meanwhile, because of the disorderly charging of massive EV, it will cause the problem of instability for the voltage and frequency in the distribution network. It will not only affect the improved quality of power supply of the distribution network but also further increase the operating cost of the distribution network. The increase in the operating cost of the distribution network will indirectly affect its payback period and annual cost.

To address the above problems, we can combine demand response strategies to rationally regulate the charging and discharging behavior of EV. As a mobile energy storage device, EV can be charged to absorb the excess wind and light energy during the low load period. Meanwhile, EV can alleviate the power supply pressure of the distribution network by feeding power to the grid during peak load

periods. It can effectively avoid problems such as voltage drops caused by insufficient power supply and further improve the power supply quality of the distribution network. Additionally, users can also reasonably arrange their own charging and discharging behaviors through demand response strategies to obtain corresponding benefits, which greatly improves user satisfaction.

4. Optimization Analysis of the Assessment Model Based on MLT

The dimensionality of the instantiation assessment scheme of PIoT in Section 2 is high, which causes the overlapping of information among various indexes. Consequently, we assess the efficiency of PIoT with increasing the workload of data collection and processing, which is not conducive to quickly and effectively assessing the efficiency of PIoT.

With the in-depth development of SG, data mining techniques represented by machine learning will be widely used in the field of PG. Among them, dimension reduction

technology is used to extract the main features of data to reduce the data dimension.

To address the above problems, this section will use MLT to optimize the assessment model. We will use this technology to mine the core information in the assessment scheme and remove the redundant information in the massive index, which reduces the dimensionality of the assessment scheme from high dimension to low dimension. It can reduce the workload of index information collection and processing with reducing the dimensionality of the assessment scheme, which will improve the timeliness of assessment.

We tried several machine learning methods such as decision tree (DT), extra tree and AdaBoost to achieve dimensionality reduction, among which the effect of DT is better. Compared with other machine learning methods, DT has the following advantages: (1) it can deal with numerical data and classified data. (2) It uses the white box model. (3) The reliability of the model can be verified by numerical statistical tests. In summary, the DT model is selected for classification training of sample data under the environment of Python 3.8.1. Next, using classification accuracy to extract certain features that play a key role in classification decision-making. The optimization process of the assessment model based on MLT is shown in Figure 4.

Here, the efficiency of PIoT under the PDS in Beijing is assessed by the optimization process of the assessment model.

Step 1: building a sample data set.

A sample data set of the distribution station in Beijing is randomly selected, as shown in Table 8. The data set of the experiment in this section consists 100 such data set.

Step 2: optimizing the application of the assessment model.

Using the DT to classify and train the data set, we can get the index importance of value and ranking, as shown in Figure 5. To make Figure 5 have a better display effect, we use the item number in Table 8 as a symbol for the index.

As shown in Figure 5, the importance values of the first four indexes are relatively large, and the other indexes are 0. Hence, we select the important values of these four indexes as the index weight after dimensionality reduction, as shown in Table 9.

The dimensionality of the assessment model is reduced by using DT, in which complexity of the algorithm is $O(nk \log_2 n)$ [32]. Here, n and k are the number of samples in the training set and the dimensionality of the data, respectively. In this simulation experiment, $n = 100, k = 23$. Consequently, the complexity of the proposed algorithm is $O(2.3 * 10^3 \log_2 100)$, with the execution time of 1.61 s.

Step 3: Validating the optimization assessment model.

Using the DT model to classify and train the dimensionality-reduced index, the classification accuracy rate
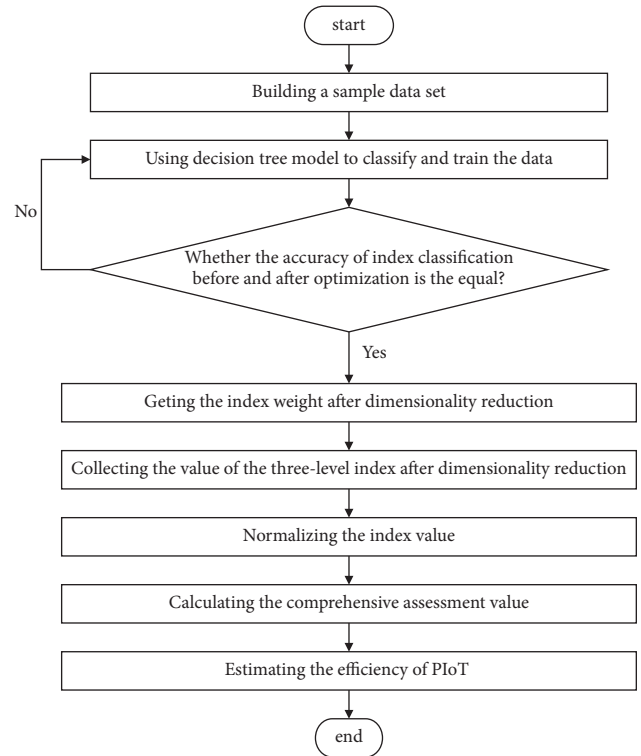
FIGURE 4: The optimization process of the assessment model based on MLT. This model is used to reduce the dimensionality of the PIoT assessment scheme, which can improve the timeliness of the assessment.

is 83%, which is the same as the 23-dimensional three-level indexes in Section 3. That is, the dimensionality-reduced indexes as a new data set can be used to assess the efficiency of PIoT, which can verify the effectiveness of the optimization assessment model.

The performance comparison experiment of the algorithm is designed. The comparison of the proposed algorithm with the existing algorithm [33, 34] is shown in Table 10. The results show that three algorithms can achieve the dimensionality reduction of the assessment scheme. Among them, the DT can reduce the assessment scheme with 3-4 dimension with the classification accuracy rate being 83%. The comprehensive performance of the DT is the best by analyzing the results.

Step 4: Evaluating the efficiency of PIoT.

Combining the normalized values of the index in Table 3 and the weight of the four indexes in Table 9 and computing the assessment value of the PIoT by using formula (3) is 0.88474. Comparing this value to Table 2, we can get the efficiency level of PIoT as excellent. The assessment result is the same as the assessment case in Section 3, which verifies the correctness of the optimization model. Furthermore, when evaluating PIoT, using four indexes as a new data set to replace the original 23 index, it improves the assessment efficiency by 82.6%. It can verify the timeliness of the optimization model in this article.

TABLE 8: A sample data of the distribution station in Beijing.

Second-level index	Three-level index		The value of three-level index
	Item no.	Item definition and meanings	
Ubiquitous perception ability	1	Terminal deployment coverage	0.921321
	2	Accuracy of data collection	0.976143
	3	Variety of terminal perception frequency	0.952878
	4	Diversity of sensing data	0.886099
	5	Ability of data sharing	0.874552
Applications' QoS guarantee	6	Reliability for meeting application requirements	0.911812
	7	Communication quality of service	0.871818
	8	Quality of data processing	0.942396
	9	Security and robustness	0.971341
Security protection ability	10	Ability of preventing data leakage	0.925245
	11	Ability of resisting natural disasters	0.967985
	12	Degree of equipment maintenance automation	0.953568
Maintenance management ability	13	Degree of precise equipment management	0.978742
	14	Flexibility of equipment delivery and configuration	0.979623
Cost	15	Cost of construction	0.954032
	16	Cost of maintenance	0.887993
Direct benefits	17	Decreased cost of human resource	0.956793
	18	Saved cost of equipment operation	0.866593
Indirect benefits	19	User satisfaction	0.921458
	20	Improved quality of power supply	0.923697
	21	Payback period	0.875962
Comprehensive index	22	Net present value	0.917689
	23	Annual cost	0.915398
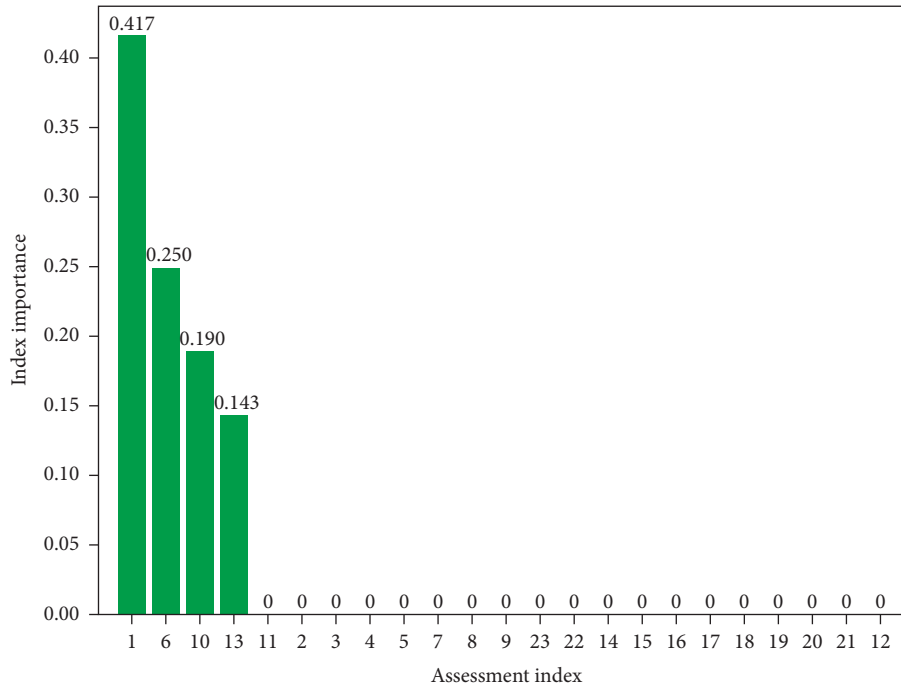
FIGURE 5: The index importance ranking.

TABLE 9: The weight of the index after dimensionality reduction.

Index after dimensionality reduction	Terminal deployment coverage	Reliability for meeting application requirements	Ability of preventing data leakage	Degree of precise equipment management
Weight	0.417	0.250	0.190	0.143

TABLE 10: The comparison of the algorithm performance.

Algorithm	The dimension of indexes after dimensionality reduction	Classification accuracy rate	The execution time (s)
Decision tree	4	0.83	1.61
Extra tree	14	0.64	1.22
AdaBoost	4	0.42	1.19

To avoid random situations in the simulation process, the model is used to conduct an assessment experiment on 1,000 communities with shared charging piles in Haidian district, Beijing. The results of multiple simulation experiments are summed and analyzed. Firstly, we use charging piles to collect the data. Secondly, the collaborative assessment model of PCA and AHP is used to assess the community. Thirdly, the optimization assessment model with using MLT is used to assess the community. Finally, we compare the level of these 1000 cells before and after optimization. Among them, 985 communities have the same grade, and the other 15 communities have different degrees before and after optimization. The difference is shown in the following situation: the ranks of the 9 cells before optimization are excellent as well as after optimization are good. The grade of the 6 cells before optimization is medium as well as that after optimization is good. In summary, the accuracy rate of the optimization assessment model is 98.5%, which verifies the accuracy of the model.

5. Conclusions

As the nerve ending of the SG, the PIoT will directly affect the holographic perception capability of the SG. Consequently, firstly, the assessment framework is designed to provide an assessment template for the efficiency assessment of PIoT. Secondly, the needs of different PSS have their own focus. Since the distribution network is the backbone of the power system, an assessment scheme covering the demand characteristics of PDS has been constructed. Finally, we build a collaborative assessment model of PCA and AHP to assess the efficiency of PIoT. On this basis, MLT is used to reduce the dimensionality of the assessment scheme, which improves the timeliness of assessment.

Data Availability

The data used to support the findings of this study are included within the article. More underlying data involve the privacy of enterprises and users and therefore cannot be published.

Conflicts of Interest

The authors declare that they have no conflicts of interest regarding the publication of this paper.

Acknowledgments

References

[1] J. B. Guo, "Scientific and technological innovation supports the construction of new power systems," 2021, http://www.chinasmartgrid.com.cn/news/20210519/638624.shtml.

[2] J. C. Liu, Y. H. Li, Y. Y. Lu, F. Xiaoxu, and Y. Suli, "Research on the influence factors of ubiquitous power internet of things for promoting consumption of wind power based on fuzzy G1-ISM in China," *Electrical Power and Energy Systems*, vol. 121, pp. 106–124, 2020.

[3] C. S. Guo, F. J. Luo, Z. X. Cai, Y. Zhao, and D. R. Zhangc, "Integrated planning of internet data centers and battery energy storage systems in smart grids," *Applied Energy*, vol. 281, pp. 1–9, 2021.

[4] A. Zanella, N. Bui, A. Castellani, V. Lorenzo, and Z. Michele, "Internet of Things for smart cities," *IEEE Internet of Things Journal*, vol. 1, no. 1, pp. 22–32, 2014.

[5] X. Liu and X. Y. Zhang, "NOMA-based resource allocation for cluster-based cognitive industrial Internet of Things," *IEEE Transactions on Industrial Informatics*, vol. 16, no. 8, pp. 5379–5388, 2020.

[6] X. Liu, M. Umair, X. B. Zhai, W. D. Lu, and C. M. Wu, "QoS-guarantee resource allocation for multibeam satellite industrial internet of things with NOMA," *IEEE Transactions on Industrial Informatics*, vol. 17, no. 3, pp. 2052–2061, 2021.

[7] J. S. Tao, M. Umair, M. Ali, and J. Zhou, "The impact of Internet of Things supported by emerging 5G in power systems: a review," *CSEE Journal of Power and Energy Systems*, vol. 6, no. 2, pp. 344–352, 2020.

[8] G. Bedi, G. K. Venayagamoorthy, R. Singh, R. R. Brooks, and K.-C. Wang, "Review of Internet of Things (IoT) in electric power and energy systems," *IEEE Internet of Things Journal*, vol. 5, no. 2, pp. 847–870, 2018.

[9] X. Y. Kong, F. Y. Sun, X. X. Huo, X. Li, and Y. Shen, "Hierarchical optimal scheduling method of heat-electricity integrated energy system based on Power Internet of Things," *Energy*, vol. 210, pp. 1–14, 2020.

[10] X. Liu and X. Y. Zhang, "Rate and energy efficiency improvements for 5G-based IoT with simultaneous transfer," *IEEE Internet of Things Journal*, vol. 6, no. 4, pp. 5971–5980, 2019.

[11] K. H. Wu, J. Y. Wang, W. Li, and Y. Zhu, "Research on the operation mode of new generation electric power system for the future energy internet," *Proceedings of the Chinese Society for Electrical Engineering*, vol. 39, no. 4, pp. 966–979, 2019.

[12] H. A. Khattak, M. A. Shah, S. Khan, I. Ali, and M. Imran, "Perception layer security in internet of things," *Future Generation Computer Systems*, vol. 100, pp. 144–164, 2019.

[13] T. Fei, Z. Ying, D. X. Li, and Z. Lin, "IoT-based intelligent perception and access of manufacturing resource toward cloud manufacturing," *IEEE Transactions on Industrial Informatics*, vol. 10, no. 2, pp. 1547–1557, 2014.

[14] M. H. Ullah and J. D. Park, "Distributed energy trading in smart grid over directed communication network," *IEEE Transactions on Smart Grid*, vol. 12, no. 4, pp. 3669–3672, 2021.

[15] G. Y. Qin, M. J. Zhang, Q. Y. Yan, C. Xu, and C. M. Kammen, "Comprehensive evaluation of regional energy internet using

a fuzzy analytic hierarchy process based on cloud model: a case in China," *Energy*, vol. 228, pp. 1–13, 2021.

[16] M. Masera, E. F. Bompard, and F. Profumo, "Smart (electricity) grids for smart cities: assessing roles and societal impacts," *Proceedings of the IEEE*, vol. 106, no. 4, pp. 613–625, 2018.

[17] C. S. Lai and G. Locatelli, "Valuing the option to prototype: a case study with generation integrated energy storage," *Energy*, vol. 217, pp. 1–15, 2021.

[18] Y. M. Liu, J. H. Zhang, X. P. Yang, S. Niu, S. Zheng, and A. Xue, "Construction method of evaluation index system of relay protection based on macroscopic and microcosmic view," *Power System Technology*, vol. 44, no. 8, pp. 3090–3096, 2020.

[19] K. Yuan, J. R. Li, Y. Song, Y. Mu, and C. Sun, "Review and prospect of comprehensive evaluation technology of regional energy internet," *Automation of Electric Power Systems*, vol. 43, no. 14, pp. 41–52+64, 2019.

[20] Z. Y. Li, *A Study on Economic Efficacy Evaluation of Smart Grid Based on Improved TOPSIS Method*, North China Electric Power University, Beijing, China, 2016.

[21] S. Hall and T. J. Foxon, "Values in the smart grid: the co-evolving political economy of smart distribution," *Energy Policy*, vol. 74, pp. 600–609, 2014.

[22] B. Zeng, J. M. Bai, W. Z. Guo, Y. Q. Yang, and M. Zeng, "Comprehensive evaluation for benefits of demand response in smart distribution networks," *Power System Technology*, vol. 41, no. 5, pp. 1603–1611, 2017.

[23] Y. M. Li and Z. Chen, "Study on regional electric energy substitution potential evaluation based on TOPSIS method of optimized connection degree," *Power System Technology*, vol. 43, no. 2, pp. 687–693, 2017.

[24] Y. J. Fang, X. L. Wang, J. Shi, X. Wu, and H. Yan, "Research on operation and economic efficiency evaluation of provincial power grid with integrated renewable energy," *Power System Technology*, vol. 41, no. 7, pp. 2138–2145, 2017.

[25] Z. M. Lu, Y. Gao, and C. B. Xu, "Evaluation of energy management system for regional integrated energy system under interval type-2 hesitant fuzzy environment," *Energy*, vol. 222, pp. 1–19, 2021.

[26] H. Liu, Y. Zhao, C. H. Gu, S. Ge, and Z. Yang, "Adjustable capability of the distributed energy system: definition, framework, and evaluation model," *Energy*, vol. 222, pp. 1–17, 2021.

[27] State administration for market regulation, standardization administration, *Internet of Things-General Principles of Stipulation on Evaluation Indicator System: GB/T 36468-2018*, Standards Press of China, Beijing, China, 2018.

[28] State administration for market regulation, standardization administration, *Information Security Technology-Security Technical Requirements of Data Transmission for Internet of Things: GB/T37025-2018*, Standards Press of China, Beijing, China, 2018.

[29] General Administration of Quality Supervision, *Inspection and Quarantine of the People's Republic of China, Standardization Administration. Information Security Technology-Disaster Recovery Specifications for Information Systems: GB/T 20988-2007*, Standards Press of China, Beijing, China, 2007.

[30] Z. H. Yu and W. L. Chin, "Blind false data injection attack using PCA approximation method in smart grid," *IEEE Transactions on Smart Grid*, vol. 6, no. 3, pp. 1219–1226, 2015.

[31] X. W. Lin, *Research on Comprehensive Evaluation of Smart City Development Based on PSF Mode*, Harbin Institute of Technology, Harbin, China, 2017.

[32] X. W. Wang and F. Liu, "Data-driven relay selection for physical-layer security: a decision tree approach," *IEEE Access*, vol. 8, pp. 12105–12116, 2020.

[33] A. Samat, C. Persello, S. Liu, E. Li, Z. Miao, and J. Abuduwaili, "Classification of VHR multispectral images using Extra Trees and maximally stable extremal region-guided morphological profile," *IEEE Journal of Selected Topics in Applied Earth Observations and Remote Sensing*, vol. 11, no. 9, pp. 3179–3195, 2018.

[34] J. Nie, S. C. Yang, Q. Ren, and D. Su, "A Novel Classification Method Based on Adaboost for Electromagnetic Emission Characteristics," in *Proceedings of the IEEE International Applied Computational Electromagnetics Society Symposium-China (ACES)*, IEEE, Beijing, China, August 2018.

Research Article

A Lightweight Modulation Classification Network Resisting White Box Gradient Attacks

Sicheng Zhang ⓘ**, Yun Lin** ⓘ**, Zhida Bao** ⓘ**, and Jiangzhi Fu** ⓘ

Harbin Engineering University, College of Information and Communication Engineering, Harbin 150000, China

Correspondence should be addressed to Jiangzhi Fu; fujiangzhi@hrbeu.edu.cn

Improving the attack resistance of the modulation classification model is an important means to improve the security of the physical layer of the Internet of Things (IoT). In this paper, a binary modulation classification defense network (BMCDN) was proposed, which has the advantages of small model scale and strong immunity to white box gradient attacks. Specifically, an end-to-end modulation signal recognition network that directly recognizes the form of the signal sequence is constructed, and its parameters are quantized to 1 bit to obtain the advantages of low memory usage and fast calculation speed. The gradient of the quantized parameter is directly transferred to the original parameter to realize the gradient concealment and achieve the effect of effectively defending against the white box gradient attack. Experimental results show that BMCDN obtains significant immune performance against white box gradient attacks while achieving a scale reduction of 6 times.

1. Introduction

The Internet of Things (IoT) is an open and comprehensive network of intelligent objects. It is deployed in different environments through various sensor devices to realize real-time collection and interaction of different monitored, connected, and interactive objects or processes [1, 2]. The IoT has been widely used in all aspects of life, including smart transportation, smart homes, smart cities, smart factories, emergency, medical care, and logistics transportation, bringing great convenience and benefits to human life, and there are still a large number of technologies that improve the efficiency of the Internet of Things constantly emerging [3, 4]. However, compared with the gradual expansion of the application range of the IoT devices on a global scale, the development of its security technology is far behind. If not defended, active malicious physical layer attacks such as deception and interference will disrupt the original communication and transmission order of the IoT, greatly reduce the communication performance of legitimate users, and even infringe on the privacy of users, harm personal safety, and affect industrial production [5–7]. Therefore, the physical layer security of the IoT has been

brought to an unprecedentedly important position. As the basis of software wireless, cognitive radio, and spectrum detection, automatic modulation recognition has become an effective means to deal with physical layer security issues [8, 9]. In addition, automatic modulation classification technology is also used in various civil and military fields, such as user legitimacy detection, spectrum detection and management, interference and identification, electronic exhibition, and threat analysis [10–13].

In recent years, artificial intelligence technology has made many achievements in the fields of image recognition and natural language processing, and it is also widely used in communication-related topics, including metalearning for channel estimation, reinforcement learning for resource scheduling, and transfer learning for stations/access points switching [14–17]. More and more researchers have combined artificial intelligence technology with signal processing technology and have achieved many very valuable results for the subject of automatic modulation classification [18]. Literature [19] proposes an adaptive extensible neural network for modulation classification in the multipath fading channel by dividing the network into the amplitude, phase, and frequency weight subnetwork.

Literature [20] proposes that the complex network is used to discover the deep features of the modulated I/Q signal for modulation signal, which has achieved superior performance. Literature [21] proposes a transfer learning-based semisupervised modulation classification to address the problem of a small number of samples that are labelled and a large number that are unlabeled in real communication scenarios. Literature [22] proposes a signal recognition and reconstruction convolutional neural networks, the first zero-shot learning work, by studying the representation of signal semantic feature space. These research results have played a huge role in promoting the subject of modulation signal classification.

However, the automatic modulation classification method based on artificial intelligence technology has the following two obvious shortcomings. (1) While the model classification performance is improved, its scale tends to increase with it, which will increase the storage complexity and computational complexity of the model to the point where the edge devices of the IoT cannot afford it [23]. (2) The deep learning model is to fit high-dimensional data, rather than truly understand the data. This leads to the existence of adversarial samples, which only add a slight disturbance to the data that humans cannot detect, which makes the model produce a very outrageous output. This will also become a threat to the security of the IoT [24]. Literature [25] constructs a convolutional neural network to classify the modulated signal and proposes an index of activation maximization to evaluate the importance of the filter in the network. The network can still obtain the same or higher accuracy when the compression rate is 80%. Literature [26] converts the modulated signal into the form of a constellation diagram and constructs a binary convolutional neural network to classify it. While maintaining the same or higher classification accuracy rate, the model storage compression can be achieved by 26 times. Literature [27] introduces a scaling factor for each neuron in CNN and enforces scaling factors sparsity via compressive sensing to screen out redundant neurons and then these neurons are pruned. Literature [28] designs a communication signal adversarial sample by adding a carefully designed counter disturbance, which can ensure that the communication performance is not damaged, while reducing the intruder's modulation classification accuracy. Literature [29] launched white box and black box attacks on the modulation signal classification model. Both attack methods can significantly reduce the classification accuracy of the model. This literature further proves that the model classification confidence is inversely proportional to the attack success rate. Literature [30] uses the generative adversarial networks for semisupervised learning, which improves the model's robustness and generalization ability for modulated signal classification. In addition, a lot of work has been carried out, focusing on the evaluation of adversarial perturbation in communication signals such as invisibility of adversarial examples, the effectiveness of adversarial attacks on signals, and fitting difference to measure the perturbed waveforms [31–33]. Therefore, the research on the automatic modulation classification model with both lightweight and antiattack has important research value for the whole problem of the IoT with a large number of edge devices.

In order to further improve the reliability of the application of artificial intelligence technology in the security of the IoT, this paper designs a binary modulation signal classification defense network (BMCDN). In the forward propagation of the binarized convolutional layer, the network parameters and input are quantized from 32-bit floating-point type to 1-bit integer type, which reduces the storage overhead of the model. In the original convolution operation, the 32-bit floating-point multiplication operation was replaced by the bit operation, and the accumulation operation was replaced by the counting operation, which reduced the calculation time of the model. In the backward propagation process of the binarized convolutional layer, the gradient of the quantized input and parameters are directly passed to the original input and parameters to update the network. At this time, the gradient obtained by the input is not its true gradient, but the gradient of its quantized value, which has the effect of gradient masking and can effectively defend against white box gradient attacks.

This paper is organized as follows. In Section 2, typical white box gradient attack methods are briefly introduced. In Section 3, the proposed defense framework BMCDN is presented and analyzed. In Section 4, the comprehensive experiments are described to verify the advantages of model scale and immunity to white box gradient attacks. Section 5 draws the conclusions.

1.1. Attacks.
According to how much information the attacker has on the target model, attack methods can be divided into white box attacks, gray box attacks, and black box attacks. Among them, white box attacks are the most commonly used method to evaluate defense performance [34]. In a white box attack, the attacker knows the network architecture, parameters, training data, etc., of the model. This paper selects fast gradient sign method (FGSM) and projected gradient descent (PGD) in the white box attack to attack the design model and evaluate its defense performance.

1.2. FGSM.
FGSM is a typical single-step attack. According to whether the attack target has a specific category, it can be divided into untargeted attack and targeted attack [35]. The FGSM algorithm is shown in the following formula:

$$\text{untargeted: } \mathbf{x}' = \mathbf{x} + \varepsilon \cdot \text{sign}\left(\nabla_x J\left(f(\mathbf{x}), y_{\text{true}}\right)\right), \quad (1)$$

$$\text{targeted: } \mathbf{x}' = \mathbf{x} - \varepsilon \cdot \text{sign}\left(\nabla_x J\left(f(\mathbf{x}), y_{\text{target}}\right)\right), \quad (2)$$

where $f(\cdot)$ donates the target model. Its input data is the modulated signal $\mathbf{x}$, and output is the classification result; $J(f(\mathbf{x}), y)$ donates the cost function between model output and label; $\nabla_x J(f(\mathbf{x}), y)$ donates the partial derivative of the cost value with respect to x; $\text{sign}(\cdot)$ will get the direction of the gradient; ϵ donates the step size of the perturbation; formula (1) indicates that perturbation is added to x to increase the loss value between the model output and the real label, while formula (2) indicates that perturbation is added

to x to decrease loss value between the model output and the target label to get the adversarial sample $\mathbf{x}'$, respectively.

1.3. PGD. PGD is a typical iterative attack, which can be seen as a combination of random perturbation and an iterative version of FGSM [36]. PGD is considered to be the most adversarial attack algorithm, under the same perturbation intensity. The PGD algorithm is shown in the following formula:

$$
\begin{aligned}
x'_0 &= x + n, \\
\text{untargeted: } x'_{i+1} &= \text{clip}_{\epsilon,x}\left(x'_i + \alpha \cdot \text{sign}\left(\nabla_x J\left(g\left(x'_i\right), y_{\text{true}}\right)\right)\right), \\
\text{targeted: } x'_{i+1} &= \text{clip}_{\epsilon,x}\left(x'_i - \alpha \cdot \text{sign}\left(\nabla_x J\left(f\left(x'_i\right), y_{\text{target}}\right)\right)\right),
\end{aligned}
\tag{3}
$$

where n is a random perturbation; α is the perturbation step length of each step. Usually, the number of iteration steps is greater than the ratio of disturbance intensity ϵ to α; $\text{clip}_{\epsilon,\mathbf{x}}(\cdot)$ will clip the adversarial example $\mathbf{x}'$ to maintain it in the ϵ−neighbourhood of original data.

2. Methods

In order to further improve the reliability of the application of artificial intelligence technology in the security of the IoT, this paper designs a binary modulation signal classification defense network. Extremely low bit width will bring storage and computational advantages. The extremely low weight bit width will give it storage and calculation advantages in forward operations. The direct return of the binarized gradient to the original parameters will also achieve the effect of gradient concealment and achieve the effect of effectively defending against white box gradient attacks.

2.1. Forward Propagation. The network binarization method selected in this paper is the deterministic binarization method among the naive binarization methods [37]. In the deterministic binarization method, the parameters of the binarized convolutional layer and the input quantization rules are as follows:

$$
w^b = \begin{cases} +1, & w \geq 0, \\ -1, & \text{otherwise,} \end{cases}
\tag{4}
$$

where w is the original full-precision parameter in the network, and w^b is the binarized parameter obtained after binarization. The sign function $\text{sign}(\cdot)$ can be used to obtain the sign of the parameter and input to realize the binarization.

In actual computer storage, setting 0 bit represents parameter value -1, and setting 1 bit represents parameter value -1. The truth value table of the multiplication of 1-bit weight and the computer variable operation after quantization is shown in Table 1.

From Table 1, we can find that the ± 1 weight multiplication operation obtained by the above quantization rule is equivalent to the "XNOR" operation of the computer's 1-bit variable. Therefore, the accumulation operation after the

TABLE 1: The truth value table of the multiplication of 1-bit weight and the computer variable operation.

Multiplication of 1-bit weight			Equivalent computer operation		
$\mathbf{W_m}$	$\mathbf{W_n}$	$\mathbf{W_m} \times \mathbf{W_n}$	V_m	V_n	$V_m \odot V_n$
1	1	1	1	1	1
1	−1	−1	1	0	0
−1	1	−1	0	1	0
−1	−1	1	0	0	1

convolution kernel operation can also be replaced by the "bitcount" counting operation. The operation rules of the binarized convolutional layer are shown in Figure 1.

2.2. Backward Propagation. The gradient during training of the binarized network is still obtained through backward propagation. The most critical step is the binarization operation, which directly affects the gradient calculation of the parameters and input before the binarization. The curve of the $\text{sign}(\cdot)$ function used in the binarization process is shown in Figure 2.

From the figure, we can see that the derivative of the function is almost zero everywhere. This will cause the gradient to be blocked when it is propagated here. In order to avoid the problem of the gradient propagation being blocked, this experimental design transfers the binarized parameters and the input gradient directly to the original parameters and input, respectively. Among them, the gradient of the original data exceeding $[-1, 1]$ is set to zero. After an update step is completed, original data will be clipped to the interval of $[-1, 1]$. A very simple example is listed, as shown in Figure 3.

In Figure 3, from left to right, a process in which weights and inputs are binarized and convolution is calculated. The lower right corner of each data indicates the respective gradient value after backpropagation. The gradient propagated to output through the previous layer is assumed to be 1. It can be seen from Figure 3 that the gradient obtained from the original input and weight is the gradient of the binarized input and weight. Although the gradients they get are not their own gradients, this at least ensures that the network can be updated and optimized. Obviously, the gradient obtained by the weight and input is not its optimal gradient, which makes the update and optimization direction in each update step not optimal.

However, this gradient propagation method will achieve a very good gradient masking effect. The core idea of the white box gradient attack is to add a disturbance to the input, which will increase the cost of the output and the label the fastest. This direction is actually the reverse of the optimal gradient of the input data. In the binary convolutional layer, this optimal gradient is hidden. As a result, it will gain high immunity against white box gradient attacks. The principle of its immunity to the white box gradient attack is shown in Figure 4.

Figure 4 shows a simplified two-dimensional contour map of the cost value of network output and label for one
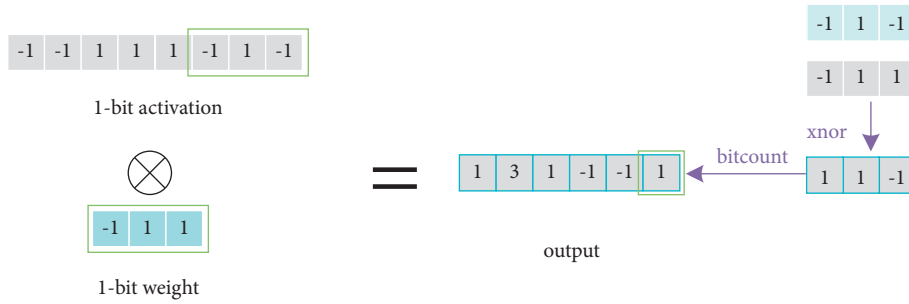
FIGURE 1: Schematic diagram of binary convolutional layer operation rules.
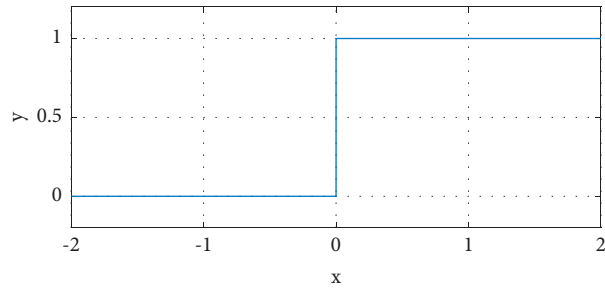

FIGURE 2: The curve of the sign($\cdot$) function.
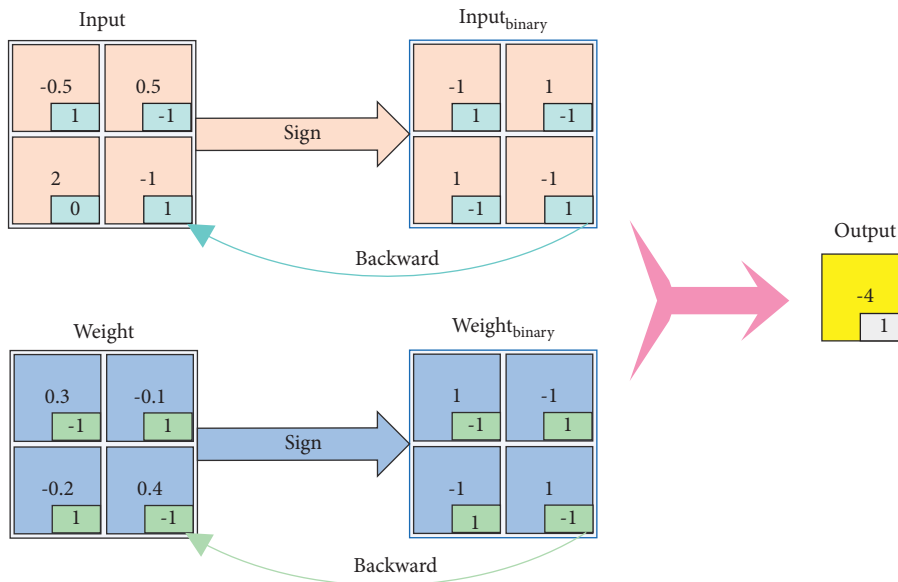

FIGURE 3: Schematic diagram of the gradient backpropagation rule of the binary convolutional layer.
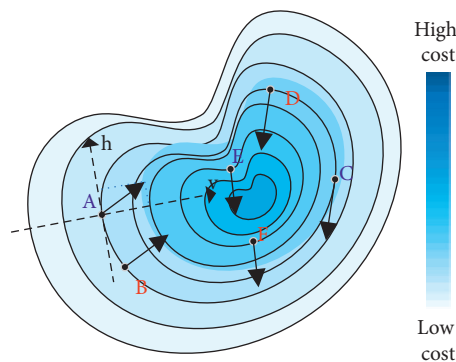

FIGURE 4: Two-dimensional contour map of the cost value.

data. The darker part has a higher cost value. The points on the same circle have the same cost value. Point A reaches point B after binarization, and point C and point D and point E and point F are the same. A data will inevitably transform from itself to its binary state. Therefore, point A and point B have the same cost value. After back-propagation, point A obtains the gradient of point B. The attack generated by the attack algorithm only produces an attack effect in the v direction, and there is no attack effect in the h direction, so the attack effect will be weakened or invalidated as point C and point D. It even produces the opposite effect of the attack as point E and point F. The training of the binary network is a process of multiple iterations. The gradient value obtained through back-propagation at one time may not be conducive to training, but the next time, a gradient that is conducive to training may be obtained. After multiple iterations, it can be ensured that the network as a whole is updated in a direction that fits the data well.

3. Architecture

This paper designs and constructs a BMCDN that directly processes the waveform domain modulation signal. In each layer of the network, we use the block structure shown in Figure 5. Among them, Float/Binary Layer is used for feature extraction and classification, BatchNormal Layer is used to normalize data to speed up training, and MaxPooling Layer implements feature fusion to enhance the antinoise performance of the network.

By analyzing the data of the modulated signal, we can find that there are a large number of fine-grained features in the signal, which enable them to carry different information in different ways. If the binarization process is carried out too early, these features will be filtered out or submerged. Therefore, the first two layers in the network designed in this paper still maintain the float-blocks to extract fine-grained features in the signal. After passing through the float-blocks, the one-dimensional data features are mapped to the high-dimensional network space, which can ensure that the subsequent binarization processing will not bring too much information loss. After the float-blocks, binary-blocks with filters of different sizes are designed to extract coarse-grained features from the data. For the feature classification step, this paper designs to use a binarized convolutional layer with a 1×1 size filter as the classification layer. Between the coarse-grained feature extraction layer and the classification layer, a transition layer is designed to be inserted to match the data size. After the classification layer, a Float Layer with a size of 1×1 convolution kernel combined with the softmax layer is designed as an output layer to obtain classification probabilities of different classifications. The structure of the BMCDN is shown in Figure 6.

4. Results and Discussion

The dataset used in this study is the public modulation signal dataset RML2018.10A published by [38]. In this dataset, 24 types of single-carrier modulation signals that are widely
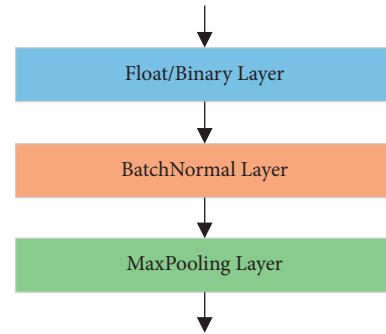
Figure 5: Schematic diagram of block structure.

used are collected, including OOK, 4ASK, 8ASK, BPSK, QPSK, 8PSK, 16PSK, 32PSK, 16APSK, 32APSK, 64APSK, 128APSK, 16QAM, 32QAM, 64QAM, 128QAM, 256QB-WC-AM-AM-WC, AM-DSB-SC, FM, GMSK, and OQPSK. The SNR ranges from −20 dB to 30 dB in 2 dB steps. The parameters of the pulse shaping filter, the multipath fading of the channel and other system, and environmental parameters are all taken into consideration when collecting data. In this paper, the dataset is divided into training set, validation set, and test set according to the ratio of 8:1:1. The experimental environment in this paper is a computer with GTX2080 GPU resources and Windows 10 operating system. The experiment is based on the PyTorch deep learning framework and the DeepRobust adversarial sample attack and defense platform [39].

4.1. Analysis of the Classification Effect of the Model. In order to obtain a clear positioning of the classification performance of the constructed BMCDN, the experimental design constructs a full-precision network with the same architecture for comparison, float modulation classification defense network (FMCDN). The two networks use the same training environment and parameters, the loss function is the cross-entropy loss function, the optimizer is adaptive moment estimation, the batch size is 256, and the learning rate is $5e − 5$. The test classification accuracy rates of the two trained models under modulated signal data with different SNR are shown in Figure 7.

From Figure 6, we can find that the classification accuracy of FMCDN and BMCDN is improved with the increase of SNR and tends to stabilize around 14 dB. The accuracy of FMCDN is stable around 96%, while the accuracy of BMCDN is stable around 90%. In the two networks with the same architecture, the parameters of FMCDN are all floating-point data, and the fitting ability of the network is obviously better than that of BMCDN, so the difference in accuracy is within expectations and acceptable.

4.2. Analysis of Model Size. In order to comprehensively analyze the performance of the two networks, this paper further evaluates the scale of the model from both the model file size and the running speed. The test environment selected for the experiment is JD AI's DABNN, a binary network reasoning framework highly optimized for ARM
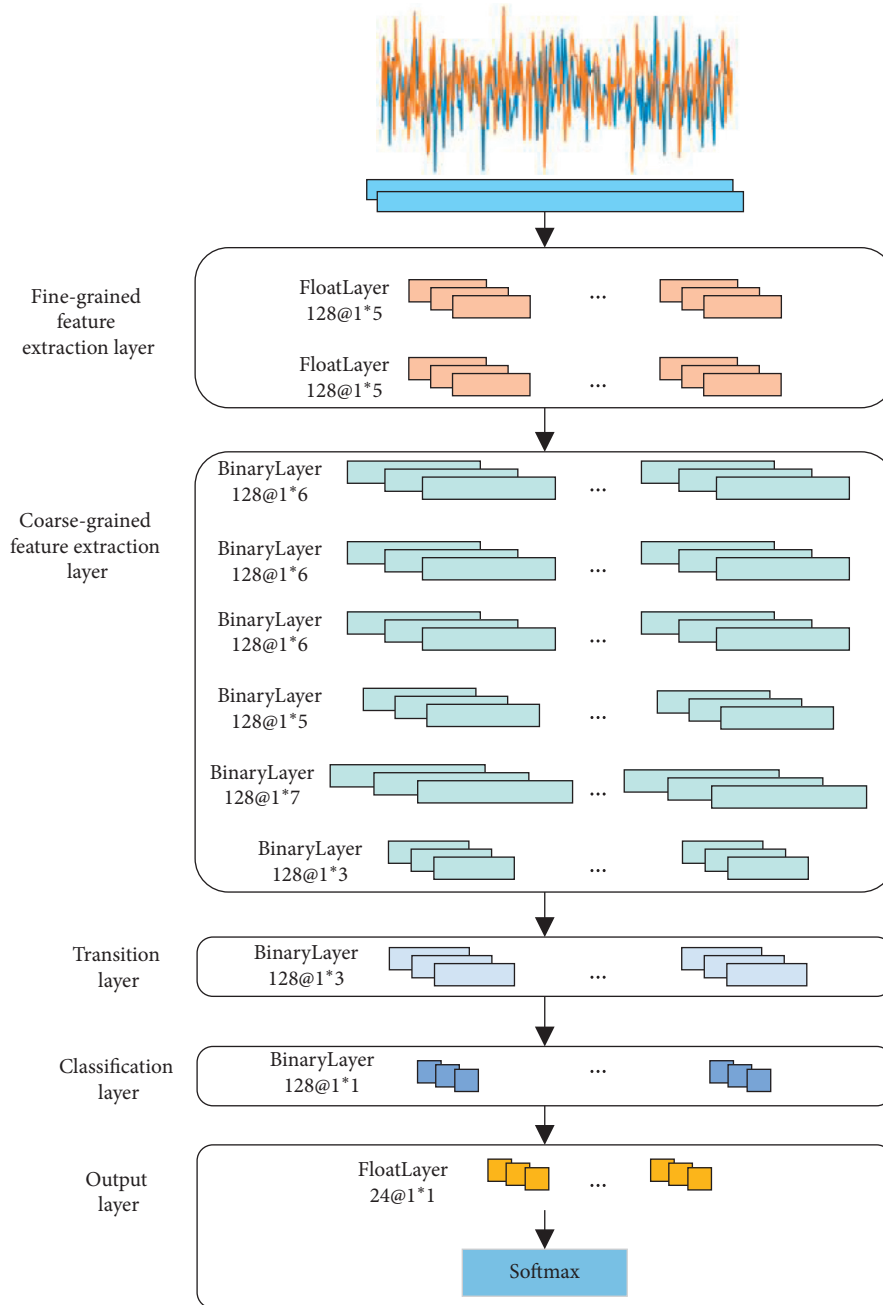
FIGURE 6: The structure of the BMCDN.

instruction set [40]. In order to obtain a more accurate and stable difference, the selected platform is a Raspberry Pi 4B with a single ARM core and a frequency of 1.5 GHz. After half an hour of startup, the model is run for 100 times to compare its average running time. The model file size and runtime difference are shown in Figure 7.

From Figure 8, we can see that the file size of the BMCDN model is less than one-sixth of the FMCDN model, and the running time is less than three-quarters of the FMCDN. In theory, the size of the binarization layer is one-third of the full-precision layer. In terms of computational complexity, floating-point multiplication operations will also be replaced with bit operations to achieve speed-up effects. The increase in speed is also related to the floating-point unit of the device. In the BMCDN, both the first two layers and the last layer remain full-precision layers, which causes the model file size to fail to reach the optimal compression limit of 32 times smaller, and some
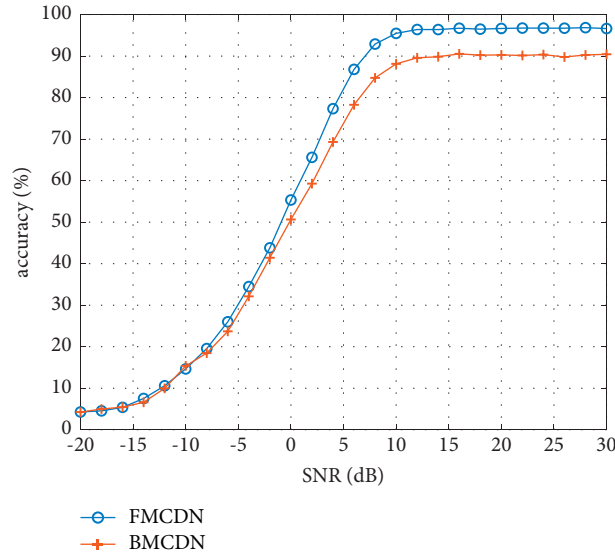
Figure 7: Test results of the two models under different SNR.
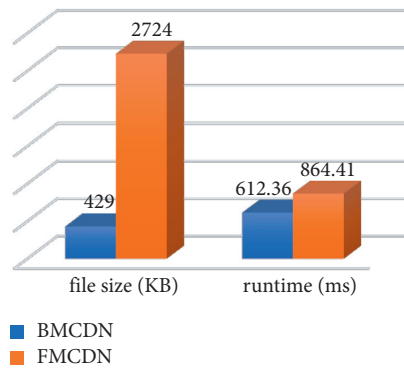
Figure 8: The attack effect of FGSM and PGD and the defensive effect after defensive training.

intermediate operations in the binarization layer are also floating-point operations, and it is reasonable to obtain the above runtime compression. The compression ratio of the model file size and runtime will increase as the proportion of the binarization layer increases.

4.3. Analysis of the Model's Antiattack Performance. This paper uses two typical white box attack methods, single-step attack FGSM, and iterative attack PGD to evaluate the antiattack performance of BMCDN and FMCDN. The perturbation intensity of the two attack methods ranges from 0 to 0.03, with a step size of 0.005. Among them, the number of iterations of PGD is the quotient of the disturbance intensity and the step size plus 5 to ensure the attack intensity. According to the classification accuracy rate in Figure 6, this paper selects representative data of SNR −8 dB, 0 dB, 8 dB, and 16 dB to attack to evaluate antiattack performance of the model. The attack effects of the two attack algorithms are shown in Figures 9(a) and 9(b).

In order to further improve the performance of the constructed model against attacks, this paper designs the use of training sets with attack disturbances to conduct defense training on the model. The perturbation intensity of the training set is 0.02. The training method and parameters of defense training are the same as the above experiment. The same attack as before is applied to the model after defensive training, and the attack effect is shown in Figures 9(c) and 9(d).

When horizontally comparing Figures 9(a) and 9(b) or Figures 9(c) and 9(d), we can find that (1) the accuracy rate decreases as the attack intensity increases for the model weather before defensive training or after defensive training. (2) For data whose classification effect is poor by the model itself, the attack algorithm is not effective against this type of data. (3) Under the same disturbance intensity, the iterative attack method PGD is more aggressive than the single-step attack method FGSM for FMCDN, while FGSM and PGD have almost the same attack effect on BMCDN. (4) Under the same disturbance intensity, BMCDN has stronger
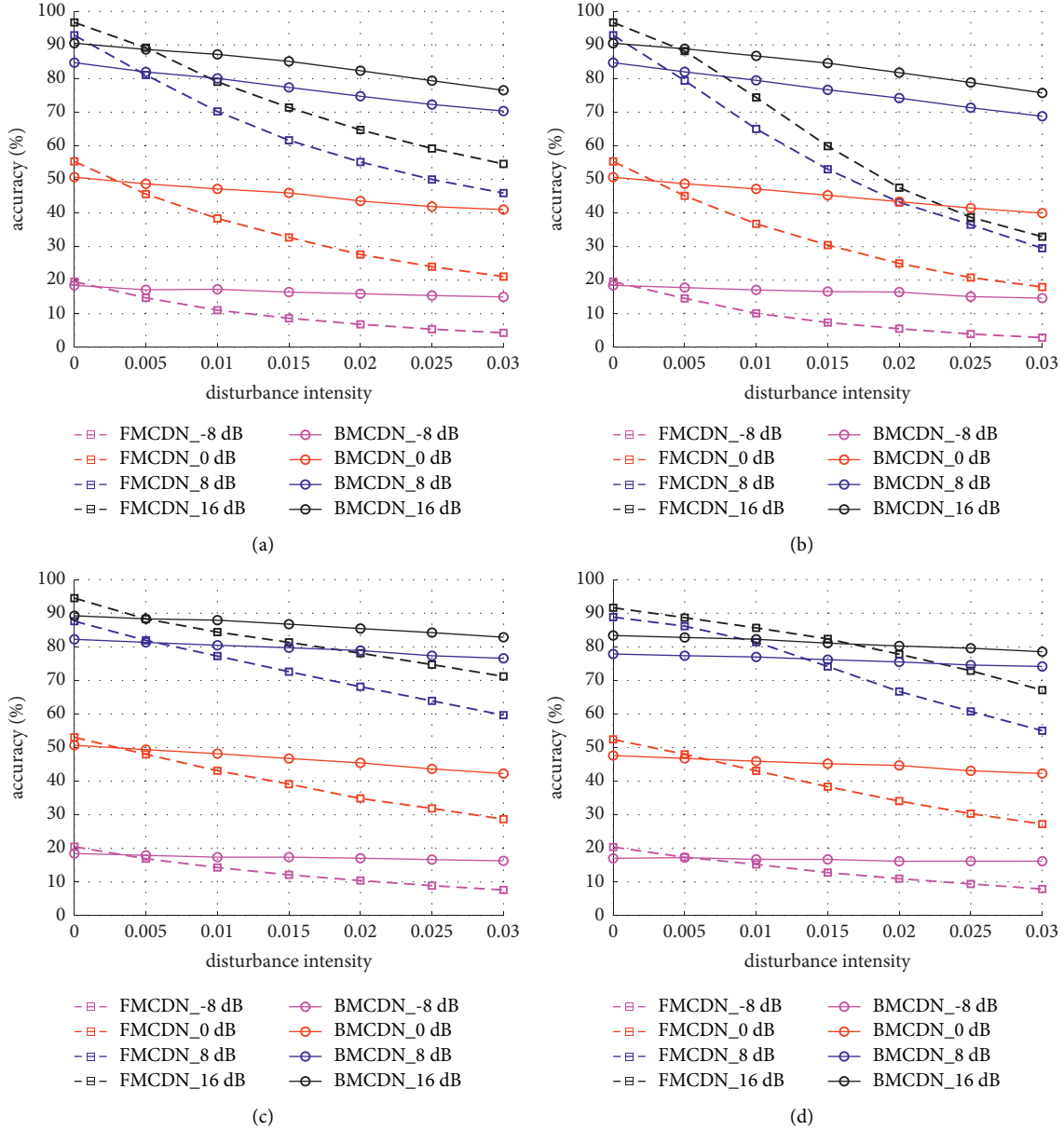
FIGURE 9: The attack effect of FGSM and PGD and the defensive effect after defensive training. (a) FGSM attack. (b) PGD attack. (c) FGSM defense. (d) PGD defense.

antiattack performance compared with FGSM. The gradient concealment of BMCDN makes the data not modified in the direction of the fastest increase in loss every time the antiperturbation is resisted. In addition, the weak disturbance is overwhelmed by the binarization operation. Therefore, BMCDN obtains a strong antiattack performance against white box gradient attacks.

When vertically comparing Figures 9(a) and 9(c) or Figures 9(b) and 9(d), we can find that (1) after defensive training, the defense performance of the two models for the two attack algorithms is improved, and the improvement of FMCDN is greater than that of BMCDN. (2) However, the antiattack performance of the FMCDN model after defensive training is weaker than that of the BMCND model before defensive training. Therefore, the optimization effect

of defense training on the decision boundary is not as good as the defense performance of gradient mask against white box gradient attacks.

5. Conclusions

Aiming at the problem of high computational complexity and vulnerability to adversarial sample attacks when artificial intelligence is applied to the issue of IoT security, this paper designs a modulation classification defense model BMCDN that combines fast inference and antiwhite box gradient attacks to detect the malicious attacks and interference in the IoT. In the BMCDN model, the binarization operation enables the multiplication and accumulation operations in the forward inference of the network to be

replaced by bit operations, which greatly reduces the amount of parameters and the computational complexity. In addition, the gradient masking in backpropagation also enables it to have the performance of resisting white box gradient attacks far exceeding the full-precision network model with the same architecture.

While obtaining the above results, we have been keeping these points in mind: (1) there is no free lunch. The model obtains the characteristics of a smaller scale and resisting white box gradient attacks, so it will inevitably show the vulnerability to certain attacks. Further research on the defense performance of BMCDN is necessary. (2) We believe that there are still redundant connections in the BMCND model, and further pruning may result in a more lightweight physical layer defense model of the IoT. (3) More complex channel models should be considered, and corresponding attacks and defense methods should be studied and designed. (4) We believe that the binarization block is the reason why its network is resistant to white box gradient attacks. Therefore, we introduce a small number of binarization blocks and retain most of the full-precision blocks, which may be able to ensure the classification performance of the model while gaining defensive performance. The research on these points will further improve the deficiencies of this paper and promote the topic of physical layer security of the IoT.

Data Availability

The RML2018.10A dataset used in the experiments is public. Please refer to the corresponding literature for download URL. The source code of the proposed method is available from the corresponding author on reasonable request, http://opendata.deepsig.io/datasets/2018.01/2018.01.OSC. 0001_1024x2M.h5.tar.gz.

Conflicts of Interest

The authors declare that are no conflicts of interest regarding the publication of this paper.

Acknowledgments

References

[1] L. D. Xu, W. He, and S. Li, "Internet of things in industries: a survey," *IEEE Transactions on industrial informatics*, vol. 10, no. 4, pp. 2233–2243, 2014.

[2] B. Wang, X. Zhang, and H. Wu, "A method of ZigBee automatic irrigation," *International Journal of Performability Engineering*, vol. 16, no. 4, pp. 639–646, 2020.

[3] X. Liu and X. Zhang, "NOMA-based resource allocation for cluster-based cognitive industrial Internet of things," *IEEE Transactions on Industrial Informatics*, vol. 16, no. 8, pp. 5379–5388, 2020.

[4] X. Liu, X. B. Zhai, W. Lu, and C. Wu, "QoS-guarantee resource allocation for multibeam satellite industrial Internet of things with NOMA," *IEEE Transactions on Industrial Informatics*, vol. 17, no. 3, pp. 2052–2061, 2021.

[5] Q. Qi, X. Chen, C. Zhong, and Z. Zhang, "Physical layer security for massive access in cellular Internet of Things," *Science China Information Sciences*, vol. 63, no. 2, pp. 1–12, 2020.

[6] S. Hameed, F. I. Khan, and B. Hameed, "Understanding security requirements and challenges in Internet of things (IoT): a review," *Journal of Computer Networks and Communications*, vol. 2019, Article ID 9629381, 14 pages, 2019.

[7] G. Gui, M. Liu, F. Tang, N. Kato, and F. Adachi, "6G: opening new horizons for integration of comfort, security, and intelligence," *IEEE Wireless Communications*, vol. 27, no. 5, pp. 126–132, 2020.

[8] S. Huang, C. Lin, W. Xu, Y. Gao, Z. Feng, and F. Zhu, "Identification of active attacks in Internet of things: joint model-and data-driven automatic modulation classification approach," *IEEE Internet of Things Journal*, vol. 8, no. 3, pp. 2051–2065, 2020.

[9] S. Huang, Y. Yao, Z. Wei, Z. Feng, and P. Zhang, "Automatic modulation classification of overlapped sources using multiple cumulants," *IEEE Transactions on Vehicular Technology*, vol. 66, no. 7, pp. 6089–6101, 2017.

[10] Y. Lin, X. Zhu, Z. Zheng, Z. Dou, and R. Zhou, "The individual identification method of wireless device based on dimensionality reduction and machine learning," *The Journal of Supercomputing*, vol. 75, no. 6, pp. 3010–3027, 2019.

[11] H. Wang, J. Li, L. Guo, D. Zheng, Y. Lin, and Z. Ruolin, "Fractal complexity-based feature extraction algorithm of communication signals," *Fractals*, vol. 25, Article ID 1740008, 2017.

[12] Y. Wang, M. Liu, J. Yang, and G. Gui, "Data-driven deep learning for automatic modulation recognition in cognitive radios," *IEEE Transactions on Vehicular Technology*, vol. 68, no. 4, pp. 4074–4077, 2019.

[13] Y. Lin, Y. Tu, Z. Dou, L. Chen, and S. Mao, "Contour stella image and deep learning for signal recognition in the physical layer," *IEEE Transactions on Cognitive Communications and Networking*, vol. 7, no. 1, pp. 34–46, 2021.

[14] S. Park, H. Jang, O. Simeone, and J. Kang, "Learning to demodulate from few pilots via offline and online meta-learning," *IEEE Transactions on Signal Processing*, vol. 69, pp. 226–239, 2021.

[15] N. Mastronarde and M. van der Schaar, "Fast reinforcement learning for energy-efficient wireless communication," *IEEE Transactions on Signal Processing*, vol. 59, no. 12, pp. 6262–6266, 2011.

[16] M. Wang, Y. Lin, Q. Tian, and G. Si, "Transfer learning promotes 6G wireless communications: recent advances and future challenges," *IEEE Transactions on Reliability*, vol. 70, no. 2, pp. 790–807, 2021.

[17] K. Anupama, Y. C. Rao, and V. K. Gurrala, "A machine learning approach to monitor water quality in aquaculture," *International Journal of Performability Engineering*, vol. 16, no. 12, pp. 1845–1852, 2020.

[18] Q. V. Pham, N. T. Nguyen, T. Huynh-The, L. B. Le, K. Lee, and W. J. Hwang, "Intelligent radio signal processing: a contemporary survey," 2020, https://arxiv.org/abs/2008.08264.

[19] G. Q. Yang, "Modulation classification based on extensible neural networks," *Mathematical Problems in Engineering*, vol. 2017, Article ID 6416019, 10 pages, 2017.

[20] Y. Tu, Y. Lin, C. Hou, and S. Mao, "Complex-valued networks for automatic modulation classification," *IEEE Transactions on Vehicular Technology*, vol. 69, no. 9, pp. 10085–10089, 2020.

[21] W. Yu, G. Guan, H. Gacanin, T. Ohtsuki, H. Sari, and F. Adachi, "Transfer learning for semi-supervised automatic modulation classification in ZF-MIMO systems," *IEEE Journal on Emerging and Selected Topics in Circuits and Systems*, vol. 10, no. 2, pp. 231–239, 2020.

[22] Y. Dong, X. Jiang, H. Zhou, Y. Lin, and Q. Shi, "SR2CNN: zero-shot learning for signal recognition," *IEEE Transactions on Signal Processing*, vol. 69, pp. 2316–2329, 2021.

[23] K. Nan, S. Liu, J. Du, and H. Liu, "Deep model compression for mobile platforms: a survey," *Tsinghua Science and Technology*, vol. 24, no. 6, pp. 677–693, 2019.

[24] C. Szegedy, W. Zaremba, I. Sutskever et al., "Intriguing properties of neural networks," 2013, https://arxiv.org/abs/1312.6199.

[25] Y. Lin, Y. Tu, and Z. Dou, "An improved neural network pruning technology for automatic modulation classification in edge devices," *IEEE Transactions on Vehicular Technology*, vol. 69, no. 5, pp. 5703–5706, 2020.

[26] S. Zhang, L. I. N. Yun, T. U. Ya, and S. Mao, "Electromagnetic signal modulation recognition technology based on lightweight deep neural network," *Journal on Communications*, vol. 41, no. 11, pp. 12–21, 2020.

[27] Y. Wang, J. Yang, M. Liu, and G. Gui, "LightAMC: lightweight automatic modulation classification via deep learning and compressive sensing," *IEEE Transactions on Vehicular Technology*, vol. 69, no. 3, pp. 3491–3495, 2020.

[28] M. Z. Hameed, A. György, and D. Gündüz, "The best defense is a good offense: adversarial attacks to avoid modulation detection," *IEEE Transactions on Information Forensics and Security*, vol. 16, pp. 1074–1087, 2020.

[29] Y. Lin, H. Zhao, Y. Tu, S. Mao, and Z. Dou, "Threats of adversarial attacks in DNN-based modulation recognition," in *Proceedings of the IEEE INFOCOM 2020-IEEE Conference on Computer Communications*, pp. 2469–2478, IEEE, Toronto, Canada, July 2020.

[30] H. Xu, Y. Ma, H.-C. Liu et al., "Adversarial attacks and defenses in images, graphs and text: a review," *International Journal of Automation and Computing*, vol. 17, no. 2, pp. 151–178, 2020.

[31] H. Zhao, Q. Tian, L. Pan, and L. Lin, "The technology of adversarial attacks in signal recognition," *Physical Communication*, vol. 43, Article ID 101199, 2020.

[32] Y. Lin, H. Zhao, X. Ma, Y. Tu, and M. Wang, "Adversarial attacks in modulation recognition with convolutional neural networks," *IEEE Transactions on Reliability*, vol. 70, no. 1, pp. 389–401, 2020.

[33] H. Zhao, Y. Lin, S. Gao, and S. Yu, "Evaluating and Improving Adversarial Attacks on DNN-Based Modulation Recognition," in *Proceedings of the GLOBECOM 2020-2020 IEEE Global Communications Conference*, pp. 1–5, IEEE, Taipei, Taiwan, December 2020.

[34] Y. Tu, Y. Lin, J. Wang, and J. Kim, "Semi-supervised learning with generative adversarial networks on digital signal modulation classification," *CMC-Computers Materials & Continua*, vol. 55, no. 2, pp. 243–254, 2018.

[35] I. J. Goodfellow, J. Shlens, and C. Szegedy, "Explaining and harnessing adversarial examples," 2014, https://arxiv.org/abs/1412.6572.

[36] A. Madry, A. Makelov, L. Schmidt, D. Tsipras, and A. Vladu, "Towards deep learning models resistant to adversarial attacks," 2017, https://arxiv.org/abs/1706.06083.

[37] H. Qin, R. Gong, X. Liu, X. Bai, J. Song, and N. Sebe, "Binary neural networks: A survey," *Pattern Recognition*, vol. 105, Article ID 107281, 2020.

[38] T. J. O'Shea, T. Roy, and T. C. Clancy, "Over-the-air deep learning based radio signal classification," *IEEE Journal of Selected Topics in Signal Processing*, vol. 12, no. 1, pp. 168–179, 2018.

[39] Y. Li, W. Jin, H. Xu, and J. Tang, "Deeprobust: a pytorch library for adversarial attacks and defenses," 2020, https://arxiv.org/abs/2005.06149.

[40] J. Zhang, Y. Pan, T. Yao, H. Zhao, and T. Mei, "Dabnn: a super fast inference framework for binary neural networks on arm devices," in *Proceedings of the 27th ACM International Conference on Multimedia*, pp. 2272–2275, Nice, France, October 21-25, 2019.

WILEY | Hindawi

Research Article

Power Optimization for Aerial Intelligent Reflecting Surface-Aided Cell-Free Massive MIMO-Based Wireless Sensor Network

Tao Zhou [ID],[1] **Kui Xu** [ID],[1] **Chunguo Li** [ID],[2] **and Zhexian Shen** [ID][1]

[1]*The College of Communications Engineering, Army Engineering University of PLA, Nanjing, China*
[2]*Southeast University, Nanjing, China*

Correspondence should be addressed to Kui Xu; lgdxxukui@sina.com

Intelligent reflecting surfaces (IRSs) have significant advantages in enhancing the coverage and reducing the deployment cost of wireless networks. This paper studies an aerial IRS- (AIRS-) enhanced cell-free massive multiple-input multiple-output- (MIMO-) based wireless sensor network (WSN) in which multiple access points (APs) serve several sensor users (SUs). Direct links between the APs and SUs are blocked due to occlusion by tall buildings. Hence, we deploy an AIRS to improve the communication quality of the SUs. Our goal is to minimize the total transmit power of all APs under a given minimum signal-to-interference-plus-noise ratio (SINR) requirement. We propose a joint iterative optimization algorithm by designing an active beamforming mechanism at each AP and a passive beamforming mechanism at the AIRS to solve this problem. Simulation results illustrate the good performance of the proposed method.

1. Introduction

Compared with fifth-generation (5G) communication, sixth-generation (6G) communication will require higher speeds, lower latency, and Internet of Everything (IoE) capabilities [1–3]. In addition, 6G will achieve integrated air-space-ground coverage, providing safe and reliable service [4–6]. As one of the core technologies for 6G, intelligent reflective surfaces (IRSs) can effectively enhance the regional coverage and reduce the energy consumption of wireless networks [7]. Therefore, IRSs have received widespread attention in recent years.

An IRS consists of many programmable subwavelength metamaterial array elements. Each element can control the amplitude and phase of electromagnetic waves to realize smart and reconfigurable transmission based on the wireless environment [8–10]. In contrast to traditional transmitters, an IRS does not perform any signal processing and merely modifies the phase and amplitude of incident electromagnetic waves. An IRS does not need to be equipped with a radio frequency link composed of filters, mixers, and power amplifiers. Therefore, IRSs can effectively reduce the costs and energy consumption of wireless networks [11, 12]. The signals reflected by an IRS can be made to be coherently superimposed at the receiver by suitably designing the reflection coefficients of the IRS. We call this approach passive beamforming [13, 14].

Cell-free (CF) massive multiple-input multiple-output (MIMO) technology breaks away from the fixed architecture of traditional cellular massive MIMO. In a CF system, multiple distributed access points (APs) provide communication services for several users in the coverage area simultaneously. All the APs are connected through backhaul links and are controlled by a smart central processing unit (CPU). The CPU can control the resource allocation in real time, thereby eliminating the cell boundaries in traditional cellular networks. Thus, the interference from different cells can be expunged [15–18].

To enhance the coverage of a wireless network, a large number of distributed APs need to be deployed. However,

limited by their deployment cost and energy consumption, high-density deployment of APs is impractical. Based on the above analysis, an IRS can be deployed in a CF massive MIMO network to enhance the communication quality. The deployed IRS can replace some APs in providing services for users. Due to its low cost and flexible deployment characteristics, the IRS can enhance the coverage of the CF massive MIMO system while reducing its deployment cost. However, due to the complex distribution of urban buildings, the deployment of an IRS (which is usually located on a wall or roof) depends on the buildings that are present in the area. Some of the best IRS deployment locations may not be suitable in practice due to topographical or architectural constraints. Therefore, to overcome the terrain limitations of traditional ground IRS deployment and make full use of air-ground resources, an aerial IRS (AIRS) was proposed as a new IRS architecture in [19, 20]. An AIRS is usually installed on a launch platform (a launch balloon or unmanned aerial vehicle, UAV) to establish a strong line-of-sight (LoS) connection. The AIRS location can then be adjusted in accordance with current service needs, in line with the user-centred principle.

In 6G communication, a large number of intelligent devices will not only provide convenience for our life but also constitute a huge wireless sensor network (WSN). The WSN requires higher transmission rate. To solve this problem, we can use the IRS to increase coverage, improve spectrum efficiency, and reduce the deployment cost of wireless networks.

Motivations and Contributions. The current research on IRSs has mainly focused on traditional cellular networks, including IRS-assisted multiple-input single-output (MISO) communication [13, 21, 22], MIMO communication [23], and multicell interference cancellation scenarios [24]. There have been only a few studies on the application of IRSs in CF massive MIMO networks, mainly focusing on the rate optimization problem [25–28], while the problem of power minimization has not been addressed. In [13, 22], the problem of power optimization for single-IRS-assisted single-cell communication was studied. However, power optimization for an IRS-aided CF massive MIMO network has not yet been investigated. In addition, the existing research mainly focuses on the single-IRS case. There are a few studies that consider the multi-IRS case. For the multi-IRS case, the IRS deployment strategy is important in enhancing the communication quality. However, few studies consider the IRS deployment strategy. Moreover, the power optimization problem in the IRS-aided WSN system has not been considered yet. Therefore, in this study, we consider the AIRS-enhanced CF massive MIMO WSN system. The main contributions are summarized as follows:

(1) In this paper, we first consider the power optimization problem for the AIRS-aided CF massive MIMO-based WSN system. Several APs serve several sensor users (SUs) with the assistance of an AIRS. This paper aims to minimize the total transmit power

of all APs under a signal-to-interference-plus-noise ratio (SINR) requirement.

(2) We propose a joint optimization algorithm to optimize the total transmission power for the single-AIRS case. Then, we extend to power optimization for the multi-AIRS case. The simulation results show the good performance of our proposed method in power savings.

(3) Moreover, we discuss the AIRS deployment strategy. Compared with centralized AIRS deployment, distributed AIRS deployment shows better performance, providing some guidelines for AIRS deployment.

1.1. Methods. Based on the idea of alternating iterations commonly used in IRS-assisted transmission optimization, we jointly optimize the beamforming vectors and AIRS reflection coefficients to solve the transmission power optimization problem. Specifically, the optimization problem is divided into two subproblems: fixing the AIRS reflection coefficients to optimize the beamforming vectors and fixing the beamforming vectors to optimize the AIRS reflection coefficients. We can obtain an optimal solution by iteratively optimizing the above two subproblems. The transmission power can be effectively reduced by using the proposed method.

1.2. Organization. In Section 2, we introduce and analyze the system model and formulate the power optimization problem. We use the Ricean channel model to characterize the air-to-ground channels. In Section 3, we introduce our proposed optimization strategy and analyze it in detail. In Section 4, we present a numerical simulation performed to verify the performance of the proposed method. Finally, in Section 5, we summarize this paper, analyze the deficiencies of this work, and then identify future research directions.

1.3. Notations. We use italic letters for constants (B) and bold lowercase letters to denote vectors ($\mathbf{p}$). Matrices are represented by bold capital letters. The argument of a complex number B is denoted by $\arg(B)$. For a vector $\mathbf{p}$, we use $\arg(\mathbf{p})$ to express its corresponding argument vector, and $\text{diag}(\mathbf{p})$ denotes a diagonal matrix whose diagonal elements are the elements in $\mathbf{p}$. $\mathbf{A}^H$ denotes the conjugate transpose of a matrix $\mathbf{A}$, and $\mathbf{A}^T$ is the transpose of a matrix $\mathbf{A}$. $\otimes$ is the Kronecker product.

2. System Model and Problem Formulation

As shown in Figure 1, in the considered CF massive MIMO-based WSN system, L multiantenna APs serve K single-antenna SUs. Tall buildings block direct links between the APs and SUs. An AIRS is deployed to enhance the quality of service (QoS) of the SUs. Suppose that each AP has the form of a uniform linear array (ULA), while the AIRS has the form of an $N_x \times N_y$ uniform plane array. Each AP has M
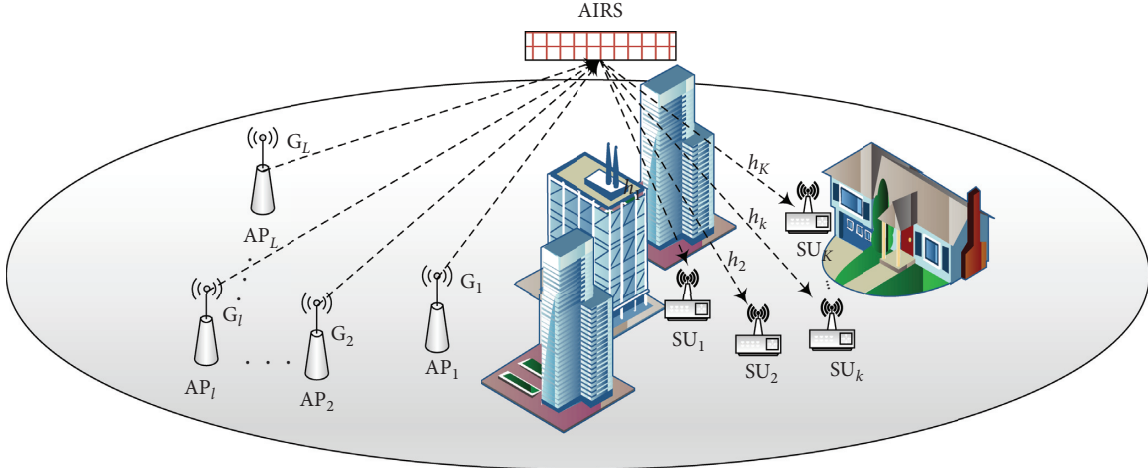
FIGURE 1: System model.

antennas. The AIRS consists of $N = N_x \times N_y$ elements, with half-wavelength spacing of the antennas/elements. Similar to [13, 22, 29–33], we characterize the channel from the l-th AP to the AIRS $\mathbf{G}_l \in \mathbb{C}^{N \times M}$ as follows:

$$\mathbf{G}_l = \sqrt{\beta_{\mathbf{G}_l}}\left(\sqrt{\frac{\kappa}{\kappa+1}}\, \psi_N(\theta_i, \varphi_i)\varsigma_M^H(\theta_i) + \sqrt{\frac{1}{\kappa+1}}\, \widetilde{\mathbf{G}}_l \right), \quad (1)$$

where $\widetilde{\mathbf{G}}_l$ denotes the non-line-of-sight (NLoS) component, whose elements are chosen from $\mathscr{CN}(0,1)$. $\beta_{\mathbf{G}_l}$ is the path loss. Here, we define $\beta_{\mathbf{G}_l}$ as

$$\beta_{\mathbf{G}_l} = \frac{a_0}{d_{\mathbf{G}_l}^2}, \quad (2)$$

where a_0 is the path loss at a reference distance of 1 m and $d_{\mathbf{G}_l}$ is the distance between the l-th AP and the AIRS. $\psi_N(\theta_i, \varphi_i)$ and $\varsigma_M(\theta_i)$ are string vectors that can be expressed as

$$\psi_N(\theta_i, \varphi_i) = \left[1, e^{-j\pi\tau \sin(\theta_i)\sin(\varphi)}, \ldots, e^{-j\pi\tau(N_x-1)\sin(\theta_i)\sin(\varphi_i)}\right]^T \otimes \left[1, e^{-j\pi\tau \sin(\theta_i)\cos(\varphi_i)}, \ldots, e^{-j\pi\tau(N_y-1)\sin(\theta_i)\cos(\varphi_i)}\right]^T. \quad (3)$$

And

$$\varsigma_M(\theta_i) = \left[1, e^{j\pi\tau \cos(\theta_i)}, \ldots, e^{j\pi\tau(M-1)\cos(\theta_i)}\right]^T. \quad (4)$$

When $\kappa = 0$, the above model reduces to the Rayleigh fading channel model. An AIRS is usually deployed at a high altitude. From an elevated position, the AIRS can more easily establish LoS links with the ground nodes, which leads to LoS-dominated channel conditions [19, 20, 34, 35]. Similarly, the channel from the AIRS to the k-th SU can be modeled as

$$\mathbf{h}_k = \sqrt{\beta_{\mathbf{h}_k}}\left(\sqrt{\frac{\kappa}{\kappa+1}}\, \psi_N(\alpha_k, \eta_k) + \sqrt{\frac{1}{\kappa+1}}\, \widetilde{\mathbf{h}}_k \right). \quad (5)$$

$\mathbf{h}_k \in \mathbb{C}^{1 \times N}$. The corresponding symbols are defined similarly to the case of $\mathbf{G}_l$.

All APs serve SUs simultaneously. The received signal at the k-th SU can be expressed as

$$
\begin{aligned}
y_k &= \sum_{l=1}^{L} \mathbf{c}_{lk}\mathbf{x}_l + \omega_k \\
&= \sum_{l=1}^{L} \mathbf{c}_{lk} \sum_{i=1}^{K} \mathbf{w}_{li}s_i + \omega_k \\
&= \sum_{l=1}^{L} \mathbf{c}_{lk}\mathbf{w}_{lk}s_k + \sum_{l=1}^{L} \mathbf{c}_{lk} \sum_{i \neq k}^{K} \mathbf{w}_{li}s_i + \omega_k,
\end{aligned}
\quad (6)
$$

where $\mathbf{x}_l$ denotes the transmit signal of the l-th AP, and $\mathbf{x}_l = \sum_{i=1}^{K} \mathbf{w}_{li}s_i$; $\mathbf{w}_{lk}$ is the beamforming vector at the l-th AP to the k-th SU; s_k is the information symbol sent to the k-th SU; ω_k is the additive white Gaussian noise (AWGN) at the k-th SU, and $\omega_k \sim \mathscr{CN}(0, \sigma^2)$; and $\mathbf{c}_{lk} \in \mathbb{C}^{1 \times M}$ is the AIRS-

reflected channel between the l-th AP and the k-th SU, which can be expressed as

$$
\begin{aligned}
\mathbf{c}_{li} &= \mathbf{h}_i \mathbf{\Phi} \mathbf{G}_l \\
&= \mathbf{v}^H \mathrm{diag}(\mathbf{h}_i) \mathbf{G}_l \\
&= \mathbf{v}^H \mathbf{U}_{li},
\end{aligned} \tag{7}
$$

where $\mathbf{\Phi} = \mathrm{diag}(e^{j\omega_1}, e^{j\omega_2}, \ldots, e^{j\omega_N}) \in \mathbb{C}^{N \times N}$ is the reflection coefficient matrix of the AIRS, $\omega_n \in [0, 2\pi)$ is the reflection coefficient of the n-th element, and $\mathbf{v} = [e^{j\omega_1}, e^{j\omega_2}, \ldots, e^{j\omega_N}]^H$. The SINR of the k-th SU can be expressed as

$$
\mathrm{SINR}_k = \frac{\left| \sum_{l=1}^{L} \mathbf{c}_{lk} \mathbf{w}_{lk} \right|^2}{\sum_{i \neq k}^{K} \left| \sum_{l=1}^{L} \mathbf{c}_{li} \mathbf{w}_{li} \right|^2 + \sigma^2}. \tag{8}
$$

In this paper, we aim to minimize the transmission power P of all APs, $P = \sum_{l=1}^{L} \sum_{i=1}^{K} \|\mathbf{w}_{li}\|^2$. Thus, the problem to be optimized is constructed as follows:

$P1$:

$$
\min_{\mathbf{v}, \mathbf{w}_{li}} \sum_{l=1}^{L} \sum_{i=1}^{K} \|\mathbf{w}_{li}\|^2, \tag{9}
$$

$$
\text{s.t. } \mathrm{SINR}_k \geq \gamma_k, \quad k = 1, 2, \ldots, K,
$$

$$
\omega_n \in [0, 2\pi), \quad n = 1, 2, \ldots, N.
$$

3. Joint Beamforming and Reflection Design

To solve $(P1)$, we need to design the beamforming mechanism at each AP and the AIRS reflection coefficients. As we can see from (7) and (9), all channels $\mathbf{c}_{lk}$ ($l = 1, \ldots, L$, $k = 1, \ldots, K$) vary with $\mathbf{\Phi}$. If we modify the AIRS reflection coefficients, the corresponding beamforming design for the APs will also change. Therefore, it is difficult to solve $(P1)$. Inspired by the traditional idea of alternating iterations in IRS-aided communication [22, 33], we propose a joint optimization strategy to solve this problem. That is, first, for fixed $\mathbf{\Phi}$, we optimize the beamforming at the APs, and then, for fixed beamforming design at the APs, that is, $\mathbf{w}_{li}$, we optimize the passive beamforming at the AIRS. The above steps are alternatively performed until convergence.

3.1. Beamforming Design for the APs.
Note that when the AIRS reflection coefficients $\mathbf{\Phi}$ are fixed, we need only to optimize $\mathbf{w}_{li}$ to minimize P. Then, $(P1)$ can be simplified as follows:

$P2$:

$$
\min_{\mathbf{w}_{li}} \sum_{l=1}^{L} \sum_{i=1}^{K} \|\mathbf{w}_{li}\|^2, \tag{10}
$$

$$
\text{s.t. } \mathrm{SINR}_k \geq \gamma_k, \quad k = 1, 2, \ldots, K.
$$

In accordance with (8), we define $\mathbf{c}_k = [\mathbf{c}_{1k}, \mathbf{c}_{2k}, \ldots, \mathbf{c}_{Lk}]$ and $\mathbf{w}_k = [\mathbf{w}_{1k} \ \mathbf{w}_{2k} \ \ldots \ \mathbf{w}_{Lk}]^T$. $\mathbf{c}_k \in \mathbb{C}^{1 \times ML}$ is the reflected channel vector of the k-th SU, and $\mathbf{w}_k \in \mathbb{C}^{ML \times 1}$ is the

beamforming vector for the k-th SU. Thus, we have $\sum_{l=1}^{L} \mathbf{c}_{li} \mathbf{w}_{lj} = \mathbf{c}_i \mathbf{w}_j$. Therefore, $(P2)$ can be converted into

$P3$:

$$
\min_{\mathbf{w}_i} \sum_{i=1}^{K} \|\mathbf{w}_i\|^2, \tag{11}
$$

$$
\text{s.t. } \frac{|\mathbf{c}_k \mathbf{w}_k|^2}{\sum_{i \neq k}^{K} |\mathbf{c}_k \mathbf{w}_i|^2 + \sigma^2} \geq \gamma_0, \quad k = 1, 2, \ldots, K.
$$

From (11), we can find that $(P3)$ is a convex problem when $\mathbf{\Phi}$ is fixed. We can use a semidefinite programming- (SDP-) based method to solve this problem. Note that

$$
\begin{aligned}
|\mathbf{c}_k \mathbf{w}_k|^2 &= \mathbf{c}_k \mathbf{w}_k (\mathbf{c}_k \mathbf{w}_k)^H \\
&= \mathrm{Tr}(\mathbf{c}_k \mathbf{c}_k^H \mathbf{w}_k \mathbf{w}_k^H) \\
&= \mathrm{Tr}(\mathbf{C}_k \mathbf{W}_k),
\end{aligned} \tag{12}
$$

where $\mathbf{C}_k = \mathbf{c}_k \mathbf{c}_k^H$ and $\mathbf{W}_k = \mathbf{w}_k \mathbf{w}_k^H$. Then, $(P3)$ can be considered to be equivalent to

$P4$:

$$
\min_{\mathbf{w}_{li}} \sum_{i=1}^{K} \mathrm{tr}(\mathbf{W}_i),
$$

$$
\text{s.t. } \mathrm{tr}(\mathbf{C}_k \mathbf{W}_k) \geq \gamma_0 \left(\sum_{i \neq k}^{K} \mathrm{tr}(\mathbf{C}_k \mathbf{W}_i) + \sigma^2 \right), \quad k = 1, 2, \ldots, K,
$$

$$
\mathbf{W}_k \succeq 0, \quad k = 1, 2, \ldots, K. \tag{13}
$$

$(P4)$ is an SDP problem, and $\mathbf{W}_k$ can be solved by using a convex optimizer such as CVX [36]. Similar to [37], $\mathbf{W}_k$ satisfies the rank-one property, and the optimal beamforming design $\mathbf{w}_k^{\mathrm{opt}}$ can be obtained via the rank-one decomposition (eigenvalue decomposition) of $\mathbf{W}_k$.

3.2. Reflection Design of the AIRS.
When the beamforming design is determined, we can optimize $\mathbf{\Phi}$ to further reduce the total transmission power. When the beamforming vectors $\mathbf{w}_k$ ($k = 1, \ldots, K$) are fixed, the objective function can be rewritten as follows:

$P5$: $\lim_{x \to \infty}$

$$
\max_{\mathbf{\Phi}} \sum_{i=1}^{K} \|\mathbf{w}_{li}\|^2,
$$

$$
\text{s.t. } \frac{\left| \sum_{l=1}^{L} \mathbf{c}_{lk} \mathbf{w}_{lk} \right|^2}{\sum_{i \neq k}^{K} \left| \sum_{l=1}^{L} \mathbf{c}_{lk} \mathbf{w}_{li} \right|^2 + \sigma^2} \geq \gamma_0, \quad k = 1, 2, \ldots, K,
$$

$$
\omega_n \in [0, 2\pi), \quad n = 1, \ldots, N. \tag{14}
$$

According to (7), $\mathbf{c}_{li} = \mathbf{v}^H \mathbf{U}_{li}$, where $\mathbf{U}_{li} = \mathrm{diag}(\mathbf{h}_i)\mathbf{G}_l$. Then, the SINR constraint in (14) can be written as

$$\frac{\left|\sum_{l=1}^{L} \mathbf{v}^H \mathbf{U}_{lk}\mathbf{w}_{lk}\right|^2}{\sum_{i \neq k}^{K}\left|\sum_{l=1}^{L} \mathbf{v}^H \mathbf{U}_{lk}\mathbf{w}_{li}\right|^2 + \sigma^2} \geq \gamma_0. \tag{15}$$

Here, we define $\mathbf{U}_k = [\mathbf{U}_{1k}, \mathbf{U}_{2k}, \ldots, \mathbf{U}_{Lk}] \in \mathbb{C}^{N \times ML}$. Then, (15) can be written as

$$\frac{\left|\sum_{l=1}^{L} \mathbf{v}^H \mathbf{U}_k \mathbf{w}_k\right|^2}{\sum_{i \neq k}^{K}\left|\sum_{l=1}^{L} \mathbf{v}^H \mathbf{U}_k \mathbf{w}_i\right|^2 + \sigma^2} \geq \gamma_0. \tag{16}$$

(P5) can be expressed as

P6:

$$\max_{\mathbf{v}} \quad \sum_{k=1}^{K} \|\mathbf{w}_k\|^2,$$

$$\text{s.t.} \quad \frac{\left|\mathbf{v}^H \mathbf{U}_k \mathbf{w}_k\right|^2}{\sum_{i \neq k}^{K}\left|\mathbf{v}^H \mathbf{U}_k \mathbf{w}_i\right|^2 + \sigma^2} \geq \gamma_0, \quad k = 1, 2, \ldots, K,$$

$$\omega_n \in [0, 2\pi), \quad n = 1, \ldots, N. \tag{17}$$

Note that (P6) is not a convex problem with a unit-modulus constraint $\omega_n \in [0, 2\pi)$, $n = 1, \ldots, N$. Moreover, the objective function does not contain $\mathbf{v}$. To solve (P6), we can only find a vector $\mathbf{v}$ to satisfy the constraints in (17). Therefore, it is difficult to solve (P6). Instead, we will rewrite (P6) as an equivalent optimization problem and relax (P6) into an SDP problem to obtain an optimal solution.

When the beamforming vectors are obtained, the current setting of $\mathbf{v}$ already satisfies the SINR constraint condition. In other words, the SINR of each SU satisfies $\mathrm{SINR}_k \geq \gamma_0$. To reduce the total transmission power, we need to find a vector $\mathbf{v}^*$ such that the new SINR constraints calculated with $\mathbf{v}^*$ satisfy the following conditions:

$$\mathrm{SINR}_k^* \geq \gamma_0^*, \quad k = 1, 2, \ldots, K,$$
$$\gamma_0^* \geq \gamma_0. \tag{18}$$

$\mathbf{v}^*$ leads to a higher SINR threshold value of γ_0^*. Thus, the transmission power can be reduced. From (17), we can find that, for the k-th SU, $\left|\mathbf{v}^H \mathbf{U}_k \mathbf{w}_k\right|^2$ is the useful component, while $\sum_{i \neq k}^{K}\left|\mathbf{v}^H \mathbf{U}_k \mathbf{w}_i\right| + \sigma^2$ is the interference-plus-noise component. Define the SINR margin of the k-th SU as χ_k, which can be expressed as

$$\chi_k = \left|\mathbf{v}^H \mathbf{U}_k \mathbf{w}_k\right|^2 - \gamma_0 \left(\sum_{i \neq k}^{K}\left|\mathbf{v}^H \mathbf{U}_k \mathbf{w}_i\right|^2 + \sigma^2\right), \quad k = 1, \ldots, K. \tag{19}$$

As discussed earlier, when the beamforming vectors are obtained, the current setting already satisfies the SINR

constraint condition in (17). Therefore, χ_k satisfies the following constraint condition:

$$\chi_k \geq \chi_0, \quad k = 1, \ldots, K, \tag{20}$$

where χ_0 is a constant that is greater than zero. χ_0 denotes the base lower bound of χ_k, $k = 1, \ldots, K$. If the base lower bound χ_0 is increased, it is easy to know that higher γ_0 can be obtained and the SINR constraints in (20) are satisfied. Therefore, to satisfy the conditions in (20), we need to maximize χ_0.

Based on the above analysis, we rewrite (P6) as

P7.1:

$$\max_{\mathbf{v}} \min \quad \chi_k,$$

$$\text{s.t.} \quad \chi_k = \left|\mathbf{v}^H \mathbf{U}_k \mathbf{w}_k\right|^2 - \gamma_0\left(\sum_{i \neq k}^{K}\left|\mathbf{v}^H \mathbf{U}_k \mathbf{w}_i\right|^2 + \sigma^2\right); \tag{21}$$

$$\chi_k \geq 0, \quad k = 1, \ldots, K,$$

$$\omega_n \in [0, 2\pi), \quad n = 1, \ldots, N.$$

Then, we use the SDP-based method to relax (P7.1) into an SDP problem. We have the following equations:

$$\left|\mathbf{v}^H \mathbf{U}_k \mathbf{w}_k\right|^2$$
$$= \mathbf{v}^H \mathbf{U}_k \mathbf{w}_k \times \left(\mathbf{v}^H \mathbf{U}_k \mathbf{w}_k\right)^H$$
$$= \mathbf{v}^H \mathbf{U}_k \mathbf{w}_k \mathbf{w}_k^H \mathbf{U}_k^H \mathbf{v} \tag{22}$$
$$= \mathbf{v}^H \mathbf{Q}_{k,k} \mathbf{v}$$
$$= \mathrm{tr}\left(\mathbf{Q}_{k,k} \mathbf{V}\right),$$

where $\mathbf{Q}_{k,k} = \mathbf{U}_k \mathbf{w}_k \mathbf{w}_k^H \mathbf{U}_k^H$ is a determined matrix and $\mathbf{V} = \mathbf{v}\mathbf{v}^H$. Then, we can rewrite (P7.1) as

P7.2:

$$\max_{\mathbf{V}} \min \quad \chi_k,$$

$$\text{s.t.} \quad \chi_k = \mathrm{tr}\left(\mathbf{Q}_{k,k}\mathbf{V}\right) - \gamma_0\left(\sum_{i=1, i \neq k}^{K} \mathrm{tr}\left(\mathbf{Q}_{k,k}\mathbf{V}\right) + \sigma^2\right);$$

$$\chi_k \geq 0, \quad k = 1, \ldots, K;$$

$$\mathbf{V} \succcurlyeq 0;$$

$$\mathrm{diag}(\mathbf{V}) = [1, 1, 1, \ldots, 1.] \tag{23}$$

(P7.2) is an SDP problem that can be solved using a convex optimization tool such as CVX.

By solving (P7.2), we can obtain an optimal solution for $\mathbf{V}$. However, $\mathbf{V}$ cannot be guaranteed to be of rank one. If $\mathbf{V}$ is of rank one, we can use eigenvalue decomposition to obtain optimal $\mathbf{v}$. When $\mathbf{V}$ is not of rank one, an approximate optimal solution can be obtained using the Gauss randomization method presented in [38].

3.3. Algorithm Implementation. The main steps of the optimization process are as follows:

(1) First, we randomly set the AIRS reflection coefficient vector $\mathbf{v}_0$ and use $\mathbf{v}_0$ to optimize the beamforming vectors.

(2) Then, we use the optimized beamforming vectors to update the AIRS reflection coefficient vector $\mathbf{v}$.

(3) We use the new AIRS reflection coefficient vector $\mathbf{v}$ to update the beamforming vectors at each AP. This iterative process is repeated until the total transmission power converges.

The specific steps are given in Algorithm 1.

3.4. Extension to the Multi-AIRS Case. Now, we will extend the optimization process to the multi-AIRS case. Let there be T AIRSs assisting the communication between L APs and K SUs. The channel from the l-th AP to the t-th AIRS is represented by $\mathbf{G}_{lt}$. The channel from the t-th AIRS to the k-th SU is represented by $\mathbf{h}_{tk}$. $\mathbf{G}_{lt}$ and $\mathbf{h}_{tk}$ are defined according to (4) and (5), respectively. The reflection coefficient matrix of the t-th AIRS is $\mathbf{\Phi}_t$ ($t = 1, 2, \ldots, T$). The channel from the l-th AP to the k-th SU reflected by the t-th AIRS can be expressed as

$$
\begin{aligned}
\mathbf{c}_{l,t,k} &= \mathbf{h}_{tk}\mathbf{\Phi}_t\mathbf{G}_{lt} \\
&= \mathbf{v}_t^H \mathrm{diag}(\mathbf{h}_{tk})\mathbf{G}_{lt}.
\end{aligned}
\tag{24}
$$

The joint channel matrix from the l-th AP to the k-th SU can be expressed as

$$
\begin{aligned}
y_k &= \sum_{l=1}^{L}\sum_{t=1}^{T}\mathbf{c}_{l,t,k}\sum_{i=1}^{k}\mathbf{w}_{li}s_i \\
&= \sum_{l=1}^{L}\sum_{t=1}^{T}\mathbf{v}_t^H\mathrm{diag}(\mathbf{h}_{tk})\mathbf{G}_{lt}\sum_{i=1}^{k}\mathbf{w}_{li}s_i \\
&= \sum_{l=1}^{L}\widetilde{\mathbf{v}}^H\mathrm{diag}(\widetilde{\mathbf{h}}_k)\widetilde{\mathbf{G}}_l\sum_{i=1}^{k}\mathbf{w}_{li}s_i \\
&= \sum_{l=1}^{L}\widetilde{\mathbf{c}}_{lk}\sum_{i=1}^{k}\mathbf{w}_{li}s_i,
\end{aligned}
\tag{25}
$$

where $\widetilde{\mathbf{c}}_{lk} = \widetilde{\mathbf{v}}^H\mathrm{diag}(\widetilde{\mathbf{h}}_k)\widetilde{G}_l$, $\widetilde{\mathbf{v}}^H = [\mathbf{v}_1^H, \mathbf{v}_2^H, \ldots, \mathbf{v}_T^H] \in \mathbb{C}^{1 \times NT}$, $\widetilde{\mathbf{h}}_k = [\mathbf{h}_{1k}, \mathbf{h}_{2k}, \ldots, \mathbf{h}_{Tk}] \in \mathbb{C}^{NT \times 1}$, and $\widetilde{\mathbf{G}}_l = [\mathbf{G}_{l1}, \mathbf{G}_{l2}, \ldots, \mathbf{G}_{lT}]^T \in \mathbb{C}^{NT \times LM}$.

The SINR expression is similar to (8), and the objective function is similar to (9). By replacing $\mathbf{c}_{lk}$ with $\widetilde{\mathbf{c}}_{lk}$, we can use the proposed Algorithm 1 to solve this problem as well.

4. Simulation Results

In this section, we present a numerical simulation of an actual communication scenario conducted to study the performance of the proposed algorithm. First, we analyse the performance of the single-AIRS case. Then, we extend to the Multi-AIRS case, and we mainly focus on the performance comparison for AIRS deployment.

4.1. Single-AIRS Case. As shown in Figure 2, three APs serve four SUs with the assistance of an AIRS. The AIRS is deployed at a fixed point (0, 75, 40). All the APs and SUs are in the *x-o-y* plane. The parameter settings are detailed in Table 1.

In Figure 3, we compare the performance under three different strategies:

(1) Beamforming optimization with random reflection design: In this setting, we randomly set the AIRS reflection coefficients and optimize the beamforming vectors $\mathbf{w}_k$ ($k = 1, 2, \ldots, K$).

(2) Zero forcing (ZF) beamforming with random reflection design: In this setting, we use the ZF beamforming strategy to set the beamforming vectors $\mathbf{w}_k$ ($k = 1, 2, \ldots, K$). In this system, we randomly set the AIRS reflection coefficients and then use the global channel to design the ZF beamforming vectors. The global channel is denoted by $\mathbf{C} \in \mathbb{C}^{K \times ML}$ and is expressed as follows:

$$
\begin{aligned}
\mathbf{C} &= \begin{bmatrix} \mathbf{c}_{11} & \mathbf{c}_{21} & \cdots & \mathbf{c}_{L1} \\ \mathbf{c}_{12} & \mathbf{c}_{22} & \cdots & \mathbf{c}_{L2} \\ \vdots & \vdots & \vdots & \vdots \\ \mathbf{c}_{1K} & \mathbf{c}_{2K} & \cdots & \mathbf{c}_{LK} \end{bmatrix} \\
&= \begin{bmatrix} \mathbf{c}_1 \\ \mathbf{c}_2 \\ \vdots \\ \mathbf{c}_K \end{bmatrix}.
\end{aligned}
\tag{26}
$$

The pseudoinverse of $\mathbf{C}$ is

$$
\begin{aligned}
\overline{\mathbf{C}} &= \mathbf{C}^H\left(\mathbf{CC}^H\right)^{-1} \\
&= [\overline{\mathbf{c}}_1, \overline{\mathbf{c}}_2, \ldots, \overline{\mathbf{c}}_K].
\end{aligned}
\tag{27}
$$

We set the beamforming vectors as follows:

$$
\mathbf{w}_k = \sqrt{p_k}\,\frac{\overline{c}_k}{\|\overline{c}_k\|_2}.
\tag{28}
$$

Then, we calculate the minimum transmit power P that satisfies the SINR constraint. P is defined as

$$
P = p_1 + p_2, \ldots, + p_k.
\tag{29}
$$

(3) ZF beamforming with exhaustion-based AIRS reflection design: In this setting, we randomly set $\mathbf{v}$ and use the ZF beamforming method 1000 times. We choose the best performance of 1000 experiments as the output.

(4) ZF beamforming with the channel gain maximization-based AIRS reflection design: In this setting, we use ZF beamforming and a channel energy maximization-based AIRS phase optimization method to design the AIRS reflection coefficient. The main consideration is that after ZF beamforming, the interference between SUs has been eliminated. One

(1) Initialize the AIRS reflection coefficient vector $\mathbf{v}_0$.
(2) Update the beamforming vectors $\mathbf{w}_k$ by solving ($P4$) and calculate the total transmission power.
(3) Use the updated beamforming vectors $\mathbf{w}_k$ to obtain $\mathbf{V}$ by solving ($P7.2$).
(4) If $\mathbf{V}$ is of rank one Obtain the optimal $\mathbf{v}$ via rank-one decomposition. Else Obtain the optimal $\mathbf{v}$ via Gauss randomization. End
(5) Repeat steps 2–4. If the absolute value of the difference of transmission power between the n-th and the $(n-1)$-th iterations is less than 0.0001, the convergence is achieved. Then output the current $\mathbf{w}_k$ and $\mathbf{v}$.
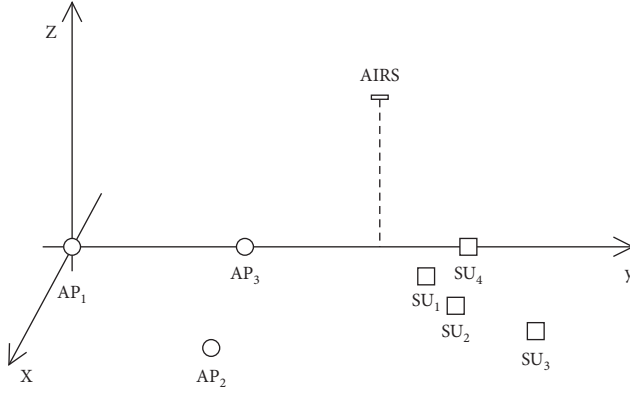
ALGORITHM 1: Joint optimization algorithm.

FIGURE 2: Simulation scenario of the single-AIRS case.

Proposed method
ZF beamforming with the channel gain maximization-based AIRS reflection design
Beamforming optimization with random reflection design
ZF beamforming with exhaustion-based AIRS reflection design
ZF beamforming with random reflection design

FIGURE 3: Performance comparison.

TABLE 1: Simulation settings.

Parameter	Value
Bandwidth	1 MHz
Number of antennas at each AP, M	20
Number of AIRS elements, N	30
Noise power	−110 dBm
Rice factor, κ	10
Coordinates of AP_1 (m)	(0, 0, 0)
Coordinates of AP_2 (m)	(0, 50, 0)
Coordinates of AP_3 (m)	(50, 50, 0)
Coordinates of AIRS (m)	(0, 90, 40)
Coordinates of SU_1 (m)	(0, 100, 0)
Coordinates of SU_2 (m)	(10, 95, 0)
Coordinates of SU_3 (m)	(20, 100, 0)
Coordinates of SU_4 (m)	(−10, 100, 0)
Antenna or element spacing, d	0.5λ

method is to maximize the total channel gain so that the beamforming gain is optimal.

First, we optimize the AIRS reflection vector $\mathbf{v}$ by the channel gain maximization-based method. Then we use $\mathbf{v}$ to design the ZF beamforming. The total channel gain is given as:

$$
\begin{aligned}
C &= \sum_{k=1}^{K} \left\| \mathbf{c}_k \right\|^2 \\
&= \sum_{k=1}^{K} \mathbf{c}_k \mathbf{c}_k^H \\
&= \sum_{k=1}^{K} \sum_{l=1}^{L} \mathbf{v}^H \mathbf{U}_{lk} \mathbf{U}_{lk}^H \mathbf{v} \\
&= \sum_{k=1}^{K} \sum_{l=1}^{L} \mathrm{tr} \left(\tilde{\mathbf{U}}_{lk} \mathbf{V} \right),
\end{aligned}
\tag{30}
$$

where $\tilde{\mathbf{U}}_{lk} = \mathbf{U}_{lk} \mathbf{U}_{lk}^H$. The objective function for optimizing $\mathbf{v}$ is formulated as follows:

FIGURE 4: Convergence analysis.

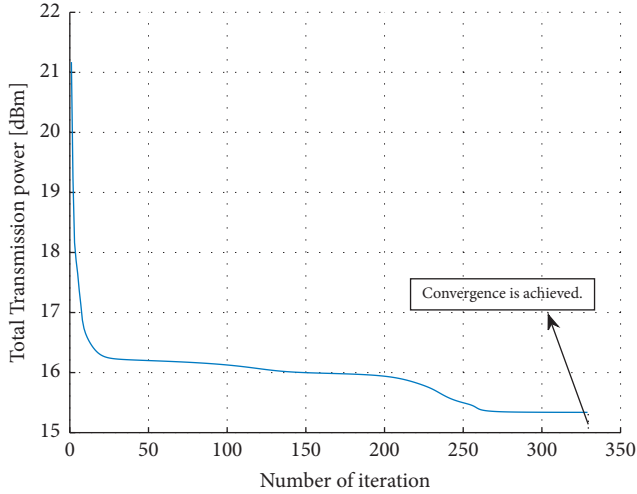$$\max_{\mathbf{V}} \sum_{k=1}^{K} \sum_{l=1}^{L} \mathrm{tr}\left(\tilde{\mathbf{U}}_{lk}\mathbf{V}\right),$$

$$\mathrm{s.t.}\,\mathbf{V} \succcurlyeq 0; \tag{31}$$

$$\mathrm{diag}\left(\mathbf{V}\right) = [1, 1, 1, \ldots, 1.]$$

Here, we use a similar approach to [22, 39] to solve this problem. Then the optimal $\mathbf{v}$ can be obtained. For brevity, the specific details have been omitted.

(5) Proposed method: In this setting, we use the proposed method to optimize both the beamforming vectors and the AIRS reflection coefficients.

As shown in Figure 3, By optimizing the AIRS reflection coefficients, the total transmission power can be effectively reduced. Overall, the proposed method shows better performance in saving the total transmission power.

In Figure 4, we analyze the convergence of the proposed algorithm. We set the target SINR to 10 dB, while the other parameters are set as before. If the absolute value of the difference of transmission power between the n-th and the $(n-1)$-th iterations is less than 0.0001, convergence is achieved. As seen from Figure 4, through iteration, the total transmission power is significantly reduced and finally converges to a value. The proposed method has strict convergence.

In Figure 5, we study the impact of the AIRS scale on the algorithm performance. We set the number of AIRS elements N to 10, 20, 30, 40, 50, and 60, and the target SINR is set to 10 dB. Figure 5 shows that as the number of AIRS elements increases, the total transmission power decreases if both the beamforming and AIRS reflection are optimized, indicating that more AIRS elements can be deployed to further reduce the transmission power with the proposed method.

4.2. Multi-AIRS Case.
Then, we study the multi-AIRS case. We mainly analyze the impact of the AIRS deployment

— Proposed method
--- Beamforming optimization with random reflection
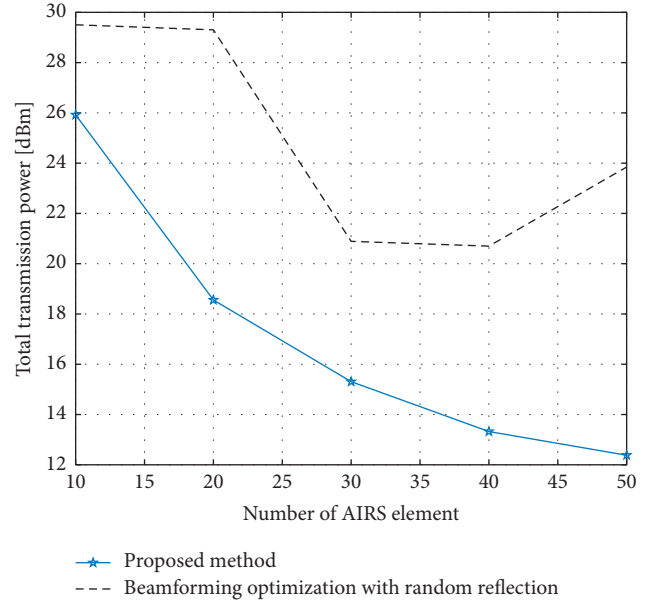
FIGURE 5: Impact of the number of AIRS elements.
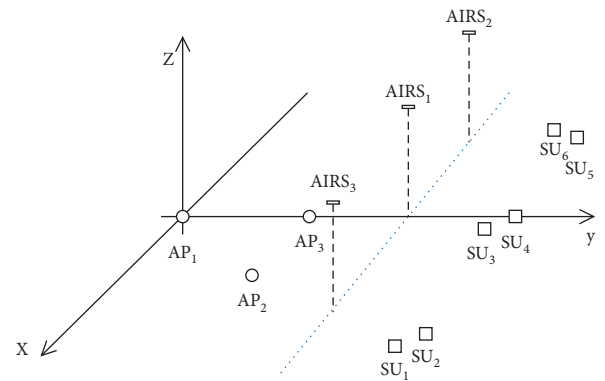
FIGURE 6: Simulation scene of multi-AIRS case.

strategy on performance. Assume that there are six SUs. As shown in Figure 6, the SUs are distributed in three communities. We aim to compare the performance of centralized and distributed AIRS deployment.

For centralized AIRS deployment, we use one AIRS to assist communication. The number of AIRS elements is set as 30. The AIRS is deployed at $(0, 90, 40)$. For distributed AIRS deployment, we use three AIRSs to assist communication. To be fair, the number of elements of each AIRS is set as 10. The AIRSs are deployed at $(0, 90, 40)$, $(60, 90, 40)$, and $(-60, 90, 40)$. The coordinates are detailed in Table 2. The other settings are the same as the single-AIRS case.

As we can see from Figure 7, the distributed AIRS deployment shows a better performance in reducing the total transmission power. One reasonable explanation is that distributed AIRS deployment can provide more flexible deployment according to the location of the SUs so that the AIRS can be deployed closer to the SUs to better assist communication. Another reason is that distributed AIRS

TABLE 2: Coordinate settings.

Parameter	Value
Coordinates of AP_1 (m)	(0, 0, 0)
Coordinates of AP_2 (m)	(50, 50, 0)
Coordinates of AP_3 (m)	(0, 50, 0)
Coordinates of $AIRS_1$ (m)	(0, 90, 40)
Coordinates of $AIRS_2$ (m)	(−60, 90, 40)
Coordinates of $AIRS_3$ (m)	(60, 90, 40)
Coordinates of SU_1 (m)	(60, 100, 0)
Coordinates of SU_2 (m)	(60, 95, 0)
Coordinates of SU_3 (m)	(0, 105, 0)
Coordinates of SU_4 (m)	(5, 100, 0)
Coordinates of SU_5 (m)	(−60, 100, 0)
Coordinates of SU_6 (m)	(−60, 105, 0)

FIGURE 7: Impact of the AIRS deployment strategy.

deployment can provide a relatively rich scattering environment because the reflection is increased. The rich scattering environmen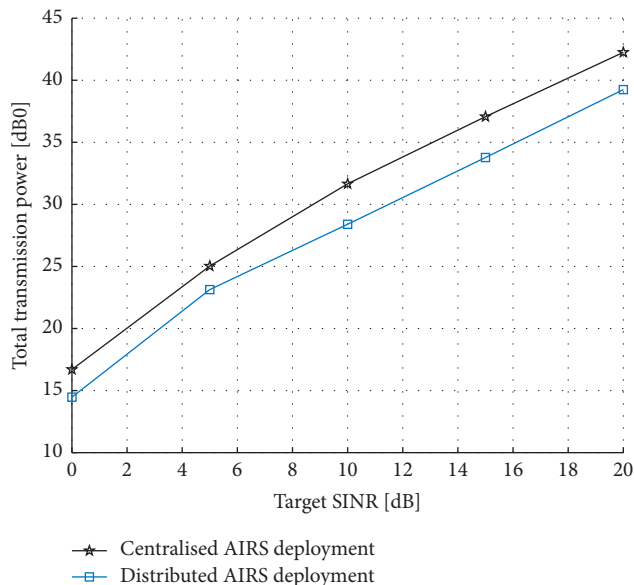t can reduce the correlation among the channels of different SUs; thus, the interference between different SUs can be suppressed.

5. Conclusion

In this paper, we study a power minimization problem in an AIRS-aided CF massive MIMO WSN system. We propose a joint optimization method to design the beamforming vectors and the AIRS reflection coefficients. Simulation results illustrate the good performance of the proposed method. This work deserves further study in the following aspects. In this paper, we simply assume that perfect channel state information (CSI) is obtained. However, channel estimation is challenging in this system. Therefore, in our future work, we will consider a suitable channel estimation method for this system. Moreover, AIRS deployment requires the location of SUs. AIRS-aided user positioning also deserves further study.

Data Availability

No data were used to support this study.

Conflicts of Interest

The authors declare that they have no conflicts of interest.

Acknowledgments

References

[1] S. Dang, O. Amin, B. Shihada, and M. Alouini, "What should 6G be?" *Nature Electronics*, vol. 3, no. 1, pp. 20–29, 2020.

[2] Z. Lv and N. Kumar, "Software defined solutions for sensors in 6G/IoE," *Computer Communications*, vol. 153, pp. 42–47, 2020.

[3] V. Ziegler, H. Viswanathan, H. Flinck, M. Hoffmann, V. Raisanen, and K. Hatonen, "6G architecture to connect the worlds," *IEEE Access*, vol. 8, Article ID 173508, 2020.

[4] S. Wan, J. Hu, C. Chen, A. Jolfaei, S. Mumtaz, and Q. Pei, "Fair-hierarchical scheduling for diversified services in space, air and ground for 6G-dense Internet of things," *IEEE Transactions on Network Science and Engineering*, 2020.

[5] Y. Pei, S. Miao, and F. Li, *Challenges and Opportunities for Terrestrial Network Operators in the Air-Space-Ground Integrated Network*, in *Proceedings of the 2020 IEEE Intl Conf on Parallel & Distributed Processing with Applications, Big Data & Cloud Computing, Sustainable Computing & Communications, Social Computing & Networking (ISPA/BDCloud/SocialCom/SustainCom)*, pp. 1400–1404, Exeter, United Kingdom, December 2020.

[6] H. Huang, S. Hu, T. Yang, and C. W. Yuan, "Full duplex non-orthogonal multiple access with layers-based optimized mobile relays subsets algorithm in B5G/6G ubiquitous networks," *IEEE Internet of Things Journal*, 2020.

[7] Q. Wu and R. Zhang, "Towards smart and reconfigurable environment: intelligent reflecting surface aided wireless network," *IEEE Communications Magazine*, vol. 58, no. 1, pp. 106–112, 2020.

[8] E. Basar, M. Di Renzo, J. De Rosny, M. Debbah, M.-S. Alouini, and R. Zhang, "Wireless communications through reconfigurable intelligent surfaces," *IEEE Access*, vol. 7, Article ID 116753, 2019.

[9] et al., "Smart radio environments empowered by reconfigurable AI meta-surfaces: an idea whose time has come," *EURASIP Journal on Wireless Communications and Networking*, vol. 2019, no. 1, 2019.

[10] M. Di Renzo, A. Zappone, M. Debbah et al., "Smart Radio Environmentsempowered by Reconfigurable Intelligent Surfaces: How it Works, State of Research, and Road ahead," 2020.

[11] et al., "Reconfigurable intelligent surfaces vs. Relaying: differences, similarities, and performance comparison," *IEEE Open Journal of the Communications Society*, vol. 1, pp. 798–807, 2020.

[12] S. Hu, F. Rusek, and O. Edfors, "Beyond massive MIMO: the potential of data transmission with large intelligent surfaces," *IEEE Transactions on Signal Processing*, vol. 66, no. 10, pp. 2746–2758, 2018.

[13] Q. Wu and R. Zhang, "Intelligent Reflecting Surface Enhanced Wireless Network: Joint Active and Passive Beamforming Design," in *Proceedings of the 2018 IEEE Global Communications Conference (GLOBECOM)*, pp. 1–6, Abu Dhabi, United Arab Emirates, December 2018.

[14] Q. Wu, S. Zhang, B. Zheng, C. You, and R. Zhang, "Intelligent reflecting surface-aided wireless communications: a tutorial," *IEEE Transactions on Communications*, vol. 69, no. 5, pp. 3313–3351, 2021.

[15] E. G. Larsson, O. Edfors, F. Tufvesson, and T. L. Marzetta, "Massive MIMO for next generation wireless systems," *IEEE Communications Magazine*, vol. 52, no. 2, pp. 186–195, 2014.

[16] J. G. Andrews, S. Buzzi, W. Choi et al., "What will 5G Be?" *IEEE Journal on Selected Areas in Communications*, vol. 32, no. 6, pp. 1065–1082, 2014.

[17] H. Q. Ngo, A. Ashikhmin, H. Yang, E. G. Larsson, and T. L. Marzetta, "Cell-free massive MIMO versus small cells," *IEEE Transactions on Wireless Communications*, vol. 16, no. 3, pp. 1834–1850, 2017.

[18] E. Nayebi, A. Ashikhmin, T. L. Marzetta, H. Yang, and B. D. Rao, "Precoding and power optimization in cell-free massive MIMO systems," *IEEE Transactions on Wireless Communications*, vol. 16, no. 7, 2017.

[19] H. Lu, Y. Zeng, S. Jin, and R. Zhang, "Enabling Panoramic Full-Angle Reflection via Aerial Intelligent Reflecting Surface," in *Proceedings of the 2020 IEEE International Conference On Communications Workshops (ICC Workshops)*, pp. 1–6, Dublin, Ireland, June 2020.

[20] H. Lu, Y. Zeng, S. Jin, and R. Zhang, "Aerial intelligent reflecting surface: joint placement and passive beamforming design with 3D beam flattening," *IEEE Transactions on Wireless Communications*, vol. 20, no. 7, pp. 4128–4143, 2021.

[21] X. Yu, D. Xu, and R. Schober, "Miso Wireless Communication Systems Via Intelligent Reflecting Surfaces: (Invited Paper)," in *Proceedings of the 2019 IEEE/CIC International Conference On Communications In China (ICCC)*, pp. 735–740, Changchun, China, August 2019.

[22] Q. Wu and R. Zhang, "Intelligent reflecting surface enhanced wireless network via joint active and passive beamforming," *IEEE Transactions on Wireless Communications*, vol. 18, no. 11, pp. 5394–5409, 2019.

[23] S. Zhang and R. Zhang, "Capacity characterization for intelligent reflecting surface aided MIMO communication," *IEEE Journal on Selected Areas in Communications*, vol. 38, no. 8, pp. 1823–1838, 2020.

[24] C. Pan, H. Ren, K. Wang et al., "Multicell MIMO communications relying on intelligent reflecting surfaces," *IEEE Transactions on Wireless Communications*, vol. 19, no. 8, pp. 5218–5233, 2020.

[25] Y. Zhang, B. Di, H. Zhang et al., "Beyond cell-free MIMO: energy efficient reconfigurable intelligent surface aided cell-free MIMO communications," *IEEE Transactions on Cognitive Communications and Networking*, vol. 7, no. 2, pp. 412–426, 2021.

[26] Z. Zhang and L. Dai, "Capacity improvement in wideband reconfigurable intelligent surface-aided cell-free network," in *Proceedings of the 2020 IEEE 21st International Workshop On Signal Processing Advances In Wireless Communications (SPAWC)*, pp. 1–5, Atlanta, GA, USA, May 2020.

[27] Y. Zhang, B. Di, H. Zhang, J. Lin, Y. Li, and L. Song, "Reconfigurable intelligent surface aided cell-free MIMO communications," *IEEE Wireless Communications Letters*, vol. 10, no. 4, pp. 775–779, 2021.

[28] S. Huang, Y. Ye, M. Xiao, H. V. Poor, and M. Skoglund, "Decentralized beamforming design for intelligent reflecting surface-enhanced cell-free networks," *IEEE Wireless Communications Letters*, vol. 10, no. 3, pp. 673–677, 2021.

[29] C. Guo, Y. Cui, F. Yang, and L. Ding, "Outage probability analysis and minimization in intelligent reflecting surface-assisted MISO systems," *IEEE Communications Letters*, vol. 24, no. 7, pp. 1563–1567, 2020.

[30] C. You and R. Zhang, "3D trajectory optimization in rician fading for UAV-enabled data harvesting," *IEEE Transactions on Wireless Communications*, vol. 18, no. 6, pp. 3192–3207, 2019.

[31] Y. Han, W. Tang, S. Jin, C.-K. Wen, and X. Ma, "Large intelligent surface-assisted wireless communication exploiting statistical CSI," *IEEE Transactions on Vehicular Technology*, vol. 68, no. 8, pp. 8238–8242, 2019.

[32] Z.-Q. He and X. Yuan, "Cascaded channel estimation for large intelligent metasurface assisted massive MIMO," *IEEE Wireless Communications Letters*, vol. 9, no. 2, pp. 210–214, 2020.

[33] H. Guo, Y. Liang, J. Chen, and E. G. Larsson, "Weighted sum-rate maximization for reconfigurable intelligent surface aided wireless networks," *IEEE Transactions on Wireless Communications*, vol. 19, no. 5, pp. 3064–3076, 2020.

[34] Y. Zeng, Q. Wu, and R. Zhang, "Accessing from the sky: a tutorial on UAV communications for 5G and beyond," *Proceedings of the IEEE*, vol. 107, no. 12, pp. 2327–2375, 2019.

[35] X. Lin, V. Yajnanarayana, S. D. Muruganathan et al., "The sky is not the limit: LTE for unmanned aerial vehicles," *IEEE Communications Magazine*, vol. 56, no. 4, pp. 204–210, 2018.

[36] M. Grant and S. Boyd, "CVX: MATLAB Software for Disciplined Convex Programming," 2016, http://cvxr.com/cvx.

[37] M. Bengtsson and B. Ottersten, "Optimal and suboptimal transmit beamforming," *Handbook Of Antennas In Wireless Communications*, CRC Press, Boco Raton, FL, USA, 2001.

[38] Y. Zhao, B. Clerckx, and Z. Feng, "Intelligent reflecting surface-aided swipt: joint waveform, active and passive beamforming design," 2020, https://arxiv.org/abs/2012.05646.

[39] W. Yan, X. Yuan, and X. Kuai, "Passive beamforming and information transfer via large intelligent surface," *IEEE Wireless Communications Letters*, vol. 9, no. 4, pp. 533–537, 2020.

WILEY | Hindawi

Research Article

Small CSI Samples-Based Activity Recognition: A Deep Learning Approach Using Multidimensional Features

Yong Tian [ID],[1] Sirou Li,[1] Chen Chen,[1] Qiyue Zhang,[1] Chuanzhen Zhuang,[1] and Xuejun Ding [ID][2]

[1]*School of Physics and Electronic Technology, Liaoning Normal University, Dalian 116029, China*
[2]*School of Management Science and Engineering, Dongbei University of Finance and Economics, Dalian 116025, China*

Correspondence should be addressed to Yong Tian; tianyong@lnnu.edu.cn and Xuejun Ding; dingxuejun@dufe.edu.cn

With the emergence of tools for extracting CSI data from commercial WiFi devices, CSI-based device-free activity recognition technology has developed rapidly and has been widely used in security monitoring, smart home, medical monitoring, and other fields. However, the existing CSI-based activity recognition algorithms need a large number of training samples to obtain the ideal recognition accuracy. To solve the problem, an attention-based bidirectional LSTM method using multidimensional features (called MF-ABLSTM method) is proposed. In this method, the signal preprocessing and continuous wavelet transform algorithms are used to construct time-frequency matrix, the sample entropy is used to characterize the statistical feature of CSI amplitudes, the energy difference at a fixed time interval is used to characterize the time-domain feature of activities, and the energy distribution of different frequency components is used to characterize the frequency-domain feature of activities. By expanding the training samples with the proposed tensor prediction algorithm, the accurate activity recognition can be realized with only a few samples. A large number of experiments verify the good performance of MF-ABLSTM method.

1. Introduction

In recent years, the activity recognition technology has developed rapidly and has been widely used in smart home, medical care, safety monitoring, and other fields. The activity recognition can be divided into wearable device [1] and device-free-based recognition technologies. The former requires the target to be equipped with wearable devices, which is inconvenient and increases the cost. The latter does not require the target to carry any devices. Therefore, the device-free activity recognition technology has become the main research direction in this field.

The device-free activity recognition can be divided into video, RSS (Received Signal Strength), and CSI- (Channel State Information-) based recognition methods. The video-based activity recognition method is a popular method [2, 3], which can recognize activity intuitively with high recognition accuracy. However, it has some inherent shortcomings such as requiring a target within the line of sight, requiring

good lighting conditions, and invasion of privacy. The RSS-based activity recognition method recognizes the activities according to the reflection, refraction, diffraction, and absorption law of radio frequency signal caused by human body [4]. However, this kind of method needs too many nodes, the cost is high, and RSS is vulnerable to environmental interference and has poor stability, so it is gradually replaced by CSI-based activity recognition method. With the rapid development of the Internet of things (IOT) [5, 6] and the emergence of tools for extracting CSI data from commercial WiFi devices, the CSI-based activity recognition method has become a research hotspot in this field and has been widely used because of its advantages such as convenient data acquisition, not requiring additional devices, not requiring target to carry devices, no limitation of illumination and line of sight, no invasion of privacy, and good data stability.

The CSI-based activity recognition methods are mainly divided into two categories: machine learning and deep

learning-based methods. The research on machine learning-based methods started earlier, for example, Support Vector Machine (SVM), K-means, and Naive Bayesian-based methods. These methods all need to denoise, intercept, and extract features for the original data and then input the processed data into the corresponding machine learning algorithms in order to recognize the activities. The above-mentioned common methods-based on machine learning have the following problems: (i) SVM is a memory-intensive algorithm, which needs complex operations to select the correct kernel function, and is not suitable for large datasets. (ii) K-means is an algorithm that needs to specify the number of clusters, and the selection of K values is usually complicated. If the clusters in the training data are not spheroidal, the K-means algorithm will lead to some poor clusters. (iii) Naive Bayesian algorithm is too simple, and the accuracy of activity recognition is poor.

In recent years, with the deepening research of deep learning technology by Stanford University and Google Inc., the deep learning algorithms have achieved excellent results in image recognition, speech recognition, and natural language processing [7–9]. Long short-term memory neural network (LSTM) is a special type of recurrent neural network (RNN) proposed by Hochreiter and Schmidhuber in 1997, which is suitable for data processing and prediction with relatively long interval and delay in time series [10]. Some scholars have applied LSTM algorithm to CSI-based device-free activity recognition method. For example, Damodaran and Schäfer [11] and Wang et al. [12] used LSTM algorithm to recognize human activities and locations, respectively, and achieved high recognition accuracy. However, the above methods only used the simple single-layer one-way LSTM algorithm which is too simple to recognize complex activities. The reason is that it is difficult to recognize the CSI changes caused by complex activities only by using the forward a priori information, so that the recognition accuracy is low. For the problem, Chen et al. [13] proposed an attention-based BLSTM method (called ABLSTM method in the paper) for passive human activity recognition. In the method, the representative features are learned bidirectionally from the original CSI, and the attention mechanism is used to assign different weights to the learned features, so as to achieve better human activity recognition performance. However, in the method, the denoised experimental data is directly input to ABLSTM network, and the features are automatically extracted by ABLSTM algorithm, which lacks feature directionality. Moreover, to achieve higher recognition accuracy, more training samples are needed, which will greatly increase the cost of collecting training samples. When the number of training samples is insufficient, overfitting problem will occur, which results in poor generalization ability of ABLSTM network, so that the accuracy of activity recognition decreases. When applying the activity recognition system, most users are unwilling to spend time on collecting training samples. For example, when the elderly people use the nursing system, they are generally unwilling to cooperate to collect a sufficient number of training samples. Therefore, how to use a small

number of training sample sets (i.e., small samples) to achieve high accuracy human target activity recognition is an urgent problem to be solved in the deep learning method. Metalearning is a common method to solve some small sample problems and mainly uses the learned prior knowledge and small samples to recognize new patterns. However, the prior knowledge can only be achieved by using a large number of training samples, so the metalearning method is not suitable for the problem of the small samples in this paper.

For the problem of small sample activity recognition proposed in this paper, firstly, we use the statistical features of CSI amplitude and time-frequency domain features to construct the feature matrix for the input of ABLSTM network, based on the method of literature [13]. Thus, our multidimensional feature ABLSTM network can extract human target activity features from the more directional data and classify the activities more accurately. Secondly, in order to further improve the recognition accuracy, we propose a tensor prediction method, which expands a small number of training samples to generate enough training samples with similar characteristics as the existing samples. Specifically, the main contributions of this paper are as follows:

(1) To reduce the cost of collecting training samples, a method to generate training samples by using tensor prediction is proposed, which can generate a large number of training samples with similar characteristics as a small number of training samples and improve the activity recognition accuracy of deep learning methods.

(2) To further improve the accuracy of ABLSTM-based human activity recognition method, an ABLSTM deep learning method using multidimensional features (MF-ABLSTM method) is proposed. In this method, the sample entropy is used to characterize the statistical feature of CSI amplitudes, the energy difference at fixed time interval is used to characterize the time domain feature of human activities, and the energy distribution of different frequency components is used to characterize the frequency domain feature of human activities. The feature vector composed of these features is input to the ABLSTM deep learning network.

(3) To verify the performance of the proposed method, a large number of experiments are carried out. The experimental results show that MF-ABLSTM method can still achieve more than 92% recognition accuracy of human activities in the case of small CSI samples.

The rest of this paper is organized as follows. Section 2 introduces the related work on human activity recognition. Section 3 introduces the tensor prediction algorithm for sample expansion. Section 4 describes the proposed MF-ABLSTM method in this paper. In Section 5, the performance of the proposed method is verified by experiments and discussed. Section 6 gives the conclusion of this paper.

2. Related Work

At present, a large number of CSI-based human activity recognition applications have emerged, including human daily activity recognition, gesture recognition, fall detection, and physiological index perception.

2.1. Daily Activity Recognition. Wang et al. [14] proposed an activity recognition algorithm based on channel selection. In the algorithm, the WiFi channel with good quality is actively selected, the extended channel which jumps seamlessly between adjacent channels is constructed, and then the time and frequency features are input to LSTM network for activity recognition. In the existing human activity recognition methods, the temporal correlation of CSI in each subcarrier is considered, but the spatial correlation is ignored. To solve this problem, Cui et al. [15] proposed the WiAReS system. In the system, not only the temporal correlation is considered, but also the spatial correlation is analyzed. While keeping the locality of temporal and spatial pattern, Convolutional Neural Network (CNN) is used to automatically extract features from CSI, and an integrated structure that integrates Multilayer Perception (MLP), Random Forest (RF), and Support Vector Machine (SVM) is proposed. Sheng et al. [16] also considered spatial-temporal information and used the CNN to automatically extract the CSI features, but they used BLSTM to recognize the activities and designed a transfer learning method. Wang et al. [17] proposed a CSI velocity model which quantifies the relationship between CSI change and human motion speed and also proposed a CSI activity model to quantify the relationship between human motion speed and human activity. By combining the two models, they achieved the high human activity recognition accuracy. Fang et al. [18] proposed a layered hybrid model based on directed statistical model for the scenario where there are new activities that are not predefined or trained in the environment. The model can be updated incrementally without collecting a large amount of training data and storing historical perception data. For this scenario, Zhang et al. [19] proposed a data augmentation method for transforming and synthesizing CSI data and designed a Dense-LSTM deep learning model to solve the overfitting problem of small-size CSI dataset.

2.2. Gesture Recognition. Abdelnasser et al. [20] used RSSI to complete gesture recognition through three steps: primitive extraction, motion recognition, and motion mapping. In the primitive extraction step, discrete wavelet denoising, edge extraction, and primitive detection are needed. In the motion recognition step, the primitive gesture is segmented and recognized. Finally, the gesture composed of several motions is determined in the motion mapping step. Ohara et al. [21] recognized gestures by using CSI extracted from smart phones. In the method, the component corresponding to the user's hand movement speed is extracted according to Doppler frequency shift, and the human gestures are recognized without knowing the target localization. Bu et al. [22] proposed a gesture recognition method based on deep transfer learning. Firstly, the CSI stream representing gestures are captured, and the gesture fragment data is extracted by using the amplitude change of CSI. Then, the gesture fragment data is expressed in the form of image matrix, and CNN is used to extract features. Finally, deep transfer learning technology is used to complete gesture recognition. Zhang et al. [23] proposed a gesture recognition system, WiNum, based on gradient boosting decision tree (GBDT). In this system, the discrete wavelet transform is used to eliminate the noise in the original CSI data, and the proposed adaptive segmentation algorithm (AGS) based on entropy difference is used to segment gestures. Experimental results show that the average recognition accuracy of the system for finger gestures reaches 91%. Thariq et al. [24] proposed a sign language recognition method based on wireless devices, which is used to recognize 30 static gestures and 19 dynamic gestures. In the method, the SVM, KNN, and neural network algorithms are used to evaluate the accuracy of gesture recognition. Experimental results show that SVM algorithm can achieve higher gesture recognition accuracy in home and office environments.

2.3. Fall Detection. CSI-based human activity recognition technology is not only applied to the human daily activity and gesture recognition, but also applied to some specific scenes, such as the fall detection of the elderly. Han et al. [25] used CSI for the first time to detect the fall behavior of the elderly, and a warning was issued when the elderly was in danger. To reduce the influence of environment on fall detection algorithm, Hu et al. [26] proposed a fall detection system, DeFall, which is independent of environment. The system consists of an offline stage and an online stage. In the offline stage, the system first models the speed and acceleration of human fall and then uses DTW to generate typical human fall characteristics. In the online stage, the system evaluates the similarity between CSI features and typical features by analyzing the real-time speed and acceleration of human body and then detects the fall behavior. To compare the performance of different deep neural network algorithms, Cheng et al. [27] evaluated the performance of fall detection using CNN, GRU, and LSTM algorithms, respectively. The experimental results show that the GRU algorithm has the best fall detection performance. However, the commercial application of deep learning algorithm is limited because of the long training time. To solve the problem, Ding et al. [28] proposed a method to automatically identify the fall state by RNN. In the method, the collected data is uploaded to the proxy server which processes the data and identifies the fall state, and the client application obtains the processing result of the algorithm from the proxy server.

2.4. Physiological Index Perception. Model-based CSI recognition method does not need offline training process and can recognize the fine-grained breathing and other life characteristics. Zhang et al. [29] proposed a method of monitoring human respiration by using Fresnel diffraction model. In this method, Fresnel diffraction model is used to

accurately quantify the relationship between diffraction gain and slight displacement of human chest, and the best respiratory monitoring position is determined by observing heatmap. The experimental results show that this method can achieve more than 98% respiratory rate monitoring accuracy. To study the influence of human body position and direction on respiration detection, Wang et al. [30] proposed the theory of the relationship between the human body position and direction and the detectability of respiration, which explains when and why people's respiration can be detected by WiFi devices. In the practical application of respiratory detection, there will inevitably be multiplayer scenarios. According to Fresnel zone model, Yang et al. [31] carefully deployed the locations of WiFi transceiver, so that the information influenced by different people can be separated from the received CSI, and the information can correspond to people. In addition, they also considered the influence of people's sleep movement and sleep posture on the signal, so as to improve the robustness of the system.

3. Training Sample Expansion

When using deep learning algorithm for activity recognition, the larger the number of CSI training samples, the higher the recognition accuracy of the algorithm. However, collecting a large number of training samples will greatly increase the collection cost, and it is not suitable for the transfer learning of the algorithm in different environments. Therefore, the existing few training samples will be extended by using the following tensor prediction algorithm in the paper.

The existing CSI training samples are expressed as three-dimensional tensor S, where the three dimensions are the number of samples u, the number of subcarriers v, and the number of sampling points w, respectively. A tensor A with twice the number of S samples is constructed, and the 2u-th and (2u+1)-th initial samples of A are equal to the u-th sample of S. The following optimization problem is constructed [32].

$$\begin{cases} \min: & \frac{1}{2}\|B - A\|_F^2, \\ s.t. & \|B\|_{tr} \leq c, \end{cases} \tag{1}$$

where B is also a three-dimensional tensor, B represents the predicted tensor of the expanded sample, c is a constant, and $\|\cdot\|_F$ and $\|\cdot\|_{tr}$ indicate F norm and trace norm, respectively. The trace norm of B can be defined as follows:

$$\|B\|_{tr} := \frac{1}{3}\sum_{i=1}^{3}\|B_{(i)}\|_{tr}, \tag{2}$$

where $B_{(i)}$ represents the matrix obtained by 'unfold' operation according to the i-th dimension of B. It can be seen from (2) that the trace norm of B is the average of the trace norms unfolded according to three dimensions of tensor. Therefore, the optimization problem of (1) is equivalent to

$$\begin{cases} \min: & \frac{1}{2}\|B - A\|_F^2 \equiv \frac{1}{6}\sum_{i=1}^{3}\|B_{(i)} - A_{(i)}\|_F^2, \\ s.t. & \frac{1}{3}\sum_{i=1}^{3}\|B_{(i)}\|_{tr} \leq c, \end{cases} \tag{3}$$

where $A_{(i)}$ represents the matrix obtained by 'unfold' operation according to the i-th dimension of A. To simplify the optimization problem of (3), Liu et al. [32] transformed (3) into the following:

$$\min_{B,A,F_i}: \frac{1}{2}\sum_{i=1}^{3}\alpha_i\|F_i - B_{(i)}\|_F^2 + \frac{1}{2}\sum_{i=1}^{3}\beta_i\|F_i - A_{(i)}\|_F^2 \\ + \sum_{i=1}^{3}\gamma_{(i)}\|F_i\|_{tr}, \tag{4}$$

where F_i is the additional matrix and α_i, β_i, and γ_i represent the weight coefficients of each item. In the tensor A, B, and the matrix F_i, only one is set to change, and the others are set to be fixed. Block coordinate descent method is used to optimize each variable, and iterative method is used to obtain the final prediction tensor.

Firstly, only F_i is set to change in the k-th iteration. The equation of optimizing matrix F_i is as follows:

$$\min_{F_i}: \frac{\alpha_i}{2}\|F_i - B_{(i)}\|_F^2 + \frac{\beta_i}{2}\|F_i - A_{(i)}\|_F^2 + \gamma_i\|F_i\|_{tr}. \tag{5}$$

Let $Z_i = U_i\sum_i V_i^T$ be the singular value decomposition of matrix Z_i, and $\sum_i$ be the diagonal matrix with diagonal elements formed by the singular value λ_{ij} of Z_i in descending order. Equation (5) can be solved as follows [32]:

$$F_i = H_{\tau_i}(Z_i) = U_i\sum_{\tau_i}V_i^T, \tag{6}$$

where $\tau_i = \gamma_i/(\alpha_i + \beta_i)$, $Z_i = (\alpha_i A_{(i)} + \beta_i A_{(i)})/(\alpha_i + \beta_i)$, and $\sum_{\tau_i} = \text{diag}(\max(\lambda_{ij} - \tau_i, 0))$.

Then, only A is set to change. The equation of optimizing tensor A is as follows:

$$\min_{A}: \frac{1}{2}\sum_{i=1}^{3}\beta_i\|F_i - A_{(i)}\|_F^2. \tag{7}$$

Equation (7) can be solved as follows:

$$A = \frac{\sum_{i=1}^{3}\beta_i \text{fold}_i(F_i)}{\sum_{i=1}^{3}\beta_i}, \tag{8}$$

where $\text{fold}(\cdot)$ is the function of synthesizing tensor and $\text{fold}_i(F_i)$ represents "fold" operation for F_i.

Finally, only B is set to change. The equation of optimizing tensor B is as follows:

$$\min_{B}: \frac{1}{2}\sum_{i=1}^{3}\alpha_i\|F_i - B_{(i)}\|_F^2. \tag{9}$$

Equation (9) can be solved as follows:

$$B = \frac{\sum_{i=1}^{3} \alpha_i \text{fold}_i (F_i)}{\sum_{i=1}^{3} \alpha_i}. \tag{10}$$

After calculating the prediction tensor B, the k-th iteration ends. The root mean square error of the two round prediction samples is less than the set threshold, or after reaching a fixed number of iterations, the iteration ends.

4. MF-ABLSTM Method

4.1. System Framework. The framework of MF-ABLSTM method proposed in this paper is shown in Figure 1. The MF-ABLSTM method is divided into two stages: offline training and online testing. Both stages need to preprocess the collected CSI data, including antenna and subcarrier selection, Gaussian filter denoising, and activity interval interception. Then, feature extraction is needed. The extracted multidimensional features include energy difference at fixed time interval, energy distribution of different frequency components, and sample entropy. In the offline training stage, the extracted multidimensional features are input into ABLSTM network for training. In the online testing stage, the extracted multidimensional features are also input into ABLSTM network, and the human activities are recognized according to the parameters obtained in the training stage.

4.2. System Implementation

4.2.1. Construction of Time-Frequency Matrix. The time domain or frequency domain features alone cannot fully characterize the influence of human activities on CSI amplitude, so the time-frequency domain combination features of samples are used. To extract the time-frequency domain features of samples, the time-frequency matrix of samples is constructed, and the specific methods are as follows: (i) The antenna data is selected for experiments according to the overall fluctuation of CSI amplitude. (ii) For 30 subcarriers of the selected antenna, the average value of CSI amplitude is calculated as the subsequent data to be processed. (iii) The original CSI amplitude contains a lot of environmental noise, so Gaussian filter is used to denoise the average value of the CSI amplitude. (iv) Because the collected CSI amplitude includes the stationary interval when the human body is still and the fluctuation interval when the human body is moving, and only the fluctuation interval contains the characteristics reflecting the human activities, the classical variance method [33] is used to intercept the filtered CSI amplitude. (v) Morlet wavelet is used to carry out continuous wavelet transform on the intercepted CSI amplitude in order to construct time-frequency matrix for subsequent feature extraction.

4.2.2. Feature Extraction. To recognize human activities more accurately, we fully explore the features that can characterize human activities from two aspects: the statistical feature and time-frequency features of CSI amplitude. We use the sample entropy of CSI amplitude as the statistical feature which can characterize the complexity of CSI amplitude. In order to characterize the change law of CSI amplitude caused by human activities, we use wavelet transform to transform CSI amplitude to time-frequency domain and construct time-frequency matrix. Then, the energy difference at fixed time interval and the energy distribution of different frequency components are used to characterize the change law of the time domain and the frequency domain, respectively. The above statistical feature and time-frequency features are combined to form the feature vector which is input to the ABLSTM network.

(1) Statistical Feature. Because different human activities have different effects on CSI amplitude, the complexity of CSI amplitude can be used as the characteristic of recognizing human activities. Sample entropy is a statistic to measure the complexity of time series. The greater the sample entropy, the higher the complexity of time series. In this paper, the sample entropy of CSI amplitude is used to characterize the complexity of CSI amplitude change caused by different human activities. The specific steps of calculating sample entropy are as follows:

(1) Let the CSI amplitude after interval interception be time series $\{y(1), \ldots, y(j), \ldots, y(n)\}$, where J represents the j-th time component, $j = 1, \ldots, n$.

(2) Let q change from 1 to $n - p + 1$, and construct $n - p + 1$ vectors $Y(q)$, where $Y(q)$ is continuous p CSI amplitudes starting from $Y(q)$, that is, $\{y(q), y(q + 1), \ldots, y(q + p - 1)\}$.

(3) Let q be $q1$ and $q2$ ($q1 \neq q2$), respectively, and define the distance between $Y(q1)$ and $Y(q2)$ as follows:

$$d[Y(q1), Y(q2)] = \max_{w=0,\ldots,p-1} |y(q1 + w) - y(q2 + w)|. \tag{11}$$

(4) Let the threshold value be $r (r > 0)$. For each $Y(q1)(q1 = 1, \ldots, n - p + 1)$, count the number of $Y(q2)(q2 = 1, \ldots, n - p + 1, \quad q1 \neq q2)$ whose $d[Y(q1), Y(q2)]$ is less than r, calculate the ratio of this number to $n - p$, and represent it as $H_{q1}^{p}(r)$. Then, calculate the average value of $H_{q1}^{p}(r)$ as follows:

$$H^p(r) = \frac{1}{n - p + 1} \sum_{q1=1}^{n-p+1} H_{q1}^p(r). \tag{12}$$

(5) Let $p = p + 1$, repeat steps (2)–(4), and calculate $H^{p+1}(r)$. Then, the sample entropy of CSI amplitude can be calculated as follows:

$$\text{Samp En}(p, r, n) = -\ln\left[\frac{H^{p+1}(r)}{H^p(r)}\right]. \tag{13}$$

To further explain the reason for using sample entropy, we randomly select ten samples from the five kinds of activity samples of boxing, falling, running, walking, and sitting, respectively, and then calculate the corresponding
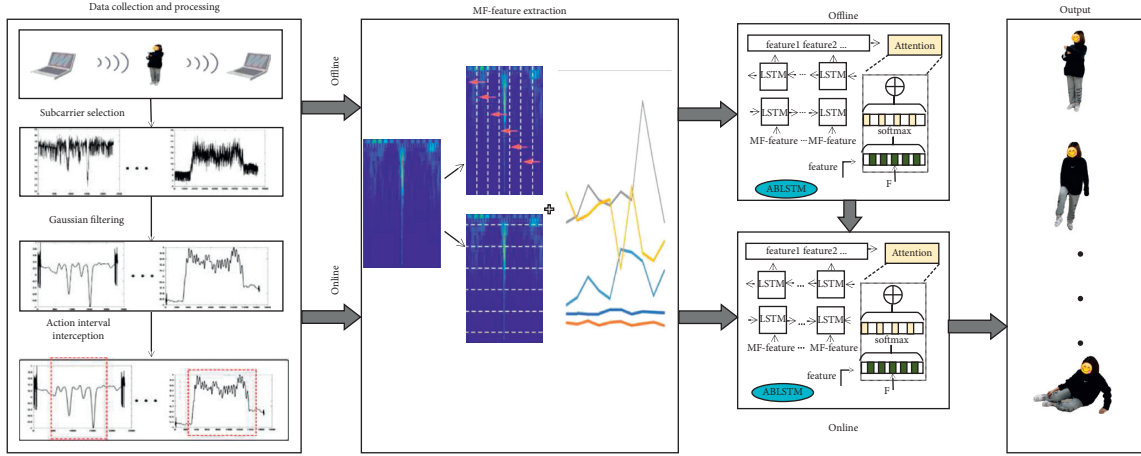
FIGURE 1: MF-ABLSTM method framework.

sample entropy. The experimental results are shown in Figure 2. Figure 2 shows the comparison results of sample entropy of CSI amplitude influenced by the five activities, where the abscissa is the sample serial number and the ordinate is the value of sample entropy. It can be seen from Figure 2 that CSI amplitudes corresponding to different human activities have different sample entropy and the sample entropy corresponding to different samples of the same activity is relatively stable. Therefore, the sample entropy of CSI amplitude is used as the statistical feature of human activity recognition in the paper.

(2) Time-Frequency Features. In this paper, CSI samples are constructed into time-frequency matrix, which contains both time domain information and frequency domain information of CSI samples. Therefore, the features characterizing different human activities are extracted from time domain and frequency domain in the paper, respectively.

Wang et al. [17] have verified that the motion speed of different human body parts is directly related to human body activities and also has a quantitative relationship with the energy of time-frequency components of CSI amplitude. Therefore, the parameters related to the energy of time-frequency components of CSI amplitude can be extracted as the features of human activity recognition. In this paper, the constructed time-frequency matrix is regarded as a time-frequency image of CSI samples. As shown in Figure 3, the time-frequency matrix can be expressed as follows:

$$TF = \begin{vmatrix} x_{11} & \cdots & x_{1j} & \cdots & x_{1n} \\ \vdots & \cdots & \vdots & \cdots & \vdots \\ x_{i1} & \cdots & x_{ij} & \cdots & x_{in} \\ \vdots & \cdots & \vdots & \cdots & \vdots \\ x_{m1} & \cdots & x_{mj} & \cdots & x_{mn} \end{vmatrix}, \qquad (14)$$

where i represents the i-th frequency component $(i = 1, \ldots, m), j$ represents the j-th time component $(j = 1, \ldots, n)$, and x_{ij} is the energy value of time-frequency component of CSI amplitude.
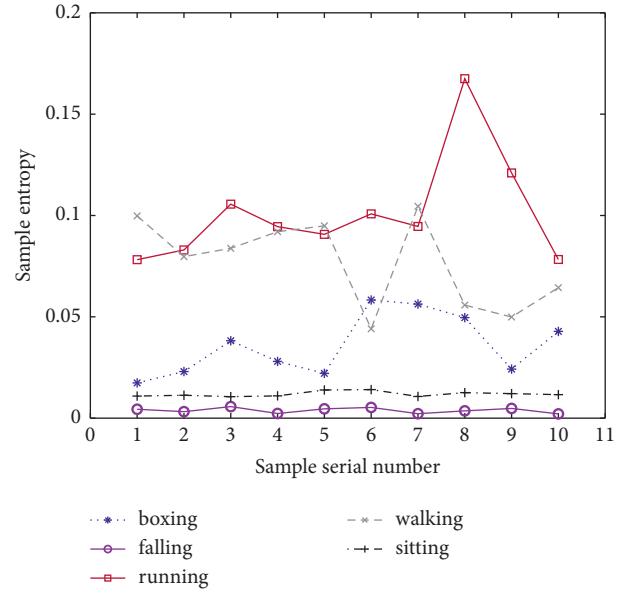

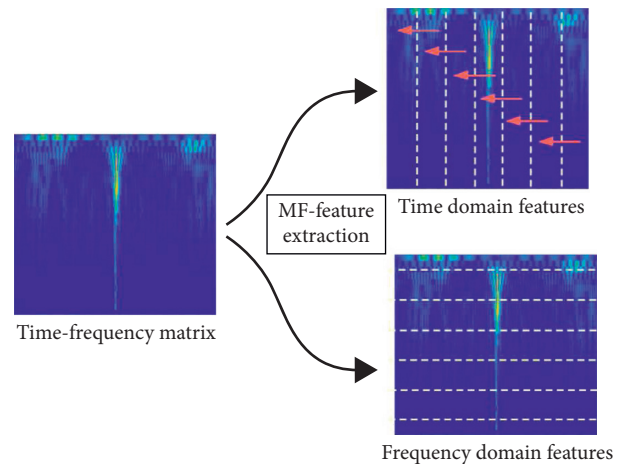FIGURE 2: Comparison of sample entropy.

FIGURE 3: Schematic diagram of time-frequency features.

To extract the time domain features in the samples that can characterize human activities, in this paper, n time components are divided into n/nstep fixed time intervals with the step length $n$step, the sum of energy values in each time interval is calculated, and then the difference between the sums of energy values in adjacent time intervals is calculated as follows:

$$\text{In Sam}TF_k = \sum_{j=1+n\text{step}*k}^{n\text{step}*(k+1)} \sum_{i=1}^{m} x_{ij} - \sum_{j=1+n\text{step}*(k-1)}^{n\text{step}*k} \sum_{i=1}^{m} x_{ij}, \tag{15}$$

where $k = 1, \ldots, n/n\text{step} - 1$ and $\text{In Sam}TF_k$ represent the time domain features in the k-th sample extracted in this paper. $\text{In Sam}TF_k$ can characterize the changes of different human activities with time and movement speed, as shown in the upper right subpicture of Figure 3.

To extract the frequency domain features in the samples, in this paper, m frequency components are divided into m/mstep fixed frequency intervals with the step length $m$step, and the sum of energy values of each frequency interval is calculated as follows:

$$\text{In Sam}FF_h = \sum_{i=1+m\text{step}*(h-1)}^{m\text{step}*h} \sum_{j=1}^{n} x_{ij}, \tag{16}$$

where $h = 1, \ldots, m/m\text{step}$ and $\text{In Sam}FF_h$ represent the frequency domain features in the h-th sample extracted in this paper. $\text{In Sam}FF_h$ can characterize the frequency domain energy distribution of different human activities, as shown in the lower right subpicture of Figure 3. The different frequencies correspond to different human motion speeds, so the different human activity has different frequency domain energy distribution.

To sum up, $\text{In Sam}TF_k$ and $\text{In Sam}FF_h$ can better characterize the changes of CSI amplitude caused by human activities in time domain and frequency domain, so using the two features can more accurately recognize human activities.

4.3. MF-ABLSTM Algorithm

4.3.1. Attention Mechanism. When people observe a scene, they will focus on specific parts according to their interest. If the specific part appears repeatedly in similar scenes, people will pay special attention to the specific part when observing. Inspired by this phenomenon, the attention mechanism of neural network came into being and is also called resource allocation method [34]. In the attention mechanism, a weight coefficient δ_{gl} is automatically generated to characterize the correlation between the hidden state $G_g (g = 1, 2, \ldots, K)$ of neural network encoder and the hidden state $M_l (l = 1, 2, \ldots L)$ of the decoder. The M_l is expressed as follows:

$$M_l = f(M_{l-1}, \text{Out}p_{l-1}, e_l), \tag{17}$$

where $\text{Out}p_{l-1}$ is the $(l-1)$-th output of neural network and e_l is the weighted sum of hidden state G_g, which is calculated as follows:

$$e_l = \sum_{g=1}^{K} \delta_{gl} G_g, \tag{18}$$

where e_l provides a mechanism for the output of decoder to pay attention to important input features. Different attention mechanisms use different methods to generate weight coefficients δ_{gl}. In this paper, the soft attention method is used [35].

4.3.2. BLSTM Algorithm. RNN is widely used in many fields, such as speech recognition [36] and image processing [37], because of its ability to process variable length sequence data. However, when processing long series data, the RNN has some problems such as gradient disappearance and gradient explosion [38]. LSTM neural network is a special kind of RNN, which solves the problems of RNN well. LSTM can retain the information that needs to be memorized for a long time and forget the unimportant information by controlling multiple gates. Therefore, LSTM has a good classification effect for long series data with correlation among data. The structure unit of LSTM is shown in Figure 4. In Figure 4, $ht-1$ and ht are the outputs of the previous and current LSTM structure units, respectively; $Ct-1$ and Ct are the memories of the previous and current LSTM structure units, respectively; $ct\prime$ is the input modulation gate; it and ot are input and output gate, respectively; and ft is the forgetting gate [39].

However, the output of LSTM structure unit is only related to the previous data and has nothing to do with the following data. In the human activity recognition, both forward and backward directions of CSI amplitude features have strong correlation. Therefore, BLSTM neural network is used in this paper, and its basic structure is shown in Figure 5. It can be seen from Figure 5 that BLSTM neural network constructs two groups of LSTM networks from the forward and backward directions. The output Fht of the forward LSTM network is related to the previous data, and the output Bht of the backward LSTM network is related to the subsequent data. The output of BLSTM structure unit at time t is

$$ht = f(w1 * Fht + w2 * Bht), \tag{19}$$

where $w1$ and $w2$ are the coefficients of Fht and Bht, respectively [40]. Therefore, the output of BLSTM neural network is determined by the whole data sequence.

5. Experimental Evaluation

5.1. Experimental Setup and Data Acquisition. In this paper, the experiments were carried out in a laboratory with an area of $5\,m \times 5\,m$. In the laboratory, there are tables, chairs, and experimental tables, and the layout of the laboratory is shown in Figure 6. In the experiment, two computers with Intel 5300 wireless network cards are used as signal transmitter and receiver, and Ubuntu 10.04 operating system and CSI tools are installed on both computers, in which the transmitter sends signals through one antenna and the
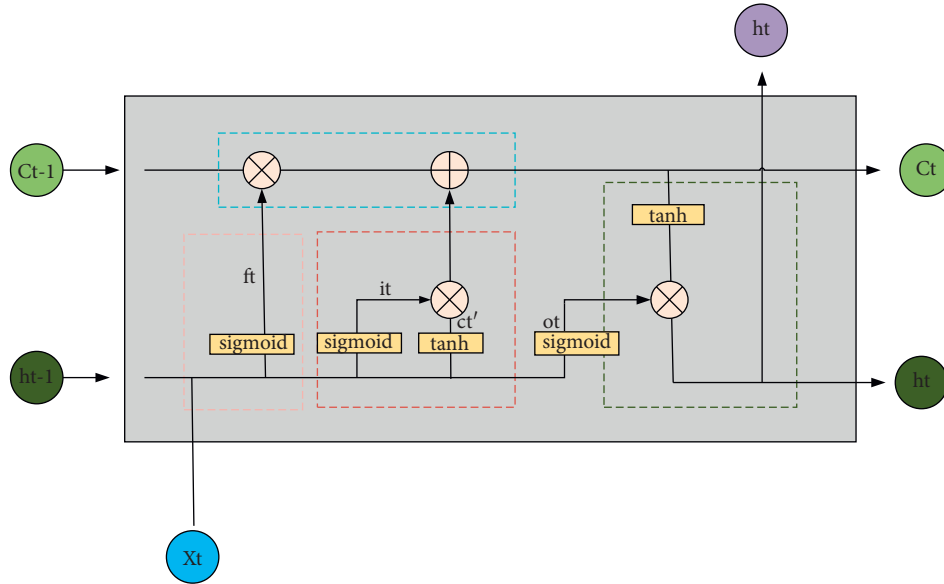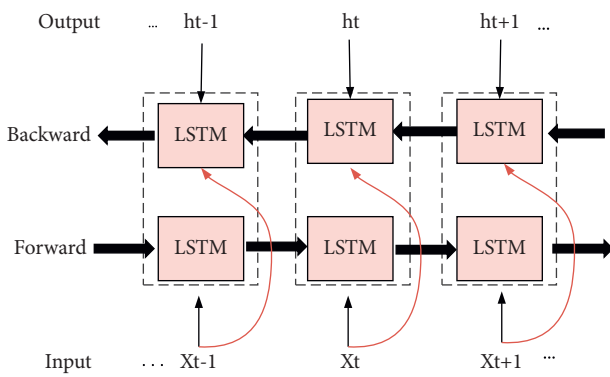
FIGURE 4: The structure unit of LSTM.

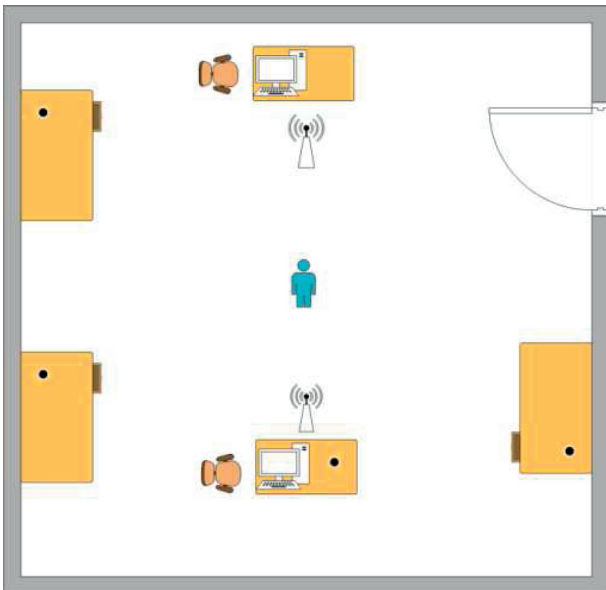FIGURE 5: The basic structure of BLSTM.

FIGURE 6: The layout of the laboratory.

receiver receives signals through three antennas. In this paper, the transmission frequency of WiFi signal is set to 2.4 GHz, the channel bandwidth is set to 20 MHz, and each antenna receives CSI data of 30 subcarriers. The distance between the transmitting and receiving antennas is 2 m, and the height from the ground is 1 m. The volunteers are located in the middle of the transceiver and perform boxing, falling, running, walking, and sitting, respectively. The receiving end uses 1000 Hz sampling frequency to collect data, each sample is collected for 4 seconds, and 98 samples are collected for each activity. In general, for small samples, about 70% and 30% samples are selected as training set and testing set, respectively. However, in order to verify the good performance of the proposed MF-ABLSTM in the case of small samples, we only randomly select 10 samples from 98 samples of each activity as the training set and the other 88 samples as the testing set in the following experiment. This way of splitting dataset can not only ensure that the number of training samples is small, but also ensure that the number of testing samples is large, so that the experimental results have good statistical significance.

5.2. Parameter Analysis

5.2.1. Analysis of Threshold Value r. The value of sample entropy is closely related to the given threshold value r. Pincus et al. [40] verified that the value of sample entropy can better measure the complexity of time series when the threshold value r is within 0.1–0.25 standard deviation of time series. Therefore, the threshold value r is set as 0.1SD, 0.15SD, 0.2SD, and 0.25SD, respectively, where SD represents the standard deviation of CSI amplitude after interval interception, and the accuracy of human activity recognition based on MF-ABLSTM algorithm is analyzed. The experimental results are shown in Figure 7. From Figure 7(a), it can be seen that the accuracy of human activity recognition is all
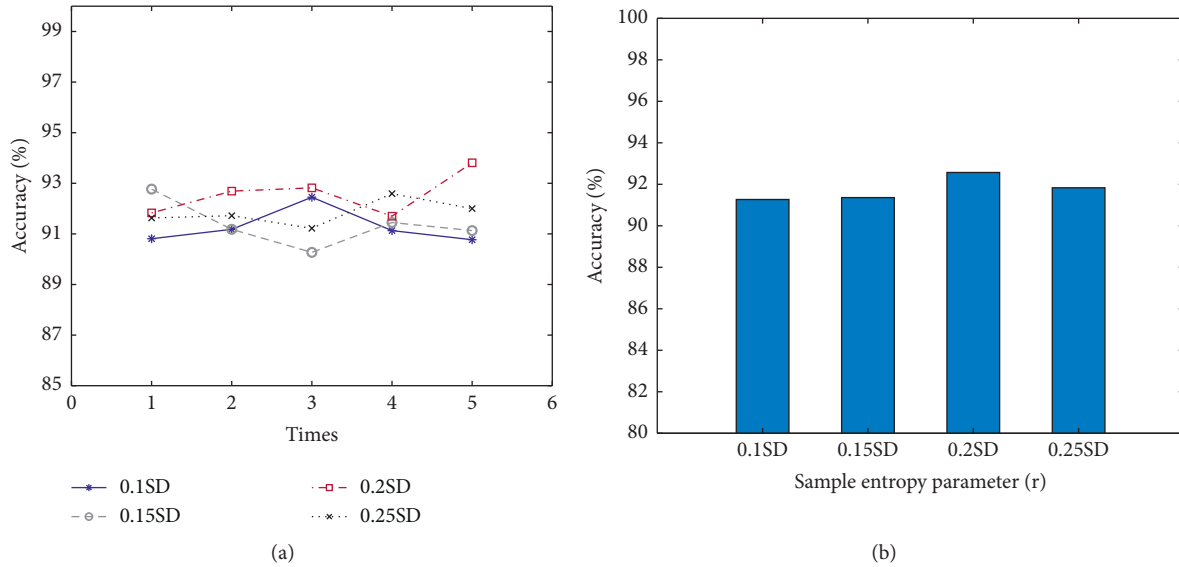
(a)

(b)

FIGURE 7: Analysis results of threshold value r. (a) Accuracy of activity recognition of 5 experiments. (b) Average accuracy of activity recognition.

above 90%, but the accuracy of five experiments is more stable and relatively high when r is 0.2SD. From Figure 7(b), it can also be seen that the average accuracy of human activity recognition is the highest, 92.6%, when r is 0.2SD, so the threshold value of sample entropy is set as 0.2SD in this paper.

5.2.2. Analysis of Step Length nstep and mstep. The time-frequency features extracted in this paper are closely related to the step length $n$step of time domain and the step length $m$step of frequency domain, so it is necessary to analyze the influence of different $n$step and $m$step on the accuracy of human activity recognition.

According to the time component length of time-frequency matrix, $n$step is set to be 20, 50, 100, 200, 350, and 700, respectively, and $m$step is set to be 1. The accuracy of human activity recognition based on MF-ABLSTM algorithm is analyzed. The experimental results are shown in Figure 8. From Figure 8(a) and Figure 8(b), it can be seen that when $n$step is 200, the average accuracy of human activity recognition is the highest, and the accuracy is relatively stable in five experiments. The reason is that $n$step is too large, which makes the number of time intervals too small, so the discrimination of activity features contained in each time interval is small, resulting in the reduction of activity recognition accuracy. When $n$step is too small, the number of time intervals is too large, and the time domain features of human activities become too complex, which in turn leads to a decrease in the accuracy of activity recognition. Therefore, $n$step is set to be 200 in this paper.

According to the frequency component length of time-frequency matrix, $m$step is set to be 1, 5, 10, 20, and 40, respectively, and $n$step is set to be 200. The experimental results are shown in Figure 9. From Figure 9(a) and Figure 9(b), it can be seen that the average accuracy of

human activity recognition decreases obviously with the increase of $m$step. This is because the frequency domain energy of human activity is mainly distributed in the low frequency part. The smaller the $m$step is, the greater the discrimination of activity features contained in the low frequency part is, and the higher the accuracy of activity recognition is. Therefore, $m$step is set to be 1 in this paper.

5.3. Analysis of MF-ABLSTM Algorithm

5.3.1. Analysis of Features. In this paper, the statistical feature, time domain feature, and frequency domain feature of CSI amplitude are used to construct feature vectors for recognizing human activities. Each of these features can represent different human activities well. To verify the effectiveness of these feature combinations, the accuracy of human activity recognition based on ABLSTM algorithm is compared and analyzed in five cases: no feature (NF), only statistical feature (SF), only time domain feature (TF), only time-frequency domain features (TFF), and time-frequency domain and statistical features (TFSF). Five experiments were conducted for each case, and the average value was taken as the final result. The experimental results are shown in Figure 10. From Figure 10, it can be seen that the accuracy of ABLSTM algorithm using the TFSF is the highest and the most stable, which is increased by 8.5%, 6.1%, 4.9%, and 1.4% compared with the NF, SF, TF, and TFF, respectively. The reason is that the four types of features characterize the human activities from different perspectives, so their combination can effectively improve the accuracy of human activity recognition.

5.3.2. Analysis of Classification Algorithms. To analyze the good performance of ABLSTM algorithm, the accuracies of human activity recognition with five classification
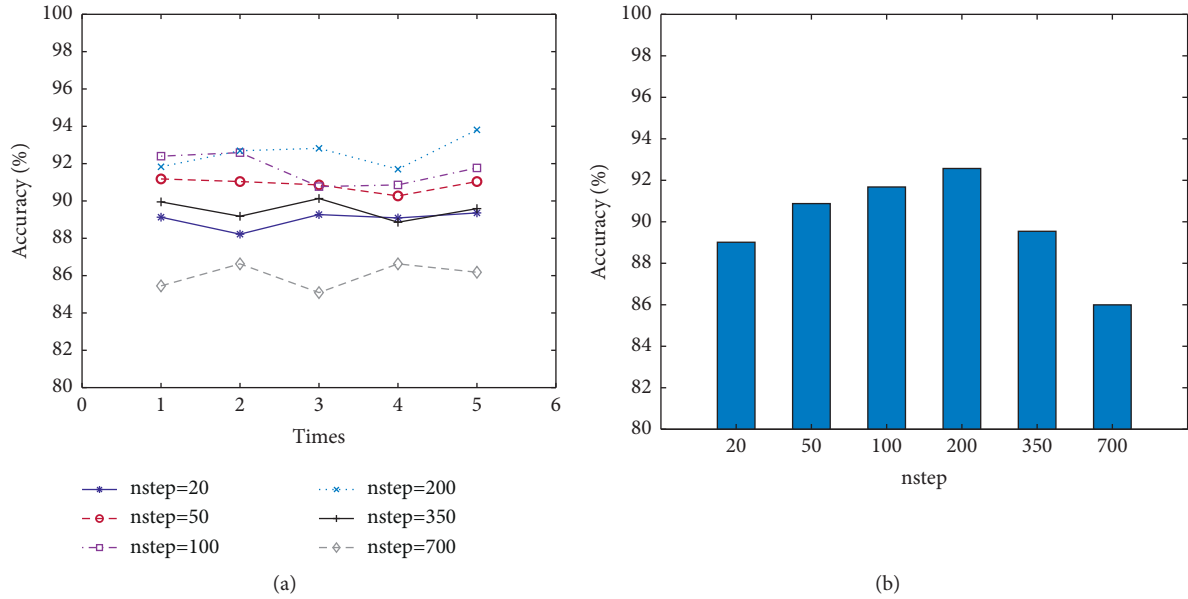
FIGURE 8: Analysis results of step length *n*step. (a) Accuracy of activity recognition of 5 experiments. (b) Average accuracy of activity recognition.
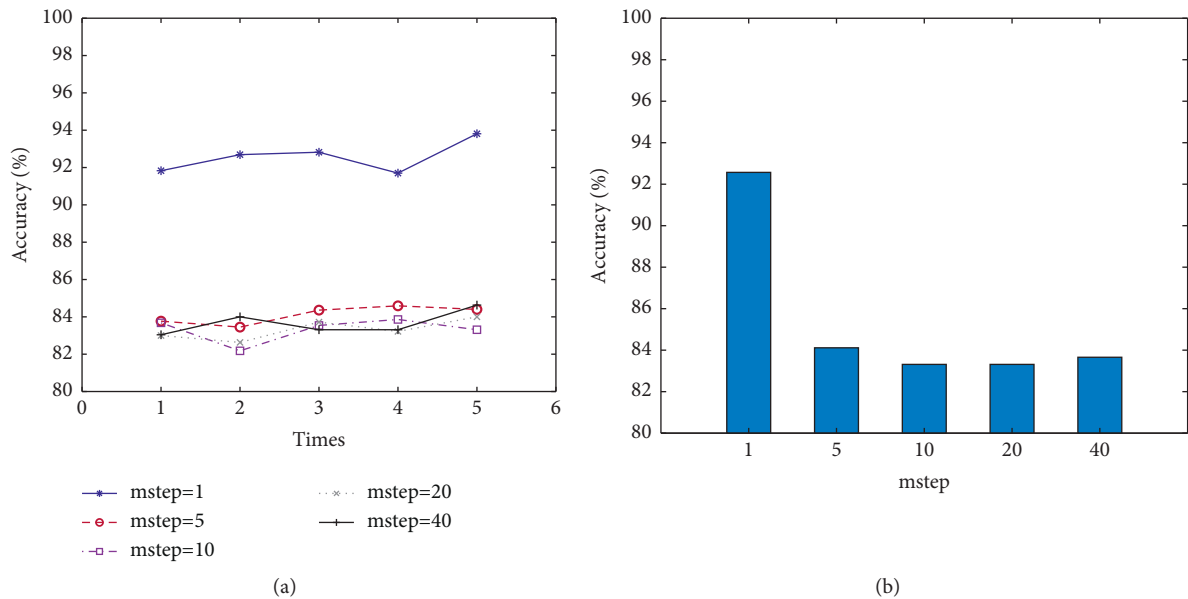

FIGURE 9: Analysis results of step length *m*step. (a) Accuracy of activity recognition of 5 experiments. (b) Average accuracy of activity recognition.

algorithms, ABLSTM, LSTM, CNN, RF, and DTW-KNN (Dynamic Time Warping-K Nearest Neighbors), are compared, when the training set is 10 samples and the features are TFSF. The experimental results are shown in Figure 11. From Figure 11(a), it can be seen that the recognition accuracy of ABLSTM algorithm used in this paper is up to 92.6%, which is 11.4%, 5.3%, 20.2%, and 18.7% higher than LSTM, CNN, DTW-KNN, and RF algorithms, respectively. To further analyze the recognition accuracy of ABLSTM algorithm for each activity, the confusion matrix of ABLSTM algorithm is constructed, as shown in Figure 11(b).

From Figure 11(b), it can be seen that the recognition accuracy of ABLSTM algorithm is more than 90% for all three activities, where the recognition accuracy (90%) for falling activity is lower and the recognition accuracy (99%) for boxing activity is higher, which further verifies the effectiveness of ABLSTM algorithm.

5.3.3. Analysis of Small Samples. The number of training samples has great influence on the recognition accuracy of ABLSTM neural network. Generally, the larger the number of
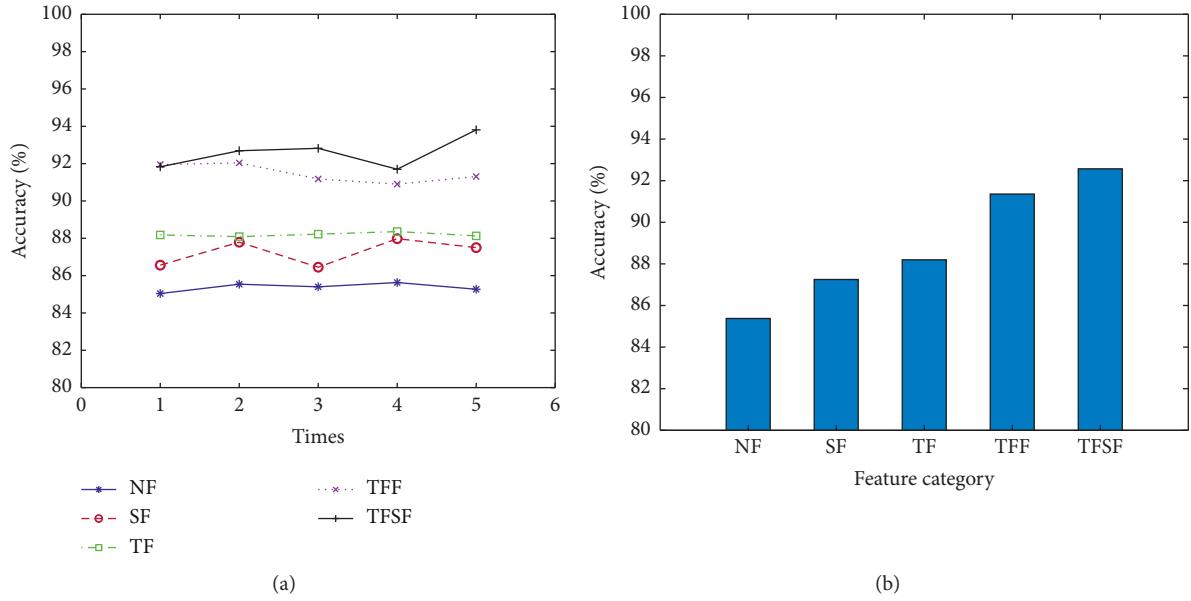
FIGURE 10: Analysis results of features. (a) Accuracy of activity recognition of 5 experiments. (b) Average accuracy of activity recognition.
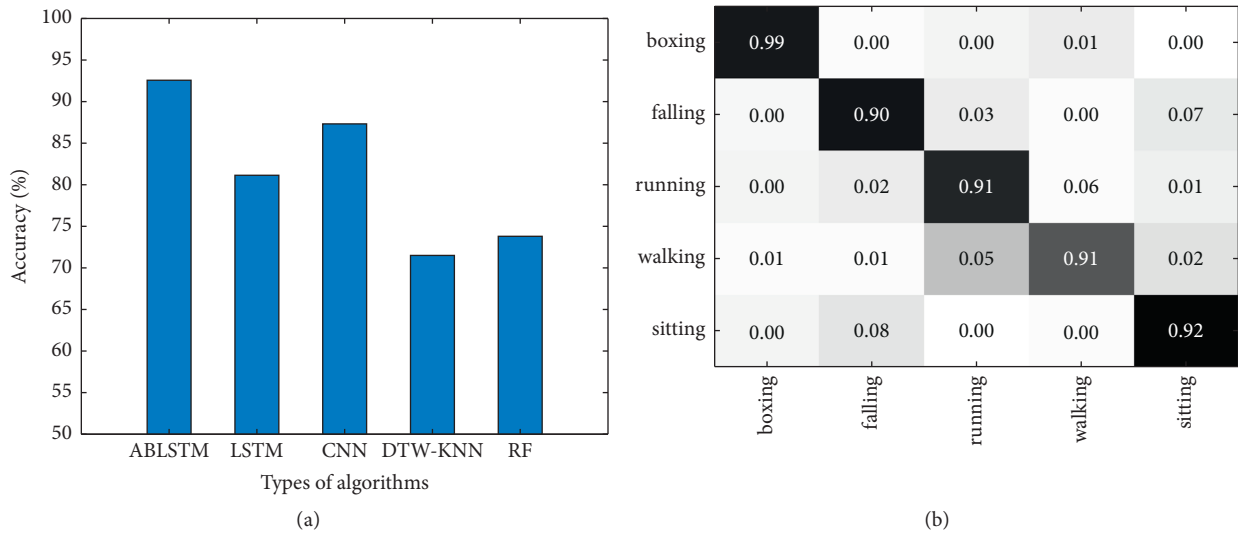

FIGURE 11: Analysis results of classification algorithms. (a) Average accuracy of activity recognition. (b) Confusion matrix of ABLSTM algorithm.

training samples, the higher the recognition accuracy of the algorithm. To verify the effectiveness of MF-ABLSTM when there are only a small number of training samples, we conduct the following experiments. We randomly select 40 samples from 98 samples of each activity as the training set and the other 58 samples as the testing set. The ABLSTM algorithm is conducted when the training samples are the first 10, 20, and 40 samples in the training set, respectively, and these experiments are represented as ABLSTM(10), ABLSTM(20), and ABLSTM(40). The MF-ABLSTM algorithm is conducted when the training samples are the 10, 20, and 40 samples where the former one is the first 10 samples in the training set and the latter two are expanded from the 10 samples the latter two are expanded from the 10 samples by using the tensor prediction algorithm proposed in this paper, respectively, and

these experiments are represented as MF-ABLSTM(10), MF-ABLSTM(20), and MF-ABLSTM(40). Then, we compare the activity recognition accuracies of the above six experiments by testing the 58 samples, and the experimental results are shown in Figure 12. From Figure 12, it can be seen that the recognition accuracy of ABLSTM algorithm is higher with the increase of the number of training samples, which shows that small samples and large samples have a great impact on the recognition accuracy of ABLSTM algorithm. However, when the training samples are 10, the recognition accuracy of MF-ABLSTM algorithm proposed in this paper is higher than that of ABLSTM(40) and is increased steadily after the proposed tensor prediction algorithm expands the training samples, which verifies the effectiveness of the method proposed in this paper to solve the problem of small samples.
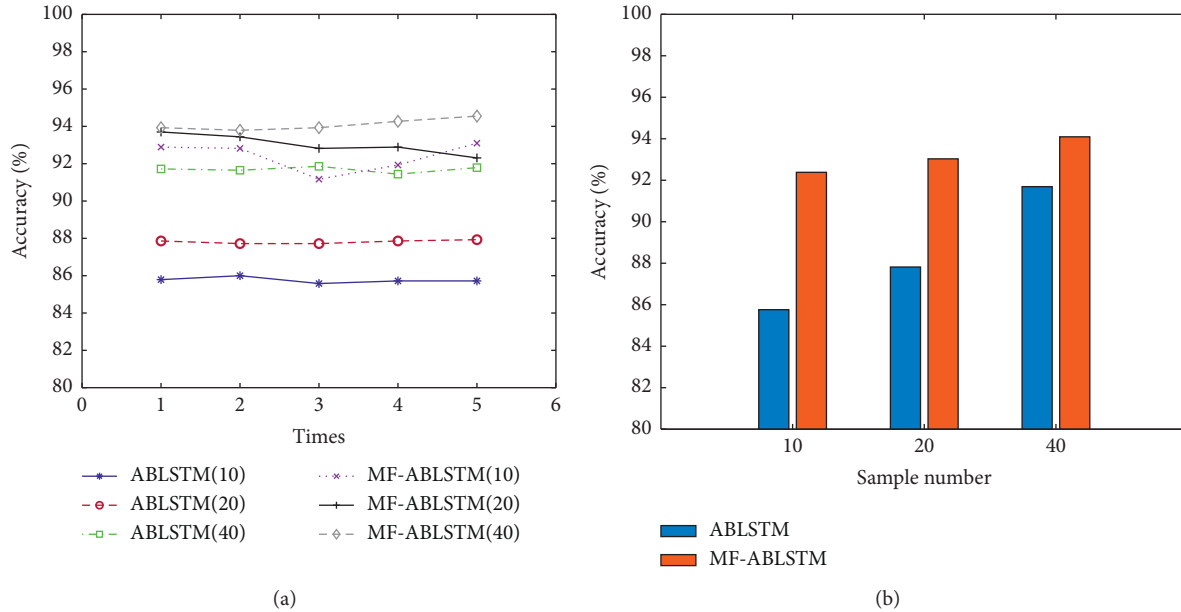
FIGURE 12: Analysis results of small samples. (a) Accuracy of activity recognition of 5 experiments. (b) Average accuracy of activity recognition.

6. Conclusion

Device-free human activity recognition technology based on CSI has become an important research direction in the field of intelligent sensing, and the related achievements emerge one after another. However, the existing research still needs a large number of training samples to obtain the ideal recognition accuracy. To solve this problem, a MF-ABLSTM human activity recognition method based on CSI small samples is proposed. In this method, the proposed tensor prediction algorithm is used to expand the training samples, the statistical features of sample entropy of CSI amplitude and the time-frequency domain features of time-frequency matrix are used to construct feature vectors representing human activities, and the ABLSTM neural network is used to recognize human activities. In this paper, the different feature combinations, the different numbers of training samples, and the performance of different classification algorithms are analyzed through experiments. The experimental results show that the MF-ABLSTM method proposed in this paper only needs to use a few training samples, which can achieve high accuracy and stability of human activity recognition.

Data Availability

The data used to support the findings of this study are available from the corresponding author upon request.

Conflicts of Interest

The authors declare that they have no conflicts of interest.

Acknowledgments

References

[1] S. Shen, K. Gu, X. R. Chen, C. X. Lv, and R. C. Wang, "Gesture recognition through sEMG with wearable device based on deep learning," *Mobile Networks and Applications*, vol. 25, pp. 2447–2458, 2020.

[2] J. C. Nunez, R. Cabido, J. J. Pantrigo, A. S. Montemayor, and J. F. Vélez, "Convolutional neural networks and long short-term memory for skeleton-based human activity and hand gesture recognition," *Pattern Recognition*, vol. 76, pp. 80–94, 2018.

[3] J. Zhang, W. Li, P. O. Ogunbona, P. Wang, and C. Tang, "RGB-D-based action recognition datasets: a survey," *Pattern Recognition*, vol. 60, pp. 86–105, 2016.

[4] S. Sigg, U. Blanke, and G. Troster, "The telepathic phone: frictionless activity recognition from WiFi-RSSI," in *Proceedings of the IEEE International Conference on Pervasive Computing & Communications*, pp. 148–155, IEEE Computer Society, Budapest, Hungary, March 2014.

[5] X. Liu, X. P. Zhai, W. D. Lu, and C. Wu, "QoS-guarantee resource allocation for multibeam satellite industrial internet of things with NOMA," *IEEE Transactions on Industrial Informatics*, vol. 17, no. 3, pp. 2052–2061, 2021.

[6] X. Liu and X. Y. Zhang, "Rate and energy efficiency improvements for 5G-based IoT with simultaneous transfer," *IEEE Internet of Things Journal*, vol. 6, no. 4, pp. 5971–5980, 2019.

[7] K. He, X. Zhang, S. Ren, and J. Sun, "Deep residual learning for image recognition," in *Proceeding of the 2016 IEEE Conference on Computer Vision & Pattern Recognition*, pp. 770–778, IEEE Computer Society, Las Vegas, NV, USA, June 2016.

[8] W. Xiong, J. Droppo, X. Huang et al., "Achieving human parity in conversational speech recognition," in *Proceedings of*

the 2017 IEEE/ACM Transactions on Audio, Speech, and Language Processing, p. 99p. 99, IEEE, September 2017.

[9] R. Sarikaya, G. E. Hinton, A. Deoras et al., "Application of deep belief networks for natural language understanding," IEEE/ACM Transactions on Audio, Speech, and Language Processing, vol. 22, no. 4, pp. 778–784, 2014.

[10] S. Hochreiter and J. Schmidhuber, "Long short-term memory," Neural Computation, vol. 9, no. 8, pp. 1735–1780, 1997.

[11] N. Damodaran and J. Schäfer, "Device free human activity recognition using WiFi channel state information," in Proceedings of the IEEE SmartWorld, Ubiquitous Intelligence & Computing, Advanced & Trusted Computing, Scalable Computing & Communications, Cloud & Big Data Computing, pp. 1069–1074, Internet of People and Smart City Innovation, Leicester, UK, August 2019.

[12] X. Wang, Z. Yu, and S. Mao, "Indoor localization using smartphone magnetic and light sensors: a deep LSTM approach," Mobile Networks and Applications, vol. 25, pp. 819–832, 2020.

[13] Z. Chen, L. Zhang, C. Jiang, Z. Cao, and W. Cui, "Wifi CSI based passive human activity recognition using attention based BLSTM," IEEE Transactions on Mobile Computing, vol. 18, no. 11, pp. 2714–2724, 2018.

[14] F. Wang, G. Wei, J. Liu, and K. Wi, "Channel selective activity recognition with WiFi: a deep learning approach exploring wideband information," IEEE Transactions on Network Science and Engineering, vol. 7, no. 1, pp. 181–192, 2018.

[15] W. Cui, B. Li, L. Zhang, and Z. Chen, "Device-free single-user activity recognition using diversified deep ensemble learning," Applied Soft Computing Journal, vol. 102, no. 4, Article ID 107066, 2021.

[16] B. Sheng, F. Xiao, L. Sha, and L. Sun, "Deep spatial-temporal model based cross-scene action recognition using commodity WiFi," IEEE Internet of Things Journal, vol. 7, no. 4, pp. 3592–3601, 2020.

[17] W. Wang, A. X. Liu, M. Shahzad, K. Ling, and S. Lu, "Device-free human activity recognition using commercial WiFi devices," IEEE Journal on Selected Areas in Communications, vol. 35, no. 5, pp. 1118–1131, 2017.

[18] L. Fang, J. Ye, and S. Dobson, "Discovery and recognition of emerging human activities using a hierarchical mixture of directional statistical models," IEEE Transactions on Knowledge and Data Engineering, vol. 32, no. 7, pp. 1304–1316, 2020.

[19] J. Zhang, F. Wu, B. Wei et al., "Data augmentation and dense-LSTM for human activity recognition using WiFi signal," IEEE Internet of Things Journal, vol. 8, no. 6, pp. 4628–4641, 2021.

[20] H. Abdelnasser, M. Youssef, and K. A. Harras, "Wigest: a ubiquitous WiFi-based gesture recognition system," IEEE Conference on Computer Communications, vol. 2015, pp. 1472–1480, 2015.

[21] K. Ohara, T. Maekawa, S. Sigg, and M. Youssef, "Preliminary investigation of position independent gesture recognition using WiFi CSI," in Proceeding of the 2018 IEEE International Conference on Pervasive Computing and Communications Workshops, pp. 480–483, Athens, Greece, March 2018.

[22] Q. Bu, G. Yang, X. Ming, T. Zhang, J. Feng, and J. Zhang, "Deep transfer learning for gesture recognition with WiFi signals," Personal and Ubiquitous Computing, vol. 2020, 2020.

[23] Y. Zhang, K. Xu, and Y. Wang, "WiNum: a WiFi finger gesture recognition system based on CSI," in Proceedings of the 2019 7th International Conference on Information Technology: IoT and Smart CityDecember, pp. 181–186, Shanghai, China, December 2019.

[24] H. Thariq, H. Ahmad, K. Narasingamurthi, H. Harket, and S. K. Phang, "DF-WiSLR: device-free WiFi-based sign language recognition," Pervasive and Mobile Computing, vol. 69, Article ID 101289, 2020.

[25] C. Han, K. Wu, Y. Wang, and L. M. Ni, "WiFall: device-free fall detection by wireless networks," in Proceedings of the IEEE Conference on Computer Communications, pp. 271–279, IEEE, Toronto, Canada, May 2014.

[26] Y. Hu, F. Zhang, C. Wu, B. Wang, and K. J. R. Liu, "A WiFi-based passive fall detection system," in Proceedings of the IEEE International Conference on Acoustics, Speech and Signal Processing, pp. 1723–1727, IEEE, Barcelona, Spain, May 2020.

[27] H. Cheng, J. Zhang, Y. Gao, and X. Hei, "Deep learning WiFi channel state information for fall detection," in Proceedings of the IEEE International Conference on Consumer Electronics, pp. 1-2, IEEE, Yilan, Taiwan, May 2019.

[28] J. Ding and Y. Wang, "A WiFi-based smart home fall detection system using recurrent neural network," IEEE Transactions on Consumer Electronics, vol. 66, no. 4, pp. 308–317, 2020.

[29] F. Zhang, D. Zhang, J. Xiong et al., "From fresnel diffraction model to fine-grained human respiration sensing with commodity WiFi devices," Proceedings of the Acm on Interactive Mobile Wearable & Ubiquitous Technologies, vol. 2, no. 1, pp. 1–23, 2018.

[30] H. Wang, D. Zhang, J. Ma et al., "Human respiration detection with commodity WiFi devices: do user location and body orientation matter?" in Proceedings of the ACM International Joint Conference on Pervasive and Ubiquitous Computing, pp. 25–36, September 2016.

[31] Y. Yang, J. Cao, X. Liu, and K. Xing, "Multi-person sleeping respiration monitoring with COTS WiFi devices," in Proceedings of the IEEE 15th International Conference on Mobile Ad Hoc and Sensor Systems, pp. 37–45, IEEE, Chengdu, China, October 2018.

[32] J. Liu, P. Musialski, P. Wonka, and J. Ye, "Tensor completion for estimating missing values in visual data," IEEE Transactions on Pattern Analysis and Machine Intelligence, vol. 35, no. 1, pp. 208–220, 2013.

[33] B. Sheng, Y. Fang, F. Xiao, and L. Sun, "An accurate device-free action recognition system using two-stream network," IEEE Transactions on Vehicular Technology, vol. 69, no. 7, pp. 7930–7939, 2020.

[34] X. Yang, R. Cao, M. Zhou, and L. Xie, "Temporal-frequency attention-based human activity recognition using commercial WiFi devices," IEEE Access, vol. 8, pp. 137758–137769, 2020.

[35] D. Bahdanau, K. Cho, and Y. Bengio, "Neural machine translation by jointly learning to align and translate," 2014, https://arxiv.org/abs/1409.0473.

[36] G. Gelly and J. Gauvain, "Optimization of RNN-based speech activity detection," IEEE/ACM Transactions on Audio, Speech, and Language Processing, vol. 26, no. 3, pp. 646–656, 2018.

[37] B. Zhao, X. Li, and X. Lu, "C. A. M.-R. N. N.: Co-attention model based RNN for video captioning," IEEE Transactions on Image Processing, vol. 28, no. 11, pp. 5552–5565, 2019.

[38] T. Mahmud, S. S. Akash, S. A. Fattah, W. P. Zhu, and M. O. Ahmad, "Human activity recognition from multimodal wearable sensor data using deep multi-stage LSTM

architecture based on temporal feature aggregation," in *Proceedings of the 63rd International Midwest Symposium on Circuits and Systems (MWSCAS)*, pp. 249–325, IEEE, Springfield, MA, USA, August 2020.

[39] N. Tavakoli, "Modeling genome data using bidirectional LSTM," in *Proceedings of the 43rd Annual Computer Software and Applications Conference (COMPSAC)*, pp. 183–188, IEEE, Milwaukee, WI, USA, July 2019.

[40] S. M. Pincus, "Approximate entropy as a measure of system complexity," *Proceedings of the National Academy of Sciences of the United States of America*, vol. 88, no. 6, pp. 2297–2301, 1991.

WILEY | Hindawi

Research Article

Energy-Saving D2D Wireless Networking Based on ACO and AIA Fusion Algorithm

Jiatong Li,[1,2] **Zhibo Li,**[1,2] **Xuanying Li,**[1,3] **and Cheng Wang** [1,4]

[1]*Tianjin Key Laboratory of Wireless Mobile Communications and Power Transmission, Tianjin Normal University, Tianjin 300387, China*
[2]*Department of Communication Engineering, College of Electronic and Communication Engineering, Tianjin Normal University, Tianjin 300387, China*
[3]*Department of Electronic Information Science and Technology, College of Electronic and Communication Engineering, Tianjin Normal University, Tianjin 300387, China*
[4]*Department of Intelligence Science and Technology, College of Artificial Intelligence, Tianjin Normal University, Tianjin 300387, China*

Correspondence should be addressed to Cheng Wang; cwang@tjnu.edu.cn

Lower energy consumption and higher data rate have been becoming the key factors of modern wireless mobile communication for the improvement of user experiences. At present, the commercialization of 5G communications is gradually promoting the development of Internet of things (IoT) techniques. Due to the limited coverage capability of direct wireless communications, the indirect device-to-device (D2D) communications using information relay, in addition to the single 5G base station deployment, have been introduced. Along with the increase of information nodes, the relay devices have to undertake the nonnegligible extra data traffic. In order to adjust and optimize the information routing in D2D services, we present an algorithmic investigation referring to the ant colony optimization (ACO) algorithm and the artificial immune algorithm (AIA). By analyzing the characteristics of these algorithms, we propose a combined algorithm that enables the improved the iterative convergence speed and the calculation robustness of routing path determination. Meanwhile, the D2D optimization pursuing energy saving is numerically demonstrated to be improved than the original algorithms. Based on the simulation results under a typical architecture of 5G cellular network including various information nodes (devices), we show that the algorithmic optimization of D2D routing is potentially valid for the realization of primitive wireless IoT networks.

1. Introduction

Since the late eighties of the last century, the Internet has been fast developing along with the progress of personal computers. Meanwhile, a concept of "connecting ubiquitous devices with Internet" emerged [1, 2] and further guided the research of the Internet of Things (IoT) for more comprehensive information sharing [3]. To date, the development of hardware techniques has made great progress. For instance, the fifth generation (5G) broadband communications employing high-frequency wavebands have unprecedentedly enhanced the data traffic performances [4]. However, it also has been noted that higher frequency leads

to greater energy consumption due to the path loss of radio wave propagation [5]. As a result, the increasing dataflow requiring higher frequency inevitably encounters a power supply problem, which may lead to the unacceptable deployment density requirement of base stations [6, 7]. Therefore, for the wireless networking of IoTs, the dataflow pressure of central base station is a critical challenge [8, 9]. Under the current hardware development level, the direct routing scenarios using the traditional station-device communication scheme may not be suitable.

Focusing on the issues above, we consider that the networking of wireless IoTs may have to fully utilize the current hardware and pursuing energy-efficient scenarios

from the algorithm aspect [10]. Following this idea, the algorithmic solutions improving the dataflow without additional energy consumption are commonly related to an indirect device-to-device (D2D) communication architecture, by which the information nodes (e.g., mobile devices) also undertake the message relay missions to reduce the data pressure of the central base station via proper routing solutions [11–13]. Thereby, figuring out an appropriate routing solution via programmed calculations and algorithms is significantly important to the D2D networking [14]. We regard that the D2D routing is somehow similar to a classical mathematic problem which is the location of logistics distribution. To efficiently find out an available routing solution (may not be exactly optimized) under the specific constraint (e.g., energy efficiency in this work), the most well-known algorithms are the ant colony optimization (ACO) and the artificial immune algorithm (AIA) [15, 16]. First, ACO algorithms are usually adopted in wireless networking, which can be divided into two categories, the direct communication and the connectionless networks. In a direct one, all the message packets in the same loop propagate via a common path, which is selected by the preliminary setup state. On the contrary, the connectionless packets in the same loop propagate via different paths [17, 18]. For the routing solution problem, the ACO algorithms envision the even and random manners of the information nodes and update the potentially optimal paths step-by-step [19]. However, these algorithms are still hindered by some limitations to this day, such as the blind search and local optimum problems. To overcome these issues, the routing scenarios employing AIA have been investigated for the fast convergence and the global optimization [20–22]. Although the information feedback in AIA programming is usually inefficient, which may lead to severely redundant iterations, the global optimizing advantage complementary to that of ACO algorithms may potentially open up a novel feasible algorithm appropriate to the iterative calculations for the wireless D2D routing paths [23].

Following these ideas, we proposed and a new algorithm, which combines the ACO and AIA principles, and quantitatively discussed the iterative calculation performances via numerical simulations. In particular, the physical environment of the D2D networking was designed based on the existing commercial 5G architecture, and the optimization constraint was accordingly selected as the reduce of energy consumptions [10, 24, 25]. According to the numerical simulation results, we showed that the newly designed algorithm significantly improves the D2D routing solutions, and the energy-saving performance may potentially enable the primitive wireless IoTs for sensor network applications.

2. Algorithm

2.1. ACO Principle. The ACO algorithm was originally developed for the vehicle routing problems (VRPs). Under this configuration, the feasible routing solutions are regarded as the paths of ants with similar mathematical models [18]. The paths of the entire ant population constitute a solution space. Here, we introduce the ACO algorithm into the D2D routing

model. After each iteration, the ant colony in ACO judges the optimization feasibility of each subset in the solution space, according to the newest pheromone concentration, and finds the optimal path. To maintain the universality, we set the number of ants $m (m \in [1, M])$, the number of nodes $n (n \in [1, N])$, and the distance between any two nodes i and j as $d_{i,j} (i, j = 1, 2, \dots n)$. At the moment t, the pheromone concentration on a path connecting the nodes i and j is $\tau_{i,j}(t)$. In particular, at the initial time, $\tau_{i,j}(0) = \tau_0$. Considering that the next visiting node selected by ant k is determined by the pheromone concentration on the connection path between corresponding relay nodes s, the propagation probability denoted $P_{i,j}^k(t)$ can be expressed as

$$P_{i,j}^k(t) = \begin{cases} \dfrac{\left[\tau_{i,j}(t)\right]^\alpha \left[\eta_{i,j}(t)\right]^\beta}{\sum_{s \in B_m}\left\{\left[\tau_{i,j}(t)\right]^\alpha \left[\eta_{i,j}(t)\right]^\beta\right\}}, & \text{node } s \in B_m, \\ \\ 0, & \text{otherwise,} \end{cases}$$

(1)

where $\eta_{i,j}(t)$ is the heuristic function, representing the expected degree of the ant transfer from node i to node j, and B_m represents the set of relay nodes visited by ant m. Especially, α is the pheromone factor, greater α leads to higher pheromone concentration effect in transfer. Similarly, β is the heuristic function factor; larger β suggests higher probability of a relay node being selected. Regarding the modelling of ACO in path routing, we assume that there are m ants in a quality of service (QoS) routing network, and the global and local pheromone updating rules are adopted [26]. Only the solution belongs to the global optimization path may lead to the increase of pheromone. We then select a constant $q_0 \in [0, 1]$ as the transfer factor and define a random variable $q \in [0, 1]$ to describe the determination of the next node. While an ant i in node r selects the next node s according to the following rules, if $q \le q_0$, the next node maximizes $[\tau_{i,j}(t)]^\alpha [\eta_{i,j}(t)]^\beta$. In contrast, if $q > q_0$, the state transfer probability determined by equation (1) remains unchanged:

$$\rho_i(r, s) = \begin{cases} \max[\text{pheromone}(r, s)], & \text{node } s \in B_m \\ 0, & \text{otherwise.} \end{cases}$$

(2)

According to equation (2), the ant transfer state determines the output probability results, which ensure the path optimization by searching the local maxima.

Following this principle, the ACO algorithms adopt the feedback mechanism and leave more concentrated pheromone in the paths, which indicates the better solutions. The positive feedback makes search processes continuously converging and finally approaching the optima. Any pheromone changes alter the surrounding environment and result in timely updates of the constraint result. Besides, if a suboptimal solution is utilized in the initial of calculation, the iterative convergence could be significantly accelerated. However, the rapid converging advantage may also induce a potential local optimum issue. As a result, other algorithms for the speed-optimum trade-off are necessary.

2.2. AIA Principle. To get rid of the local optimum hindrance, the node prediction step planning for the more effective global routing suggests the AIA principle [27]. Under the classical AIA configuration, the antigens represent the subsets of a solution space, and the antibodies represent the coding sets of corresponding relay nodes. The antigen-antibody affinity indicates the recognition strength of a target node. Thus, the affinity function could be designed as a location model of the transmission of the node:

$$A_v = \frac{1}{F_v}$$

$$= \frac{1}{\sum_{i \in N}\left[\sum_{j \in M_i}\left(\omega_i d_{i,j} Z_{i,j}\right)\right] - C\sum_{i \in N}\min\left\{\left(\sum_{j \in M_i} Z_{i,j}\right) - 1, 0\right\}},$$

(3)

where F_v is the objective function, N is the set of all nodes, M_i is a subset including the nodes i away from the base station closer than s, w_i is the data volume of node i, $d_{i,j}$ is the distance between the nodes i and j, C is a manually selected large positive constant, and $Z_{i,j}$ is the distribution relation of the transmission data traffic between the central base station and a relay node. In the denominator of equation (3), the second term represents the punishment for the spatial solution violating the distance constraint. In addition, the similarity among antibodies is expressed as

$$S_{v,s} = \frac{k_{v,s}}{L},$$

(4)

where $k_{v,s}$ is the number of same bits of two antibodies v and s and L is the length (number of bits) of antibody. Then, the antibody concentration can be obtained as

$$C_v = \frac{1}{N}\sum_{j \in N} S_{v,s}.$$

(5)

Thereby, according to the affinity A_v and the concentration C_v above, the reproductive probability of an individual node is determined as

$$P = \alpha\frac{A_v}{\sum A_v} + (1 - \alpha)\frac{C_v}{\sum C_v},$$

(6)

where α is an arbitrary constant factor. In equation (6), the individual fitness applies a positive effect on the expected reproduction probability. Higher affinity is helpful to the global optimization. However, due to the application of random searching, the efficiency of programming iteration and convergence are usually limited. On the basis of the discussion above, we considered to design a combined algorithm, which manages to concurrently take the advantages of ACO and AIA.

2.3. ACO/AIA Algorithmic D2D Routing. Under the current cellular network architecture, the deployment density increase of wireless devices (e.g., cellphones, unmanned equipment, and sensor array) results in the much greater data traffic pressure of the central base station. Thus, the traditional direct connection strategies are usually not available, especially on the energy consumption management aspect [28, 29]. In order to handle this difficulty, the D2D networking exploiting wireless devices as the relay nodes has to be proposed as a potentially applicable approach. Because of the requirement of routing determination in D2D networking, the algorithm performances in converging speed and accuracy are significantly important. As a result, the selection of information propagation paths has to be readily determined with the global optimization. As we discussed above, two representative algorithms (i.e., ACO and AIA) support the iterative programming for the optimal routing determination, and occupy advantages complementary to each other [30]. Therefore, we tried to combine them together to concurrently preserve their advantages. In this work, the D2D routing is discussed as a typical wireless IoT networking mission under the existing 5G architecture [25].

The main idea of ACO/AIA fusion algorithm is replacing the worst antibody with the code represented by the best ant, thus to realize the information exchange between ACO and AIA. By using AIA, a series of starting times from the solution space can be selected to generate antibodies, and the ACO algorithm uses the solution space as the search range. On the basis of equation (1), we can further deduce the iterative update of pheromone $\tau_{i,j}(t)$ described by

$$\tau_{i,j}(t + 1) = (1 - \psi)\tau_{i,j}(t) + \psi_{\tau_0},$$

(7)

where $\psi \in (1, 0]$ is a constant, $\tau_0 = (mF_{nn})^{-1}$ is the initial value of the pheromone trajectory between the channel nodes, and F_{nn} is the fit value calculated by the nearest distance heuristic algorithm. Then, according to the guardian behavior in AIA, the optimal solution generated by ACO is used to stimulate the local search process. Meanwhile, the updating rules of pheromone trajectory are defined by

$$\tau_{i,j}(t + 1) = (1 - \rho)\tau_{i,j}(t) + \rho\Delta\tau_{i,j}(t), \quad \rho \in (0, 1],$$

(8)

where ρ is the volatile coefficient of pheromone and $\tau_{i,j}(t)$ is the pheromone increment of at t. At the time t, the ants pass through the node once, the local and global pheromones need updates. The pheromone parameters are adjusted according to equations (1) and (2) to prevent the local optimal solution. The affinity function A_v obtained by equation (3) is used to define the final D2D algorithm pheromone update:

$$\text{pheromone}(i, j) = \begin{cases} (1 - p)\,\text{pheromone}(i, j) + \rho A_v, & \text{nodes } i,\ j \text{ on path,} \\ (1 - p)\,\text{pheromone}(i, j) + b\rho A_v, & \text{otherwise.} \end{cases}$$

(9)

In equation (9), $b \in (0, 1)$ is a constant, which prevents the exceeding pheromone concentrations on multipath. Before the D2D routing optimization algorithm is complete, it maintains the iteration until the final convergence is obtained.

While the ACO/AIA fusion algorithm is proposed, we continue to discuss the constraint for the D2D networking optimization. Since our target is realizing a technically practical IoT scenario based on D2D routing, the optimization constraint is correspondingly set to make the total energy consumption minimized, at least lower than the traditional station-device direct communications. As the current communication techniques have almost approached the information channel capacity close to the Shannon limit, the data rate in this work is estimated by the upper limit. Then, based on the existing 5G architecture, we define the service zone covered by a single base station. Simply, we set a regular hexagon with the side length of $d_{\max} = 60$m. According to the Friis transmission formula, the data rate becomes a univariate function of the distance d. Therefore, the data rates of station-device (R_{bs}) and device-device (R_{dv}) are expressed as follows:

$$\begin{cases} R_{bs} = W_{EH}\log_2\left[1 + \dfrac{P_{bs_{\max}}^{tran}G\left(c/4\pi f_{EH}d\right)^2}{p_n W_{EH}}\right], & d \in [0, d_{\max}], \\\\ R_{dv} = W_{SH}\log_2\left[1 + \dfrac{P_{dv_{\max}}^{tran}G\left(c/4\pi f_{SH}d\right)^2}{p_n W_{SH}}\right], & d \in [0, d_{\max}]. \end{cases}$$

(10)

In equation (10), $f_{EH} = 50$GHz and $f_{SH} = 2.4$GHz indicate the carrier wave frequencies of base station (extreme high frequency, EHF) and wireless devices (special high frequency, SHF), respectively. Accordingly, $W_{EH} = 500$ MHz and $W_{SH} = 24$MHz are the typical bandwidths of EHF and SHF, $P_{bs_{\max}}^{tran} = 400$W and $P_{dv_{\max}}^{tran} = 1$W are the typical power levels of EHF and SHF, $P_n = 3.981 \times 10^{-21}$WHz^{-1} is the noise background power density, $c = 3 \times 10^8$ms^{-1} is the radiowave propagation speed, and $d \leq d_{\max} = 60$m is the distance between any two nodes. The distribution of all the wireless devices, as well as the relay nodes, within a service zone is assumed to obey the Gaussian distribution. Therefore, in a representative loop l containing N_l nodes, the time length of D2D communication T_l is deduced as

$$\begin{aligned} T_l &= \sum_{n_l=1}^{N_l} T_{l,n_l} \\ &= \sum_{n_l=1}^{N_l}\left(\frac{1}{R_{l,n_l}}\sum_{i=1}^{n_l} I_{l,i}\right). \end{aligned}$$

(11)

Based on equation (11), the total energy consumption can be calculated using T_l values (including the values of devices T_{l,n_l} and base station T_{l_D2D}). Therefore, the optimization constraint for energy saving is expressed as

$$E = P_{dv_{\max}}^{tran}\sum_{n_l}^{N_l} T_{l,n_l} + P_{bs_{\max}}^{tran} T_{l\ D2\ D}.$$

(12)

By using equation (12), the ACO/AIA algorithm can be executed as an iterative program, until the convergence indicates the minimal energy consumption.

3. Simulation Results and Discussion

On the basis of the algorithm and constraint we discussed above, the D2D routing for the networking of an energy-saving IoT was testified via the programming iteration. After each iteration, the constraint result is calculated and fed back to the next iteration for the asymptotic minimization of constraint [30]. In particular, according to the existing 5G standard, the D2D sequence information amount sent by a base station is set as a constant of 10 Mb, and the data amount of a device is randomly generated obeying the Gaussian distribution within the range of 50–200 Mb. The programming scheme of out ACO/AIA fusion algorithm is illustrated in Figure 1, and the parameters used in the programming are provided in Table 1. In addition, to verify the performance advantage of our new algorithm, the classical ACO and AIA algorithms are also testified under the completely same conditions for comparisons [31].

Following the scheme in Figure 1, we first generate the information nodes (wireless devices) within a hexagonal cellular network service zone. As shown in Figure 2, the node positions including data amounts are randomly generated (30 nodes as a representative example in Figure 2(a)). The positions and data amounts of 30 nodes are also detailed in Table 2. While all the nodes are covered by a central base station, a traditional station-device direct connection model is constructed (Figure 2(b)).

We then executed the programming iterations based on the 30-node example (Figure 2) and presented the routing results in Figure 3. Comparing with the classical ACO and AIA algorithms, our novel fusion algorithm significantly reduces the large-span connections. And, the interferences between loops are also reduced. These numerical simulation results imply that the ACO/AIA fusion algorithm might be valid for the avoidance of local optimization disadvantages in the conventional algorithms.

Furthermore, the iterative optimization performances were quantitatively testified in the networking of 30-node situation. As shown in Table 3, all the results acquired from three algorithms approach stability after around 300-time iterations. However, the ACO/AIA algorithm exhibits much higher energy efficiency than the other two algorithms, as shown in Figure 4. The much higher energy consumption levels of ACO and AIA algorithms, especially the classical ACO algorithm, provide the relatively high final results, which imply the local optimization issue as we mentioned above.

Moreover, in order to further verify the universality of our algorithm in the energy-saving optimization, the cases including more devices (information nodes) were tested.
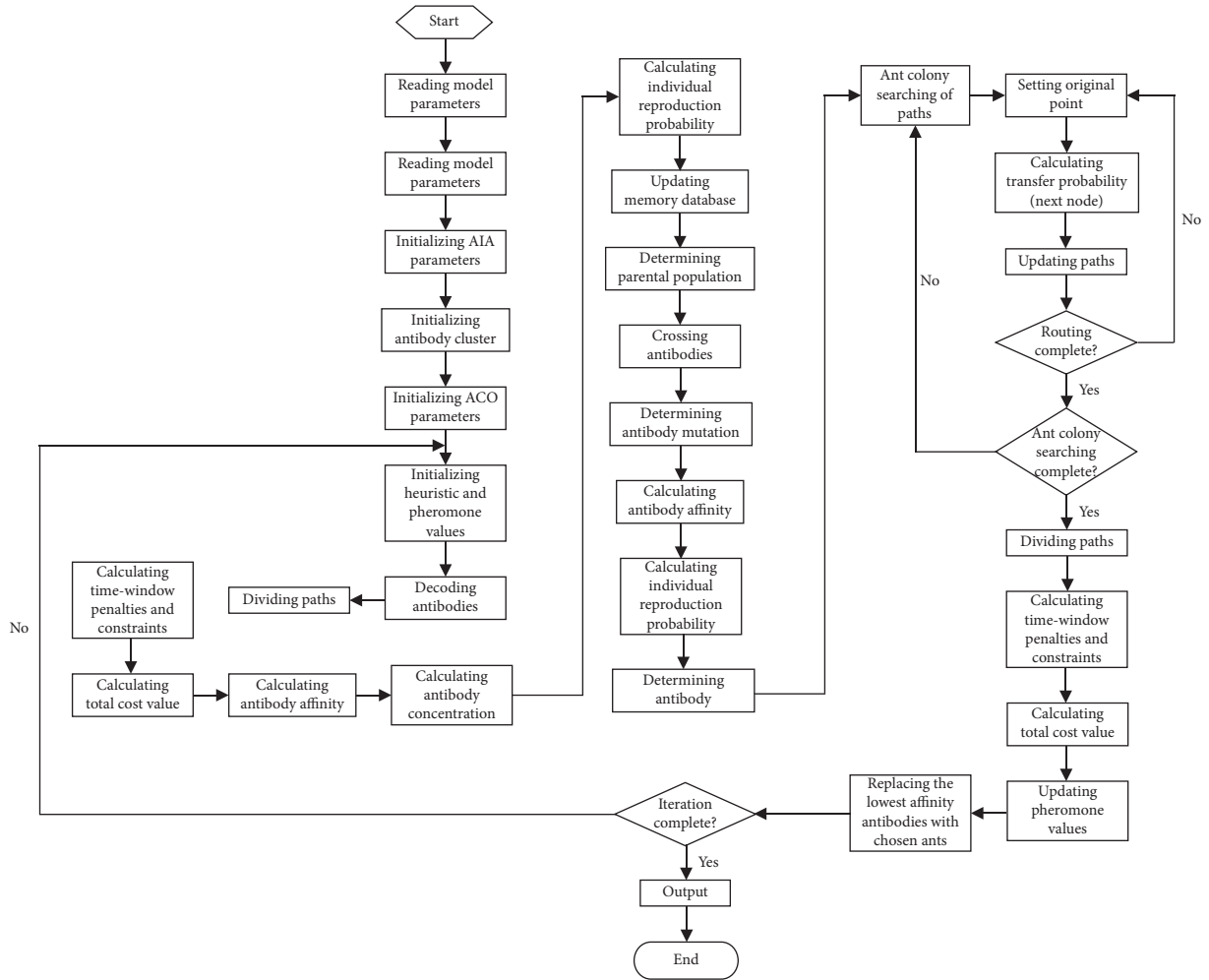
Figure 1: Programming scheme of the ACO/AIA algorithm for energy-saving optimization.

Table 1: Algorithm programming parameters.

Parameters	Value
Population size	100
Memory capacity	10
Crossover probability	0.5
Mutation probability	0.1
Diversity evaluation parameter	0.95
Pheromone index	2
Heuristic index	3
Pheromone volatility coefficient	0.1
Pheromone enhancer	1

As shown in Figure 5, the representative examples of D2D networking of 70, 150, 200, and 300 nodes optimized by using the ACO, AIA, and ACO/AIA fusion algorithms, respectively, are compared with each other. We discovered the consistent regularity that the ACO/AIA algorithm possesses the best energy efficiency and the convergence performance.

Besides, we would like to note that although D2D routing significantly enhances the energy efficiency, the time latency in indirect connections is an inevitable issue hindering the practical applicability. To overcome the time-delay hindrance, the final solution may still focus on the hardware developments, together with the algorithm investigations.
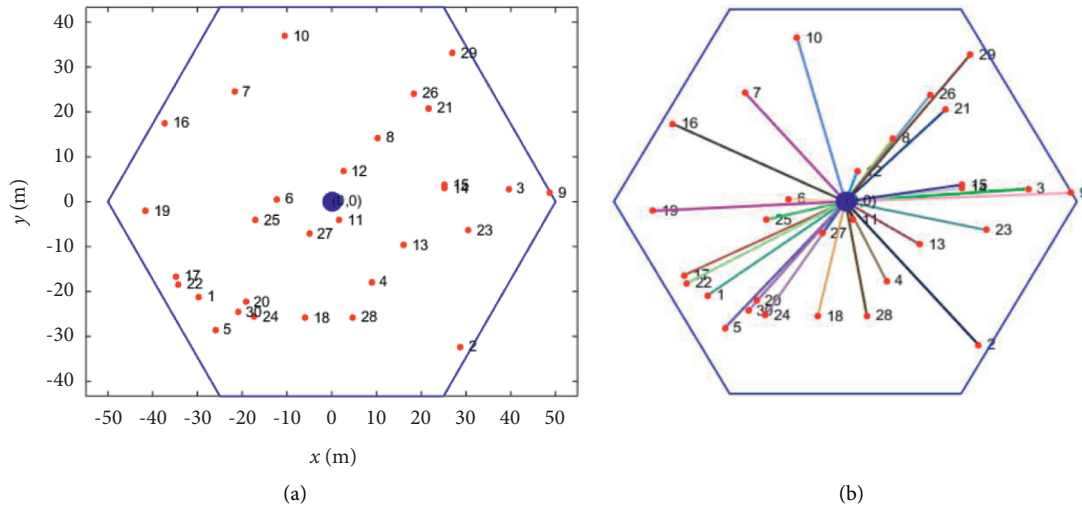
(a)

(b)

Figure 2: A representative wireless networking model containing 30 nodes. (a) Random generation of information nodes within a service zone. (b) Traditional direct communication strategy.

Table 2: Node position and data amount information corresponding to Figure 2.

| Node	x-coordinate (m)	y-coordinate (m)	Data size (Mb)
0	0	0	0
1	−29.75076725	−21.1451	98
2	28.8074986	−32.3711	82
3	39.51346795	2.855766	93
4	8.864290527	−17.8691	111
5	−26.04441642	−28.5067	119
6	−12.29841177	0.593461	89
7	−21.67998262	24.53206	98
8	10.27037863	14.25358	86
9	48.77741011	1.931686	110
10	−10.43393433	36.8657	126
11	1.760926681	−4.10528	80
12	2.552906914	6.706503	52
13	16.18910379	−9.73259	79
14	25.22775935	2.95136	70
15	25.23375902	3.787866	104
16	−37.32864055	17.53824	120
17	−34.73651287	−16.5719	83
18	−5.951438079	−25.8198	86
19	−41.53044014	−2.10741	83
20	−19.18381344	−22.3525	82
21	21.70052876	20.78692	89
22	−34.21303177	−18.425	58
23	30.45716541	−6.42097	112
24	−17.23243667	−25.5631	76
25	−16.96341148	−4.05674	61
26	18.38068225	24.12656	101
27	−4.98049597	−7.19577	143
28	4.651289738	−25.7734	108
29	26.93717204	33.05046	102
30	−20.95107025	−24.6377	59
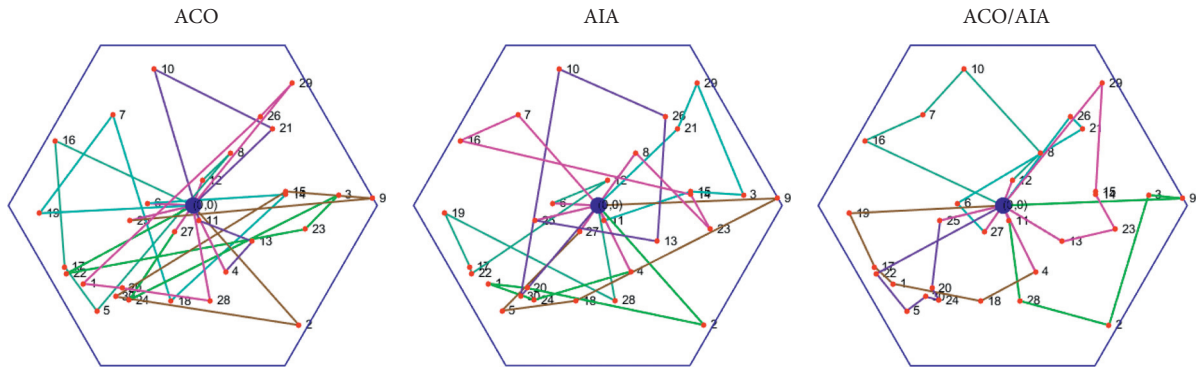
FIGURE 3: D2D routing results acquired from ACO, AIA, and ACO/AIA fusion algorithms (30 nodes in Figure 2).

TABLE 3: Optimization trends of energy-saving D2D networking (30-node) along with the iterations of ACO, AIA, and ACO/AIA fusion algorithms.

| The number of iterations	Total energy consumption		
	ACO	AIA	ACO/AIA
1	292150.8678	325210.4059	242842.1009
2	194461.987	325210.4059	242842.1009
3	194461.987	325210.4059	240157.053
. . .	. . .	. . .	. . .
. . .	. . .	. . .	. . .
100	194461.987	227245.5209	98898.74869
. . .	. . .	. . .	. . .
200	194461.987	128434.1946	76446.35832
. . .	. . .	. . .	. . .
300	194343.9423	125626.1345	73241.97747
301	194343.9423	125626.1345	73241.97746
302	194343.9423	125626.1345	73241.97746
303	194343.9423	125626.1345	73241.97746
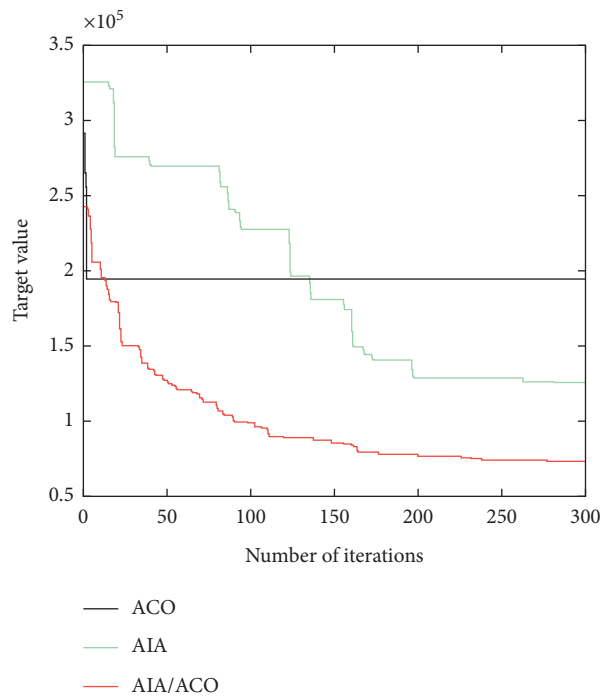
FIGURE 4: Energy efficiency optimization trends of ACO, AIA, and ACO/AIA fusion iterations.
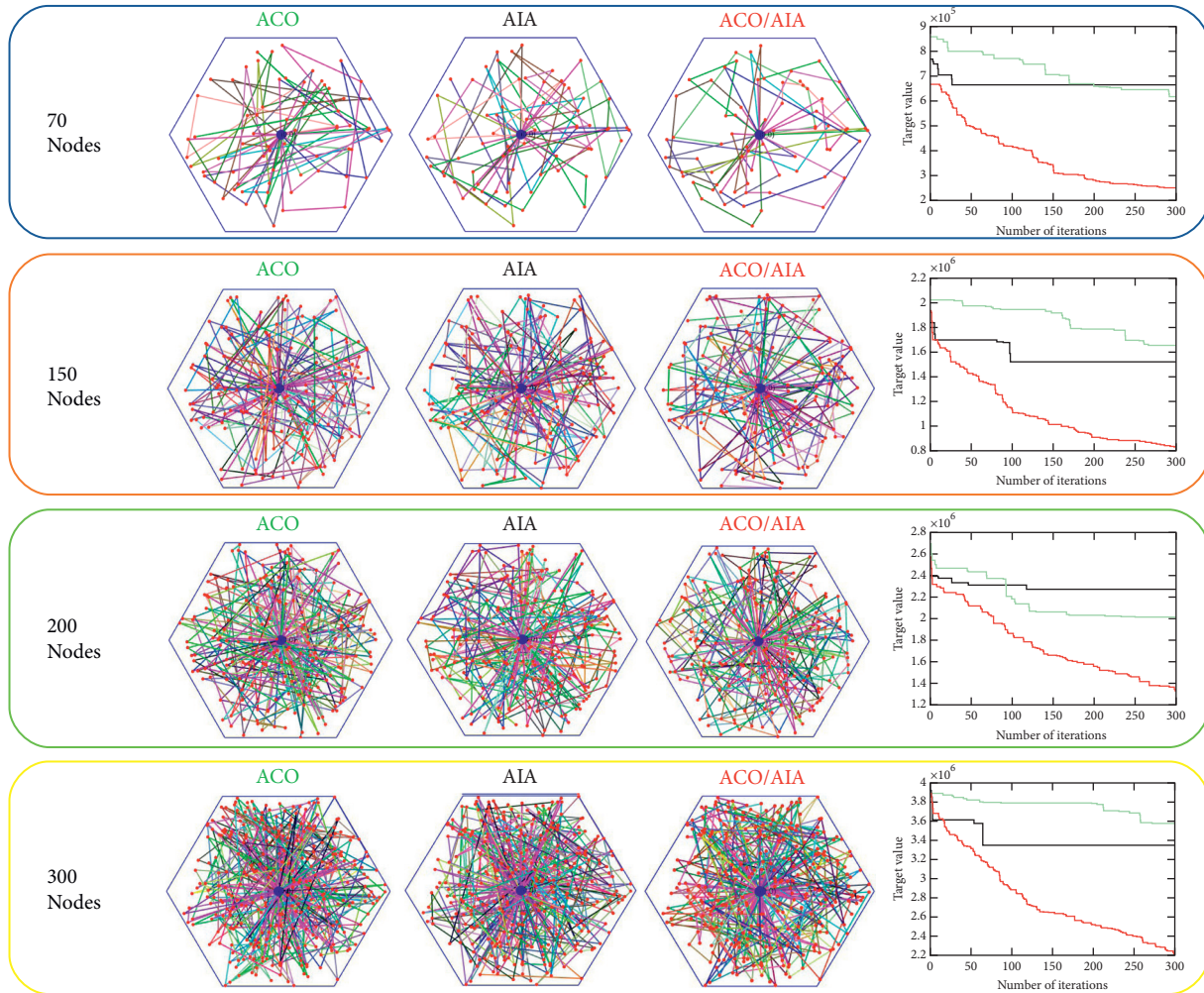
FIGURE 5: D2D routing results of 70, 150, 200, and 300 nodes optimized by ACO, AIA, and ACO/AIA fusion algorithms. Obviously, the ACO/AIA fusion algorithm provides much high iteration efficiency in the optimization for energy saving.

4. Conclusion

In summary, we investigated the D2D routing scenarios for the energy-efficient networking from the algorithm aspect. Based on the numerical simulation results, we illustrated that the program iteration is a technical option for the construction of primitive D2D wireless IoTs, under the current hardware developing level. More importantly, we proposed a D2D routing algorithm based on the classical ACO and AIA algorithms. By testing the iterative optimization under the energy-saving constraint, the novel ACO/AIA fusion algorithm provides more satisfactory converging performances than traditional algorithms. The authors regard that the exploration of wireless IoT networking could be moved forward following this algorithmic method, concurrent to the hardware developments.

Data Availability

The data used to support the findings of this study are available from the corresponding author upon request.

Conflicts of Interest

The authors declare no conflicts of interest.

Acknowledgments

References

[1] K. Ashton, "That 'internet of things' thing," *RFID Journal*, vol. 22, no. 7, pp. 97–114, 2009.

[2] B. Zhang, W. Liu, Q. Li et al., "Directional modulation design under a given symbol-independent magnitude constraint for secure IoT networks," *IEEE Internet of Things Journal*, 2020.

[3] L. Atzori, A. Iera, and G. Morabito, "The internet of things: a survey," *Computer Networks*, vol. 54, no. 15, pp. 2787–2805, 2010.

[4] W. Saad, M. Bennis, and M. Chen, "A vision of 6G wireless systems: applications, trends, technologies, and open research problems," *IEEE Network*, vol. 34, no. 3, pp. 134–142, 2019.

[5] J. Wu, H. Shen, R. Yin, Y. He, J. Li, and C. Wang, "Displaying images on a plane of rotation via mutual inductance coupling wireless controls," *Ad Hoc Networks*, vol. 107, Article ID 102256, 2020.

[6] B. Zhang, W. Liu, J. Ma et al., "Sparse antenna array based positional modulation design with a low-complexity metasurface," *IEEE Access*, vol. 8, Article ID 177640, 2020.

[7] C. Wang, B. Zhang, Y. Li, and X. Zhao, "Suspended graphene hydroacoustic sensor for broadband underwater wireless communications," *IEEE Wireless Communications*, vol. 27, no. 5, pp. 44–52, 2020.

[8] B. Nishina and Q. Chen, "Estimation of equivalent current distribution of modulated EM radiation source," *IEEE Transactions on Antennas and Propagation*, vol. 64, no. 4, pp. 1334–1341, 2016.

[9] B. Zhang, W. Liu, Y. Li, X. Zhao, and C. Wang, "Directional modulation design under maximum and minimum magnitude constraints for weight coefficients," *Ad Hoc Networks*, vol. 98, Article ID 102034, 2020.

[10] W. Ejaz, M. Naeem, A. Shahid, A. Anpalagan, and M. Jo, "Efficient energy management for the internet of things in smart cities," *IEEE Communications Magazine*, vol. 55, no. 1, pp. 84–91, 2017.

[11] H. Wu, X. Gao, S. Xu, D. O. Wu, and P. Gong, "Proximate device discovery for D2D communication in LTE advanced: challenges and approaches," *IEEE Wireless Communications*, vol. 27, no. 4, pp. 140–147, 2020.

[12] B. Zhang, W. Liu, Y. Li, X. Zhao, C. Zhang, and C. Wang, "Symbol-independent weight magnitude design for antenna array based directional modulation," *Ad Hoc Networks*, vol. 101, Article ID 102097, 2020.

[13] K. Doppler, M. Rinne, C. Wijting, C. Ribeiro, and K. Hugl, "Device-to-device communication as an underlay to LTE-advanced networks," *IEEE Communications Magazine*, vol. 47, no. 12, pp. 42–49, 2009.

[14] C. Di, B. Zhang, Q. Liang, S. Li, and Y. Guo, "Learning automata-based access class barring scheme for massive random access in machine-to-machine communications," *IEEE Internet Things Journal*, vol. 6, no. 4, pp. 6007–6017, 2018.

[15] I. Aydin, M. Karakose, and E. Akin, "A multi-objective artificial immune algorithm for parameter optimization in support vector machine," *Applied Soft Computing*, vol. 11, no. 1, pp. 120–129, 2011.

[16] M. Dorigo and C. Blum, "Ant colony optimization theory: a survey," *Theoretical Computer Science*, vol. 344, no. 2-3, pp. 243–278, 2005.

[17] B. Zhang, W. Liu, Y. Li, X. Zhao, and C. Wang, "Directional modulation design under a constant magnitude constraint for weight coefficients," *IEEE Access*, vol. 7, Article ID 154711, 2019.

[18] D. Martens, M. D. Backer, R. Haesen, J. Vanthienen, M. Snoeck, and B. Baesens, "Classification with ant colony optimization," *IEEE Transactions on Evolutionary Computation*, vol. 11, no. 5, pp. 651–665, 2007.

[19] M. Dorigo, M. Birattari, and T. Stutzle, "Ant colony optimization," *IEEE Computational Intelligence Magazine*, vol. 1, no. 4, pp. 28–39, 2006.

[20] M. Pedemonte, S. Nesmachnow, and H. Cancela, "A survey on parallel ant colony optimization," *Applied Soft Computing*, vol. 11, no. 8, pp. 5181–5197, 2011.

[21] B. Zhang, W. Liu, Q. Li et al., "Metasurface based positional modulation design," *IEEE Access*, vol. 8, Article ID 113807, 2020.

[22] D. Dasgupta, "Advances in artificial immune systems," *IEEE Computational Intelligence Magazine*, vol. 1, no. 4, pp. 40–49, 2006.

[23] S. Cui, A. J. Goldsmith, and A. Bahai, "Energy-efficiency of MIMO and cooperative MIMO techniques in sensor networks," *IEEE Journal on Selected Areas in Communications*, vol. 22, no. 6, pp. 1089–1098, 2004.

[24] M. Waqas, Y. Niu, Y. Li et al., "Mobility-aware device-to-device communications: principles, practice and challenges," *IEEE Communications Surveys & Tutorials*, vol. 18, no. 7, pp. 3658–3668, 2019.

[25] K. David and H. Berndt, "6G vision and requirements: is there any need for beyond 5G?" *IEEE Vehicular Technology Magazine*, vol. 13, no. 3, pp. 72–80, 2018.

[26] S. Reddy, "Multi-path selection based on fractional cuckoo search algorithm for QoS aware routing in MANET," *Sensor Review*, vol. 39, no. 2, pp. 218–232, 2019.

[27] Q. Yu, J. Ren, J. Zhang et al., "An immunology-inspired network security architecture," *IEEE Wireless Communication*, vol. 27, no. 5, pp. 168–173, 2020.

[28] L. Zou, J. Chen, L. Lv, and B. He, "Capacity enhancement of D2D aided coordinated direct and relay transmission using NOMA," *IEEE Communications Letters*, vol. 24, no. 10, pp. 2128–2132, 2020.

[29] P. Popovski and H. Yomo, "Wireless network coding by amplify-and-forward for bi-directional traffic flows," *IEEE Communications Letters*, vol. 11, no. 1, pp. 16–18, 2007.

[30] J. Li, M. Li, J. He, W. Shi, and C. Wang, "D2D routing aided networking for efficient energy consumption management of wireless IoT," *Ad Hoc Networks*, vol. 123, Article ID 102636, 2021.

[31] R. Shafin, L. Liu, V. Chandrasekhar, H. Chen, J. Reed, and J. C. Zhang, "Artificial intelligence-enabled cellular networks: a critical path to beyond-5G and 6G," *IEEE Wireless Communications*, vol. 27, no. 2, pp. 212–217, 2020.

WILEY | Hindawi

Research Article

Randomization-Based Dynamic Programming Offloading Algorithm for Mobile Fog Computing

Wenle Bai,[1] Zhongjun Yang [iD],[2] Jianhong Zhang,[3] and Rajiv Kumar[4]

[1]*Information Science and Technology, North China University of Technology, Shijingshan District, Beijing 100043, China*
[2]*School of Information Science and Technology, North China University of Technology, Shijingshan District, Beijing 100043, China*
[3]*North China University of Technology, Beijing, China*
[4]*Department of Electronics and Communication As a Professor, Jaypee University of Information Technology, Waknaghat, India*

Correspondence should be addressed to Zhongjun Yang; 1076943446@qq.com

Offloading to fog servers makes it possible to process heavy computational load tasks in local devices. However, since the generation problem of offloading decisions is an N-P problem, it cannot be solved optimally or traditionally, especially in multitask offloading scenarios. Hence, this paper has proposed a randomization-based dynamic programming offloading algorithm, based on genetic optimization theory, to solve the offloading decision generation problem in mobile fog computing. The algorithm innovatively designs a dynamic programming table-filling approach, i.e., iteratively generates a set of randomized offloading decisions. If some in these sets improve the decisions in the DP table, then they will be merged into the table. The iterated DP table is also used to improve the set of decisions generated in the iteration to obtain the optimal offloading approximate solution. Extensive simulations show that the proposed DPOA can generate decisions within 3 ms and the benefit is especially significant when users are in multitask offloading scenarios.

1. Introduction

With the increasing popularity of smart devices, smart applications provide a rich user experience while placing stringent demands on computing power. Due to the limitations of mobile devices, it becomes a challenge to maintain the quality of service when traditional devices are faced with heavy computational demands. To solve this problem, mobile fog computing (MFC) [1] has been proposed to compensate for the lack of computing power in local devices. And, it alleviates the computing congestion of cloud by offloading tasks to fog nodes at the edge of the network, as well.

In MFC, there are two major problems to be solved. The first is how to determine whether a task should be offloaded or not. The other is how to balance the delay performance and energy consumption as much as possible, while offloading tasks. In order to solve the above problems, some

offloading algorithms have been proposed in the literature. In [2], by modeling task generation as a Poisson process, the processing in the server is modeled as an $M/M/1$ model. A closed-form expression for the offloading delay is derived to find the global optimal solution with the lowest latency performance. Subdividing a task into the offloadable and non-offloadable part, the study in [3] constructs an opportunistic offloading model. A delayed offloading model is introduced in [4], in which tasks will wait as long as possible until the WIFI link is available to offload before the dead time arrives. Aiming at minimizing the energy consumption, the work in [5] develops an offloading interaction model based on the auction mechanism, while the authors of [6] propose an incentive propagation mechanism (IPM) algorithm.

In the traditional MFC network, a key research point is the joint design of the offloading decision and system resource allocation to optimize system effectiveness. The

study in [7] proposes a fair and energy-minimized task offloading (FEMTO) algorithm, which considers three important characteristics: the energy consumption of the offloading, the historical average energy of the F-AP, and the priority of the F-AP. The offloading decision problem and the uplink channel assignment problem are designed as a quadratic constrained quadratic programming (QCQP) problem in [8]. Then, the proposed matrix algorithm is used to solve the QCQP problem to obtain the suboptimal solution. The offloading problem in [9] is solved by transforming it into a nonconvex QCQP problem and then solving that with the proposed semidefinite relaxation algorithm.

With the boon of deep learning in recent years, some studies have combined deep learning with the MFC. The study in [10] proposes a joint computational offloading and resource allocation algorithm based on deep reinforcement learning (DRL), which is used for deriving a suboptimal solution for the optimization problem. A deep learning-based offloading algorithm is proposed in [11], which uses the trained DNN to generate offloading decisions for each task. The work in [12] introduces an empirical replay technique based on the reinforcement learning, which improves the convergence rate of the offloading algorithm. Similarly, the study in [13] adds a layer of the LSTM network to the deep Q network, which is used for predicting the amount of tasks to be received by the fog node at the next moment. Compared to the deep Q algorithm, the algorithm with the LSTM network can arrive at the optimal decision faster. Although these intelligent algorithms have very high offloading accuracy, the training of the network requires a long time. Meanwhile, these excessively complex algorithms will additionally increase the computational burden of IoT (Internet of Things) devices. Hence, they are not applicable for real-time computational offloading of MFC networks in time-varying environments.

In this work, attention is paid to the task offloading problem in an MFC network and a dynamic programming offloading algorithm (DPOA) based on randomization is proposed to solve the offloading decision generation problem. The achievements obtained in this paper are as follows:

(1) Randomization is introduced in the DPOA, where the system periodically generates a random set of offloading decisions of 1 or 0. And, these randomized decisions are used to construct a two-dimensional dynamic programming (DP) table, as well.

(2) The DP table is populated in a novel way, which avoids the double computation of the common decision cells in the generated random set. After enough iterations of the algorithm, the optimal approximate solution can be obtained from a query of the populated DP table.

(3) Extensive simulations show that the algorithm is highly responsive. And, the algorithm maintains optimal approximate decision generation within 3 ms for a wide range of system parameter settings.

The rest of this paper is as follows: the model of the MFC network and the closed-form expressions for latency and energy consumption are presented in Section 2, as well as the construction of an energy-latency weighted sum minimization problem. The DPOA is referred in Section 3. Section 4 mainly provides the analysis of simulations. And, the conclusions are given in the last section.

2. Network Model and Problem Formulation

2.1. Network Model. As shown in Figure 1, the network model investigates an MFC network consisting of multiple users, a single fog access point (F-AP), and a remote cloud server, where users interact with the F-AP through a wireless channel for data interaction. The F-AP and the cloud server are interconnected with an optical fiber. Assume that each user has N mutually independent tasks to compute, denoted as $N = \{1, 2, \ldots, N\}$. Each task is indivisible to the user and can be processed either locally, offloaded to a F-AP for processing or further to the cloud server.

The offloading decision of the n-th task at the local side is represented by the binary variable $X_F^n \in \{0, 1\}$. Then, $X_F^n = 0$ ($X_F^n = 1$) represents the task that will be processed at the local side (offloaded to the fog). Similarly, let $X_C^n \in \{0, 1\}$ represent the n-th task's decision that is on the fog side. $X_C^n = 0$ denotes the task that will remain on the fog side for computation, and, conversely, $X_C^n = 1$ represents the task being further offloaded to the cloud.

2.2. Problem Formulation. In the local computing mode, as the task is computed only in the local processor without involving data upload, the total energy and total time consumed are equal to those of the processor. The size of n-th task is denoted by M_n. Let κ and f_L represent the energy consumption per bit of task computed and the computation rate (cycle/s) at the local device, respectively. The energy consumption and latency of M_n computed locally are

$$E_L^n = \kappa M_n, \tag{1}$$

$$T_L^n = \frac{M_n \phi}{f_L}, \tag{2}$$

where ϕ indicates the number of CPU revolutions required that processes per bit of data (cycle/bit), which is determined by the CPU process. Without loss of generality, it is presumed that the all covered ϕ of the devices in this paper are all equal.

When $X_F^n = 1$ is in place, the task will be offloaded to the nearest F-AP over the wireless network. The task offloaded to the fog will be redistributed by the algorithm, and some will be further offloaded to the cloud server. According to [9, 11, 14, 15], it is known that the offloading backhaul data is extremely small, much smaller than of the offloaded, so the return cost is chosen to be ignored. Let the transmission rate between users and F-AP be B_F; then, the transmission time to the fog is
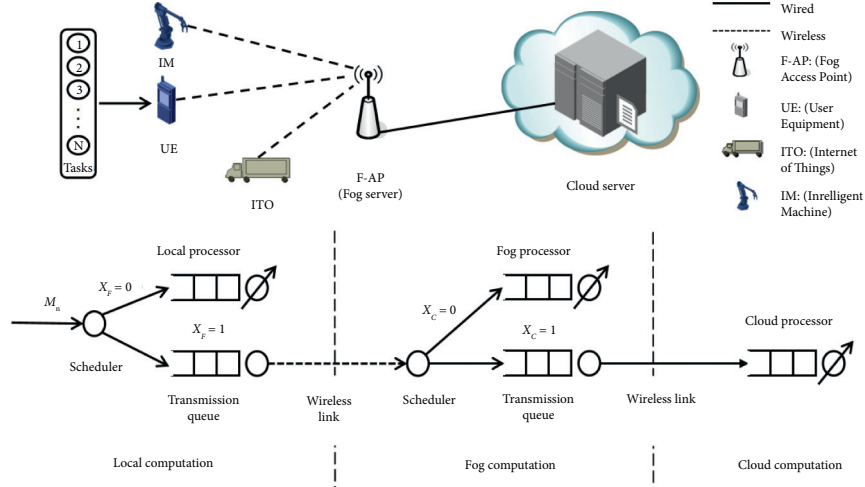
FIGURE 1: Network scenarios and offloading computation models for mobile fog computing.

$$T_{tF}^n = \frac{M_n}{B_F}. \tag{3}$$

With f_F denoting the processing rate of the fog server, the computation time consumed in the fog is

$$T_F^n = \frac{M_n\phi}{f_F}. \tag{4}$$

About the cloud computing model, F-APs are interconnected with the cloud server through the fiber and the transfer rate between both is expressed in terms of B_C. Then, the total time cost from the local side to the cloud can be recorded as

$$T_{tC}^n = \frac{M_n}{B_F} + \frac{M_n}{B_C}. \tag{5}$$

Representing the processing rate of the cloud server by f_C, the cloud computing time cost for the n-th task is

$$T_C^n = \frac{M_n\phi}{f_C}. \tag{6}$$

For energy consumption, as the essence of offloading is to handle complex or large tasks, which is difficult for the local side, this paper only considers the transmission and standby energy consumption in the local device while ignoring the energy cost at the server. Hence, the transmission energy consumption of the n-th task offloading to the fog is shown in

$$E_t^n = \alpha M_n, \tag{7}$$

where α is the energy consumption of the local device that transmits per bit of data.

In addition, the output of the local device is modeled as an $M/M/1$ queue and the system distributes the $n+1$th task only when the n-th has been processed. Meanwhile, if task n is offloaded, the local device will remain in the standby mode. Using P to present the standby power of the device, the standby energy consumption during offloading M_n can be expressed as E_w^n:

$$E_w^n = P \cdot \left[X_F^n\left(T_{tF}^n + T_F^n\right) + X_F^n X_C^n\left(T_{tC}^n + T_C^n\right)\right]. \tag{8}$$

For any user in the MFC network, the total latency and energy consumption of processing all tasks can be expressed, respectively, as follows:

$$T = \sum_{n=1}^{N}\left[(1 - X_F^n)T_L^n + X_F^n\left(1 - X_C^n\right)\left(T_{tF}^n + T_F^n\right) + X_F^n X_C^n\left(T_{tC}^n + T_C^n\right)\right], \tag{9}$$

$$E = \sum_{n=1}^{N}\left[X_F^n E_t^n + \left(1 - X_F^n\right)E_L^n + E_w^n\right]. \tag{10}$$

In order to minimize the total energy and time consumption to complete all tasks, this paper introduces a system utility Θ defined as a weighted sum of energy and latency, as shown in

$$\Theta(\mathbf{X}) = E + \gamma T, \tag{11}$$

where $\mathbf{X} = \{X_F^n, X_C^n \mid n \in \mathbf{N}\}$ and $\gamma \in [0, +\infty)$; (J/s) is the weight variable. When $\gamma = 0$, the system will focus only on the energy performance, and if a balance between energy and latency is to be maintained, then $\gamma = 1$ is required. For $\gamma > 1$, the system focuses more on the rapidity of the offloading.

After that, an optimization problem (P) is constructed to minimize the overall utility of the system $\Theta(\mathbf{X})$ with the help of optimizing the offloading decision $\mathbf{X}$ for each task. The optimization problem is as follows:

$$\text{P: } \Theta^*(\mathbf{X}) = \underset{\mathbf{X_F}, \mathbf{X_C}}{\text{minimize}}\,(E + \gamma T), \tag{12a}$$

$$\text{subject to } X_F \in \{0, 1\}, \tag{12b}$$

$$X_C \in \{0, 1\}, \tag{12c}$$

$$T \le T_{\text{limit}}, \tag{12d}$$

$$\text{gamma} \ge 0. \tag{12e}$$

where (12b) and (12c) constrain the binary nature of the offloading decision. Besides, (12d) is the offloading time limit. If the latency is greater than the time limit, then the decision will not be adopted. Moreover, the algorithm will add an extremely large penalty value, such as $\Theta^*(\mathbf{X}) = \Theta^*(\mathbf{X}) + \sigma$ where $\sigma = 10^9$, to the system utility at this point to force the decision to be eliminated in subsequent comparisons.

Generally speaking, a binary decision problem of this kind belongs to the N-P problem, which has no exact solution by default. In the next section, we will propose a dynamic programming offloading algorithm, which is based on randomized decision, to find the optimal approximate solution of such problems. Furthermore, the definitions of the symbols used in this paper are shown in Table 1.

3. DPOA

In this section, a dynamic programming offloading algorithm for the MFC network, the DPOA, is proposed, in which the two-dimensional DP table is constructed to pick the current optimal binary decision for each task.

Because of the similarity of the decision algorithms for the fog decision and the cloud decision, the algorithm is mainly used as an example at the fog server in this section. Since cloud-side decisions and fog-side decisions do not affect each other, when calculating fog-side decisions, we assume that all the decisions of the tasks in the cloud are 0, for example, $X_C^n \equiv 0$ $(\mathbf{X}_C = \{X_C^n \equiv 0 | n \in \mathbf{N}\})$.

To store and display the offloading decisions corresponding to each task, as shown in Figure 2, a DP table of size $N*N$ is constructed. Particularly, N is the total number of tasks. After the algorithm begins with H round-robin operations and a set of N randomly offloaded decision elements, denoted as $\Lambda_h, h \in \{1, 2, \ldots, H\}$ is generated in each cycle. In particular, there is no connection between the set of random decisions and the offloading task. While obtaining the generated set of offloading decisions for the current cycle, the system assigns the decisions to the previously constructed DP table according to a specific law. For example, 0 is assigned to the next horizontal cell while 1 is to the next vertical cell. Exceptionally, the starting position is $(1, 2)$ if the first decision is 0 and $(2, 1)$ is for 1. In addition, the construction of the DP table is based on the randomization theory in [9].

As an example, assuming $N = 6$, the algorithm constructs a $6*6$ DP table. Let all the decision sets generated by the first cycle be $\Lambda_1 = 010010$ and suppose the decision during the second cycle is $\Lambda_2 = 110101$ (as shown in Figure 2(a) with blue numbers) or $\Lambda_2 = 100110$ (in Figure 2(b) with red numbers) with two examples. As the first place of Λ_1 is 0, the starting cell is $(1, 2)$. Since the second place of Λ_1 is 1, the next vertical cell of the previous cell $(1, 2)$ will be assigned to 1, such as $(2, 2) = 1$. Similarly, with the third place being 0, the next horizontal cell of cell $(2, 2)$ will be assigned to 0, i.e., $(2, 3) = 0$. The table is filled according to the above rules so as to get the table in Figure 2.

Once the decision set Λ_h is generated, it is first filled into the table according to the rules and the overall system utility

TABLE 1: Symbols used in the paper.

Symbol	Meaning
M_n	Data size of users n-th task
X_F^n	Local-to-fog offloading decision of users n-th task
	$X_F^n = \begin{cases} 1 & \text{offloading} \\ 0 & \text{local} \end{cases}$
X_C^n	Fog-to-cloud offloading decision of users n-th task
	$X_C^n = \begin{cases} 1 & \text{cloud} \\ 0 & \text{fog} \end{cases}$
f_L	Local computing rate
f_F	Fog computing rate
f_C	Cloud computing rate
B_F	Bandwidth between the local and fog
B_C	Bandwidth between the fog and cloud
T_L^n	Local processing time of users n-th task
k	Energy cost of the device computed per bit of data
T_F^n	Fog processing time of users n-th task
α	Energy consumption per bit of data in local-to-fog transmission
T_C^n	Cloud processing time of users n-th task
P	Device standby power
T_{tF}^n	Transmission delay of n-th task from the local to fog
ϕ	Number of CPU revolutions required to process per bit of data
T_{tC}^n	Transmission delay of n-th task from the fog to cloud
T	Total delay of the user
E_L^n	Local energy consumption of users n-th task
γ	The relative importance of delay and energy
E_t^n	Uploaded energy cost of users n-th task
σ	System-set penalty value
E_w^n	Standby energy cost of the device when it offloads task n
E	Total energy cost of the user
H	Number of algorithm iterations
Λ_h	The set of random offloading decisions produced at the h-th iteration
Λ_h^*	The h-th offloading decision set after updating
η	Relative offloading accuracy rate

$\Theta(\mathbf{X}_h)$ is calculated at the same time, in which $\mathbf{X}_F = \Lambda_h$ and $\mathbf{X}_C \equiv 0$. Obviously, if the number of iterations is large enough, there will be cases that the Λ_h has a common subset with the previous cells in the table with different decisions, as in $(2, 2)$ in Figure 2(b). We will consider the utility values $\Theta(0, 0)$ and $\Theta(1, 0)$ for the cell under different offloading decisions, respectively, and select the decision corresponding to the lowest value to replace the original one. Then, the updated set is noted as Λ_h^*, followed by updating the overall system utility at this point as $\Theta(\mathbf{X}_h^*)$, specifically $\mathbf{X}_F = \Lambda_h^*$.

When all the elements in Λ_h are filled, the final $\Theta(\mathbf{X}_h^*)$ is compared with the system utility $\Theta(\mathbf{X}_{h-1}^*)$ of the h-1th cycle. In the special case, when h is equal to 1, then the $\Theta(\mathbf{X}_0)$ for the 0-th time is equal to the system utility corresponding to the full 0 set as Λ_0. If the utility value of the current loop is greater than of the previous one, the new set is replaced with the old like $\Lambda_h^* = \Lambda_{h-1}^*$. Furthermore, the utility value of the current loop is replaced with the old value as $\Theta(\mathbf{X}_h^*) = \Theta(\mathbf{X}_{h-1}^*)$, as well. Conversely, if the existing utility value is less than the value of the previous loop, the existing offloading decision is held without change.

Figure 2: Two examples of filling out the DP table.

Having completed all the cycles, the decision set Λ_H^* after the H-th cycle is the optimal offloading decision $\mathbf{X}_F$ in the local-to-fog stage, i.e., $\mathbf{X}_F = \Lambda_H^*$. Obviously, if the number of cycles is sufficient, the constructed DP table will be filled up. Once the arbitrary set of offloading decisions generated at this point is filled into the table, the resulting updated set Λ_h^* is set as the corresponding optimal solution of the algorithm. And, the code of the DPOA is detailed in Algorithm 1.

For the decision algorithm on the cloud server, it is approximately the same as on the fog. Furthermore, if the fog decision for task n satisfies $X_F^n = 0$, then its cloud decision is also 0 ($\{X_C^n = 0 \mid X_F^n = 0, n \in \mathbf{N}\}$). In the next section, a large amount of simulations will be used to verify the speed and accuracy of the DPOA.

4. Evaluation and Simulation

In this section, extensive simulation is provided to evaluate the offloading performance of the DPOA. Specifically, it is assumed that the number of tasks to be offloaded by the user is 20, whose size is randomly distributed in the range of 2 MB to 20 MB. Furthermore, the computational energy consumption of the tasks is 3.25×10^{-7} J/bit [9] when being processed in the local device and 1.42×10^{-7} J/bit [9] is for the transmit energy per bit of the device. And, the standby power of the device is constant at 40 mw. Moreover, the processing speed of the local device, the fog server, and the cloud server is set to $f_L = 2.1 \times 10^8$ cycle/s, $f_F = 5 \times 10^9$ cycle/s, and $f_C = 10 \times 10^9$ cycle/s [9], respectively. The wireless transmission rate between the local and F-AP is 15 Mbps and from the fog to cloud is 40 Mbps [15]. Besides, $\phi = 100$ cycle/s, $T_{\text{limit}} = 1200$ ms, $H = 500$, and $\gamma = 1$ J/s are further set.

The proposed DPOA is compared with the existing SRA (semidefinite relaxation approach) algorithm in the literature [9] and the Greedy algorithm, as shown in Figure 3. Besides, the data when the tasks are computed all locally and all in the cloud are added for reference. Figure 3 illustrates that offloading tasks can significantly reduce the processing latency and energy consumption compared to local computation. The addition of fog computation (DPOA, SRA, and Greedy) to the system can further reduce the utility compared to only cloud computation. From the data in Figure 3, it can be seen that the DPOA is able to find a better solution compared to the mentioned benchmark algorithm (SRA [9] and Greedy).

Here, we define the relative offloading accuracy rate of the DPOA, denoted by η:

$$\eta = \frac{\Theta(\text{SRA})}{\Theta(\text{DPOA})}. \tag{13}$$

where $\Theta(\text{SRA})$ denotes the system utility value corresponding to the decision generation by the SRA algorithm, while $\Theta(\text{DPOA})$ represents the value of the DPOA under the same parameters.

Figure 4 analyzes the performance of the algorithm at different numbers of iterations. In Figure 4(a), the relative accuracy rate increases gradually as the number of iterations continues to increase. When the number of H is higher than 500, the value of the rate tends to be smooth, i.e., the algorithm reaches the convergence state. As the number of iterations increases, the system utility value of the DPOA is decreasing, such as the line graph in Figure 4(b). And, when H is greater than 500, the system utility value tends to be stable. However, from the histogram in Figure 4(b), higher H values correspond to higher decision time points for the system, so that a single increase in the number of iterations may weaken the rapidity of the algorithm.

In Figure 5, we consider the offloading when the user is in a wireless transmission rate variation scenario with a transmission rate B_F range of 5 Mbps to 25 Mbps. As can be seen in Figure 5(a), the energy under the DPOA is much lower than that of the full cloud computing and outperforms that of the benchmark algorithm. In a poor communication scenario, such as $B_F = 5$ Mbps, all-local computation is more cost-effective than offloading in terms of energy consumption because of the relatively heavy energy

Input: number of tasks N; size of tasks $M_n, n \in \mathbf{N}$;
Output: optimal offloading decision set Λ_H^*;
(1) **Initialization:** initialize the DP table and set the T_{limit};
(2) **for** $h = 1, 2, \ldots, H$ **do**
(3) Generate random offloading decision sets Λ_h;
(4) Fill in the DP table according to the rules and calculate the system utility $\Theta(\mathbf{X}_h)$ for Λ_h;
(5) **if** *(the filled decisions have a common set and not the same as the cells in the previous table)* **then**
(6) Calculate the system utility corresponding to this decision and the original decision, respectively;
(7) Select the decision corresponding to the lower value to replace the original decision;
(8) Renew Λ_h^* and $\Theta(\mathbf{X}_h^*)$;
(9) **else**
(10) Execute the following: $\Lambda_h^* = \Lambda_h$ and $\Theta(\mathbf{X}_h^*) = \Theta(\mathbf{X}_h)$;
(11) **if** $(\Theta(\mathbf{X}_h^*) > \Theta(\mathbf{X}_{h-1}^*))$ **or** $(T > T_{\text{limit}})$ **then**
(12) Execute the following: $\Lambda_h^* = \Lambda_{h-1}^*$ and $\Theta(\mathbf{X}_h^*) = \Theta(\mathbf{X}_{h-1}^*)$;

ALGORITHM 1: DPOA.
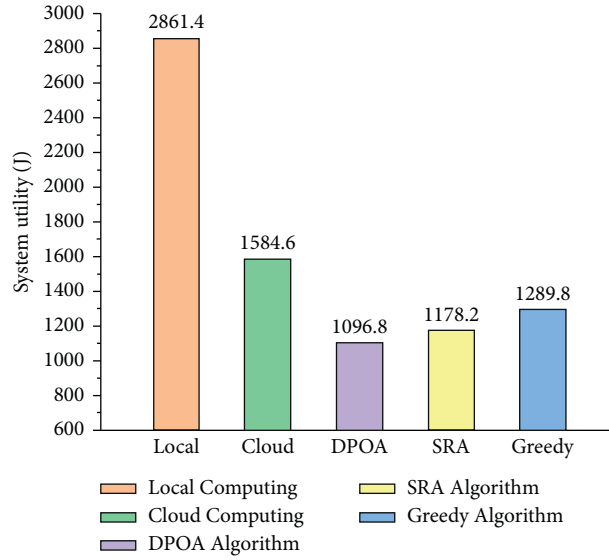
FIGURE 3: Comparison of the system utility for different algorithms.
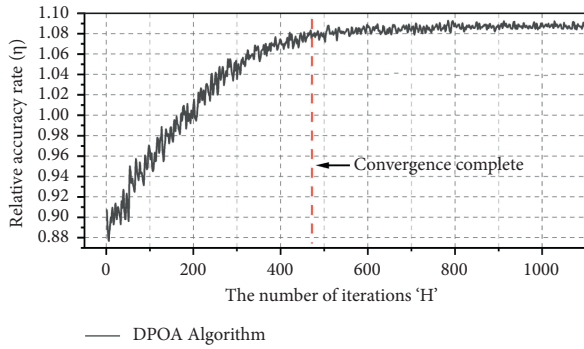
(a)
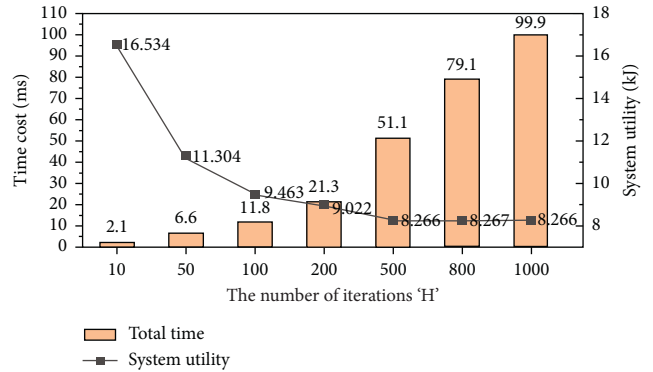
(b)

FIGURE 4: Performance under different number of iterations "H": (a) convergence of the DPOA; (b) total time cost and system utility.
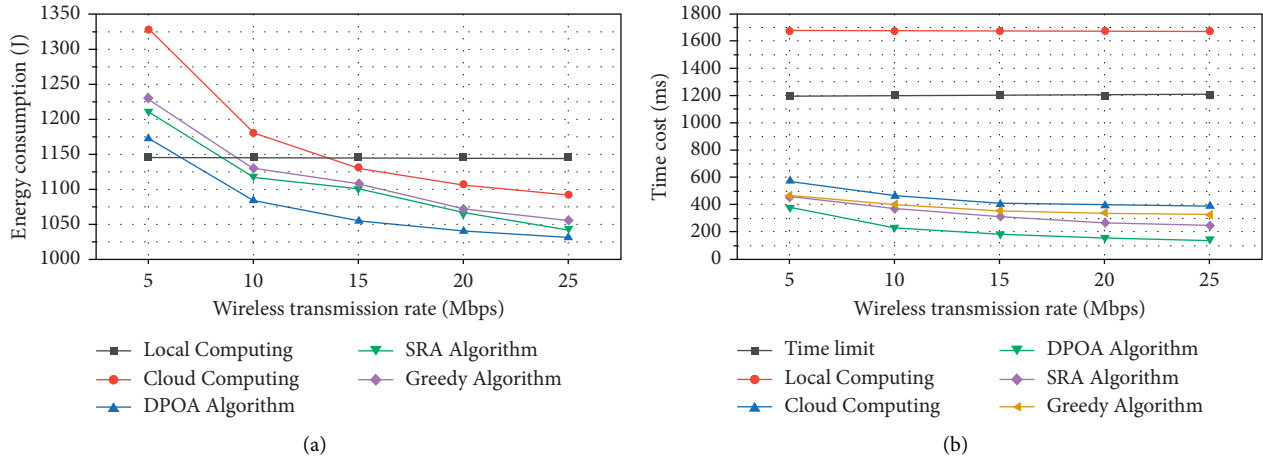
FIGURE 5: Comparison of the DPOA and the benchmark algorithms (SRA [5] and Greedy), when time limit = 1200: (a) energy consumption; (b) time cost.
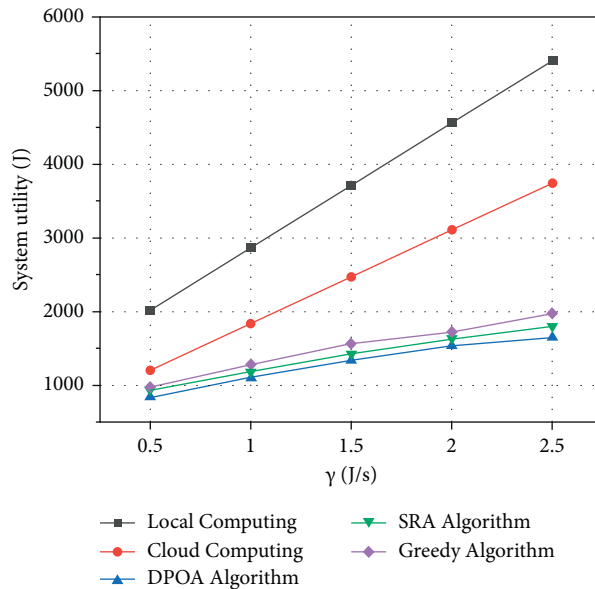

FIGURE 6: System utility values of different offloading algorithms under different γ.

consumption required to offload. However, it is noticed in Figure 5(b) that the all-local computation exceeds the time limit, so the optimal solution is the DPOA in comparison.

The relationship between the time cost and the wireless transmission rate is exhibited in Figure 5(b). As the transmission rate increases, the advantage of offloading computation over non-offloading becomes gradually obvious and the latency of the system to perform offloading computation decreases.

As illustrated in Figure 6, the performance of the algorithm for different γ has been investigated. It can be seen from the figure that as the value of γ increases, the system utility also increases gradually. However, the utility of the DPOA is always lower than that of the SRA and the Greedy, which means that the DPOA gives a superior approximate solution in comparison. Based on Figures 3, 5, and 6, it can be concluded that the DPOA consistently outperforms the

mentioned benchmark algorithm in terms of comprehensive offloading performance.

More specifically, the time cost of this algorithm in generating offloading decisions under different numbers of tasks is also analyzed, as shown in Figure 7. Not surprisingly, it can be noticed that the decision-elapsed time of the DPOA increases almost linearly as the number of tasks increases from 10 to 35. At the same time, the average decision time curve shows that with the changing number of tasks, the algorithm can steadily maintain the optimal offloading decision within 3 ms. The above experiments illustrate that the algorithm can handle the massive task offloading problem without reducing its own efficiency and is suitable for multitask offloading scenarios.

In Figure 8, we further investigate the impact of the time limit (T_{limit}) on the energy efficiency of the algorithm. Adopting the energy consumption in the case of all-local
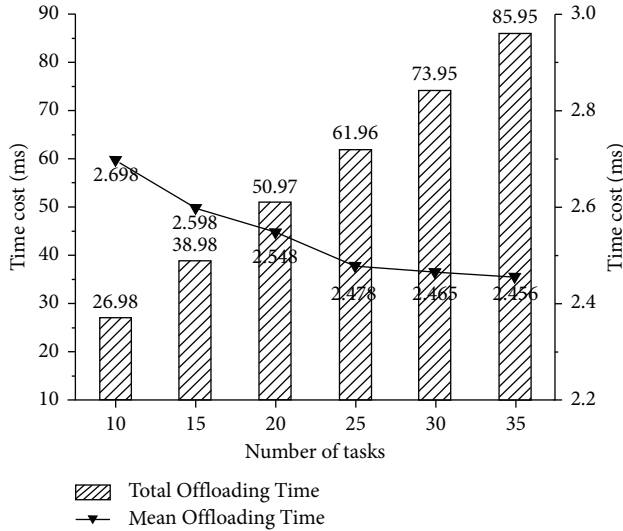
FIGURE 7: Time cost for generating decision under different number of tasks using the DPOA.
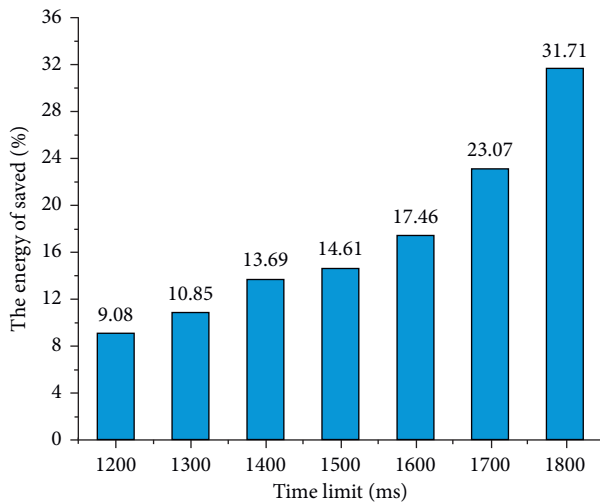

FIGURE 8: Percentage of energy saved by using the DPOA compared to the all-local computing method, under different time limits.

computing as the benchmark, Figure 8 shows the percentage energy savings of T_{limit} relative to the benchmark. It can be seen from the figure that as the time limit is gradually relaxed, more tasks can be offloaded to the server and thus more energy can be saved. Compared with the all-local computing model, the DPOA can reduce the energy consumption of the local device processing tasks by about 9% to 32% while meeting the time constraints.

5. Conclusion

Aiming at the offloading decision generation problem in MFC, this paper proposes a randomization-based dynamic programming offloading algorithm, DPOA, to solve this problem. The algorithm uses randomization to cyclically generate a random set of offloading decisions while

constructing an overall system utility $\Theta(\mathbf{X})$, including the total energy and time cost, to dynamically populate the DP table by minimizing the system utility. The simulation results verify that the proposed algorithm is accurate and outperforms the existing benchmark algorithm. Furthermore, the DPOA can better adapt to scenarios with changing transmission rates. However, at higher network rates, it will offload as many tasks as possible to the server, thus converging quickly to the optimal solution. Besides, the algorithm can generate near-optimal offloading decisions in 3 ms and its time cost does not increase drastically with the number of tasks. In conclusion, we hope that this DPOA can be applied in decision time-sensitive MFC scenarios, such as smart IoT in 6G, to improve the efficiency of real-time system offloading.

Data Availability

The underlying data supporting the results of this study can be found at the official website of Beijing Natural Science Foundation.

Conflicts of Interest

The authors declare that they have no conflicts of interest.

Acknowledgments

References

[1] P. Habibi, M. Farhoudi, S. Kazemian, S. Khorsandi, and A. Leon-Garcia, "Fog computing: a comprehensive architectural survey," *IEEE Access*, vol. 8, Article ID 69105, 2020.

[2] M. Xu, Z. Zhao, M. Peng, Z. Ding, T. Q. S. Quek, and W. Bai, "Performance analysis of computation offloading in fog-radio access networks," in *Proceedings of the 2019 IEEE International Conference on Communications (ICC)*, pp. 1–6, Shanghai, China, May 2019.

[3] J. Wang, T. Lv, P. Huang, and P. T. Mathiopoulos, "Mobility-aware partial computation offloading in vehicular networks: a deep reinforcement learning based scheme," *China Communications*, vol. 17, no. 10, pp. 31–49, Oct. 2020.

[4] H. Wu and K. Wolter, "Stochastic analysis of delayed mobile offloading in heterogeneous networks," *IEEE Transactions on Mobile Computing*, vol. 17, no. 2, pp. 461–474, 1 Feb. 2018.

[5] R. Besharati and M. H. Rezvani, "A prototype auction-based mechanism for computation offloading in fog-cloud environments," in *Proceedings of the 2019 5th Conference on Knowledge Based Engineering and Innovation (KBEI)*, pp. 542–547, Tehran, Iran, March 2019.

[6] L. Yang, H. Zhu, H. Wang, H. Qian, and Y. Yang, "Incentive propagation mechanism of computation offloading in fog-enabled D2D networks," in *Proceedings of the 2018 IEEE 23rd International Conference on Digital Signal Processing (DSP)*, pp. 1–4, Shanghai, China, November 2018.

[7] G. Zhang, F. Shen, Z. Liu, Y. Yang, K. Wang, and M. Zhou, "FEMTO: fair and energy-minimized task offloading for fog-

enabled IoT networks," *IEEE Internet of Things Journal*, vol. 6, no. 3, June 2019.

[8] M. Mukherjee, S. Kumar, Q. Zhang et al., "Task data offloading and resource allocation in fog computing with multitask delay guarantee," *IEEE Access*, vol. 7, Article ID 152911, 2019.

[9] M. Chen, B. Liang, and M. Dong, "A semidefinite relaxation approach to mobile cloud offloading with computing access point," in *Proceedings of the 2015 IEEE 16th International Workshop on Signal Processing Advances in Wireless Communications (SPAWC)*, pp. 186–190, Stockholm, Sweden, July 2015.

[10] G. M. S. Rahman, T. Dang, and M. Ahmed, "Deep reinforcement learning based computation offloading and resource allocation for low-latency fog radio access networks," *Intelligent and Converged Networks*, vol. 1, no. 3, pp. 243–257, Dec. 2020.

[11] X. Zhu, S. Chen, S. Chen, and G. Yang, "Energy and delay co-aware computation offloading with deep learning in fog computing networks," in *Proceedings of the 2019 IEEE 38th International Performance Computing and Communications Conference (IPCCC)*, pp. 1–6, London, UK, October 2019.

[12] X. Wang, X. Wei, and L. Wang, "A deep learning based energy-efficient computational offloading method in Internet of vehicles," *China Communications*, vol. 16, no. 3, pp. 81–91, March 2019.

[13] F. Jiang, R. Ma, C. Sun, and Z. Gu, "Dueling deep Q-network learning based computing offloading scheme for F-ran," in *Proceedings of the 2020 IEEE 31st Annual International Symposium on Personal*, pp. 1–6, London, UK, September 2020.

[14] M. A. Sharkh and M. Kalil, "A dynamic algorithm for fog computing data processing decision optimization," in *Proceedings of the 2020 IEEE International Conference on Communications Workshops (ICC Workshops)*, pp. 1–6, Dublin, Ireland, June 2020.

[15] W. Bai, Z. Ma, Y. Han et al., "Joint optimization of computation offloading, data compression, energy harvesting, and application scenarios in fog computing," *IEEE Access*, vol. 9, Article ID 45462, 2021.

WILEY | Hindawi

Research Article

Real-Time Facial Expression Recognition System for Video Big Sensor Data Security Application

Zhi Yao ,[1] **Hailing Sun** ,[1] **and Guofu Zhou**[1,2]

[1]*Guangdong Provincial Key Laboratory of Optical Information Materials and Technology & Institute of Electronic Paper Displays, South China Academy of Advanced Optoelectronics, South China Normal University, Guangzhou 510006, China*
[2]*Shenzhen Guohua Optoelectronics Technology Co., Ltd., Shenzhen 518110, China*

Correspondence should be addressed to Hailing Sun; sunsmile1225@163.com

Facial video big sensor data (BSD) is the core data of wireless sensor network industry application and technology research. It plays an important role in many industries, such as urban safety management, unmanned driving, senseless attendance, and venue management. The construction of video big sensor data security application and intelligent algorithm model has become a hot and difficult topic in related fields based on facial expression recognition. This paper focused on the experimental analysis of Cohn–Kanade dataset plus (CK+) dataset with frontal pose and great clarity. Firstly, face alignment and the selection of peak image were utilized to preprocess the expression sequence. Then, the output vector from convolution network 1 and β-VAE were connected proportionally and input to support vector machine (SVM) classifier to complete facial expression recognition. The testing accuracy of the proposed model in CK + dataset can reach 99.615%. The number of expression sequences involved in training was 2417, and the number of expression sequences in testing was 519.

1. Introduction

Video is the best data type with largest amount and high degree of industrialization in BSD applications. Facial data is becoming more important for research. Facial expression recognition and analysis is the basic supporting technology of the above applications. It has become a hot and difficult topic to construct a security application and intelligent algorithm model of video BSD based on facial expression recognition [1, 2]. The main task of facial expression recognition is to realize automatic, reliable, and efficient facial information extraction and recognition.

The research direction of facial expression recognition includes hardware detection and programming recognition. Turabzadeh et al. achieved accuracy of 47.44% in automatic emotional detection by Field Programmable Gate Array (FPGA) [3]. Then, Mehta et al. realized emotion recognition in augmented reality (AR) by Microsoft HoloLens (MHL) [4]. The programming direction was aimed at optimizing the

structure of model. There were lots of datasets in the field of facial expression recognition, such as dataset Multi-PIE and CK+ [5, 6]. Mao et al. utilized the Kinect sensor to track facial action unit (AU) and feature point position (FPP) to achieve about 80% accuracy [7]. In addition, Yang et al. achieved accuracy of 97.3% by extracting the information of expression components on CK+ dataset [8]. Zhang et al. proposed an end-to-end deep learning model that utilized GAN network to achieve 91.8% accuracy on Multi-PIE dataset [9].

Some scholars had also carried out experiments from other research directions except for the optimization of network [10]. Meng et al. achieved recognition accuracy of 95.37% on CK+ dataset as well as maintaining identity characteristics [11]. Cheng and Wang considered that facial expression recognition should be analyzed differently in different fields [12]. Facial expression recognition and psychology were very popular in recent years. Picard proposed the idea of emotional computing in 1997 [13]. Ekman

and Friesen proposed Facial Action Coding System (FACS) to define facial emotions [14]. Geometric analysis and appearance analysis were applied to facial expression recognition on this basis [15].

Nowadays, the research of facial expression recognition involved deep learning, psychological analysis, physiological analysis, education, and other disciplines [16]. Its application and research had gradually expanded to three-dimensional and multiangle directions [17]. However, the low efficiency of the above methods and excessive facial influencing factors remained to be resolved [18]. In this paper, face alignment and the selection of peak image were utilized to enhance data features. Then, the output vector from convolution network 1 and β-VAE were connected proportionally and input to SVM classifier to complete facial expression recognition. The proposed model has advantages in accuracy compared with related models.

2. Materials and Methods

The recognition of facial expression sequence described in this paper is mainly divided into three processes: preprocessing of expression sequence, feature extraction of expression sequence, recognition, and classification of expression sequence.

2.1. Preprocessing of Expression Sequence.
The CK+ dataset including frontal face is utilized in this paper. The dataset includes 123 themes, 593 sequences, and 7 expression labels. Expression labels consist of anger, contempt, disgust, fear, happiness, sadness, and surprise. It is a pity that only 327 of the 593 expression sequences have expression labels, which are the research object of this paper. The significant reason for choosing CK+ dataset is that the expression label corresponds to an expression sequence rather than a single expression. In addition, the main application scene of the proposed model is the standard frontal expression recognition.

The dataset has the disadvantages of small amount and irrelevant noise although it has the above advantages and is preprocessed to improve the accuracy of facial expression recognition and the stability of training process. This section mainly consists of face alignment of images and selection of expression peak images.

2.1.1. Face Alignment of Images.
The original dataset has standard facial pose, but it is inevitable to have redundant image noise. Therefore, multitask convolutional neural network (MTCNN) is utilized to align the image [19].

The principle of MTCNN is that the matching of multiple regression frames can accurately locate the frame of input face image. MTCNN is designed by the cascade of proposal network (P-Net), refine network (R-Net), and output network (O-Net) in terms of network structure. Firstly, the input image is input to P-net, and the output vector shown in Figure 1 is obtained subsequently. Its length is 2, 4, and 10, respectively, representing the classification score of bounding boxes (bbox), the offset of bbox, and the

value of landmark. In P-net, the classification score is utilized to select initial bbox, whose specific location is calibrated by the offset of bbox. Then, these bboxes are selected based on Intersection over Union (IoU). The threshold of IoU is set in advance. The repetition of this operation can eliminate massive overlapping bbox. Finally, the reserved bbox is moved based on coordinates and modified to enter R-Net.

The output type of R-net and O-net is the same as P-Net's as shown in Figure 1, and their goal is to further adjust the size and location of the bounding box. MTCNN can get the accurate bbox and landmark coordinates of input image on the premise of avoiding deformation and retaining more details.

The role of MTCNN in this paper is aimed at completing accurate face alignment, so the landmark is not utilized. The diagram of IoU is shown in Figure 2.

The two rectangular frames shown in Figure 2 are predicted box and ground truth, respectively. In each output of network, the coordinate of bbox corresponding to the highest value of score is intersected and calculated to find the IoU. The value of IoU is compared and selected with the value of threshold, and the maximum score is saved and transferred [20].

2.1.2. Selection of Expression Peak Images.
The basis of the operation in this section is that the expression sequence contains initial calm expression and peak expression. But only the peak expressions are processed when the expression sequence feature is extracted. Therefore, the structural similarity (SSIM) is utilized to calculate similarity to complete the selection of peak images [21].

SSIM is an index utilized to measure the similarity of images and is utilized to judge the structural similarity between two images. The SSIM of two images includes brightness comparison, contrast comparison, and structure comparison [22]. Firstly, the average gray value of image is calculated, as shown in the following equation:

$$\mu_x = \frac{1}{N} \sum_{i=1}^{N} x_i. \tag{1}$$

x_i represents the pixel value of the image and N represents the size of window utilized in calculation. A window of $[N \times N]$ is taken from the image every time, and it will be continuously slid in the calculation process of SSIM. The overall SSIM of the image will be obtained by averaging the local value of SSIM. Then, the average gray μ_x can be utilized to calculate the gray standard deviation σ_x in the following equation:

$$\sigma_x = \left(\frac{1}{N-1} \sum_{i=1}^{N} \left(x_i - \mu_x \right)^2 \right)^{1/2}. \tag{2}$$

After basic parameters are obtained, the three image comparison indices mentioned above are calculated, respectively, as shown in the following equations:
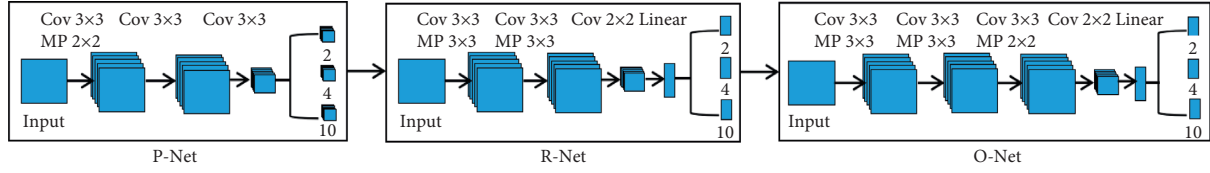
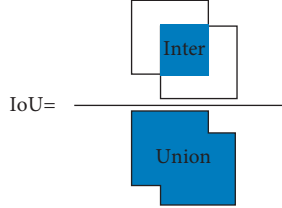FIGURE 1: Flowchart of face alignment.

FIGURE 2: IoU calculation principle diagram.

$$I(x, y) = \frac{2\mu_x \mu_y + C_1}{\mu_x^2 + \mu_y^2 + C_1}, \tag{3}$$

$$c(x, y) = \frac{2\sigma_x \sigma_y + C_2}{\sigma_x^2 + \sigma_y^2 + C_2}, \tag{4}$$

$$s(x, y) = \frac{\sigma_{xy} + C_3}{\sigma_x \sigma_y + C_3}. \tag{5}$$

C_1, C_2, and C_3 are constants. They are utilized to avoid the denominator of fraction approaching 0. The value of SSIM can be obtained by multiplying the above three indicators, as shown in the following:

$$\text{SSIM}(x, y) = \frac{(2\mu_x \mu_y + C_1) \cdot (2\sigma_{xy} + C_2)}{(\mu_x^2 + \mu_y^2 + C_1) \cdot (\sigma_x^2 + \sigma_y^2 + C_2)}, \tag{6}$$

where C_3 in is represented by C_2; then, the similarity between images can be measured by SSIM. The rules defined in Algorithm 1 are utilized in experiment when peak images are selected.

The dataset utilized by the model in this paper can be selected from each expression image sequence after the parameters p_1 and p_2 are obtained.

2.2. The Principle of Feature Extraction. The ultimate goal of this paper is aimed at classifying the CK+ dataset exactly. Therefore, the task of this section is to fully extract features of input facial expression images. Features extracted by the proposed model consist of two parts. The first part is facial texture features extracted by the network 1 composed of 2D convolutional network. The second part is generative features extracted by β-VAE autoencoder.

2D convolution has universality for feature extraction. An example on CK+ dataset is shown in Figure 3.

2D convolution is developed from one-dimensional signal convolution. 2D image convolution changes the direction of one-dimensional convolution into the width and height directions of image at the same time.

Therefore, 2D image convolution is performed on the pixels of image.

The convolution kernel with a specified template size is utilized to perform sliding convolution. The convolution process shown in Figure 3 performs multiplication and addition of parts with the same value. The distribution of values in convolution kernel can represent the distribution of pixels in the window of image. Pixels of expression image shown in Figure 3 are an enlarged representation rather than real situation. The structure of network 1 of the proposed model is shown in Figure 4.

The reason why grayscale image is utilized instead of RGB is that there are differences in the background brightness of the image on CK+ dataset. This effect can be reduced by image graying and face alignment described in Section 2.1.1.

In addition to network 1, the proposed model introduces β-VAE network to extract the generative features of facial images. VAE network is a network modification of codec, whose feature vectors of middle layer can be expressed in the form of Gaussian distribution. This is because the superposition of Gaussian distribution can fit any distribution, which makes the VAE network more representative. The network structure of codec is shown in Figure 5 [23].

$q(\cdot)$ is the distribution function of the encoding part, and $p(\cdot)$ is the distribution function of the decoding part. The process of codec is aimed at training the distribution of coding network and decoding network. The intermediate vector z can well represent the generative features of input image when restored image x' and input x are infinitely close. Each sample z corresponds to a set of μ and σ for VAE. The sum of all Gaussian distributions in integration domain is the original distribution $p(x)$ and objective function equation:

$$p(x) = \int_z p(z)p(x|z)\mathrm{d}z. \tag{7}$$

$p(x)$ can be expressed as follows by introducing logarithmic computation:

$$\log p(x) = \int_z q(z|x)\log p(x)\mathrm{d}z$$
$$= \int_z q(z|x)\log\left(\frac{p(z, x)}{q(z|x)}\right)\mathrm{d}z + \int_z q(z|x)\log\left(\frac{q(z|x)}{p(z|x)}\right)\mathrm{d}z. \tag{8}$$

The second term of (8) can be defined in the following equation based on the definition of divergence:

Input: image similarities after ranking in sequence S, similarity reference value s_0, the number of images in sequence n, images i_1,
images i_2, the number t, similarity between i_1 and i_2 s_{12}, and flag parameter f.
Output: the starting point where the peak image appears p_1, The ending point where the peak image appears p_2.
(1)   **for all** images $\in$ image sequence **do**
(2) $t = 0$, $f = 0$
(3) $S =$ similarities of images sequence
(4)   **if** $S[-1] - S[0] > 0.2$ **then**
(5) $s_0 = S[0] + 0.15$
(6)   **else if** $S[-1] - S[0] < 0.1$ **then**
(7) $s_0 = S[0] + 0.03$
(8)   **else**
(9) $s_0 = S[0] + 0.05$
(10)   **while** $t < n - 1$ **do**
(11) $i_1 =$ image $[t]$
(12) $i_1 =$ image $[t + 1]$
(13)   **if** $s_{12} < s_0$ **and** $f = 0$ **then**
(14) $p_1 = t + 1$
(15) $f = 1$
(16)   **else if** $s_{12} > 0.915$
(17) $p_2 = t$
(18) $f = 1$
(19)   else
(20) $p_2 = n - 1$
(21) $t = t + 1$
(22)   **if** $p_2 - p_1 > \text{round}\,((2/5)n)$ **then**
(23) $p_1 = \text{round}\,((2/5)n) - 1$
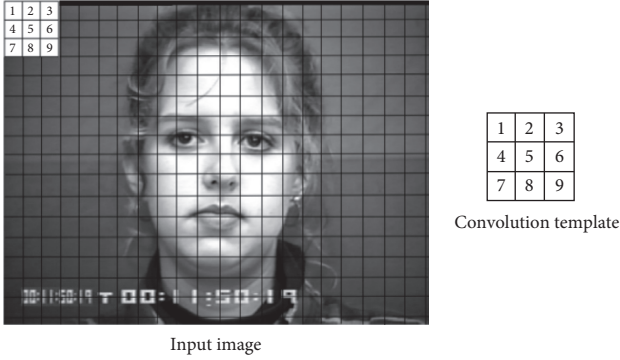
ALGORITHM 1: Rule for image sieving.

Input image

FIGURE 3: Principle of 2D image convolution.

$$\int_z q(z|x)\log\left(\frac{q(z|x)}{p(z|x)}\right) \mathrm{d}z = \mathrm{KL}(q(z|x)\|p(z|x)). \quad (9)$$

The minimum value of (8) is defined as its former part since the value of (9) is greater than 0. The value of $\log p(x)$ is fixed when $p(x|z)$ is fixed. Therefore, the value of KL divergence approaches 0 by adjusting $q(z|x)$ and $p(x|z)$. The $\log p(x)$ can be equivalent to the former part of equation (8). Then, the following equation can be obtained:

$$L = \int_z q(z|x)\log\left(\frac{p(z,x)}{q(z|x)}\right)\mathrm{d}z. \quad (10)$$

The following result can be obtained by splitting and expressing the divergence of (10):

$$L = -\mathrm{KL}(q(z|x)\|p(z)) + \int_z q(z|x)\log p(z|z)\,\mathrm{d}z. \quad (11)$$

The latter part of (11) is image loss function, and the former part can be calculated by its variance and average. Then, the following can be obtained by splitting the former part:

$$-KL(q(z|x)\|p(z)) = \int_z q(z|x)\log p(z)\mathrm{d}z \\ - \int_z q(z|x)\log q(z|x)\mathrm{d}z. \quad (12)$$

$p(z)$ is assumed to obey the distribution of $(0, 1)$, and the following result can be obtained by (12):

$$-KL(q(z|x)\|p(z)) = \frac{1}{2}\sum\left[1 + \log(\sigma^2) - \mu^2 - \sigma^2\right]. \quad (13)$$

The distribution of z is composed of multiple Gaussian distributions. But it is necessary to introduce a penalty coefficient β to (11). This process can reduce the influence of irrelevant factors [24]. Then, the following equation can be obtained:

$$L = -\beta \cdot \mathrm{KL}(q(z|x)\|p(z)) + \int_z q(z|x)\log p(x|z)\,\mathrm{d}z. \quad (14)$$

The output vectors obtained by β-VAE were connected to the output vectors obtained by the network 1 in a ratio of $1 : 5$. Then, they were input into SVM classifier to complete the classification.
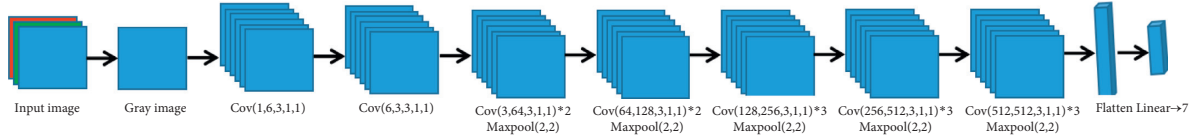
FIGURE 4: The structure of network 1 composed of 2D convolution.
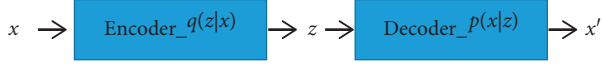

FIGURE 5: The structure of codec.

2.3. Calculation Parameters Involved in the Model. In this section, some relevant parameters involved in the calculation appeared. Their values are shown in Table 1.

2.4. The Overall Structure of the Model. A combination of feature extraction network and SVM classifier was utilized. Partial facial differences and the influence of noise can be reduced by the facial texture features and the generative features. The overall structure of the proposed model is shown in Figure 6.

3. Results and Discussion

3.1. Preprocessing of Expression Sequence. The CK+ dataset utilized for model training required face alignment and selection of peak image. This process was carried out sequentially since the noise of image background needed to be reduced first to obtain highest testing accuracy. Partial result of face alignment is shown in Figure 7.

The selection of peak images achieved the deletion of edge expressions. Peak images were screened and saved based on Algorithm 1. Partial result of comparison is shown in Figure 8.

The dataset was divided after finishing the preprocessing of it. The ratio of training set, validation set, and testing set was $0.7 : 0.15 : 0.15$.

3.2. Neural Network Parameter Settings. The training parameters of network 1 and β-VAE are shown in Tables 2 and 3, respectively.

The task of network 1 focused mainly on the extraction of facial texture features, so the size of input images is $[224, 224]$.

The specific parameters required for β-VAE are shown in Table 3.

The β-VAE took a long time to train as a generative model, so its input size was set to $[64, 64]$. This model was utilized to extract generative features of image that cannot be captured by network 1.

3.3. Model Evaluation Method. The evaluation of the proposed model in the paper was the accuracy of the testing set, which was calculated by the matching degree between the

TABLE 1: Convolution network training parameters.

Parameter	Value
Threshold of IoU	$[0.6, 0.7, 0.8]$
N	11
C_1	$(0.01 \times 255)^2$
C_2	$(0.03 \times 255)^2$
C_3	$1/2 (0.03 \times 255)^2$
β	2

testing set label and the result of model. The calculation equation of the accuracy was

$$\text{accuracy} = \frac{\text{TP} + \text{TN}}{\text{TP} + \text{FN} + \text{FP} + \text{TN}}, \quad (15)$$

where TP refers to the number of target classes predicted as target classes, TN refers to the number of nontarget classes predicted as nontarget classes, FN refers to the number of nontarget classes predicted as target classes, and FP refers to predict the target class as the number of nontarget classes.

3.4. Experimental Results. Results of the proposed model were mainly divided into two parts: the feature extraction part and the training part of SVM classifier.

This section described the feature extraction part of the proposed model. The β-VAE introduced by the proposed model consumed many epochs and its loss decreased slowly. The training process is shown in Figure 9.

Intermediate vector extracted by β-VAE was generative, although the process of extraction was slow.

Another component of the proposed model was convolutional network 1. Lenet5 and Vgg19 were utilized as contrast networks to prove the good adaptability of the proposed model. The training process was carried out with the same training parameters. The result of verification is shown in Figure 10.

The verification accuracy of three models on the training set had risen to a high position as shown in Figure 10. The accuracy of the three models on the testing set was 99.422%, 90.366%, and 98.844%, respectively.

Network 1 had the highest accuracy and its rate of accuracy tended to stabilize quickly compared with the other model. But its testing accuracy was lower than the verification accuracy. Network 1 needed to be combined with β-VAE to achieve final effect. The output vectors of above two models were connected by the ratio of $5 : 1$. The training of SVM included the selection of kernel function γ and penalty coefficient c. The selection result of the kernel function is shown in Figure 11.
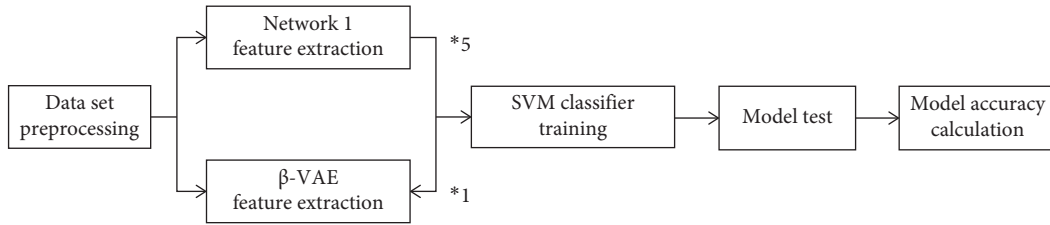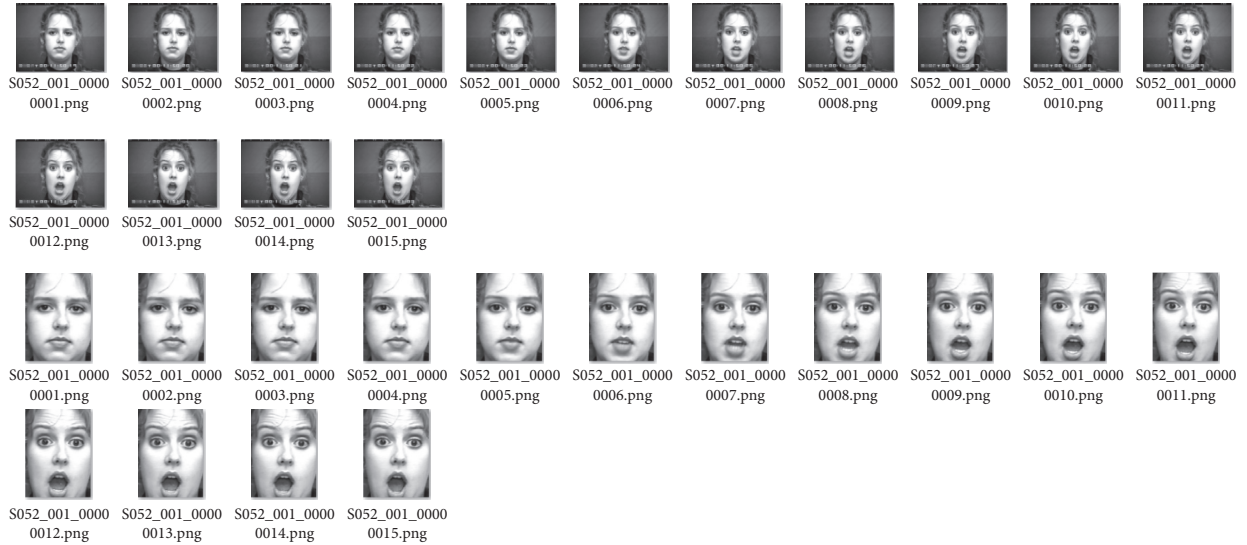
Figure 6: The overall structure of the model.

Figure 7: The comparison of face alignment result.

Figure 8: Partial result of comparison.

Table 2: Training parameters of convolution network 1.

Parameter	Value
Batch_size	12
Image_size	[224, 224]
Learning_rate	$1e-3$
Epoch	30

Table 3: Training parameters of β-VAE.

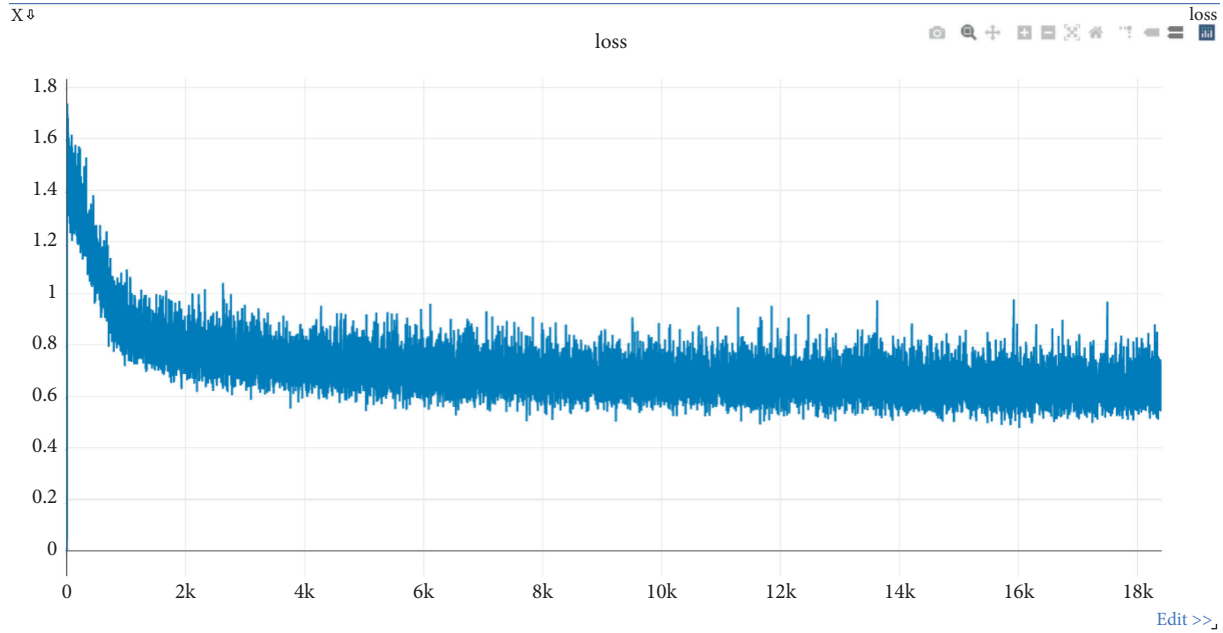| Parameter	Value
Batch_size	32
Image_size	[64, 64]
Learning_rate	$1e-3$
Epoch	200

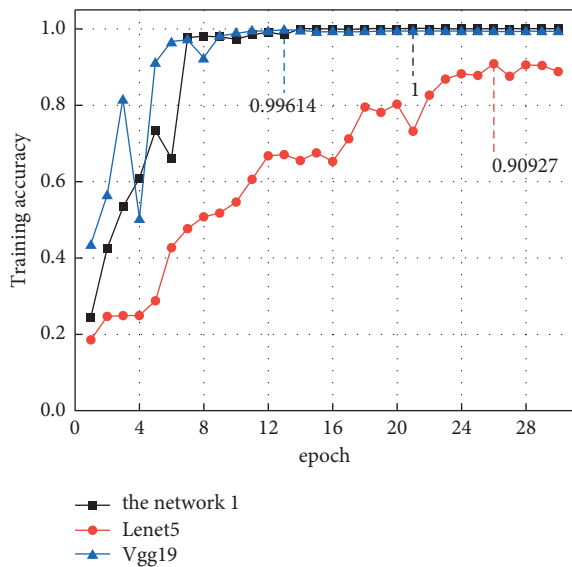FIGURE 9: The training process of β-VAE.

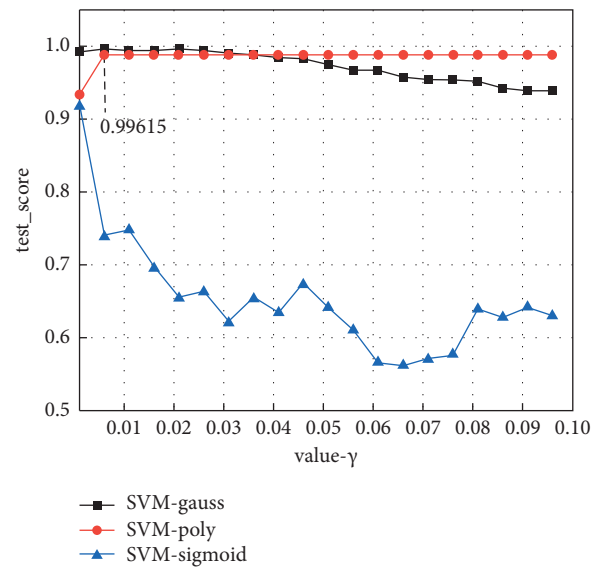FIGURE 10: The training process of models.

FIGURE 11: The classification accuracy of SVM classifier on testing set varied with different kernel functions and values of γ.

It can be found that the highest testing accuracy was 99.615% when the kernel function was Gauss, and its value was 0.006. The peak testing accuracy was about 98.844% and 91.715%, respectively, when the kernel function was poly and sigmoid. The best value of γ corresponding to three kernel functions can be determined to be 0.006, 0.006, and 0.001 via fine-tuning. Then, the penalty coefficient c can be adjusted to obtain final classifier. Its process is shown in Figure 12.

It can be found that only sigmoid kernel function was sensitive to changes in value of c. The testing accuracy of the proposed model was 99.615% when its kernel function was Gauss, the value of γ is 0.006, and c was 15.

Final accuracy had a small improvement in recognition compared with the network 1, but it was significantly higher than other comparison models. The above results were obtained from experiments on the preprocessed dataset. The training process on original CK+ dataset is shown in Figure 13.

It can be found from Figure 13 that the performance of models on the original dataset was worse, because their input image had too much interference and noise. Lenet5 has the largest drop, which illustrated the limitation of insufficient depth of convolutional network. The models at this time
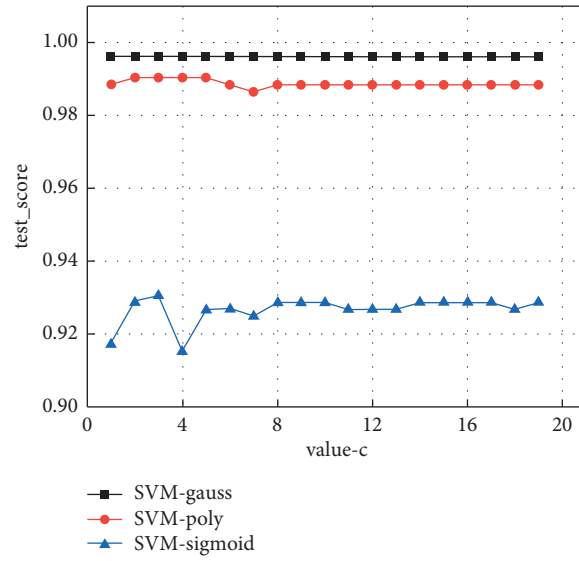
Figure 12: The classification accuracy of SVM classifier on testing set varied with different kernel functions and values of c.
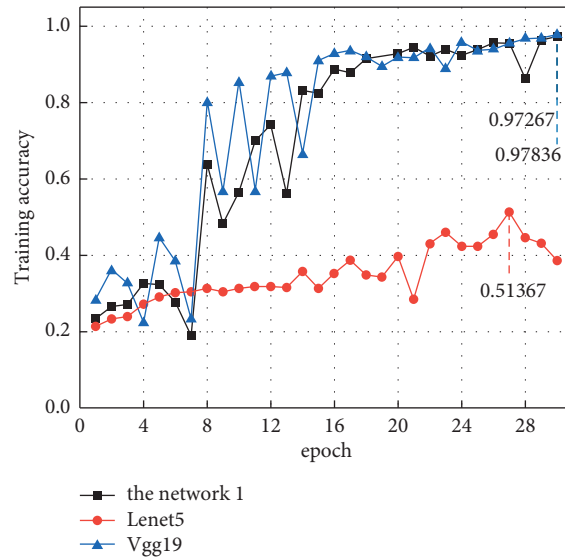

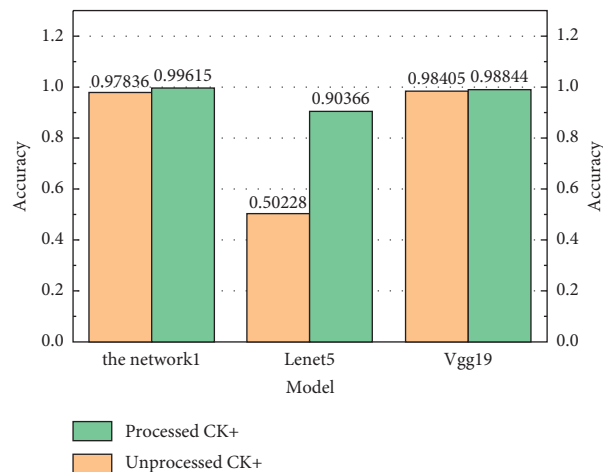Figure 13: The original CK+ dataset training process result.

Figure 14: Testing set test accuracy before and after dataset preprocessing.
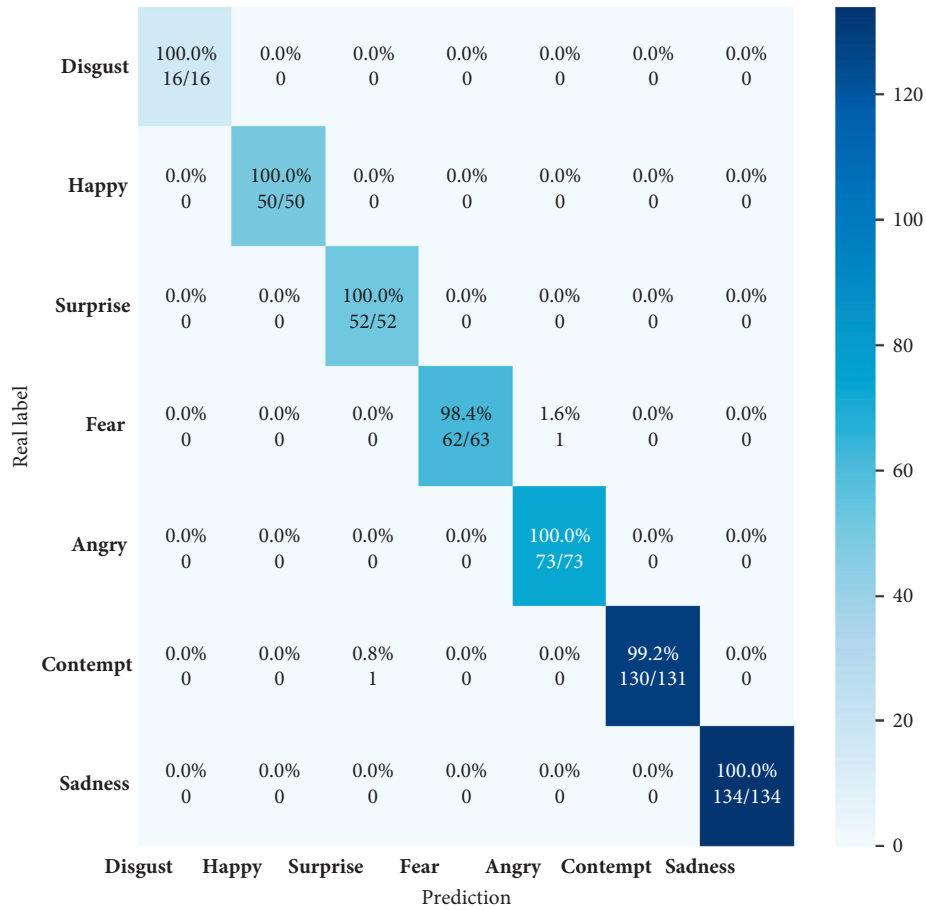
FIGURE 15: Confusion matrix of classification results of the proposed model.

were tested on the testing set, and the final comparison result is shown in Figure 14.

It can be found from Figure 14 that the highest testing accuracy of the proposed model is 99.615%, which further illustrated the rationality and advancement of it. Confusion matrix was utilized to further display recognition results of the proposed model, which is shown in Figure 15.

The following conclusions can be obtained by analyzing Figure 13:

(1) The quality of input image was high, and there is no error in other facial expression recognition except for fear and contempt

(2) A fear expression had similarity to an angry expression

(3) The result of disgust expression recognition was random due to its small number of samples

4. Conclusions

The facial expression recognition model proposed in the paper can achieve a great testing accuracy. The image preprocessing process made the proposed model converge faster and more stably. It had a significant effect on improving recognition accuracy. In summary, the proposed model had certain advantages and practicability in high-quality frontal expression recognition.

Data Availability

The CK+ data set was used to support this study and its application details are in http://www.jeffcohn.net/wp-content/uploads/2020/04/CK-AgreementForm.pdf. The data set is cited at relevant places within the text as references.

Conflicts of Interest

The authors declare that they have no conflicts of interest.

References

[1] A. Diete, T. Sztyler, L. Weiland et al., "Recognizing grabbing actions from inertial and video sensor data in a warehouse scenario," *Procedia Computer Science*, vol. 110, pp. 16–23, 2014.

[2] S. Kwon, D. Park, H. Bang, and Y. Park, "Real-time and parallel semantic translation technique for large-scale streaming sensor data in an IoT environment," *Journal of KIISE*, vol. 42, no. 1, pp. 54–67, 2015.

[3] S. Turabzadeh, H. Meng, R. M. Swash, M. Pleva, and J. Juhar, "Facial expression emotion detection for real-time embedded system," *Technologies*, vol. 6, 2018.

[4] D. Mehta, M. Siddiqui, and A. Javaid, "Facial emotion recognition: a survey and real-world user experiences in mixed reality," *Sensors*, vol. 18, no. 2, 416 pages, 2018.

[5] R. Gross, I. Matthews, J. Cohn, T. Kanade, and S. Baker, "Multi-PIE," *Image and Vision Computing*, vol. 28, no. 5, pp. 807–813, 2010.

[6] P. Lucey, J. F. Cohn, T. Kanade et al., "The extended Cohn-Kanade dataset (CK+): a complete dataset for action unit and emotion-specified expression," in *Proceedings of the 2010 IEEE Computer Society Conference on Computer Vision and Pattern Recognition-Workshops*, pp. 94–101, IEEE, San Francisco, CA, USA, June 2010.

[7] Q.-r. Mao, X.-y. Pan, Y.-z. Zhan, and X.-j. Shen, "Using Kinect for real-time emotion recognition via facial expressions," *Frontiers of Information Technology & Electronic Engineering*, vol. 16, no. 4, pp. 272–282, 2015.

[8] H. Y. Yang, U. Ciftci, and L. J. Yin, "Facial expression recognition by de-expression residue learning," *International Journal of Computer Science and Engineering*, vol. 3, no. 2, pp. 2220–2224, 2018.

[9] F. Zhang, T. Zhang, Q. Mao et al., "Joint pose and expression modeling for facial expression recognition," in *Proceedings of the IEEE/CVF Conference on Computer Vision and Pattern Recognition*, pp. 3359–3368, Salt Lake, UT, USA, June 2018.

[10] C. M. Kuo, S. H. Lai, and M. Sarkis, "A compact deep learning model for robust facial expression recognition," in *Proceedings of the IEEE/CVF Conference on Computer Vision and Pattern Recognition Workshops (CVPRW)*, Salt Lake, UT, USA, June 2018.

[11] Z. Meng, P. Liu, J. Cai et al., "Identity-aware convolutional neural network for facial expression recognition," in *Proceedings of the 12th IEEE International Conference on Automatic Face & Gesture Recognition (FG 2017)*, pp. 558–565, Washington, DC, USA, June 2017.

[12] L. T. W. Cheng and J. W. Wang, "Enhancing learning performance through classroom response systems: the effect of knowledge type and social presence," *International Journal of Management in Education*, vol. 17, no. 1, pp. 103–118, 2019.

[13] R. W. Picard, *Affective Computing*, The MIT Press, Cambridge, MA, USA, 2019, https://www.media.mit.edu/groups/affective-computing/overview/.

[14] P. Ekman and W. V. Friesen, "Facial action coding system (FACS): a technique for the measurement of facial actions," *Rivista di Psichiatria*, vol. 12, no. 47, pp. 126–138, 1978.

[15] L. Shan and W. Deng, "Deep facial expression recognition: a survey," *IEEE Transactions on Affective Computing*, no. 99, p. 1, 2018.

[16] E. Yadegaridehkordi, N. F. B. M. Noor, M. N. B. Ayub, H. B. Affal, and N. B. Hussin, "Affective computing in education: a systematic review and future research," *Computers & Education*, vol. 142, Article ID 103649, 2019.

[17] J. Wang, L. J. Yin, X. Z. Wei et al., "3D facial expression recognition based on primitive surface feature distribution," in *Proceedings of the IEEE Computer Society Conference on Computer Vision and Pattern Recognition*, vol. 2, pp. 1399–1406, New York, NY, USA, June 2006.

[18] W. B. Putra and F. Arifin, "Real-time emotion recognition system to monitor student's mood in a classroom," *Journal of Physics: Conference Series*, vol. 1413, Article ID 012021, 2019.

[19] K. Zhang, Z. Zhang, Z. Li, and Y. Qiao, "Joint face detection and alignment using multitask cascaded convolutional networks," *IEEE Signal Processing Letters*, vol. 23, no. 10, pp. 1499–1503, 2016.

[20] B. R. Jiang, R. X. Luo, J. Y. Mao et al., "Acquisition of localization confidence for accurate object detection," 2018, https://arxiv.org/abs/1807.11590.

[21] Y. Y. Hu, S. Yang, W. H. Yang et al., "Towards coding for human and machine vision: scalable face image coding," *IEEE Transactions on Multimedia*, pp. 1–6, 2020.

[22] Z. Wang, A. C. Bovik, H. R. Sheikh, and E. P. Simoncelli, "Image quality assessment: from error visibility to structural similarity," *IEEE Transactions on Image Processing*, vol. 13, no. 4, pp. 600–612, 2004.

[23] D. P. Kingma and M. Welling, "Auto-encoding variational Bayes," *Clinical Orthopaedics and Related Research*, vol. 10501 page, 2014.

[24] I. Higgins, L. Matthey, A. Pal et al., "Beta-VAE: learning basic visual concepts with a constrained variational framework," 2016, https://openreview.net/forum?id=Sy2fzU9gl.

WILEY | Hindawi

Research Article

Deep Grid Scheduler for 5G NB-IoT Uplink Transmission

Han Zhong [1,2] **Ruize Sun** [1] **Fengcheng Mei** [1] **Yong Chen** [1] **Fan Jin** [3]
and Lei Ning [1]

[1]*College of Big Data and Internet, Shenzhen Technology University, Shenzhen, China*
[2]*College of Applied Technology, Shenzhen University, Shenzhen, China*
[3]*Shenzhen Winoble Technology Co., Ltd, Shenzhen, China*

Correspondence should be addressed to Lei Ning; ninglei@sztu.edu.cn

Since the birth of narrowband Internet of Things (NB-IoT), the Internet of Things (IoT) industry has made a considerable progress in the application for smart cities, smart manufacturing, and healthcare. Therefore, the number of UEs is increasing exponentially, which brings considerable pressure to the efficient resource allocation for the bandwidth and power constrained NB-IoT networks. In view of the conventional algorithms that cannot dynamically adjust resource allocation, resulting in a low resource utilization and prone to resource fragmentation, this paper proposes a double deep Q-network (DDQN)-based NB-IoT dynamic resource allocation algorithm. It first builds an NB-IoT environment model based on the real environment. Then, the DDQN algorithm interacts with the NB-IoT environment model to learn and optimize resource allocation strategies until it converges to the optimum. Finally, the simulation results show that the DDQN-based NB-IoT dynamic resource allocation algorithm is better than the traditional algorithm in the resource utilization, average transmission rate, and UE average queuing time.

1. Introduction

With the advancement of science and technology, the IoT is being used more and more widely in various industries [1]. In order to meet the needs of the IoT industry, it has redesigned a new communication solution for the IoT, which is called the NB-IoT [2]. The access system was proposed in the 69th plenary meeting of the 3rd generation (3GPP) organization. The NB-IoT system focuses on low-complexity and low-throughput radio access technology. The main research goals include improved indoor coverage, support for a large number of low-throughput user equipment, lower latency sensitivity, and ultralow equipment cost, low equipment power consumption, and network architecture. For the use scenarios of NB-IoT, the relevant technical characteristics of NB-IoT are as follows [3]:

(1) Low power consumption: NB-IoT uses power save mode (PSM) and extended discontinuous reception (eDRX) to reduce power consumption. It is estimated that a 5Wh battery can provide maximum battery life up to 10 years.

(2) Channel bandwidth: the bandwidth is 200 kHz, including a guard band of 20 kHz.

(3) Coverage enhancement: NB-IoT achieves coverage enhancement mainly by increasing the uplink power spectral density and repeated transmission so that outdoor coverage is large and indoor penetration is improved. In the same frequency band, compared with the existing general packet radio service, general packet radio service (GPRS) network coverage increased by 20 dB, the maximum coupling loss (MCL) can reach 164 dB, and the coverage area is expanded 100 times.

(4) A large number of equipment access: it can support a large number of low-throughput terminals, up to 50 K connections per cell. Under the coverage of the same base station, NB-IoT can support up to 50–100 times the number of access devices compared to the existing wireless technology.

(5) Low cost: NB-IoT only supports FDD half-duplex mode, which is cheaper than full duplex. The cost of the module is less than US$5. It is expected to be

reduced to US$2-3 by 2020, and a single antenna is used for transmission. It can also reduce the complexity of chip processing, thereby reducing costs.

Based on the characteristics above, NB-IoT can locate devices with poor channel transmission conditions or delay tolerance and can be widely used in smart homes, smart cities, smart grids, healthcare, smart manufacturing, and smart logistics [4–6].

Although NB-IoT technology is developing in full swing, it still faces the challenges of spectrum efficiency, system capacity, and interference coexistence [7]. NB-IoT introduces processes such as repeated transmission and reinitialization of the scrambling sequence, which increases the complexity of part of the NB-IoT physical layer processing process [8]. Narrowband physical uplink shared channel (NPUSCH) has a bandwidth of only 180 kHz. It not only carries uplink data services but also needs to transmit response information indicating whether the narrowband physical downlink shared channel (NPDSCH) has been successfully received. Therefore, efficient use of spectrum resources is very necessary [9].

Therefore, how NB-IoT allocates spectrum resources for UEs efficiently is a key issue. In view of the low resource utilization of traditional resource allocation algorithms, fragmentation is prone to occur, and the average waiting delay is high, and this article proposes a DDQN-based dynamic resource allocation algorithm. This article first builds an NB-IoT environment model based on the real environment. The DDQN algorithm interacts with the NB-IoT environment model and stores historical experience in the experience pool to accumulate data for subsequent model training and learning. After learning and iteration, the algorithm is better than the traditional algorithm in resource utilization, average transmission speed, and average waiting time.

The rest of the paper is organized as follows. A relate work on NB-IoT is provided in Section 2. Section 3 presents the experimental design, including the environment model of NB-IoT uplink and the proposed of DDQN algorithm. The performance analysis is reported in Section 4. We finally conclude the paper in Section 5.

2. Relate Work

At present, most machine-type communications are still based on the LTE scheduler [10]. Using the LTE scheduler can maximize the overall transmission success rate and minimize the machine-to-machine (M2M) delay. In [11], EDDF-based LTE scheduling procedures have been shown to be effective in maximizing the transmission success rate and minimizing delay. In [12], Afrin et al. proposed a schedular based on an OPNET simulation model of an LTE TDD system. The scheduler can satisfy the uplink delay budget for more than 99% of packets for bursty delay sensitive M2M traffic even when the system is fully loaded with regard to the data channel utilization. However, this requires additional signaling overhead to transmit the waiting time at the head of the queue.

In order to solve the static problem of the algorithms, adaptive algorithms have also been extensively studied in the resource allocation of NB-IoT. In [13], Sampath et al. used an adaptive algorithm to develop an analytical outer loop power control model to deal with signal-to-interference ratio fluctuations. Li et al. [14] studied the influence of uplink interference on link adaptation in heterogeneous networks and proposed a cooperative uplink adaptation scheme using cooperation between base stations. In [15], a novel algorithm for improving outer loop link adaptation (OLLA) convergence speed in the downlink of long-term evolution (LTE) is presented. The algorithm is validated with a connection-level simulator, fed with real connection traces collected from a live LTE network. In [16], the potential of OLLA to cope with the aforementioned problem is studied, and a dynamic OLLA (d-OLLA) algorithm is proposed.

In order to optimize the resource allocation of NB-IoT, some resource issues for NB-IoT have also been studied. Su et al. [17] propose a method for active detection and processing of redundant rules. In [18], a new Aloha-based tag identification protocol is presented to improve the reading efficiency of the EPC C1 Gen2-based UHF RFID system. Min Oh et al. [19] proposed an efficient small data transmission scheme in the 3GPP NB-IoT system. For the efficient use of radio resources, the proposed scheme enables devices in an idle state to transmit a small data packet without the radio resource control connection setup process. This can improve the maximum number of supportable devices in the NB-IoT system which has insufficient radio resources. Recently, Huang et al. [20] identified radio resource scheduling issues for NB-IoT systems and provided a comprehensive performance evaluation. Then, the authors proposed an NB-IoT downlink scheduling algorithm. Wu et al. [21] proposed a deep Q-learning network (DQN) method used to control the hand-over (HO) procedure of the user equipment (UE) by well capturing the characteristics of wireless signals/interferences and network load. In [22], a multiagent deep Q-network- (DQN-)based dynamic joint spectrum access and mode selection (SAMS) scheme is proposed for the SUs in the partially observable environment. Zhang et al. [23] proposed a two-step deep reinforcement learning-based algorithm to solve nonconvex and dynamic optimization problem. However, the above research studies have not addressed how to reduce resource fragmentation. In our previous work [24], we propose a dynamic resource allocation algorithm without theoretical analyses for the NB-IoT uplink scheduling problem and did not consider the waiting delay of the UE.

In this article, we consider the waiting delay of the UE and the NB-IoT scheduling problem for 3GPP NB-IoT cellular networks. The objective is to maximize resource utilization and reduce resource fragmentation while ensuring UE has a short waiting time delay. Therefore, we propose a dynamic resource scheduling algorithm based on deep reinforcement learning to optimize the resource utilization of NB-IoT. In Section 3, we will first introduce the system model and the problem formulation will be presented as follows.

3. System Model and Problem Formulation

In this section, we first introduce the NB-IoT uplink system model and give some parameter settings in the NB-IoT uplink. Then, we will model and analyze the resource allocation problem based on the NB-IoT uplink system model.

3.1. The System Model of NB-IoT Uplink. NB-IoT uplink frequency domain resources are the same as downlink, and frequency domain resources are 180 kHz, using SC-FDMA [3]. Taking into account the low-cost requirements of NB-IoT devices, it is necessary to support single frequency (single tone) transmission in the uplink. In addition to the original 15 kHz, a new subcarrier spacing of 3.75 kHz has been set for a total of 48 subcarriers. Considering that 3.75 kHz is rarely used in real commercial environments, this article only considers the case of 15 kHz, which is divided into 12 subcarriers in the frequency domain. For the uplink, NB-IoT defines two physical channels: NPUSCH and NPRACH (narrowband physical random access channel) and demodulation reference signal (DMRS). NPRACH allocation in the frequency domain is periodically allocated by the evolved node B (eNB). The UE transmits the NPRACH on the fixed frequency domain resources allocated by the eNB, and the remaining channels are used for NPUSCH transmission. NPUSCH is used to transmit uplink data and control information. NPUSCH transmission can use single tone or multitone transmission.

Compared with the physical resource block (PRB) as the basic resource scheduling unit in long-term evolution (LTE), the resource unit of the NB-IoT uplink shared physical channel NPUSCH is scheduled with a flexible combination of time-frequency resources. The basic unit of scheduling is called resource unit (RU). NPUSCH has two transmission formats, the corresponding resource units are different, and the content of transmission is also different. NPUSCH format 1 is used to carry the uplink-shared transmission channel UL-SCH, to transmit user data or signaling, and the UL-SCH transmission block can be scheduled and sent through one or several physical resource units. The occupied resource unit includes two formats, which are single tone and multitone. NPUSCH format 2 is used to carry uplink control information, such as ACK/NAK response. The specific RU of single tone and multitone is defined in Table 1.

The value of RU in NPUSCH is determined by TBS, MCS, and the number of repetitions. The specific RU value is calculated from Table 2.

3.2. Problem Formulation. In this section, we study the NB-IoT uplink resource allocation problem over NB-IoT networks. The objective is to maximize the resource utilization of NB-IoT and reduce resource fragmentation. The system model can be formulated as follows.

First of all, NB-IoT does not support measurement reports. According to the difference in minimum path loss (MCL), 3GPP defines three coverage levels: normal coverage, extended coverage, and extreme coverage. The MCL corresponding to the three coverage levels is no higher than

144 dB, no higher than 154 dB, and no higher than 164 dB. Under different coverage levels, NPUSCH and NPRACH channels use different MCS and repetition times.

NPRACH is periodically transmitted in the NB-IoT uplink, and the number of repetitions $N_{\text{rep}}^{\text{NPRACH}}$ corresponding to the three coverage levels is 2, 4, and 8. The unit length of NPRACH $N_{\text{slots}}^{\text{NPRACH}}$ is 2 ms. And, the number of PRACH subcarriers N_{sc}^{NPRACH} is configured by the base station; then, the resource R_{NPRACH} occupied by a NPRACH resource can be expressed as

$$R_{\text{NPRACH}} = N_{\text{rep}}^{\text{NPRACH}} * N_{sc}^{\text{NPRACH}} * N_{\text{slots}}^{\text{NPRACH}}. \quad (1)$$

The starting subcarrier index of the NPRACH resource $N_{\text{scoff set}}^{\text{NPRACH}}$ is configured by the base station, and the default base station configuration is used in this article, which is 8, 16, and 32.

The UE transmits data through the NPUSCH, and the relevant parameters of the NPUSCH are indicated by the Format N0 of the DCI in the NPDCCH, including the modulation and coding scheme I_{TBS}, the number of repetitions $N_{\text{rep}}^{\text{NPUSCH}}$, the number of time slots $N_{\text{slot}}^{\text{UL}}$, and the subcarrier indication N_{sc}^{NPUSCH}. From the modulation and coding scheme I_{TBS} and the data size DS to be transmitted, we can check Table 2 and calculate N_{R}:

$$N_{\text{RU}} = \arg \min \left[\text{TBS} \left(I_{\text{TBS}} \right) > = \text{DS} \right]. \quad (2)$$

Then, the resource R_{NPUSCH} occupied by a NPUSCH transmission can be calculated by the formula

$$R_{\text{NPUSCH}} = N_{\text{RU}}^{*} N_{sc}^{\text{NPUSCH}} * N_{\text{slot}}^{\text{UL}} * N_{\text{rep}}^{\text{NPUSCH}}. \quad (3)$$

The utilization of frequency domain resources on a time domain resource U_i can be expressed as the sum of NPRACH and NPUSCH occupying the time domain resource at that moment divided by the number of NB-IoT subcarriers. The formula is as follows:

$$U_i = \frac{\sum R_i^{\text{NPUSCH}} + \sum R_i^{\text{NPRACH}}}{N_{sc}^{RA}}. \quad (4)$$

Constrained by the communication protocol [25], the allocation of wireless resources needs to consider the period, so the goal we pursue is to maximize U_i at each moment and minimize the fragmentation of resources at each moment:

$$\left(a_{sc}, a_t \right) = \arg \max U_i. \quad (5)$$

4. Dynamic Resource Allocation Algorithm Based on DDQN

Reinforcement learning is one of the important tools in the field of machine learning. It is widely used to deal with Markov dynamic programming problems [26, 27]. As shown in Figure 1, the AI engine is designed as an agent that combines deep learning and reinforcement learning. The agent interacts with the Mac layer in NB-IoT and observes the resource occupancy and UE request as the state of the environment from the Mac layer. The AI engine generates

TABLE 1: NPUSCH RU format.

NPUSCH Format	Subspacing (kHz)	Sub Num	TS Num	Duration (ms)
1	3.75	1	16	32
1	15	1	16	8
1	15	3	8	4
1	15	6	4	2
1	15	12	2	1
2	3.75	1	4	8
2	15	1	4	2

TABLE 2: Transport block size (TBS) table for NPUSCH.

I_{TBS}	N_{RU}							
	1	2	3	4	5	6	7	8
0	16	32	56	88	120	152	208	256
1	16	32	56	88	120	152	208	256
2	32	72	144	176	208	256	328	424
3	32	72	144	176	208	256	328	424
4	56	120	208	256	328	408	552	680
5	56	120	208	256	328	408	552	680
6	88	176	256	392	504	600	808	1000
7	104	224	328	472	584	712	1000	1224
8	120	256	392	536	680	808	1096	1384
9	136	296	456	616	776	936	1256	1544
10	144	328	504	680	872	1000	1384	1736

corresponding actions to allocate corresponding resources to the UE.

The agent optimizes and adjusts the strategy through the rewards of environmental feedback and repeats this process until the optimal strategy is finally obtained. In reinforcement learning, Q learning is a very effective learning method and is widely used in various fields. Different from the SARSA algorithm and other on-policy algorithms, Q learning is updated according to the improved strategy of $q(s_{t+1}, *)$, so as to achieve closer target value. Its goal formula can be defined as

$$U_t = R_{t+1} + \gamma R_{t+2} + \cdots + \gamma^{n-1} R_{t+n} + \gamma^n \max_{a \in A(S_{t+n})} q(S_{t+n}, a_{(sc,t)}). \tag{6}$$

Q learning updates the action value based on the above formula, which easily leads to maximization deviation and makes the estimated $q^{(0)}(\cdot, \cdot)$ action value too large. Therefore, double Q learning is introduced. The double Q learning algorithm uses two independent action value estimates and $q^{(1)}(\cdot, \cdot)$ and replaces $\max_a q(S_{t+1}, a_{(sc,t)})$ in Q learning with $q^{(0)}(S_{t+1}, \arg\max_a q^{(1)}(S_{t+1}, a_{(sc,t)}))$ or $q^{(0)}(S_{t+1}, \arg\max_a q^{(1)}(S_{t+1}, a_{(sc,t)}))$. Since $q^{(0)}$ and $q^{(1)}$ are independent estimates, there is

$$E\left[q^{(0)}(S_{t+1}, A^*)\right] = q(S_{t+1}, \arg\max_a q^{(1)}(S_{t+1}, a_{(sc,t)})). \tag{7}$$

In the process of double learning, both $q^{(0)}$ and $q^{(1)}$ are updated gradually, and each step of learning can select any one of the following two to update with equal probability:

$$U_t^{(0)} = R_{t+1} + \gamma q^{(1)}(S_{t+1}, \arg\max_a q^{(0)}(S_{t+1}, a_{(sc,t)})),$$
$$U_t^{(1)} = R_{t+1} + \gamma q^{(0)}(S_{t+1}, \arg\max_a q^{(1)}(S_{t+1}, a_{(sc,t)})). \tag{8}$$

The traditional Q learning algorithm can effectively obtain the optimal strategy when the state space and action space are small. However, in actual situations, the state space and action space of the agent are very large. At this time, it is difficult for the Q learning algorithm to achieve the ideal effect. Therefore, a deep Q network composed of a combination of Q learning and neural network can solve this problem well.

Reinforcement learning data is usually nonstatic, non-independent, and uniformly distributed. One state of data may continue to flow in, and the next state is usually highly correlated with the previous state. Therefore, small deviations in the value of the Q function will affect the entire strategy. As a supervised learning model, deep neural networks require data to meet independent and identical distribution. In order to break the correlation between data, DQN adopts the method of experience replay, storing the past training data in the form of (s_t, a_t, r_t, s_{t+1}) in the experience pool, and randomly extracts part of the data each time as the input of the neural network for training. Through the use of experience replay, the correlation between the original data is broken, and the training data become more independent and evenly distributed.

The network composed of double Q learning and DQN is called double deep Q network (DDQN). In the DDQN, only the evaluation network is used to determine the action, and the target network is used to determine the estimate of the return. The algorithm process of the DDQN is shown in Algorithm 1.
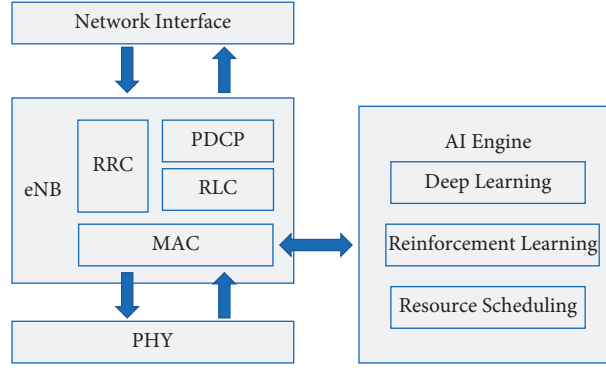
FIGURE 1: The interaction process between AI engine and NB-IoT environment.

Initialize the evaluation network $q(\cdot, \cdot; w)$ and target network $q(\cdot, \cdot; w_{\text{target}})$
for episode in episodes do
    initialize and choose state $S_{(\text{NPUSCH, NPRACH, UE})}$ from NB-IoT MAC
    while episode not end do
        sampling $q(S, \cdot; w)$ and get action $A_{\text{sc},t}$
        observation from NB-IoT MAC and get reward R and next state S'
        store experience $(S, A_{\text{sc},t}, R, S') \longrightarrow D$
        $D \longrightarrow (S_i, A_{(\text{sc},t)i}, R_i, S'_i)_{(i \in B)}$
        $U_i = R_i \cdot + \gamma q(S'_i, \arg\max_a q(S'_i, a_{\text{sc},t}; w); w_{\text{target}})$
        update w
        $S \leftarrow S'$
        if batch size $\geq$ memory capacity then
            update $w_{\text{target}} \leftarrow w$
        end if
    end while
end for

ALGORITHM 1: Procedure of double deep Q network.

In view of the characteristics of NB-IoT uplink data transmission, the state observed by the agent is divided into 12 frequency domains, and the distribution of resource utilization in each frequency encounter on the time axis is used as the feature of each frequency domain. At the same time, the state also includes UE data size, NPUSCH format, transmission quality, number of repetitions, and the number of N_{RU}. The corresponding action taken by the agent is to allocate the corresponding resources required by the UE in the frequency domain resources. Therefore, the action of the agent is composed of 12 actions, corresponding to the divided 12 frequency domain positions.

5. Performance Evaluation

In this section, we present the analysis of NB-IoT dynamic resource allocation algorithm based on DDQN. First, we introduce the NB-IoT environment model parameters and the DDQN algorithm model parameters, and then, we will give a specific performance comparison between the DDQN algorithm and the traditional algorithm.

5.1. Model Parameter Settings. In order to verify whether the DDQN algorithm can achieve better results in a complex network environment, this paper simulates the NB-IoT uplink data link NPUSCH to establish an environment model. Every second, an average of 1000 UEs need to establish a connection to transmit data, and the communication quality of each UE is randomly selected. According to the distribution of communication quality in real scenarios [5], this article divides the communication quality into three types: good, medium, and poor, and their probability corresponds to 60%, 30%, and 10%. When each UE establishes a connection, the communication quality is randomly determined according to the probability. According to the characteristics of NB-IoT data transmission in real life, the data transmission volume is generally 50-250 bytes, and the data volume of the UE in the simulation is also randomly generated based on this range. The simulation model and deep reinforcement learning constructed in this paper are implemented by Python, and the DDQN algorithm is designed and trained based on PyTorch. The values of the network parameters and deep reinforcement learning parameters in this experiment are shown in Tables 3 and 4. The neural network used for training is a fully connected neural network, which contains a hidden layer, and the hidden layer contains 50 neurons. The activation function used by each neuron is ReLU. The size of the discount factor determines

TABLE 3: NPUSCH parameters.

Parameter name	Parameter value
Channel bandwidth	180
Subcarrier spacing	15
I_{TBS}	1, 2, 3, 4, 5, 6, 7, 8, 9, 10
NPUSCH repetitions	0, 8
Data size	Range (50, 250)

TABLE 4: DDQN algorithm parameters.

Parameter name	Parameter value
Greedy policy, ε	0.9
Reward discount, γ	0.9
Learning rate, α	0.01
Target update frequency	100
Batch size	256
Memory capacity	5000
Actions	12
States	13

how much the algorithm attaches importance to current returns and future returns. The smaller the discount factor is, the more the algorithm tends to have short-term high returns. Since a series of actions need to be made in this experiment, in order to obtain a longer-term high return, this article sets the discount factor to 0.9.

Based on the parameters of Tables 3 and 4, the experiment scenario is simulated. In this experiment, dynamic resource scheduling is performed on the 180 kHz NB-IoT uplink data link NPUSCH. On average, 1,000 UEs are scheduled per second, and the number of iteration rounds is 100,000. Calculate the average resource utilization, average transmission speed, and average waiting delay after each dynamic scheduling as the performance evaluation index. Specific performance comparison will be shown in the following.

5.2. Analysis of NB-IoT Dynamic Allocation Algorithm Based on DDQN. In this simulation, 1,000 UE request data transmission every second, and the communication quality distribution of UE is designed to be 60% with good quality, 30% with medium communication quality, and 10% with poor communication quality. In 100,000 iterations, the actual UE distribution per second is shown in Figure 2. The figure shows the average distribution of three communication qualities per second within 100s. The three communication qualities are all at 60% and 30% and 10% fluctuate, of which good communication quality is slightly higher than 60%.

According to the data size sent by NB-IoT, in reality, the amount of data transmitted by the UE is set to be randomly distributed between 50 and 250. In this simulation, the average data size actually transmitted per second is shown in Figure 3. Compared with the average data size of good communication quality and medium communication quality, the average transmission data size of UEs with poor communication quality fluctuates greatly. The three types of data size variance are shown in Figure 4. This phenomenon is because the

number of UEs is small, and the randomly distributed number is much lower than the number with good communication quality and medium communication quality.

In this simulation, the UE will use the communication quality and data volume shown in Figures 2 and 4 as the UE's communication characteristics and, respectively, use DDQN dynamic resource allocation algorithm and traditional resource allocation algorithm for resource allocation. Calculate the average resource utilization rate, average transmission speed, and average waiting time delay after each dynamic scheduling as evaluation indicators. The simulation results are shown in Figures 5–7.

As shown in Figure 5, it is a comparison chart of the average resource utilization between the DDQN dynamic resource allocation algorithm and the traditional algorithm. The resource utilization rate is obtained by calculating the utilization of the 12 subcarriers divided by the 180 kHz frequency domain. The average resource utilization rate is obtained by dividing the resource utilization rate per millisecond by the total number of UEs in history.

Through comparison, it can be found that, in the initial 10,000 iterations, the resource utilization rate of the DDQN dynamic resource allocation algorithm fluctuates greatly, and the agent is still in the exploratory stage, and the average resource utilization rate fluctuates sharply between 50% and 80%. Between 10,000 iterations and 20,000 iterations, the fluctuation of the DDQN dynamic resource allocation algorithm has been greatly reduced, and its resource utilization rate is better than that of the transmission resource allocation algorithm. After 20,000 iterations, the average resource utilization of the DDQN dynamic resource allocation algorithm can be stabilized at about 83%, which is an improvement of about 7% compared to the traditional dynamic resource allocation algorithm.

Figures 6 and 7 show the corresponding data transmission speed and the average waiting time of the UE. The sum of the data size carried by each subcarrier in one of the time domains is used as the data transmission speed per

FIGURE 2: The distribution of the three communication qualities.
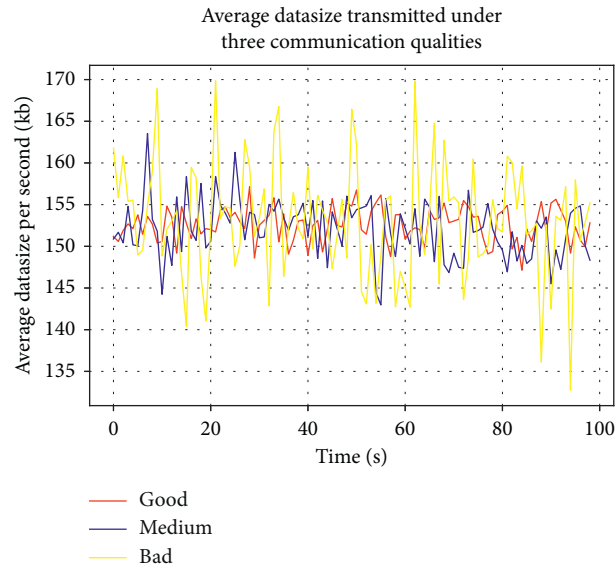

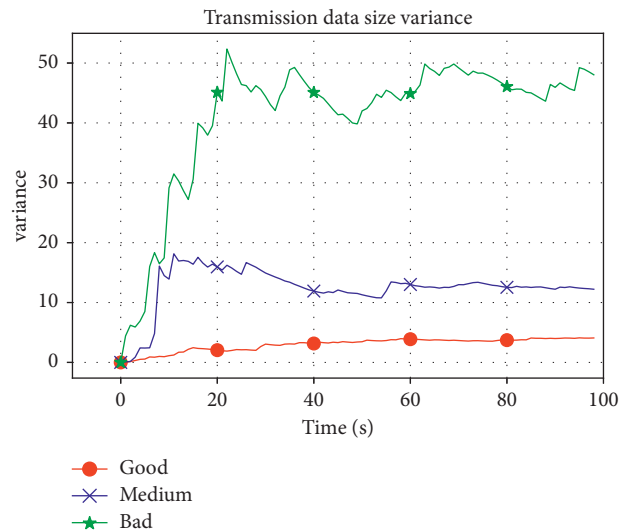FIGURE 3: Average data size transmitted under three communication qualities.

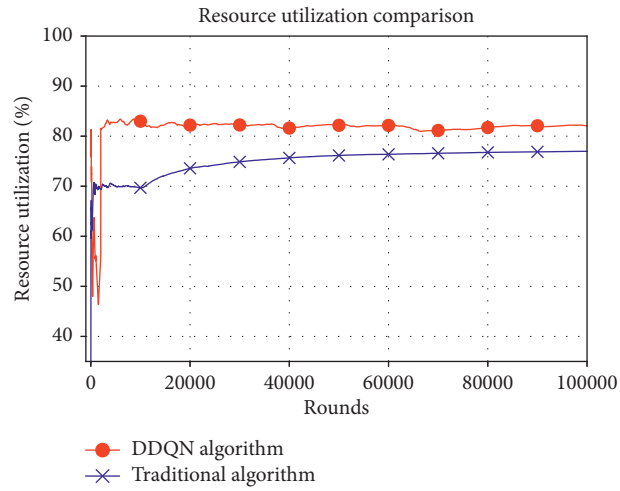FIGURE 4: Transmission data size variance.

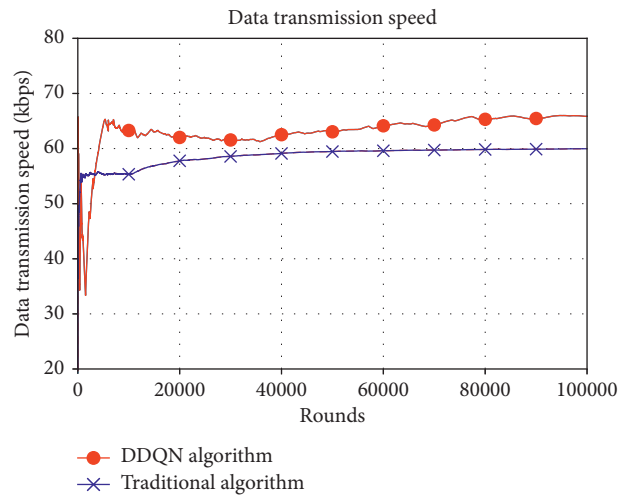FIGURE 5: Resource utilization comparison.

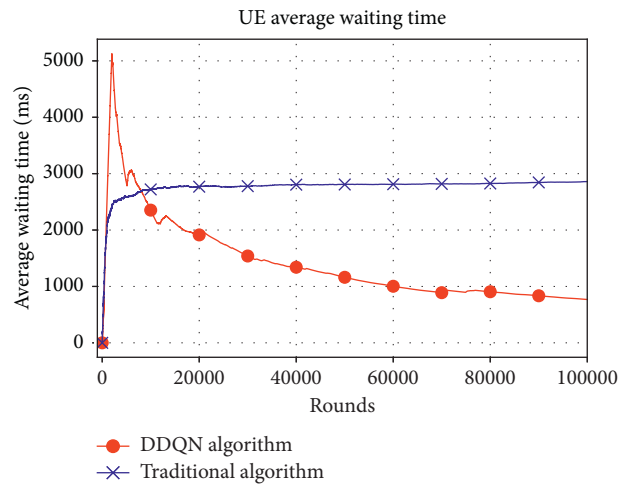FIGURE 6: Data transmission speed.

FIGURE 7: UE average waiting time.

millisecond, and the sum of historical data is calculated and the average value is taken as the data transmission speed at each moment. The period from the UE sending the request to the beginning of data transmission is defined as the waiting time of the UE, and the average value of the sum of the historical waiting time of the UE is taken as the average waiting time of the UE at each moment.

When the number of iterations is before 10,000, the resource utilization rate fluctuates drastically, the corresponding data transmission speed also fluctuates drastically, and the average waiting time of the UE is longer. When the number of iterations is between 10,000 and 20,000, the data transmission speed increases exponentially due to the increase in resource utilization and finally stabilizes at about 65, which is a 5% increase compared to traditional resource allocation algorithms. After the DDQN resource allocation algorithm is stable after 60,000 iterations, the average waiting time of the UE is less than 1, which is a 66% improvement compared to the traditional resource allocation algorithm.

In this simulation, we compared the DDQN dynamic resource allocation algorithm and the traditional resource allocation algorithm from the three dimensions of average resource utilization, average transmission speed, and average waiting time. In the simulation results, the DDQN algorithm is better than the traditional resource allocation algorithm in three aspects. DDQN improves the resource utilization of NB-IoT, reduces resource fragmentation, and increases the transmission speed and greatly shortens the average waiting time of the UE.

6. Conclusion

In this paper, we propose an NB-IoT uplink data transmission optimization algorithm based on deep reinforcement learning. The algorithm considers the time-frequency domain resources of NB-IoT as the state space, the frequency domain position as the action, the neural network as the error function, and the resource utilization as the reward and punishment value. DDQN is designed to interact with the environment and iteratively train the algorithm model. Compared with the traditional algorithm, the simulation results have improved the resource utilization and the data transmission rate. Meanwhile, the average waiting time of the UE has also been greatly shortened. Therefore, this algorithm model can effectively solve the dynamic scheduling problem of NB-IoT under the circumstance of the data transmission for massive devices. In the future, we will introduce a software radio platform and embed algorithms into the platform. Use the combination of software and hardware to further verify the performance of the algorithm.

Data Availability

The data used to support the findings of the study are available from the corresponding author upon request.

Conflicts of Interest

The authors declare that they have no conflicts of interest.

References

[1] U. Raza, P. Kulkarni, and M. Sooriyabandara, "Low power wide area networks: an overview," *IEEE Communications Surveys Tutorials*, vol. 19, no. 2, pp. 855–873, 2017.

[2] A. Haridas, V. S. Rao, R. V. Prasad, and C. Sarkar, "Opportunities and challenges in using energy-harvesting for NB-IoT," *SIGBED Review*, vol. 15, no. 5, pp. 7–13, 2018.

[3] Y. Miao, W. Li, D. Tian, M. S. Hossain, and M. F. Alhamid, "Narrowband internet of things: simulation and modeling," *IEEE Internet of Things Journal*, vol. 5, no. 4, pp. 2304–2314, 2018.

[4] A. Kumar Sultania, C. Delgado, and J. Famaey, "Implementation of NB-IoT power saving schemes in ns-3," in *Proceedings of the 2019 Workshop on Next-Generation Wireless with ns-3, WNGW*, pp. 5–8, Association for Computing Machinery, New York, NY, USA, June 2019.

[5] R. Zhang, Z. Han, T. Zheng, and L. Ning, "Trajectory mining-based city-level mobility model for 5G NB-IoT networks," *Wireless Communications and Mobile Computing*, vol. 2021, Article ID 5356193, 12 pages, 2021.

[6] W. Lu, Yu Ding, Y. Gao et al., "Resource and trajectory optimization for secure communications in dual-uav-mec systems," *IEEE Transactions on Industrial Informatics*, p. 1, 2021.

[7] W. Lu, P. Si, G. Huang et al., "Swipt cooperative spectrum sharing for 6g-enabled cognitive iot network," *IEEE Internet of Things Journal*, p. 1, 2020.

[8] L. Feltrin, G. Tsoukaneri, M. Condoluci et al., "Narrowband IoT: a survey on downlink and uplink perspectives," *IEEE Wireless Communications*, vol. 26, no. 1, pp. 78–86, 2019.

[9] X. Liu and X. Zhang, "Rate and energy efficiency improvements for 5G-based IoT with simultaneous transfer," *IEEE Internet of Things Journal*, vol. 6, no. 4, pp. 5971—–5980, 2019.

[10] X. Liu, X. B. Zhai, W. Lu, and C. Wu, "QoS-guarantee resource allocation for multibeam satellite industrial internet of things with NOMA," *IEEE Transactions on Industrial Informatics*, vol. 17, no. 3, pp. 2052–2061, 2021.

[11] I. M. Delgado-Luque, F. Blánquez-Casado, M. Garcia Fuertes et al., "Evaluation of latency-aware scheduling techniques for M2M traffic over LTE," in *2012 Proceedings of the 20th European Signal Processing Conference (EUSIPCO)*, pp. 989–993, ISSN, Bucharest, Romania, August 2012.

[12] N. Afrin, J. Brown, and J. Y. Khan, "A delay sensitive LTE uplink packet scheduler for M2M traffic," in *Proceedings of the 2013 IEEE Globecom Workshops (GC Wkshps)*, pp. 941–946, Atlanta, GA, USA, December 2013.

[13] A. Sampath, P. Sarath Kumar, and J. M. Holtzman, "On setting reverse link target SIR in a CDMA system," in *Proceedings of the Technology in Motion 1997 IEEE 47th Vehicular Technology Conference*, pp. 929–933, ISSN, Phoenix, AZ, USA, May 1997.

[14] Q. Li, Y. Wu, S. Feng, P. Zhang, and Y. Zhou, "Cooperative uplink link adaptation in 3GPP LTE heterogeneous networks," in *Proceedings of the 2013 IEEE 77th Vehicular Technology Conference (VTC Spring)*, pp. 1–5, ISSN, Dresden, Germany, June 2013.

[15] A. Durán, M. Toril, F. Ruiz, and A. Mendo, "Self-optimization algorithm for outer loop link adaptation in LTE," *IEEE Communications Letters*, vol. 19, no. 11, pp. 2005–2008, 2015.

[16] M. Gatnau Sarret, D. Catania, F. Frank et al., "Dynamic outer loop link adaptation for the 5G centimeter-wave concept," in *Proceedings of European Wireless 2015; 21th European Wireless Conference*, pp. 1–6, Budapest, Hungary, May 2015.

[17] J. Su, R. Xu, S. Yu, B. Wang, and J. Wang, "Redundant rule detection for software-defined networking," *KSII Transactions on Internet and Information Systems*, vol. 14, no. 6, pp. 2735–2751, 2020.

[18] J. Su, R. Xu, S. Yu, B. Wang, and J. Wang, "Idle slots skipped mechanism based tag identification algorithm with enhanced collision detection," *KSII Transactions on Internet and Information Systems*, vol. 14, no. 5, pp. 2294–2309, 2020.

[19] S.-M. Oh and J.S. Shin, "An efficient small data transmission scheme in the 3GPP NB-IoT system," *IEEE Communications Letters*, vol. 21, no. 3, pp. 660–663, 2017.

[20] C.-W. Huang, S.-C. Tseng, P. Lin, and Y. Kawamoto, "Radio resource scheduling for narrowband internet of things systems: a performance study," *IEEE Network*, vol. 33, no. 3, pp. 108–115, 2019.

[21] M. Wu, W. Huang, K. Sun, and H. Zhang, "A DQN-based handover management for SDN-enabled ultra-dense networks," in *Proceedings of the 2020 IEEE 92nd Vehicular Technology Conference (VTC2020-Fall)*, pp. 2577–2465, ISSN, Victoria, Canada, November 2020.

[22] N. Yang, H. Zhang, and R. Berry, "Partially observable multi-agent deep reinforcement learning for cognitive resource management," in *Proceedings of the GLOBECOM 2020 - 2020 IEEE Global Communications Conference*, pp. 1–6, Taipei, Taiwan, December 2020.

[23] Y. Zhang, X. Wang, and Y. Xu, "Energy-efficient resource allocation in uplink NOMA systems with deep reinforcement learning," in *Proceedings of the 2019 11th International Conference on Wireless Communications and Signal Processing (WCSP*, pp. 2472–7628, ISSN, Xi'an, China, October 2019.

[24] Z. Han, R. Zhang, F. Jin, and L. Ning, "Optimization of NB-IoT uplink resource allocation via double deep Q-learning," in *In Proceedings of the 10th International Conference on Communications, Signal Processing, and Systems (CSPS)*, Chang Bai Shan, China, August 2021.

[25] S. Sinche, D. Raposo, N. Armando et al., "A survey of IoT management protocols and frameworks," *IEEE Commun. Survey. Tutorials*, vol. 22, no. 2, pp. 1168–1190, 2020.

[26] N. Yang, H. Zhang, K. Long, H. Hsieh, and J. Liu, "Deep neural network for resource management in NOMA networks," *IEEE Transactions on Vehicular Technology*, vol. 69, no. 1, pp. 876–886, 2020.

[27] N. Jiang, Y. Deng, A. Nallanathan, and J. A. Chambers, "Reinforcement learning for real-time optimization in NB-IoT networks," *IEEE Journal on Selected Areas in Communications*, vol. 37, no. 6, pp. 1424–1440.